

Decao Yin

Experimental and Numerical Analysis of Combined In-line and Cross-flow Vortex Induced Vibrations

Thesis for the degree of philosophiae doctor

Trondheim, January 2013

Norwegian University of Science and Technology
Faculty of Engineering Science and Technology
Department of Marine Technology



NTNU – Trondheim
Norwegian University of
Science and Technology

NTNU

Norwegian University of Science and Technology

Thesis for the degree of philosophiae doctor

Faculty of Engineering Science and Technology
Department of Marine Technology

© Decao Yin

ISBN 978-82-471-4136-6 (printed version)
ISBN 978-82-471-4138-0 (electronic version)
ISSN 1503-8181

Doctoral Theses at NTNU, 2013:23



Printed by Skipnes Kommunikasjon as

Abstract

This thesis presents results from experimental and numerical investigations of the hydrodynamic forces on a rigid cylinder moving with prescribed orbits in uniform flow. The hydrodynamic forces are measured in both in-line (IL) and cross-flow (CF) directions. The measurements are processed to find excitation and added mass coefficients at discrete frequencies. The numerical simulations are used to illustrate the vortex shedding modes and are compared with the experimental results.

The hydrodynamic coefficients obtained from the harmonic forced motion experiments of a rigid cylinder do not always represent forces on a cross section of a flexible beam. The orbits used in the forced motion experiments are therefore extracted from the measured motions of cross sections of a flexible pipe under uniform and shear flows. Both periodic and observed orbits within a time window are applied as prescribed motions. Higher order displacement components are present in such orbits.

IL response amplitudes from combined IL and CF response are larger than pure IL response amplitudes. The hydrodynamic coefficients obtained from the periodic experiments are often larger than those obtained from the pure IL tests. Higher order displacement components are more common in the IL direction than in the CF direction, and higher order IL displacement components will cause larger hydrodynamic forces in both directions. The hydrodynamic coefficients obtained from periodic motion tests are adequate for representing quasi-periodic observed motions. For chaotic observed motions, periodic orbits will yield hydrodynamic coefficients with larger uncertainties.

Results from numerical analyses using large eddy simulation (LES) indicate that this method can be used to identify vortex shedding patterns and predict hydrodynamic forces under certain Re numbers and orbits.

Acknowledgements

This work has been carried out at the Centre for Ships and Ocean Structures (CeSOS), sponsored by the Research Council of Norway, at Norwegian University of Science and Technology (NTNU).

First, I would like to thank my supervisor Professor Carl Martin Larsen for guiding me during this research work. Valuable and constructive suggestions, fruitful discussions, critical comments are gratefully acknowledged. His patience and encouragement are highly appreciated.

I wish to thank Ida M. Aglen for great team work and help in MCLab during the experiments, post-processing of the experimental data, discussions and proof reading of my thesis. Special thanks to Dr. Zhiyong Huang for sharing his knowledge and experience of CFD calculation and helping me with building numerical model.

Thanks to Dr. Jie Wu, Dr. Elizabeth Passano and Dr. Philippe Mainçon for the fruitful discussions and proofreading of my thesis. Thanks to Dr. Kristoffer Høyem Aronsen and Dr. Prashant Kumar Soni for discussion and providing their pre- and post-processing script of experimental data.

I want to express my thanks to Dr. Trygve Kristiansen for his help providing me the model test data. Thanks to NTNU/MARINTEK laboratory staff, Torgeir Wahl, Knut Arne Hegstad and Ole Erik Vinje for their help with experiments. A special thank to Dr. Jan Vissher for helping with setting up of PIV equipment and post-processing of data. Thanks to Dr. Chittiappa Muthanna for sharing his experience in PIV experiments.

I would like to thank Dr. Zhen Gao and Dr. Shixiao Fu (SJTU) for fruitful discussions and suggestions. Thanks Dr. Muk Chen Ong, Dr. Dan Yang, Dr. Bingjie Guo and Dr. Tufan Aslan for their help with CFD calculation.

I'm also grateful to Dr. Karl Erik Kaasen and Halvor Lie from MARINTEK for sharing their experience and knowledge in processing the experimental data and during the research work.

I wish to thank all my fellow PhD students and postdocs in Marine Technology Centre for their help and friendship. Special thanks to Dr. Limin Yang, Dr. Biao Su, Dr. Wenbin Dong, Dr. Huirong Jia, Dr. Jørgen Hals and Jona Johari.

During my study, the administrative assistance and help from Ms. Sigrid Bakken Wold, Ms. Marianne Kjøllås, Ms. Karelle Gilbert, Ms. Linda Grønstad, Ms. Annika Bremvåg and Ms. Jannike Gripp are highly appreciated.

Thanks to Norwegian Deepwater Programme (NDP) for allowing me to use and publish some of the results.

I would like to thank Prof. Bjørnar Pettersen, Prof. Shan Huang and Senior Advisor. Finn Gunnar Nielsen for assessing my thesis and serving as my defence committee.

Last but not least, I'm grateful to my family and friends. Special thanks to my father for his sacrifice and support.

Contents

Abstract	i
Acknowledgements	iii
Nomenclature	xi
I Theory Background	1
1 Introduction	3
1.1 Motivation	3
1.2 Scope	4
1.3 State of the art	5
2 Problem Description & Theory	9
2.1 Environmental load	9
2.1.1 Wave	9
2.1.2 Current	9
2.2 Structure	11
2.3 Disturbed flow and vortex formation	14
2.3.1 Boundary layer	14
2.3.2 Vortex formation and flow regimes	14
2.4 Vortex induced vibrations	18
2.4.1 Introduction of VIV	18
2.4.2 Dimensionless parameters	20
2.4.3 Higher order motions/forces	25
2.4.4 Lock in	26
2.4.5 Drag amplification	27
2.4.6 Reynolds number effect	27
2.5 Experimental methods	29

2.5.1	Rigid cylinder free vibration experiments	30
2.5.2	Rigid cylinder-forced motion experiments	34
2.5.3	Flexible riser	41
2.6	VIVANA	42
2.6.1	General introduction	42
2.6.2	Excitation force model	43
2.6.3	Time sharing in VIVANA	44
2.7	A time-domain method	46
2.8	Numerical methods	49
2.8.1	Basic equations	49
2.8.2	Turbulence modelling	49
2.8.3	Research of forced motion of a rigid cylinder using LES	52
II	Experimental Methods	55
3	NDP High Mode VIV Tests	57
3.1	Test set-up	57
3.1.1	MARINTEK Ocean Basin	57
3.1.2	Test rig	57
3.1.3	Riser model	59
3.1.4	Coordinate systems	60
3.1.5	Instrumentation and measurements	62
3.1.6	Data acquisition	62
3.2	Test program and test procedures	63
3.2.1	Instrumentation verification and calibration tests. . .	63
3.2.2	Air and In-Water Decay Tests	63
3.2.3	Riser VIV Tests	63
3.3	Data processing and preparation to forced motion test . . .	64
3.3.1	Time window	64
3.3.2	Band-pass filter	64
3.3.3	Modal analysis	64
3.3.4	Choice of cases for forced motion tests	69
3.3.5	Definition of periodic orbits	70
4	Forced Motion Experiments	71
4.1	Test set-up	71
4.1.1	Facilities	71
4.1.2	Instruments	72
4.1.3	Coordinate system	76
4.1.4	Definition of phase angle	76

4.2	Modelling laws	78
4.2.1	Geometric similarity	78
4.2.2	Reynolds number	79
4.2.3	Non-dimensional frequency	79
4.2.4	Amplitude ratio	80
4.3	Test procedure	80
4.3.1	Decay tests	80
4.3.2	Stationary tests	82
4.3.3	Harmonic forced motion tests	82
4.3.4	Daily test	83
4.3.5	Main test matrix	83
4.4	Execution of the experiment	85
4.5	Signal processing procedure	87
4.5.1	Time window	87
4.5.2	Carriage motion signals	87
4.5.3	IL and CF motion signals	87
4.5.4	Force signals	88
4.6	Hydrodynamic coefficients	88
4.6.1	Fourier series	88
4.6.2	Band-pass filtering signal	89
4.6.3	Hydrodynamic coefficients for each frequency component	89
4.7	Analysis of forced motion tests with observed orbits	91
4.7.1	Drawback of the Fourier transform	91
4.7.2	Envelope detection	91
4.7.3	Statistical analysis	92
4.8	Processing and analysis of PIV data	93
4.8.1	Basic equations	93
4.8.2	PIV data post processing	93
5	Uncertainty Analysis and Quality Control	95
5.1	General description	95
5.1.1	Error and Uncertainty	95
5.2	Data Reduction Equations (DRE)	97
5.2.1	General	97
5.2.2	DRE for the hydrodynamic coefficients	99
5.3	Individual uncertainties in the DRE	101
5.3.1	Uncertainty in water density	101
5.3.2	Uncertainty in the cylinder diameter and length	102
5.3.3	Uncertainty in the cylinder mass	102

5.3.4	Uncertainties in the IL and CF displacements	103
5.3.5	Uncertainty in towing velocity	103
5.3.6	Uncertainty in drag force	103
5.3.7	Uncertainty in the decomposed force	103
5.4	Additional Error Sources	105
5.4.1	Residual flow	105
5.4.2	Cylinder end conditions	106
5.4.3	Blockage effect	106
5.4.4	Effective towing tank length	106
5.5	Uncertainty analysis results	107
5.5.1	Residual flow	107
5.5.2	Drag coefficient	108
5.5.3	Excitation coefficient	108
5.5.4	Added mass coefficient	109
5.5.5	Repeatability	109
5.5.6	2 nd order replication	111
III	Numerical Method	115
6	CFD numerical calculation	117
6.1	Pre-processing: computational model & mesh generation . . .	117
6.1.1	Mesh generation	117
6.1.2	Boundary conditions	119
6.1.3	Time step	121
6.1.4	Boundary layer	121
6.1.5	Mesh independence test	121
6.2	FLUENT solver	122
6.2.1	Turbulence model	122
6.2.2	Dynamic mesh	122
6.2.3	User Defined Functions (UDF)	123
6.2.4	Parallel Computing	123
IV	Results	125
7	Observations & Discussions	127
7.1	Results of the NDP High Mode VIV Tests	127
7.1.1	Global responses of a flexible beam	127
7.1.2	Local response: Characterisation of response types . .	129
7.2	Results of the forced motion experiments	135

7.2.1	Stationary: Drag coefficient and Strouhal number . . .	135
7.2.2	Harmonic: IL & CF vs. pure CF	136
7.2.3	Harmonic: IL & CF vs. pure IL	136
7.2.4	Periodic: Sensitivity of orbits	137
7.2.5	Periodic: Contour plots	140
7.2.6	Periodic: Higher order components	150
7.2.7	Periodic: Broad band and frequency drift	151
7.2.8	Periodic tests of uniform flow cases	153
7.2.9	Periodic: Self-excited transition	158
7.2.10	Energy transfer for Case N2340, periodic motions . . .	161
7.2.11	Non-periodic: Observed orbit experiments	164
7.3	Numerical simulation results	170
7.3.1	Two-dimensional analysis of Case N2030	170
7.3.2	3D analysis of harmonic ‘Figure 8’ orbits	172
7.3.3	3D simulation of Case N2340: Drag coefficients	175
7.3.4	3D simulation of Case N2340: Vortex shedding modes contour plot	177
7.3.5	3D simulation of Case N2340: Comparison of force time histories	178
7.3.6	3D simulation of Case N2340: Transient z vorticity . .	183
V	Conclusions & Future work	195
8	Conclusions	197
8.1	Principle Contributions	197
8.1.1	Forced motion experiments	197
8.1.2	2D and 3D CFD simulation	199
8.2	Recommendations for Future Work	200
	Bibliography	200
A	Calibration	211
A.1	Calibration of force sensors	211
A.2	Calibration of motion sensors	217
B	Orbits applied in forced motion experiments	219
C	Equations used in uncertainty analysis	231
D	2nd order replication level cases	233

E	Displacements in time-space of NDP cases	239
F	Higher order harmonic displacements and forces	243
G	Additional 3D simulation results of Case N2340	249

Nomenclature

Abbreviations

1D	One dimensional
2D	Two dimensional
3D	Three dimensional
CF	Cross-flow
CFD	Computational Fluid Dynamics
DNV	Det Norske Veritas
DOF	Degree of freedom
DRE	Data reduction equation
DVD	Digital videodisc
FFT	Fast Fourier Transform
IL	In-line
LES	Large Eddy Simulation
max	Maximum value
MCLab	Marine Cybernetics Laboratory
MGCplus	A data acquisition system for laboratory from HBM company
min	Minimum value
MIT	Massachusetts Institute of Technology
NDP	Norwegian Deepwater Program

NTNU	Norwegian University of Science and Technology
PIV	Particle image velocimetry
RP	Recommended practice
SGS	Sub-Grid Scale
UDF	User-defined function
UMF	Uncertainty magnification factor
VIV	Vortex induced vibration

Roman Upper Case Symbols

A	Oscillation amplitude
A^*	Normalized oscillation amplitude, $\frac{A}{D}$
$A_{CF/IL,MC}$	Oscillation amplitude in CF or IL direction in MCLab forced motion tests
$A_{CF/IL,NDP}$	Oscillation amplitude in CF or IL direction in NDP tests
$A_{CF/IL}$	Oscillation amplitude in CF or IL direction
C	Damping coefficient
C_D	Drag coefficient
C_L	Lift coefficient
$C_{a,IL/CF,n}$	Added mass coefficient for n^{th} harmonic component in IL or CF direction
$C_{e,IL/CF,n}$	Excitation coefficient for n^{th} harmonic component in IL or CF direction
D	Cylinder diameter
D_{MC}	Cylinder diameter of MCLab
D_{NDP}	Cylinder diameter of NDP tests
E	Young's modulus
F_A	Added mass force

F_E	Excitation force
F_H	Hydrodynamic force
F_{H0}	Amplitude of hydrodynamic force
$F_{IL,mean}$	Average drag force, average IL force.
F_{IL}	Drag force, IL force.
H_{max}	Maximum wave height
I	Area moment of inertia
K	Stiffness
KC	Keulegan-Carpenter number
L	Cylinder length
L_c	Correlation length
M	Mass of test cylinder
M_A	Added mass of test cylinder
R	Correlation coefficient
Re	Reynolds number
St	Strouhal number
T	Oscillation period
T_w	Wave period
U	Current velocity. In-line coordinate of small carriage in MCLab.
U^*	Normalized velocity, $\frac{U}{f_0 D}$.
U_d	Soliton currents due to internal waves
U_r	Reduced velocity
U_s	Stokes drift current velocity
U_t	Tidal current velocity
U_w	Wind generated current velocity

U_{MC}	Towing velocity in MCLab
U_{NDP}	Towing velocity in NDP tests
U_{set-up}	Current velocity
V_{200}	Water particle velocity at 200 m depth
V_{max}	Maximum water particle velocity
W	Cross-flow coordinate of small carriage in MCLab
X	Towing direction of main carriage in MCLab
Z	Cross-flow coordinate of small carriage in MCLab

Greek Symbols

α	Exponent. Phase angle between IL and CF displacement
δ	Thickness of boundary layer
ϵ	Strain
Λ	Spanwise correlation length
λ	Wave length; scale factor
λ^*	Normalized wave length, $\frac{U}{f_{osc}D}$
μ	Viscosity
ω	Circular frequency
ω_{osc}	Circular oscillation frequency
ϕ	Phase angle between hydrodynamic force and the motion
π	3.14159
ρ	Water density
τ	Time variable
θ	Absolute sensitivity coefficient
ν	Kinematic viscosity

Roman Lower Case Symbols

\bar{m}	Mass ratio
\ddot{x}	Cylinder acceleration
\dot{x}	Cylinder velocity
\hat{f}	Non-dimensional oscillation frequency
f_0	Cylinder eigen frequency in still water
f_v	Vortex shedding frequency of a moving cylinder
$f_{osc,MC}$	Oscillation frequency of forced motion tests in MCLab
$f_{osc,NDP}$	Oscillation frequency of NDP tests
$f_{osc,CF/IL}$	Oscillation frequency in CF or IL direction
f_{osc}	Oscillation frequency
f_{st}	Vortex shedding frequency of fixed cylinder
g	Acceleration of gravity, ms^{-3}
h	Water depth
h_0	Reference water depth
k	Wave number
l_c	Correlation length
m	Mass
m^*	Mass ratio
t	Time variable. Wall thickness of NDP pipe
u_1	Residual flow velocity
u_r	Relative velocity
x	Cylinder displacement, displacement in IL direction
z	Vertical coordinate, displacement in CF direction

Part I

Theory Background

Chapter 1

Introduction

1.1 Motivation

As the offshore oil and gas industry has developed, focus has moved from shallow and moderate water depths to deep water area, which causes traditional exploitation and production systems to be unsuitable.

Marine risers constitute the main connection between a floating platform and the well-heads or manifold on the seabed. The response of marine risers shows that vortex-induced vibrations (VIV) will occur frequently due to currents, and VIV may cause costly and environmentally-damaging fatigue failures. In the deep waters of the Gulf of Mexico and offshore West Africa, the wave climate is milder than in the North Sea, and VIV may account for the largest contribution to riser fatigue damage. As water depth increases, damage related to wave and vessel motion may stay approximately the same or diminish, but currents exist and exert forces over the whole length of risers, making VIV more important in deeper water. However, VIV of long risers is generally less understood than other load effects, and this has led to an intensive research activity in recent years (Trim et al., 2005).

To predict VIV and include its influence during the design process, empirical models has been established based on hydrodynamic coefficients obtained from experiments. During the past decades, a lot of research has been done on a rigid cylinder with one degree of freedom (DOF) forced motions. Most of the previous work has used harmonic motions, which are not likely to occur in nature. Hydrodynamic coefficients for ‘realistic’ combined in-line (IL) and cross-flow (CF) VIV are needed in order to develop more reliable empirical methods for response prediction. Focus of present research will

be on forced motions of a rigid cylinder that follows orbits found from experiments with a flexible beam in sheared current. These experiments included cases with response at high mode orders.

1.2 Scope

Direct measurement of local forces on a long flexible beam subjected to VIV is not feasible. Local forces can be estimated by inverse analysis (Mainçon et al., 2008). An alternative method is to identify the cross section orbits at a number of positions along the flexible pipe and use these as forced motions for a rigid cylinder in uniform flow. By keeping the Reynolds number, non-dimensional frequency and amplitude ratio identical for the two types of experiments, forces measured on the rigid cylinder will become a direct scaling of the forces on the corresponding cross section of the flexible beam. This experimental technique was applied by Soni (2008), but his tests included only uniform flow cases for a flexible beam experiment. The purpose of the present work has been to apply the same experimental method to flexible beam cases with sheared flow, and thereby obtain a more general basis for hydrodynamic coefficients to be applied in empirical models for combined IL and CF VIV (Yin and Larsen, 2010).

Hydrodynamic forces for combined IL and CF VIV are studied using both experimental and numerical methods. Focus will be on forced motion tests which use measured orbits of cross sections along a flexible pipe in sheared current profiles with high mode response.

‘High mode VIV experiment’ was a set of experiments carried out by the Norwegian Deepwater Programme (NDP), (Braaten and Lie, 2005). Based on the data from these tests, the orbits of cross sections on the flexible beam were generated, and then used in forced motion test with a rigid cylinder with much larger diameter. Forces were measured at the ends of the cylinder model.

Particle Image Velocimetry (PIV) technique was applied to identify the vortex pattern in the wake for selected test cases.

Numerical calculation has been performed and results were compared to observations from forced motion experiments including the use of PIV. The differences between calculations and observations have been identified and the reasons of the deviation explained.

1.3 State of the art

Three main categories of experimental work have been done to study VIV:

1. Free oscillation of rigid cylinders
 - a. Pure CF: Vikestad (1998), Williamson and Jauvtis (2004)
 - b. Combined CF & IL: Moe and Wu (1990), Sarpkaya (1995), Williamson and Jauvtis (2004), Dahl et al. (2006)
2. Forced oscillation of rigid cylinders
 - a. Pure CF: Sarpkaya (1978), Gopalkrishnan (1993), Morse and Williamson (2009)
 - b. Pure IL: Aronsen (2007)
 - c. Combined CF & IL: Aronsen (2007), Dahl (2008), Soni (2008)
3. Free oscillation of flexible beams: Huse et al. (1998), Chaplin et al. (2005), Braaten and Lie (2005), Vandiver et al. (2006), Soni (2008)

In order to find the fatigue damage imposed by VIV, three types of models are developed:

1. Parametric response models: One example is *DNV-RP-F105 Free spanning pipelines* (2006), using amplitude envelope curves established from experiments data and full scale test to estimate fatigue damage from VIV. The IL response amplitude ratio is mainly a function of reduced velocity and stability parameter, while for CF direction, the amplitude ratio is mainly a function of reduced velocity and current flow velocity ratio.
2. Empirical models: These will use empirical force coefficients in a response model of a flexible beam, SHEAR7 and VIVANA are examples of such programs. Both programs lack coefficients for the combined CF & IL vibrations and higher order components are not taken into account.
3. Computational Fluid Dynamics (CFD) is also an important tool. However, due to high requirement of computing time, CFD still can not be used extensively for practical VIV predictions.

Figure 1.1 shows the classification of various VIV prediction models based on the situation 10 years ago.

2.5⁶ The empirical models

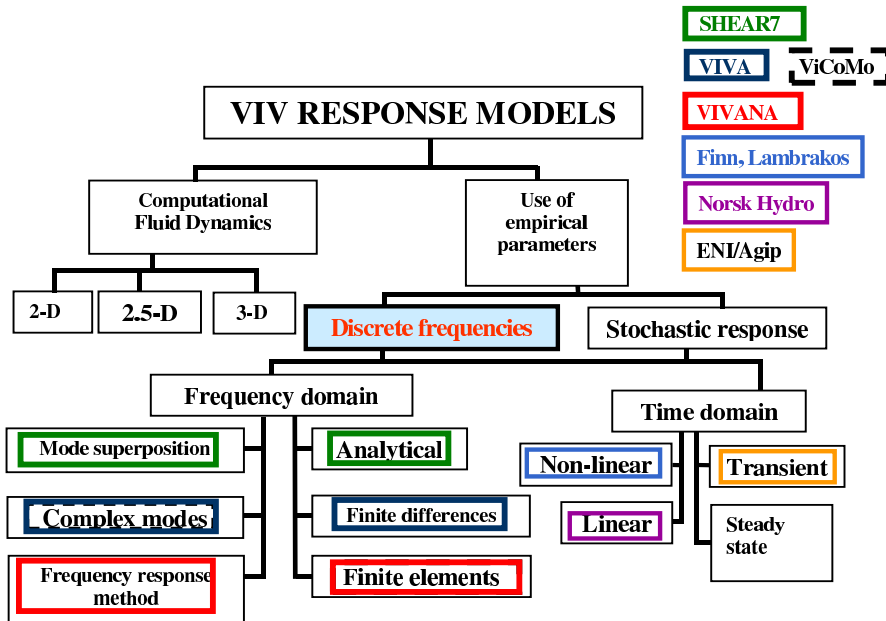


Figure 2.11: Classification of VIV models credited Larsen et al [27].
 Figure 1.1: Classification of VIV prediction models (Larsen et al., 2001).

Figure 2.11 shows the classification of VIV models available to conduct the VIV analysis of slender marine structures [27]. This section will only deal with the empirical force coefficient models and this results have been widely used in the empirical frequency domain prediction of GF response for slender body dynamic coefficient models. VIVA[10], SHEAR7[44] and VIVANA are all based on the excitation zone (excitation coefficient) model from Gopalkrishnan.

It is well known that pure CF response of slender beams will not happen; there will always be an IL component as well. The underlying assumption VIVA follows the iterating procedure to find the response frequency, shape and amplitude for the use of data from pure CF tests has been that the IL component will not have a large influence on GF response. This has, however, been proved to be wrong. It contains an extensive database for different types of cross-sections. The tests behind these coefficients include also the single/double/triple frequency oscillations. On the other hand, SHEAR7 considers uniform cross-sections, which implies modeling limitations. It gives results at six frequencies for use of defined added mass. The Strouhal number should also be defined as input.

1. IL response for a flexible beam will normally start at a lower flow speed than CF. Hence, IL motions may contribute significantly to fatigue accumulation during long periods with low current speed. This effect is in particular of interest for free spanning pipelines.

VIVANA

VIVANA [28], [48] is developed for analysis of VIV and is based on a set of empirical coefficients for added mass, external forces and damping. Figure 2.12(a) shows the added mass will hence give a larger number of stress cycles than CF.

2. IL response will have a frequency that is twice the CF frequency and will hence give a larger number of stress cycles than CF.

3. Active mode shapes for IL response will normally have higher order than for CF. Thus IL dynamic bending stresses might become higher than CF even if the amplitudes are lower.

Pure IL response of flexible beams will take place at the primary mode at low reduced velocities simply because the frequency of IL forces is twice the CF frequency. Hence, coefficients for pure IL response are of interest, which was the motivation for Aronsen (2007). He carried out forced motion tests on a rigid cylinder with pure IL motions. The coefficients are in particular of interest for calculating fatigue for free spanning pipelines (Larsen et al., 2007).

The combination of IL and CF response has attracted increasing interest during recent years (Larsen and Lie, 2008). It has been observed that CF motions will change the IL response significantly as compared to pure IL response. The IL amplitude will increase, and the CF and IL response frequencies will be decided by an adjustment of their added mass. The interaction is not fully understood, but it is obvious that Aronsen (2007)'s results are inadequate for predicting IL response when CF response also is present. Hence, there is a need for coefficients valid for combined IL and CF response.

To sum up, the interaction between CF and IL VIV and the effect of higher order components are not fully understood, and the primary goal of the present research work is to improve the understanding of these phenomena.

Chapter 2

Problem Description & Theory

2.1 Environmental load

Wind, wave, current and earthquake are main environment loads on ocean structures. In this thesis, wave and current loads will be discussed.

2.1.1 Wave

For marine structures, first order wave forces with the period range $3 - 24s$ are conventionally assumed to have significant energy (Larsen, 2007). If linear wave theory is applied with respect to infinite water depth, wave parameters of the two boundaries of this range and a typical wave condition in North Sea can be calculated, see Table 2.1.

From Table 2.1, we can see, even under extreme conditions with $T_w = 24 s$, wave velocity decreases to 50% of it at the surface. In shallow water, wave induced vibrations should be taken into account, while in this thesis, only risers located in the water with moderate and deep water depth are considered, and hence wave effects are neglected.

2.1.2 Current

Ocean currents could be generated by many factors, the most common categories are (*10th International Ship and Offshore Structures Congress (ISSC)*, 1988):

- local wind generated currents, U_w

Table 2.1: Wave parameters, calculated using linear wave theory.

T_w (wave period)	(s)	3	15	24
$\lambda = \frac{gT_w^2}{2\pi}$ (wave length)	(m)	14	351	900
$k = \frac{2\pi}{\lambda}$ (wave number)	(-)	0.448	0.018	0.007
$H_{max} = \frac{\lambda}{7}$	(m)	2	50	128
$V_{max} = \frac{\pi H_{max}}{T_w}$	(m/s)	2.1	6.7	16.8
$V_{100} = V_{max}e^{-k100}$	(m/s)	0.076	1.1	8.4

H_{max} = Maximum wave height,

V_{max} = Maximum water particle velocity,

V_{100} = Water particle velocity at 100 m depth.

- tidal currents, U_t
- component generated by Stokes drift, U_s
- from major ocean circulation, depending on geographical location, U_m
- soliton currents due to internal waves generated by density gradients, U_d
- component due to set-up phenomena and storm surges, U_{set-up}

The total surface current velocity U can be expressed as:

$$U = U_w + U_t + U_s + U_m + U_d + U_{set-up} \quad (2.1)$$

In general, the current velocity varies in space and time, $U = U(x, y, z, t)$. From the design point of view, it is common to assume the current only varies with water depth at a given position. (*8th International Ship and Offshore Structures Congress (ISSC)*, 1982) suggests that the tidal and local wind components described as:

$$U_t(z) = \begin{cases} U_t(0), & \text{for } -(h - 10) \leq z \leq 0 \\ U_t(0)\log_{10}(1 + \frac{9z}{10-h}), & \text{for } -h < z < -(h - 10) \end{cases} \quad (2.2)$$

$$U_w(z) = \begin{cases} U_w(0)\frac{h_0+z}{h_0}, & \text{for } -h_0 \leq z \leq 0 \\ 0, & \text{for } z < -h_0 \end{cases} \quad (2.3)$$

DNV-RP-C205 Environmental conditions and environmental loads (2009) recommends for the tidal component:

$$U_t(z) = U_t(0)\left(\frac{h+z}{h}\right)^\alpha, \text{ for } z \leq 0 \quad (2.4)$$

where $U_t(0)$ and $U_w(0)$ are tidal and wind generated current velocity at the still water level; $U_t(z)$ and $U_w(z)$ are tidal and wind generated current velocity at water level z ; h is water depth; h_0 is the reference depth and can be chosen as 50 m (*10th International Ship and Offshore Structures Congress (ISSC)*, 1988); z is vertical coordinate; α is exponent, typically taken as $1/7$.

The current velocity varies with water depth, and this variation depends on the local oceanographic climate, the vertical density distribution and the water flux. Deep water profiles could be complicated, as the direction can even change 180 degrees with depth (*DNV-RP-C205 Environmental conditions and environmental loads*, 2009). In open sea, the tidal velocity may be up to $\approx 0.5 \text{ m} \cdot \text{s}^{-1}$. From the design point of view, a typical total current velocity in the North Sea is 1 m/s (Faltinsen, 1990).

2.2 Structure

Slender structures are common structures in offshore industry, such as risers of various utilities and pipelines used for transportation. Figure 2.1 shows different types of riser in offshore structures.

Structure parameters

Structure parameters describe cylinder geometry, density and damping. The following parameters have been used.

Length to diameter ratio

This is the ratio of cylinder length (L) to its diameter (D) and it provides a measure of the geometric shape:

$$\frac{L}{D} \quad (2.5)$$

As the oil and gas industry moves towards deep sea, the length of risers varies from hundreds to thousands of meters. The diameter depends on the riser type, the typical diameter of different type risers is shown in Table 2.2. Generally, the riser has a diameter less than one meter, which gives a length-to-diameter ratio up to $O(10^4)$.

Still water Eigenfrequency

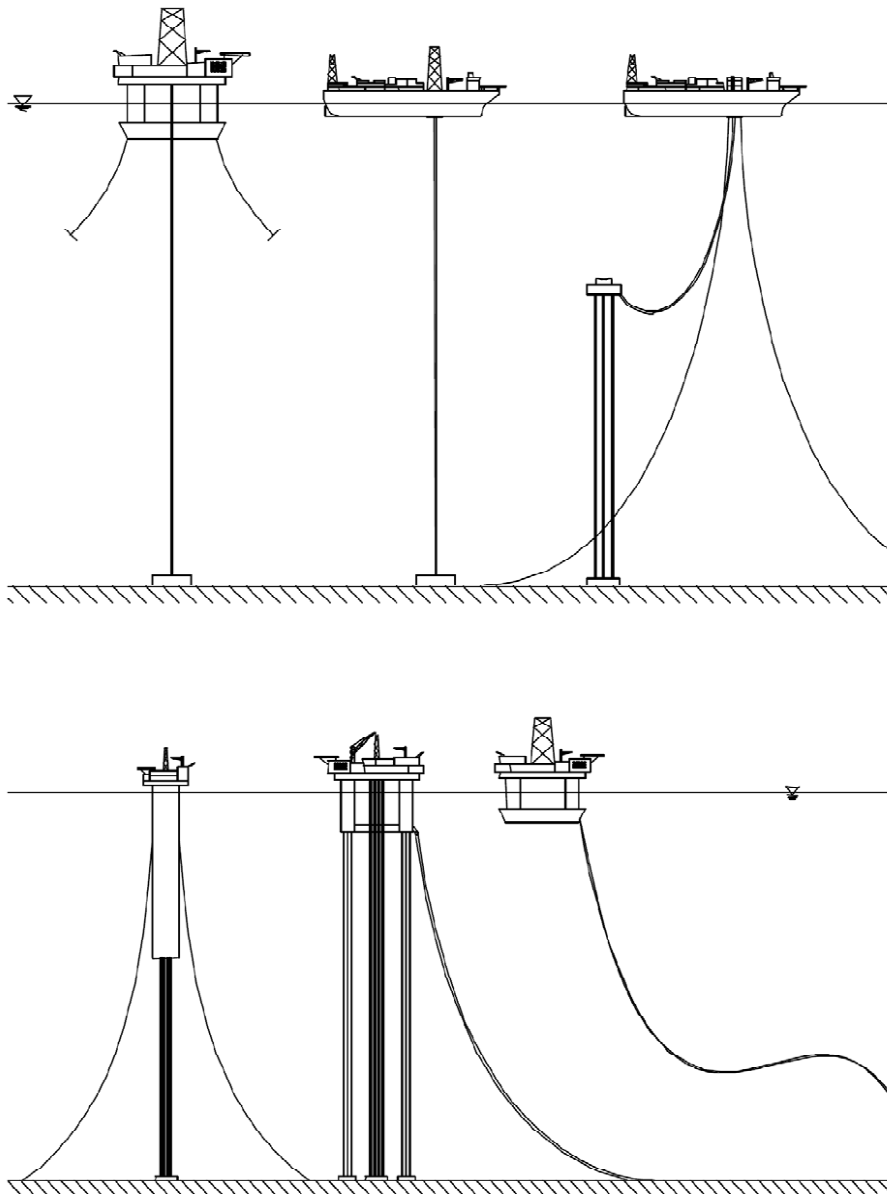


Figure 2.1: Examples of metallic riser configurations and floaters, from *DNV-OS-F201 Dynamic risers* (2010).

Table 2.2: Typical riser diameters (Larsen, 2008).

Riser type	Typical diameter (m)
Drilling riser	0.55
Production riser	0.22
Export riser	0.30
Workover riser	0.18

An eigenmode may be expressed by:

$$\phi(x) = \phi_0 \sin\left(\frac{n\pi}{l}x\right), \quad n = 1, 2, 3, \dots \quad (2.6)$$

where l is the riser length and ϕ_0 is the amplitude.

For a tension dominated beam with moment-free end support in both ends, the eigen-frequency of the n^{th} mode is:

$$\omega_{s,n} = \frac{n\pi}{l} \sqrt{\frac{T}{m}}, \quad n = 1, 2, 3, \dots \quad (2.7)$$

where T is the tension in the string, and m is cylinder mass per unit length.

For a bending dominated beam, the eigen-frequencies are:

$$\omega_{b,n} = \frac{n^2\pi^2}{l^2} \sqrt{\frac{EI}{m}}, \quad n = 1, 2, 3, \dots \quad (2.8)$$

where EI is the beam stiffness.

Since both beams have the same mode shapes, taking both tension and bending into account, Eqn. (2.7) and (2.8) become:

$$\omega_{bs} = \frac{n\pi}{l} \sqrt{\frac{T}{m} + \frac{n^2\pi^2}{l^2} \cdot \frac{EI}{m}}, \quad n = 1, 2, 3, \dots \quad (2.9)$$

Mass ratio

The ratio of the cylinder mass per unit length to the mass of fluid it displaces is called the mass ratio:

$$\bar{m} = \frac{m}{\frac{\pi}{4}\rho D^2} \quad (2.10)$$

where m is structural mass, ρ is density of water.

2.3 Disturbed flow and vortex formation

2.3.1 Boundary layer

This discussion is based on Sumer and Fredsøe (1997) and Zdravkovich (2002).

As a flow passes a stationary circular cylinder, or a circular cylinder moves in a fluid at rest, the flow around the surface of the cylinder and in the wake changes with increasing relative velocity between the fluid and the cylinder.

The disturbed flow can be roughly divided into three regions, shown in Figure 2.2:

1. **Boundary layer:** Two layers attached to the surface of the cylinder. The thickness of the boundary layers δ is very small compared with D . For example, the thickness of laminar boundary layer is $\frac{\delta}{D} = O(\frac{1}{\sqrt{Re}})$, which $\delta/D \ll 1$ for Re larger than $O(100)$. Due to the small thickness, the velocity increases from zero on the surface to free stream velocity, which causes a high velocity gradient normal to the cylinder surface, see Figure 2.2b. So, for a Newtonian fluid, the shear stress must be considered here.
2. **Shear layer:** The boundary layers around the cylinder are subjected to a favourable pressure gradient downstream followed by a small region of adverse pressure gradient. The boundary layers will separate due to this gradient imposed by the divergent geometry of the flow environment at the rear side of the cylinder. The point where the separation of boundary layer happens is named the separation point, see Figure 2.2a. The separated boundary layers continue to develop downstream and then form shear layers.
3. **Wake:** After the separation point, the wide downstream region of separated flow is called wake.

2.3.2 Vortex formation and flow regimes

A non-dimensional parameter, Reynolds number (Re), defined by the ratio of inertial forces to viscous forces was first introduced by Stokes (1851), but then Reynolds (1883) popularized it, so it was named as Reynolds number. In the case of flow past a circular cylinder, it is defined as:

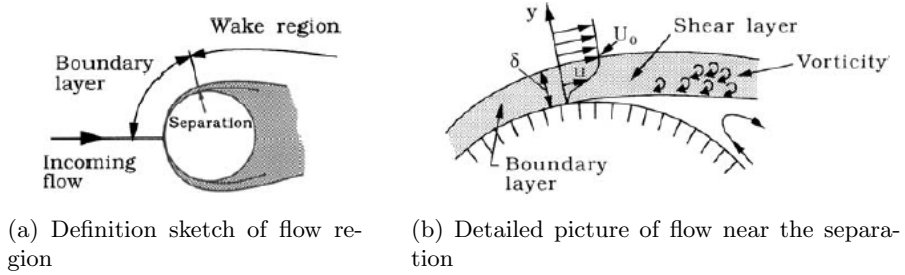


Figure 2.2: Flow regime definition sketch (Sumer and Fredsøe, 1997).

$$Re = \frac{\text{Inertia force}}{\text{Viscous force}} = \frac{UD}{\nu} \quad (2.11)$$

where U is the flow velocity, ν is the kinematic viscosity.

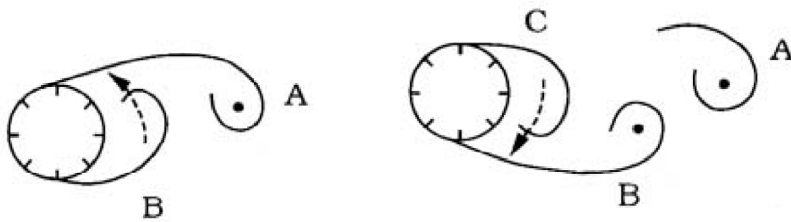
Vortex formation and shedding

When $Re > 5$, boundary layers will separate due to the large adverse pressure gradient at the rear side of the cylinder and shear layers are formed, see Figure 2.2b. Before separation, the boundary layers contain a large amount of vorticity, which is transferred into the shear layers formed downstream of the separation point. The shear layers will roll up into vortices, with the same direction as the vorticity in the boundary layers.

Sumer and Fredsøe (1997) describes the vortex shedding process. As Re increases, the formed vortices become unstable when exposed to small disturbance for $Re > 40$. The vortex at one side of the cylinder will grow larger than the other side. Since these two vortices have opposite vorticity direction, the inner sides of these will have the same velocity direction, and this velocity vector drives Vortex B across the wake, see Figure 2.3a. Furthermore Vortex B will cut off the vorticity supply of Vortex A from the boundary layer. At this instant, Vortex A is shed and convected downstream to the wake.

A new vortex (Vortex C) will be formed after shedding of Vortex A, and vortex B will act the same way as Vortex A. The supply of vorticity will be cut off by Vortex C and it is shed into the wake, see Figure 2.3b.

Vortices shed alternatively in this way and a vortex street formed in the wake, which is called *von Kármán* vortex street.



(a) Prior to shedding of Vortex A, Vortex B is being drawn across the wake

(b) Prior to shedding of Vortex B, Vortex C is being drawn across the wake.

Figure 2.3: Vortex shedding process (Sumer and Fredsøe, 1997).

Vortex shedding pattern

Figure 2.4 shows the sketches and vorticity field of different vortex shedding modes. The classification and sketches given herein are defined by Williamson and Roshko (1988), Williamson and Govardhan (2004), Jauvtis and Williamson (2004) and Morse and Williamson (2009).

- 2S mode: there is only one vortex shedding into wake in each half cycle.
- 2P mode: there is one pair of vortices shedding into wake every half cycle.
- $P + S$ mode: a pattern where in each cycle a vortex pair and a single vortex are shed.
- $2P_o$ mode: in 2P mode, a secondary vortex in each pair of vortices is much weaker than the primary (first) vortex.
- $2P + 2S$ mode: comprises two vortex pairs forming at the top and bottom of the body trajectory as in the 2P mode, but with the inclusion of single vortices between each vortex pair.
- 2T mode: comprises a triplet of vortices being formed in each half cycle.
- 2C mode: each half cycle comprises two co-rotating vortices formed.

Mode	Sketch	Vorticity field
2S		
2P		
P+S		
2P ₀		
2P+2S		
2T		
2C		

Figure 2.4: Sketches and vorticity field of various vortex shedding modes, Williamson and Roshko (1988), Williamson and Govardhan (2004), Jauvtis and Williamson (2004) and Morse and Williamson (2009).

Flow regimes

The detailed flow regimes according to different Re number is shown in Figure 2.5.

The Re numbers used in this thesis is in the *subcritical* zone, which is $300 < Re < 3 \cdot 10^5$. Here, the wake is completely turbulent, while, the boundary layers around the cylinder surface still remain laminar over the whole subcritical range.

The division of Reynolds number is not definite. Blevins (1990) decreased the *subcritical* range to $300 < Re < 1.5 \cdot 10^5$, and he stated that the laminar boundary layers separate at about 80° aft of the leading edge of the cylinder and that the vortex shedding is strong and periodic in this regime.

The range $1.5 \cdot 10^5 < Re < 3.5 \cdot 10^6$ is called *transitional* range. In this range, the cylinder boundary layer becomes turbulent, and the separation points move aft to 140° . Regular and stable vortex shedding is disturbed by the laminar separation bubbles and 3D effects, consequently causing a broader spectrum of shedding frequencies for smooth surface cylinders.

Pure CF VIV experiments indicate that both response amplitudes and hydrodynamic coefficients approaches stable values inside the subcritical flow regime when Re exceeds $1.5 \cdot 10^4 - 2.0 \cdot 10^4$. For Re below $1.5 \cdot 10^4$ the hydrodynamic coefficients are significantly influenced by varying Re (Sarpkaya, 2004).

In practice, offshore structures experience high Reynolds number flow. For instance, Re for a current with velocity of 1 m/s past a riser with diameter 0.5 m is approximately $5 \cdot 10^5$.

2.4 Vortex induced vibrations

2.4.1 Introduction of VIV

The surface force may be divided into two orthogonal components: a pressure component and a viscous component. By integrating these forces along the surface, the total fluid force is found. When considering VIV, pressure forces are prominent, and viscous forces are neglected. Since the vortices shed alternatively from each side, the resulting force on the cylinder oscillates. The shedding of vortices generates time varying pressure over the


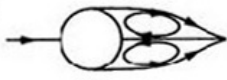







a)		<p>No separation. Creeping flow</p> <p>$Re < 5$</p>
b)		<p>A fixed pair of symmetric vortices</p> <p>$5 < Re < 40$</p>
c)		<p>Laminar vortex street</p> <p>$40 < Re < 200$</p>
d)		<p>Transition to turbulence in the wake</p> <p>$200 < Re < 300$</p>
e)		<p>Wake completely turbulent.</p> <p>A: Laminar boundary layer separation</p> <p>$300 < Re < 3 \times 10^5$</p> <p>Subcritical</p>
f)		<p>A: Laminar boundary layer separation</p> <p>B: Turbulent boundary layer separation; but boundary layer laminar</p> <p>$3 \times 10^5 < Re < 3.5 \times 10^5$</p> <p>Critical (Lower transition)</p>
g)		<p>B: Turbulent boundary layer separation; the boundary layer partly laminar partly turbulent</p> <p>$3.5 \times 10^5 < Re < 1.5 \times 10^6$</p> <p>Supercritical</p>
h)		<p>C: Boundary layer com- pletely turbulent at one side</p> <p>$1.5 \times 10^6 < Re < 4 \times 10^6$</p> <p>Upper transition</p>
i)		<p>C: Boundary layer comple- tely turbulent at two sides</p> <p>$4 \times 10^6 < Re$</p> <p>Transcritical</p>

Figure 2.5: Description of flow regimes (Sumer and Fredsøe, 1997).

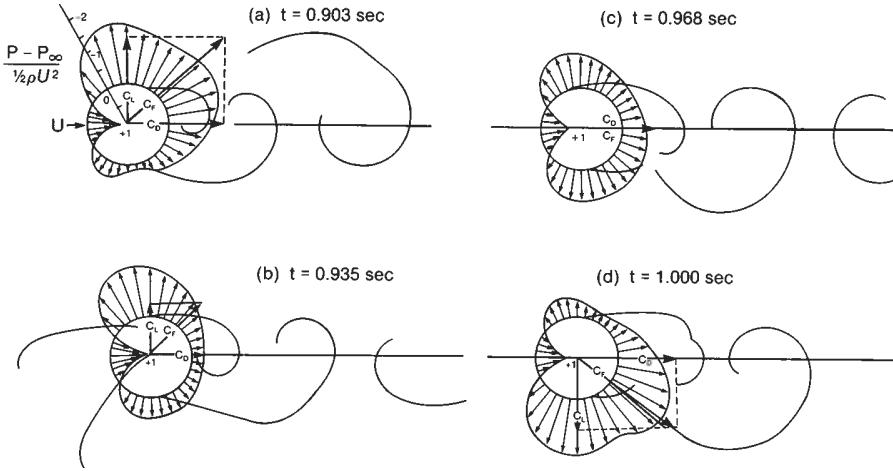


Figure 2.6: A sequence of simultaneous surface pressure fields and wake forms at $Re = 112,000$ for approximately $T/3$ of vortex shedding (Drescher, 1956).

cylinder, see Figure 2.6. By integrating the pressure on the cylinder surface we may find the force in CF (force perpendicular to the flow) direction and drag force in IL (force parallel to the flow) direction. Obviously, the lift force oscillates at the vortex shedding frequency, while the drag force oscillates at twice the vortex shedding frequency.

2.4.2 Dimensionless parameters

In order to describe the VIV phenomenon, various dimensionless parameters are used. Definitions are given in Halse (1997), Vikestad (1998) and Skaugset (2003). The dimensionless parameters used in this thesis are defined below.

Flow parameters

Flow parameters are used to describe flow conditions. In addition to Re given by Eq.(2.11), there is another parameter:

Strouhal number, St

St is the dimensionless proportionality constant given as the ratio between the predominant frequency of vortex shedding and the diameter of cylinder

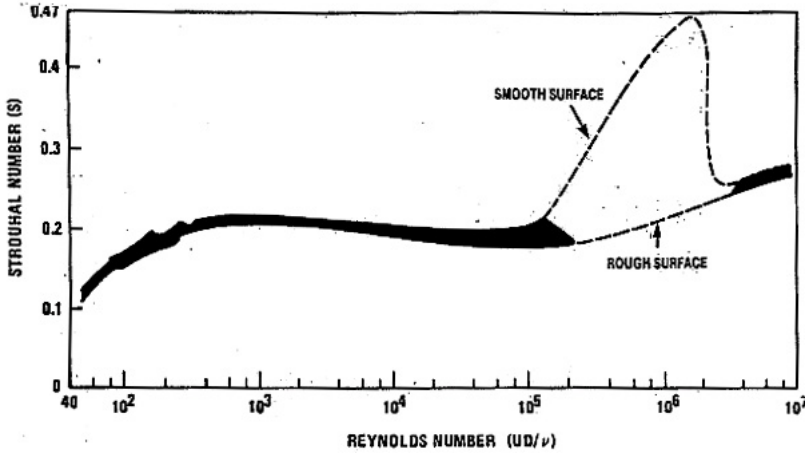


Figure 2.7: Strouhal number-Reynolds number relationship for circular cylinders (Blevins, 1990).

divided by the free stream velocity:

$$St = \frac{f_{st}D}{U} \quad (2.12)$$

where f_{st} is the vortex shedding frequency of a fixed cylinder in water, which means a full cycle of vortex shedding process; U is the free stream velocity.

The Strouhal number is a function of Reynolds number for any given cross-section, Figure 2.7 shows its variation for a circular cylinder. For a circular cylinder, St is approximately constant at 0.2 for a wide range of Reynolds number.

Keulegan-Carpenter number, KC

This number consider a stationary structure in a oscillating flow, and it is defined as:

$$KC = \frac{U_m}{fD} = \frac{2\pi U_m}{\omega D} = \frac{U_m T}{D} \quad (2.13)$$

where U_m is amplitude of flow velocity, and f is the oscillation frequency (for an oscillating structure in calm water, U_m is the structure motion velocity and f is the structure oscillating frequency). Large KC number defines a condition that is close to steady state current.

Turbulence intensity

A steady, turbulent flow $u(x, y, z, t)$ can be described as a sum of time average component \bar{u} and fluctuating component $u'(t)$ (White, 2003):

$$u(t) = \bar{u} + u'(t) \quad (2.14)$$

For flows which contain a periodic component, then

$$u(t) = \bar{u} + \tilde{u} + u'(t) \quad (2.15)$$

where $\tilde{u}(x, y, z, t) = \frac{1}{N} \sum_{j=1}^N u(x, y, z, t + jT) - \bar{u}(x, y, z)$.

It is important to distinguish time average turbulence intensity and phase average turbulence intensity (time dependent) (Nielsen, 1992). Time averaged turbulence intensity is defined as root-mean-square of fluctuating component:

$$u'_{rms} = (\bar{u'^2})^{0.5} \quad (2.16)$$

While the phase average turbulence intensity (time dependent) is $(\tilde{u'^2})^{0.5}$.

It can be normalized by free stream velocity (Blevins, 1990):

$$\frac{u'_{rms}}{U} \quad (2.17)$$

Interaction parameters

The fluid-structure interaction parameters are defined in the following:

Amplitude ratio

The amplitude ratio is used to describe the oscillation amplitude in forced oscillation experiments and response amplitude in free vibration experiments. The subscript indicates the direction of the oscillation.

$$\left(\frac{A}{D}\right)_{IL/CF} \quad (2.18)$$

Oscillation frequency, f_{osc}

If the oscillation is one DOF in IL direction, the oscillation frequency is $f_{osc,IL}$, as long as there is CF component, the oscillation frequency is $f_{osc,CF}$.

Non-dimensional frequency, \hat{f}

The non-dimensional frequency is defined as:

$$\hat{f} = \frac{f_{osc}D}{U} \quad (2.19)$$

For a riser with uniform cross section shape exposed to sheared current, assuming the whole riser has unique response frequency, the non-dimensional frequency increases with decreasing current velocity.

Reduced velocity, U_r

The reduced velocity is defined as:

$$V_r = \frac{U}{f_0D} \quad (2.20)$$

where f_0 is the natural frequency of the cylinder in still water. This definition is in consist with (Aronsen, 2007; Dahl, 2008). In other literatures, it is also named as ‘Velocity ratio’, U^* (Jauvtis and Williamson, 2004), other symbols such as V_{r0} (Wu, 2011), U_r (Vikestad, 1998; Soni, 2008)

In order to compare with other results, we define ‘true reduced velocity’ as the ratio between the path length in flow direction per cycle and the cylinder diameter by using oscillation frequency:

$$U_r = \frac{\text{Path length per cycle}}{\text{Diameter}} = \frac{UT_{osc}}{D} = \frac{U}{f_{osc}D} \quad (2.21)$$

same definition but with other symbols are: $U_{r,true}$ (Vikestad, 1998), V_r (Wu, 2011).

Relative strain

Based on the assumption that a flexible beam has sinusoidal modes in both directions, and the order of dominating modes for IL is twice the order for CF response, which is a tension dominated pipe (see Eq.2.7), the relative bending strain from CF and IL response can be calculated as (Soni et al., 2009):

$$\frac{\varepsilon_{IL}}{\varepsilon_{CF}} = \frac{4A_{IL}/D}{A_{CF}/D} = 4 \frac{A_{IL}}{A_{CF}} \quad (2.22)$$

where ε_{IL} and ε_{CF} are bending strain in IL and CF directions.

Correlation of the wake

In the turbulent wake regime ($Re > 200$), vortex shedding doesn't occur uniformly, but in cells along the length of the cylinder. The average length of the cells (L_c) is listed in Table 2.3. The average length of vortex cells increases considerably when the cylinder is oscillated in the cross-flow direction.

Table 2.3: Average vortex cell lengths vs. Reynolds number of smooth cylinders, from Sumer and Fredsøe (1997).

Re	L_c	Source
$40 < Re < 150$	(15-20)D	Gerlach and Dodge (1970)
$150 < Re < 10^5$	(2-3)D	Gerlach and Dodge (1970)
$1.1 \cdot 10^4 < Re < 4.5 \cdot 10^4$	(3-6)D	El Baroudi (1960)
$\geq 10^5$	0.5D	Gerlach and Dodge (1970)
$2 \cdot 10^5$	1.56D	Humphreys (1960)

The lift force acting on a section of cylinder with unit length can be given by:

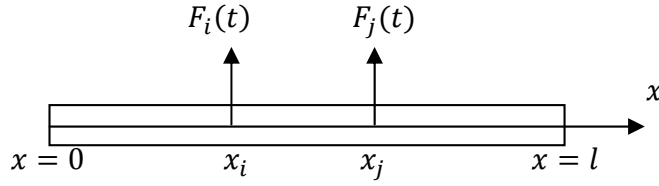
$$dF(t) = \frac{1}{2} \rho C_L U^2 D \sin(2\pi f_{st} t + \alpha) \quad (2.23)$$

where C_L is the lift coefficient, which has to be found from experiments. Sarpkaya and Isaacson (1981) reported a value of 1.35; while Ottesen Hansen (1982) recommended 0.9. C_L varies with Re and oscillation amplitude of a non-fixed pipe (Vandiver, 1993). α is a phase angle that will vary along the cylinder. It is crucial for calculating the resulting force on a long cylinder (Larsen, 2007).

To describe the variation of phase angle, the concept of correlation length is introduced here (Ottesen Hansen, 1982; Larsen, 2007). Considering the forces acting at two positions along the pipe, see Figure 2.8, the cross correlation function is assumed to be exponential:

$$r_{ij}(|x_i - x_j|) = \exp\left[-\frac{2|x_i - x_j|}{l_c}\right] \quad (2.24)$$

where l_c is the *correlation length*.

Figure 2.8: Correlation between F_i and F_j .

The resulting force amplitude F_a on the cylinder shown in Figure 2.8 is given by:

$$F_a = \sqrt{\int_0^l \int_0^l dF_a(x_1) dF_a(x_2) r_{12}(|x_i - x_j|) dx_1 dx_2} \quad (2.25)$$

where r_{12} is given by Eq. (2.24) and $dF_a(x) = \frac{1}{2}\rho C_L(x)U(x)^2 D(x)$.

Assume the flow is uniform and the cylinder has constant diameter, the force is:

$$F_a = dF_a \sqrt{\int_0^l \int_0^l \exp\left[-\frac{2|x_i - x_j|}{l_c}\right] dx_1 dx_2} \quad (2.26)$$

The total force will be time varying:

$$F(t) = F_a \sin(2\pi f_v t) = \frac{1}{2}\rho C_L^* U^2 D \quad (2.27)$$

where C_L^* is called *effective lift coefficient* and it can be measured from experiments.

$$C_L^* = C_L \sqrt{\int_0^l \int_0^l \exp\left[-\frac{2|x_i - x_j|}{l_c}\right] dx_1 dx_2} \quad (2.28)$$

Once C_L is known and C_L^* is measured, l_c can be found by using Eq. (2.28). For a fixed cylinder, the correlation length is seen to be 1D to 5D.

2.4.3 Higher order motions/forces

Jauvtis and Williamson (2004) found a clear force component at 3 times of the dominant frequency in addition to the fundamental frequency when the amplitude in CF increased, which is attributed to the ‘2T’ vortex shedding mode, see Figure 2.4.

Based on the experiments at Lake Seneca and Gulf Stream, Vandiver et al. (2006) found that the fatigue damage caused by the higher harmonic response component could be twenty to forty times the fatigue damage of the primary frequency in CF direction.

Aronsen (2007) compared experimental results of three different rigid cylinder forced motion test (pure CF, pure IL, combined IL and CF) with harmonic motions, he concluded that higher order harmonic forces has close relation with IL oscillations. Relative amplitude of higher order harmonic CF forces to the first harmonic increases with increasing IL oscillation amplitude. This is also verified by Dahl (2008).

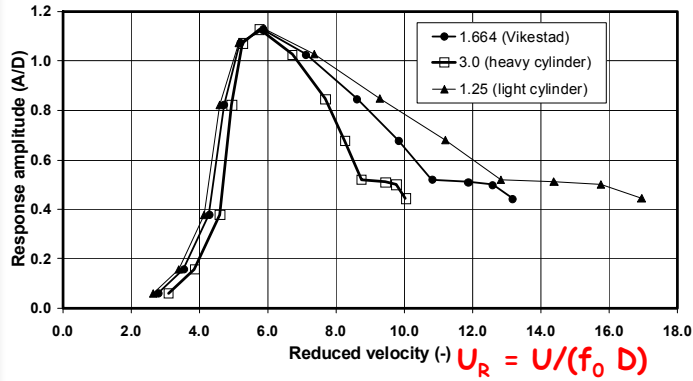
Modarres-Sadeghi et al. (2010) developed a method to estimate the fatigue life of risers continuously along the span direction of the riser without introducing more instruments mounted on the risers. The estimation of NDP tests showed that higher harmonic strain and acceleration components are important, a large 3rd harmonic contribution and sometimes a 5th harmonic are observed for the majority of test cases: for linear sheared flow cases, the higher harmonics are about 1/3 of total; while for the uniform flow cases, they are around 50% of total. This calls for including higher harmonic components when performing fatigue damage calculations.

2.4.4 Lock in

‘Added mass’ is defined as the hydrodynamic force component in phase with the acceleration of the cylinder in IL or CF direction. In a given flow condition, varying added mass adjusts the eigenfrequency of the cylinder, causing oscillation frequency f_{osc} to become a compromise between f_0 (eigenfrequency in still water) and f_{st} (vortex shedding frequency of fixed cylinder), confer Larsen (2000). Consequently, in actual flow condition, $f_{osc} = f_v$, and it is also eigenfrequency of the cylinder, (Sarpkaya, 1995), this phenomena is called ‘Lock-in’. The influence of added mass on the cylinder depends on the dry mass of the cylinder, as for two cylinders with the same dimensions, the lighter one will suffer more influence from added mass than the other, see Figure 2.9.

ed velocity" plot
 rs with varying
 A heavy
 ll have a more
 onse
 it will be less
 o added mass
 an a cylinder with
 ratio

The mass ratio is important for the amplitude vs. reduced velocity curve



22

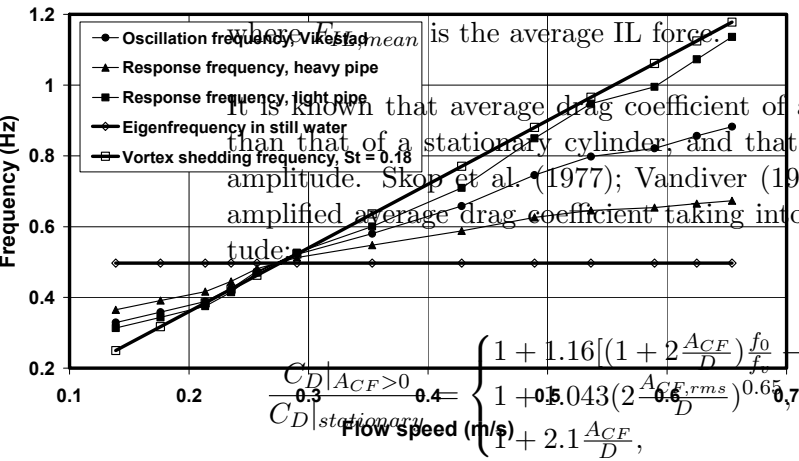
Figure 2.9: Response amplitude vs reduced velocity curve (Larsen, 2000).

2.4.5 Drag amplification

- and also the response frequency curve

The average drag coefficient is defined as:

$$C_D = \frac{F_{IL,mean}}{\frac{1}{2}\rho DLU^2} = \frac{\lim_{k \rightarrow \infty} \frac{\int_t^{t+kT} F_{IL}(\tau) d\tau}{kT}}{\frac{1}{2}\rho DLU^2} \quad (2.29)$$



where $F_{IL,mean}$ is the average IL force.

It is known that average drag coefficient of a oscillating cylinder is larger than that of a stationary cylinder, and that it is a function of transverse amplitude. Skop et al. (1977); Vandiver (1983); Blevins (1990) suggested amplified average drag coefficient taking into account of transverse amplitude:

$$C_D = \begin{cases} 1 + 1.16 \left[\left(1 + 2 \frac{ACF}{D} \right) \frac{f_0}{f_r} - 1 \right]^{0.65}, & \text{Skop et al. (1977)} \\ 1 + 0.043 \left(2 - \frac{ACF}{D} \right)^{0.65}, & \text{Vandiver (1983)} \\ 1 + 2.1 \frac{ACF}{D}, & \text{Blevins (1990)} \end{cases} \quad (2.30)$$

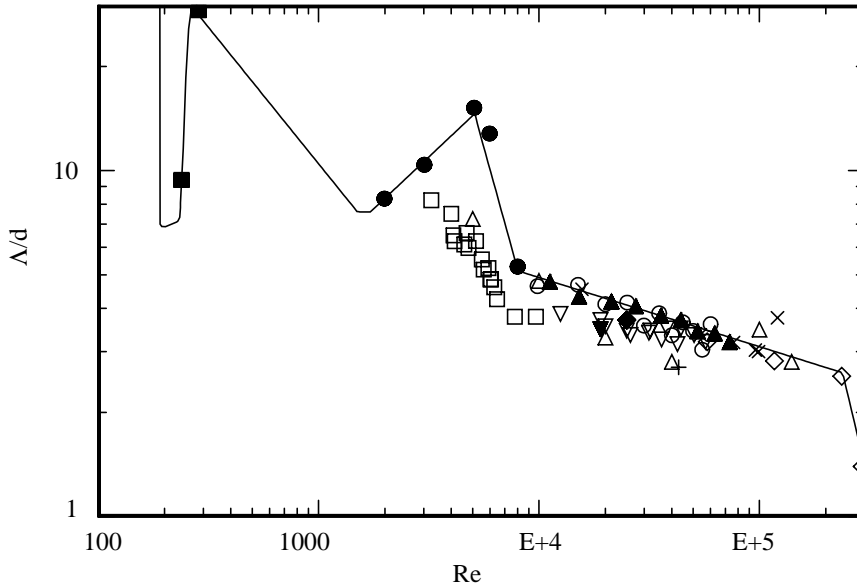
20

2.4.6 Reynolds number effect

Norberg (2003) reviewed previous research on fluctuating lift force acting on a cylinder as function of flow speed, varying mass ratio in one direction, covering a range of Re from 47 to 2×10^5 from onset of vortex shedding to almost the end of subcritical. A cylinder will not be able to adjust its eigenfrequency in the same way as a cylinder with low mass ratio since added mass is a relatively smaller contribution to total mass than for a cylinder with high mass ratio.

flow regime (see Figure 2.5).

C. Norberg / Journal of Fluids and Structures 17 (2003) 57–96



Normalized spanwise correlation length versus Reynolds number: \square , Leehey and Hanson (1971); \blacklozenge , Bearman and Wadcock (1973); \blacktriangleleft , Kacker et al. (1974); \blacktriangleright , Bruin and Davies (1975); \circ , Sonnevile (1976); \blacktriangledown , Novak and Tanaka (1977); ∇ , Moeller (1982); \triangle , Iida et al. (1997); \blacksquare , $d = 3\text{ mm}$; \bullet , $d = 6\text{ mm}$; \blacktriangle , $d = 40\text{ mm}$; \blacklozenge , Bruin and Davies (1975); \blacktriangledown , Novak and Tanaka (1975); \circ , Sonnevile (1976); \blacksquare , $d = 3\text{ mm}$; \bullet , $d = 6\text{ mm}$; \blacktriangle , $d = 40\text{ mm}$; (Norberg, 2003).

and Leehey (1984) ($Tu = 0.9\%$) and Mohr (1981) ($Tu = 1.0\%$). A summary of previous laboratory experiments of both sectional and total lift fluctuations, for $Re < 3 \times 10^5$ and $Tu \leq 2\%$, is found in Table 1; numerical results (2-D/3-D) are summarized in Appendix B.

Figure 2.10 shows the normalized spanwise correlation length vs Re . It is seen that the correlation length is independent of the degree of turbulence in the shedding region. On the contrary, the correlation length is strongly dependent on the Reynolds number. The correlation length scaled by the diameter, Λ/d (Section 2.1), is the same for all the data. This quantity is even larger than for the r.m.s. lift coefficient (Ribeiro, 1992). In fact, up to now, there are no reliable measurements of Λ/d for $Re < 2 \times 10^3$. In an attempt to fill this gap of information, a near-wake spanwise correlation study was carried out, extending down to $Re = 230$ (Morse and Williamson, 2009) compared contour plots of fluid force on the cylinder in the plane of normalized amplitude and wavelength (see Figure 2.15) at two Reynolds numbers (4000 and 12000). The only difference is that the zero-excitation contour in the 2D regime has a distinctly higher amplitude at $Re = 12000$. Both the fluid force regimes and the shape of fluid excitation contours are similar. But still, more evidence is needed to conclude that results from at these two Reynolds number are valid through the whole Reynolds number range.

0.3, which coincides with the Reynolds number with inception of low-spectral-quality shedding (Fig. 1). The value of $Re \approx 5 \times 10^3$ has been suggested in Norberg (1998) to be due to a spanwise resonance phenomenon in vortical structures of mode B (Williamson, 1988b, 1996b) and shear-layer vortices (Bloor, 1964; Wu et al.

main objective of this work is to make an overview of the fluctuating lift acting on a circular cylinder, especially, the influence of Reynolds number and the relation between fluctuating lift and flow features in the near-wake

2.5 Experimental methods

The control equation of a simple one degree-of-freedom dynamic system is:

$$M\ddot{x} + C\dot{x} + Kx = F_H \quad (2.31)$$

where M is the oscillating structure mass, C is damping coefficient, K is the stiffness, F_H is the hydrodynamic force, x is the displacement.

Given that the force F_H is harmonic, the response will also be harmonic:

$$x = A\sin(\omega t) \quad (2.32)$$

$$\dot{x} = \omega A\cos(\omega t) \quad (2.33)$$

$$\ddot{x} = -\omega^2 A\sin(\omega t) \quad (2.34)$$

where A is oscillating amplitude, ω is circular oscillation frequency, and t is time.

The total hydrodynamic force F_H which is the pressure resultant on the surface of the model is defined as (Larsen, 2000):

$$\begin{aligned} F_H &= F_{H0}\sin(\omega t + \phi) \\ &= F_{H0}\sin(\omega t)\cos(\phi) + F_{H0}\cos(\omega t)\sin(\phi) \end{aligned} \quad (2.35)$$

or:

$$F_H = F_A\sin(\omega t) + F_E\cos(\omega t) \quad (2.36)$$

where F_{H0} is the amplitude of hydrodynamic force, ϕ is the phase angle between hydrodynamic force and the motion. The first term in the right side in Eq. (2.36) is the added mass force F_A and the second is excitation force F_E .

Insert Eqs. 2.32 to 2.36 into Eq.2.31, than it changes to:

$$\begin{aligned} &M[-\omega^2 A\sin(\omega t)] + C[\omega A\cos(\omega t)] + K[A\sin(\omega t)] \\ &= F_{H0}\sin(\omega t + \phi) \end{aligned} \quad (2.37)$$

or:

$$\begin{aligned} &M[-\omega^2 A\sin(\omega t)] + C[\omega A\cos(\omega t)] + K[A\sin(\omega t)] \\ &= F_A\sin(\omega t) + F_E\cos(\omega t) \end{aligned} \quad (2.38)$$

2.5.1 Rigid cylinder free vibration experiments

In free vibration experiments, the energy is balanced at steady state, so the damping term and excitation force in Eqn. 2.38 disappear:

$$M[-\omega^2 A \sin(\omega t)] + K[A \sin(\omega t)] = F_A \sin(\omega t) \quad (2.39)$$

then moving the added mass force into the left side:

$$(M + M_A)[- \omega^2 A \sin(\omega t)] + K[A \sin(\omega t)] = 0 \quad (2.40)$$

CF free vibration

Free vibration of an elastically mounted rigid cylinder has been studied by several researchers, and many fundamental topics are discussed in the comprehensive reviews (Sarpkaya, 1979; Bearman, 1984; Williamson and Govardhan, 2004).

Feng (1968)'s experimental results, in which the mass ratio is as high as $m^* \approx 250$ were widely used, because the experiment was performed in the air. Two response branches (initial branch and lower branch) are clearly seen in Feng (1968)'s high mass ratio experiments, see Figure 2.11, and there is a hysteretic mode between them.

From the ocean engineering point of view, however a much lower mass ratio is encountered, normally of the order of 1 (see section 2.2).

Khalak and Williamson (1999) performed similar type experiment in water with a much lower mass ratio ($m^* = 10.1$) than Feng (1968), and they observed another response branch, which is called 'upper branch'. From Figure 2.11 it is seen the transition between the initial and upper branches shows a hysteresis, while the transition from the upper branch to the lower branch shows an intermittent switching (Morse and Williamson, 2009).

Response amplitude results from pure CF free vibration experiments done by Vikestad (1998) are shown in Figure 2.12. It shows that VIV takes place for a wide range of reduced velocity for this case, this can also be seen in Figure 2.11. While the mass ratio in Vikestad (1998) is 1.664, the reduced velocity range for a higher mass ratio cylinder will be narrower, see Figure 2.9.

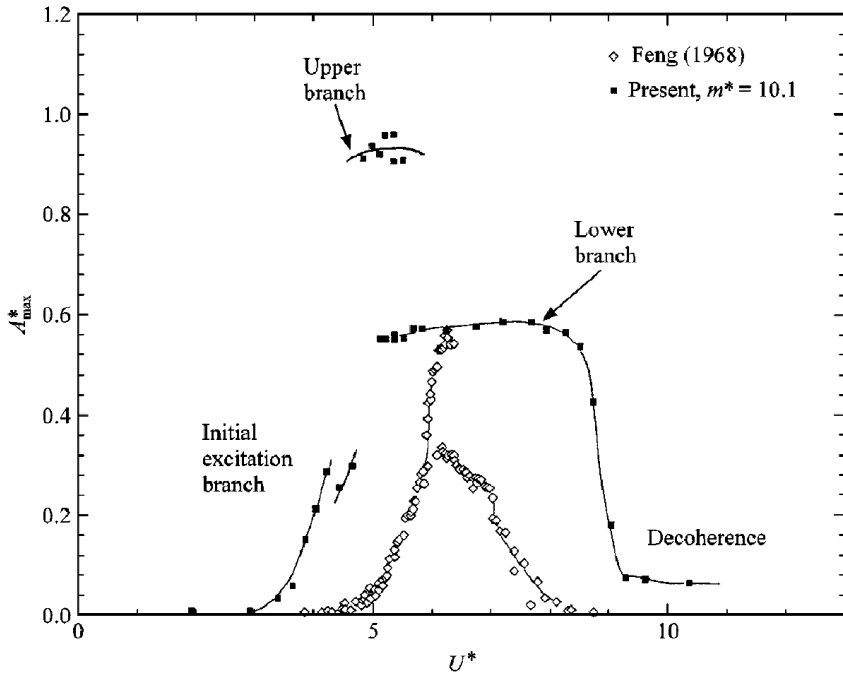


Figure 2.11: Peak amplitude ratio plot versus reduced velocity. It shows clearly the three response branches (initial, upper and lower). This low m^* type of response ($m^* = 10.1$) is distinct from Feng (1968)'s high m^* type ($m^* = 248$), in which there are only two branches (initial and lower) (Khalak and Williamson, 1999).

IL free vibration

Johansen (2004) and Huse (2004) performed pendulum tests in IL direction to extract hydrodynamic force coefficients from the transient phase, both excitation tests and decay tests were carried out.

Combined IL & CF free vibration

Moe and Wu (1990) conducted combined IL and CF free vibration experiments at $Re = 5,000 \sim 45,000$, and compared with pure CF free vibration experimental results. Larger CF response amplitudes are seen in two degrees of freedom than pure CF experiments. In order to compare the free vibration of a cylinder with forced vibrations, the true reduced velocity (or non-dimensional frequency) must be kept the same between them.

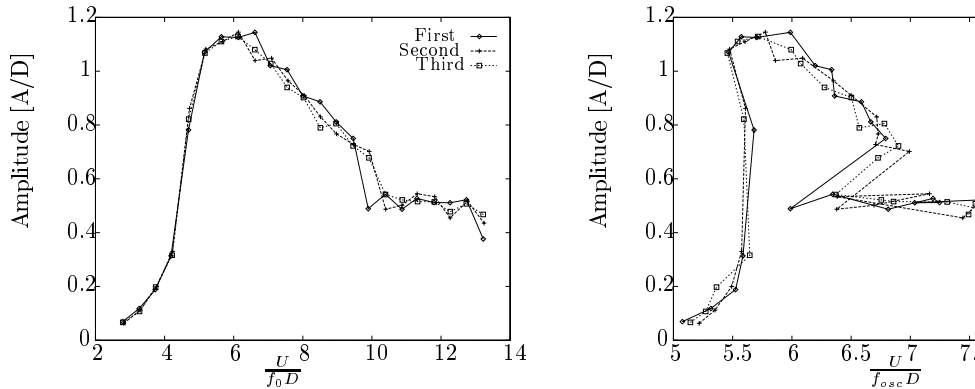


Figure 2.12: CF response amplitude results from Vikestad (1998)'s free vibration experiments. (a) Displacement $(\sqrt{2})(\frac{A}{D})_{rms}$ as function of reduced velocity (b) Displacement $(\sqrt{2})(\frac{A}{D})_{rms}$ as "true reduced velocity"

Figure 5.12: Displacement vs. reduced velocity

In Sarpkaya (1995)'s experiments, two ratios between IL and CF natural frequency were applied (1:1 and 2:1), and he also observed a different CF response amplitude in two degrees of freedom than pure transverse experiments. When the natural frequency ratio was equal to one, a much larger $(A/D)_{CF}$ and a shift of peak response to higher reduced velocity were seen. The CF amplitude response curve had two peaks at different reduced velocities.

the reduced velocity, while Fig. 5.12(b) uses the "true reduced velocity". As one discrepancy is larger when using the "true reduced velocity". From Fig. 5.12(a) there is a small difference between the two tests for $U_r < 8$. The peak displacement for U_r ranges from 1 to 5 and the displacement increases from 0.2 A/D up to 15,000. A main difference between the two tests is that the displacement increases nearly linearly with the natural frequency ratio. In the Sarpkaya (1995) tests, the reduced velocity is exactly the same. One finding is that when $U_r < 5$, IL motion is most pronounced. We also note that the range for maximum response is only from 5.5 to 6.5. Scale two plots may make the discrepancies more visual in Fig. 5.12(b). An other way to call the "true reduced velocity" results are to introduce the non-dimensional frequency $\hat{f} = \frac{f_{osc} D}{U}$. The A_{CF} can be as high as 1.5D, and '2T' vortex shedding mode was found (Figure 2.4).

Dahl (2008) tuned the natural frequency ratio between IL and CF and the from 1:1 to 2:1 in his free vibration experiments. In Fig. 5.13, the displacement is plotted as function of \hat{f} as large CF response is completed, the drag amplification was studied. Large 3rd harmonic force component in CF direction was highlighted. It was also observed periodic orbital motion at a natural frequency ratio 1:9, while the zero lift has the same shape as Fig. 5.13. If there was absolutely no structural damping apparatus, the lines giving the displacement should more or less correspond to zero

Vortex-induced vibration for two degrees of freedom

35

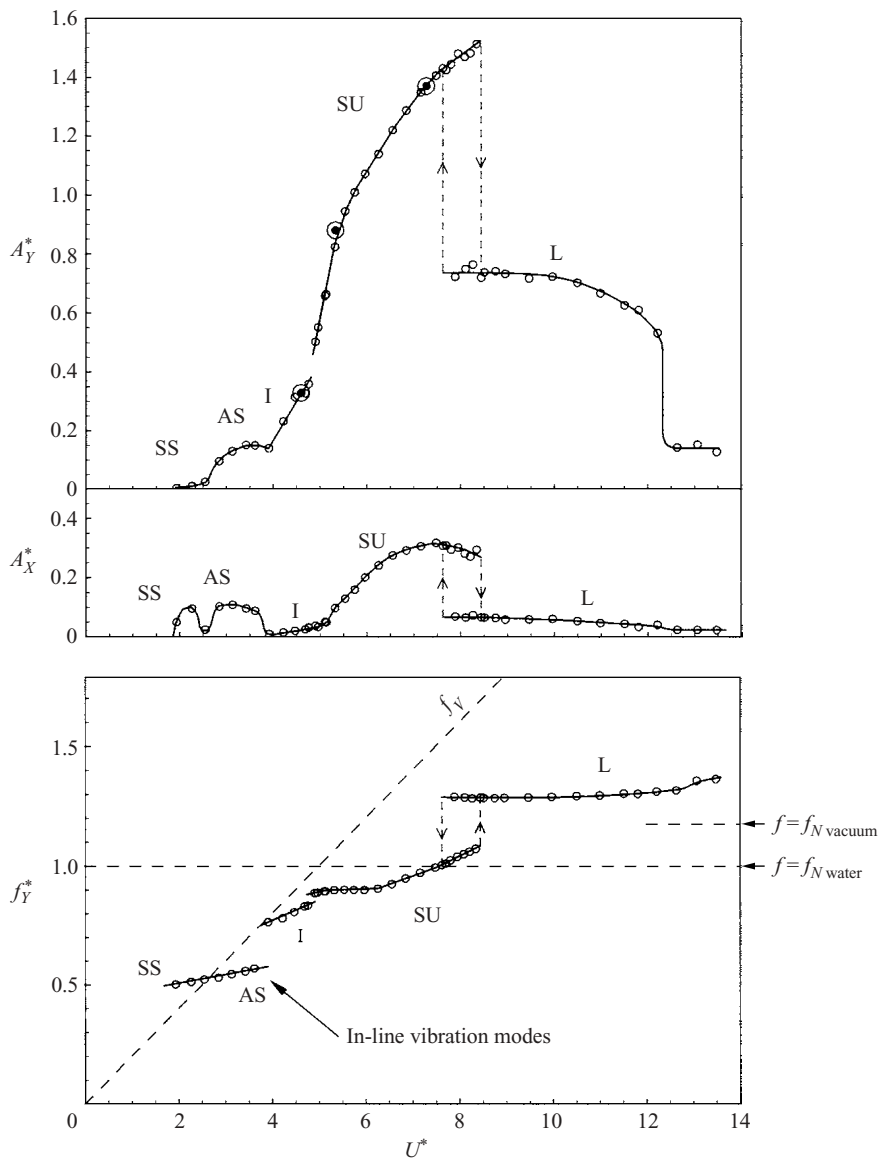


Figure 5. Response of the system for 'low' mass ratios ($m^* = 2.6$). Response amplitudes (A_X^* and A_Y^*) and transverse frequency (f_Y^*) are plotted versus normalized velocity (U^*). The overlap regime between the super-upper branch (SU) and the lower branch (L) exhibits a hysteresis, indicated by the arrows in the inset plot, when the super-upper branch and the lower branch exhibits a hysteresis (Jauvtis and Williamson, 2004).

Although the super-upper branch will be shown later to correspond with a vortex mode different from the 2P mode, it is interesting that it starts at a (low-amplitude) 2P boundary, and also terminates at a (high-amplitude) 2P mode boundary in the Williamson–Roshko map (after which the vortex formation desynchronizes from the body motion in this map). The significance of the super-upper branch for X, Y vibrations terminating at the 2P boundary (relevant to Y-only motion), is not clear, and might represent a coincidence. Another surprising feature of such a presentation in the Williamson–Roshko map is that the super-upper branch is a 2P mode, while the lower branch is a 1P mode.

dual lock-in showed at a ratio equals to 2.

2.5.2 Rigid cylinder-forced motion experiments

By reorganizing the terms in Eq. 2.37, we have:

$$M[-\omega^2 A \sin(\omega t)] - F_{H0} \sin(\omega t + \phi) = \text{Measured force} \quad (2.41)$$

$$(M + M_A)[-\omega^2 A \sin(\omega t)] - F_E \cos(\omega t) = \text{Measured force} \quad (2.42)$$

In Eq. (2.42), the hydrodynamic force was decomposed into two parts, one is in phase with acceleration (added mass), the other is in phase with velocity (excitation force).

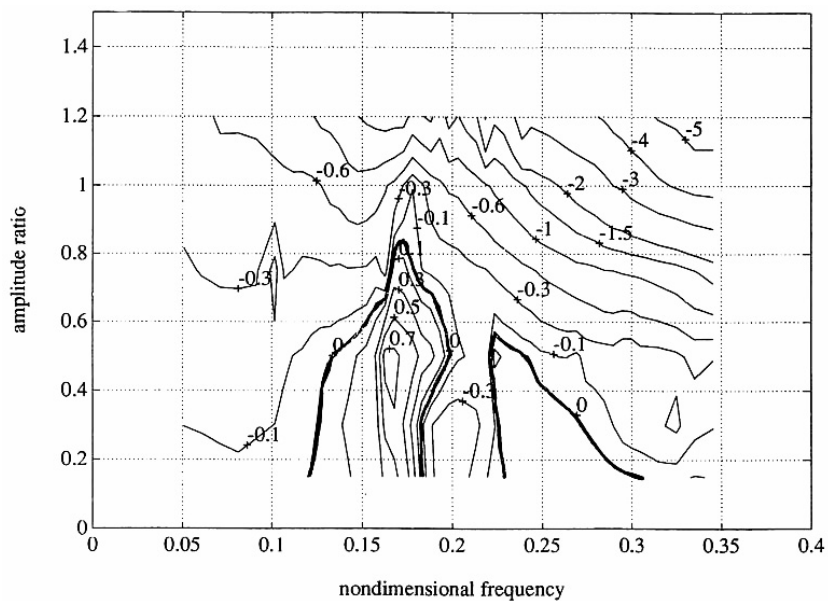
Pure CF harmonic forced motion

Many researchers put their efforts into experiments with a cylinder undergoing forced motions perpendicular to the incoming flow (CF). This work can be found as early as Bishop and Hassan (1964). They found a phase shift of lift force when the vibration takes place near Strouhal frequency, and that the wake can both excite and damp the oscillation.

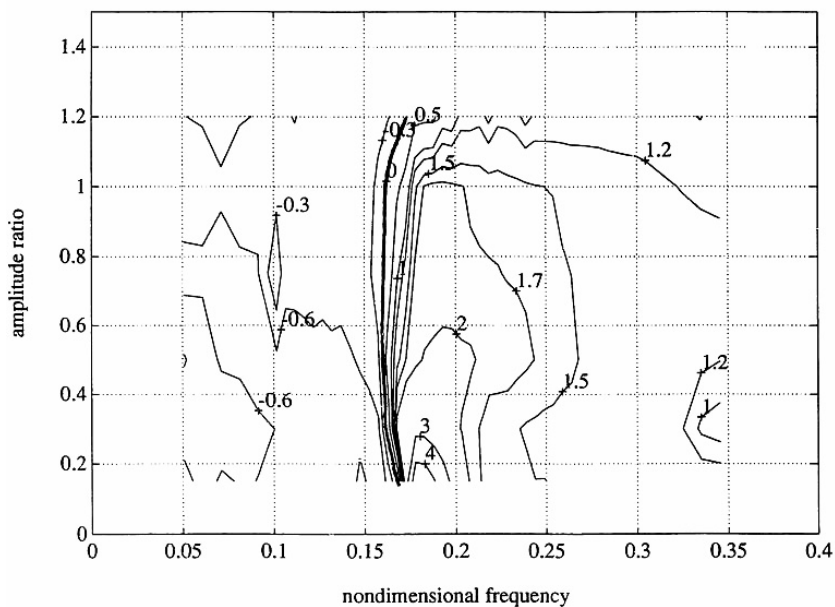
Williamson and Roshko (1988) tried to establish an amplitude-wavelength map that connects the response and vortex shedding mode, vortex shedding modes such as ‘2S’ and ‘2P’ were named.

The most widely used hydrodynamic coefficient database for VIV prediction is given by Gopalkrishnan (1993). He carried out a series of pure CF forced oscillation tests on a rigid cylinder at a fixed $Re = 10,000$. Figure 2.14 shows the contour plots of hydrodynamic excitation and added mass coefficients that he established.

Morse and Williamson (2009) conducted forced motion experiments with prescribed pure CF oscillation over a wide regime of amplitudes and frequencies. High-resolution contour plots of fluid force in the plane of normalized amplitude and wavelength at two different Re number (4,000 and 12,000) were produced, see Figure 2.15. A new vortex shedding mode ‘ $2P_O$ ’ which is similar to 2P mode but with a weaker second vortex of each pair was observed. The force-contour data make it easier to predict the response of a freely vibrating rigid cylinder.



(a) Pure CF excitation coefficients



(b) Pure CF added mass coefficients

Figure 2.14: Contour plots of excitation coefficients and added mass coefficients from pure CF force oscillation tests at $Re = 10,000$ by Gopalkrishnan (1993).

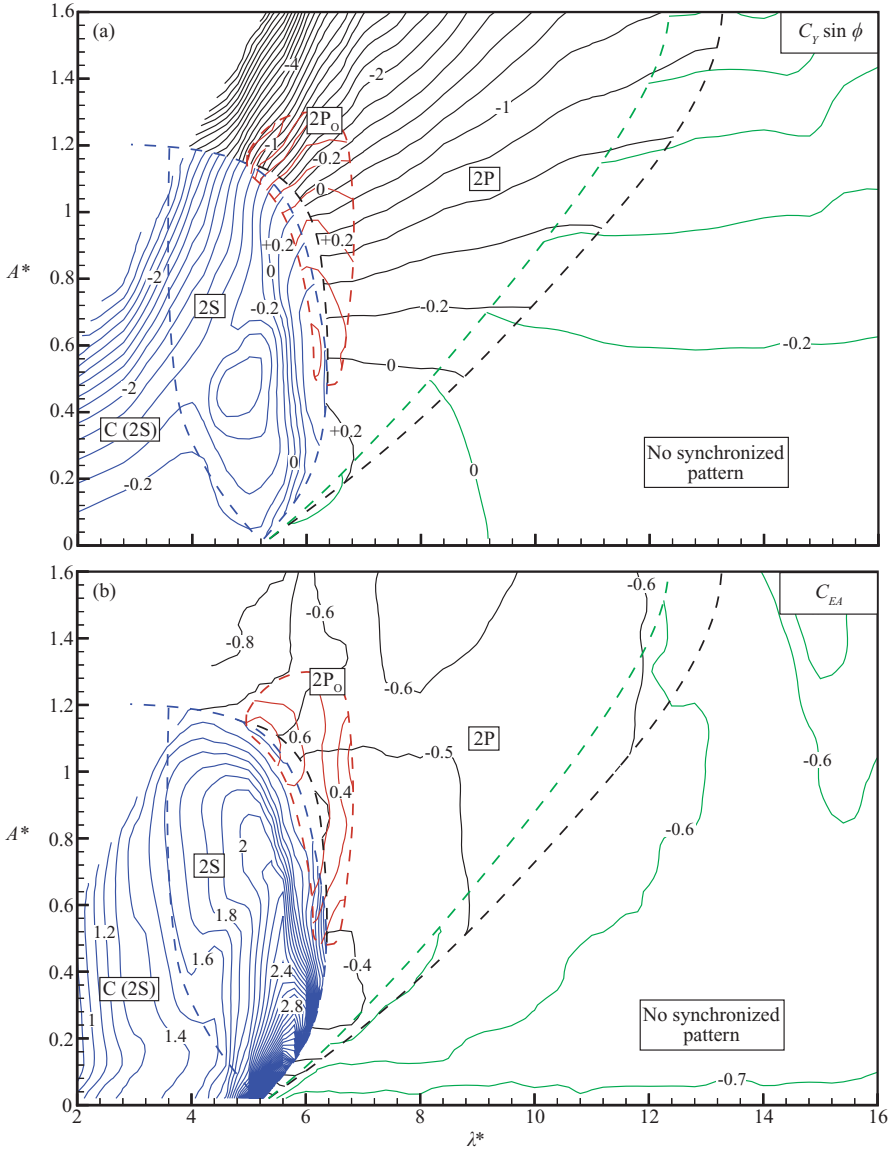


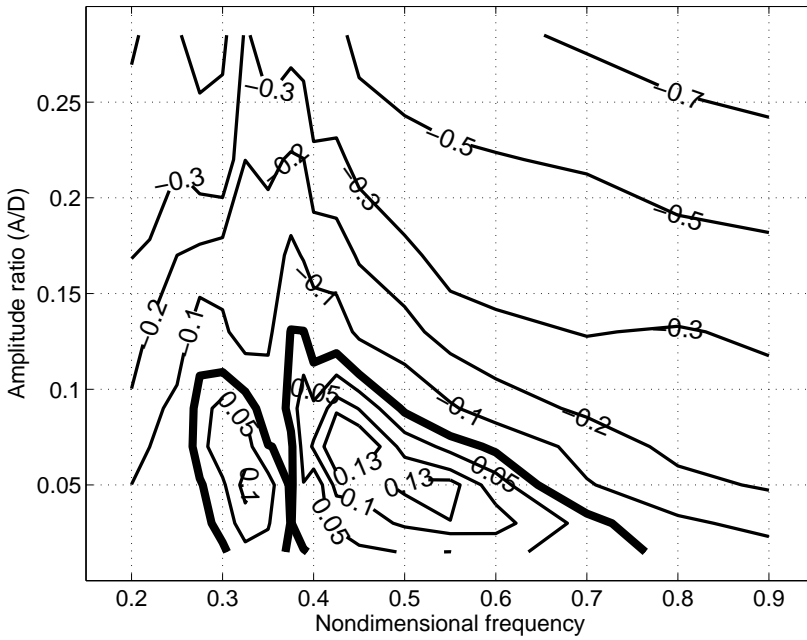
FIGURE 19. Contours of (a) the force in phase with velocity, $C_Y \sin \phi$, normalized ‘fluid excitation’, and (b) the effective added mass for $Re = 12,000$ with boundaries between modes indicated by the dashed lines. We could not obtain data in the upper left corner due to the limits of our facilities. Contour interval is 0.2 for $C_Y \sin \phi$ and 0.1 for C_{EA} . Boundaries between modes are indicated by the dashed lines. Lack of data in the upper left corner (for zero damping) as a function of the Reynolds number is compiled for free vibration experiments by Govardhan & Williamson (2006), and Morse and Williamson (2009).

$$A_{PEAK}^* = \log(0.41 Re^{0.36}), \quad (A2)$$

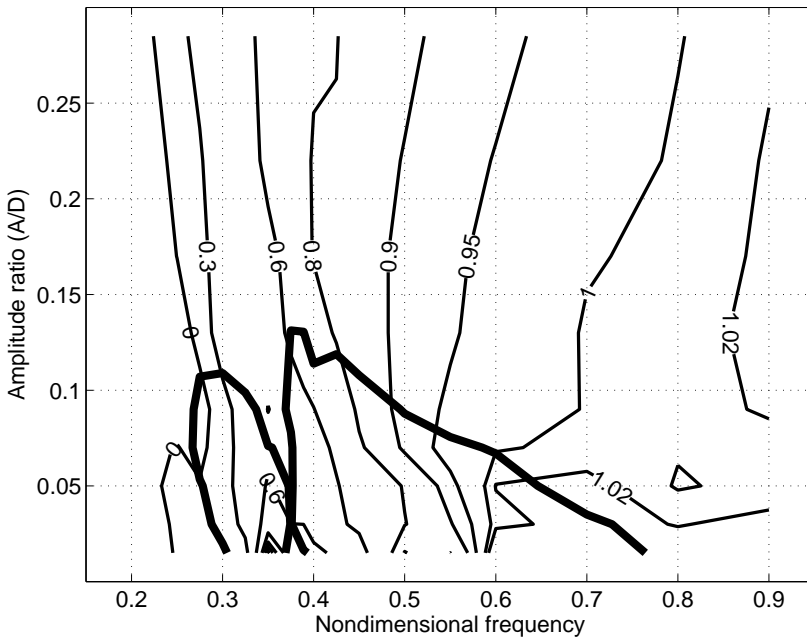
Pure IL harmonic forced motion

Over decades, few researchers has paid attention to vibration in the direction of free stream, Mercier (1973) found the drag coefficients of a cylinder oscillating in line with steady flow for varying Re , V_r and KC numbers. The conclusion was at reduced velocities lower than 3, the drag coefficient was strongly dependent on KC , while as reduced velocities increased, the drag coefficient was less and less dependent on KC .

Aronsen (2007) performed forced motion experiment on a cylinder with 10 cm diameter and 2 m length with pure IL motions at $Re = 24,000$. Contour plots of excitation coefficients and added mass coefficients were created, see Figure 2.16. His results are used to predict VIV of free span pipelines at low reduced velocity where response in CF direction is not seen. However, considering the response with both IL and CF directions, the amplitude of IL is much larger than pure IL response. This indicates that Aronsen (2007)'s coefficients database is not valid for combined IL and CF VIV prediction.



72 Figure 6.4: Contour plot of dynamic excitation coefficient for pure IL excitation



(b) Pure IL added mass coefficients

Figure 6.5: Contour plot of added mass coefficient in IL direction. The thick black line is the zero contour of the dynamic excitation coefficient, Figure 6.4, included to illustrate the excitation regions

Figure 2.16: Contour plots of excitation coefficients and added mass coefficients from pure IL force oscillation tests at $Re = 24,000$ by Aronsen (2007). The 1st instability region ranges from 0.27 to 0.375 with a maximum amplitude ratio of 0.13, while the 2nd instability region ranges from 0.27 to 0.375 with a maximum amplitude ratio of 0.11.

Added mass coefficient, $C_{a,IL}$. Figure 6.5 shows a contour plot of the added mass coefficient which is based on the force in phase with acceleration as shown in Eqn. (4.11). The thick black line shows the zero contour of the dynamic excitation coefficient and has been included to indicate the two excitation regions. The figure shows that the added mass

Combination of IL and CF harmonic forced motion

Jeon and Gharib (2001) demonstrated the IL effect from two aspects: Firstly, the phase between IL and CF motion will influence the phase between lift force and motion, which furthermore influences the energy transfer. Secondly, the wake mode could be changed due to presence of IL motion, they discovered a change from ‘2P’ to ‘2S’ in the vortex shedding mode (see Figure 2.4).

Aronsen (2007) also did some two degree of freedom forced motion tests and compared with pure IL and pure CF test results. An important discovery was the relationship between higher order harmonic CF force and IL motion, as discussed in section 2.4.3.

Dahl (2008) performed a large set of forced motion experiments with 2304 individual tests at two Reynolds number (8760 for reduced velocities greater than or equal to 6 and 6860 for reduced velocities less than 6). He used four variables: CF amplitude ratio, IL amplitude ratio, phase angle between IL and CF and reduced velocity. He found that third harmonic forces increase almost linearly as a function of IL amplitude.

Combined of IL and CF forced motion using observed motion

Strip theory assumption

Considering a section of a long flexible riser, due to the fluid-structure interaction, the hydrodynamic force coefficients must be functions of A_{CF} , A_{IL} , \hat{f} , θ (phase between IL and CF motion) and Re . In addition, A_{CF} , A_{IL} will have more than one harmonic component. A detailed diagram of different types of forced motion experiments are shown in Figure 2.17. In the figure, the forced motion experiments are classified by the motions: harmonic motion and observed motion from flexible beams. The parameters used to define the motions are illustrated with open circle and linked with the experiment type. Resulting higher order force is marked as filled circle. Non-periodic observed motion experiment is linked to each parameter with dash dot lines since all the parameters are not fixed as other experiment types.

It is impossible to consider each parameter individually, simply because VIV is a complex fluid-structure coupled phenomenon. However, considering a flexible pipe, and assuming that forces depend on local motions and there

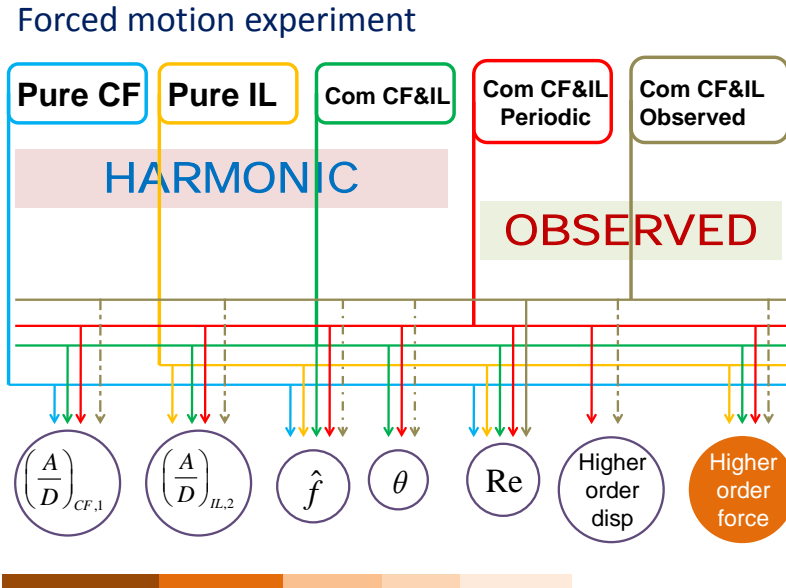


Figure 2.17: Different types of forced motion rigid cylinder tests.

is no hydrodynamic communications along the pipe, following steps could be used to find hydrodynamic coefficients:

1. Select a set of cross sections along the flexible pipe.
2. Identify the orbits of each cross section.
3. Keep amplitude ratio, \hat{f} and Re the same, run forced motion test with identified orbits.
4. Calculate hydrodynamic coefficients.
5. Build a data base and use it to predict VIV of risers and pipelines.

Soni (2008) first applied orbits measured from flexible beam experiments as forced motion orbits in rigid cylinder experiments. A flexible pipe was towed in the towing tank III at MARINTEK, Trondheim. By processing measured acceleration signals, the motions of the pipe were calculated and used for forced motion tests. His flexible pipe tests were all subjected to uniform flow.

2.5.3 Flexible riser

Brika and Laneville (1993) used a long flexible circular cylinder with a aspect ratio $L/D \approx 100$. Using smoke visualization technique, they first verified that initial response branch and lower branch associate with two different vortex shedding modes ‘2S’ and ‘2P’ respectively.

Large scale field test with a 90 m long riser subjected to shear current were performed in 1997 at Hanøytangen 30 km north of Bergen, Norway. The geometry model scale was about 1 : 15, which means the results could be used for production risers with length up to 1500 m length. Huse et al. (1998) found VIV may induce resonant axial vibrations causing dramatic stresses. Baarholm et al. (2006) performed fatigue analysis on Hanøytangen tests. They observed that fatigue damage was proportional to U^7 and U^4 (U is flow velocity) when natural frequencies of the riser were tension stiffness dominated and bending stiffness dominated respectively. The transition point between two regions seems equal to *the current velocity where the eigenfrequency to a tensioned string is approximately equal to the eigenfrequency to an un-tensioned beam*. For the lowest modes, corresponding to tensioned dominated risers, IL has a significant contribution to fatigue damage; while at highest current speeds, related to bending stiffness dominated risers, CF dominates the fatigue.

Lie and Kaasen (2006) processed the Hanøytangen high mode test data. An interesting observation from this work is that the average r.m.s CF displacement along the riser is independent of towing speed and has a magnitude around 0.25D, which is lower than previous experiments. In IL direction, this value is 0.05-0.08D.

High mode VIV model tests with long flexible reiser model were initiated by NDP, and is reported in Braaten and Lie (2005). Both bare riser and risers with different types of strakes were tested under uniform and triangular shear flow conditions.

Trim et al. (2005) investigated the NDP experimental results and confirmed that IL fatigue damage was as important as CF fatigue damage. Response of bare riser was quite different from riser covered with helical strakes, which means that strakes of different dimensions and types are effective in reducing VIV fatigue of flexible risers. However, performance of the $5.0D/0.14D$ (pitch/height) strakes in uniform or uniform-like currents was found to be worse than the $17.5D/0.25D$ (pitch/height) in mitigating VIV damage. This

calls for a parameter study to find the most effective strakes. The experimental results indicate that partially covered risers (from the end with highest velocities) will have a response that is dominated by the highest vortex shedding frequency from the bare part of the riser. They suggested when applying partial strake coverage strategy, the flow field experienced by the exposed riser section should also be considered.

Trough analyses of NDP High Mode VIV Tests, Modarres-Sadeghi et al. (2011) claimed that chaotic response is a generic feature of VIV of flexible risers, more details are introduced in section 7.1.2. In general, the riser response is irregular (broad-banded or chaotic, Modarres-Sadeghi et al. (2011)) and the degree of irregularity increases with the current speed.

A research group at Massachusetts Institute of Technology (MIT) and Deepstar Consortium conducted two field experiments in and near the Gulf Stream from the Research Vessel, Walton Smith in 2004 and 2006. The two experiments are referred to as Miami I and Miami II respectively (Vandiver et al., 2006, 2009). The presence of higher harmonic vibrations were demonstrated, and the fatigue induced by 3rd harmonic was estimated. They concluded that higher order harmonics should be considered for risers subjected to strong currents.

Travelling/Standing waves

The Miami II (Vandiver et al., 2009) experiments showed that for a tension dominated riser in sheared current and with high mode response, travelling waves are dominant. It also showed that travelling waves are linked to reduced velocity.

Wu (2011) classified combined IL and CF response types into five different groups with respect to travelling wave or standing wave response.

2.6 VIVANA

2.6.1 General introduction

VIVANA is a semi-empirical software for prediction of VIV of slender marine structures subjected to ocean current (Larsen et al., 2009). A finite element model with tensioned beam elements is used.

A brief summary of analysis procedure is listed below (Larsen et al., 2009; Larsen, 2000):

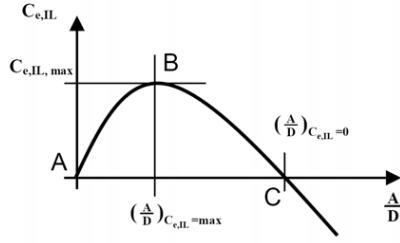
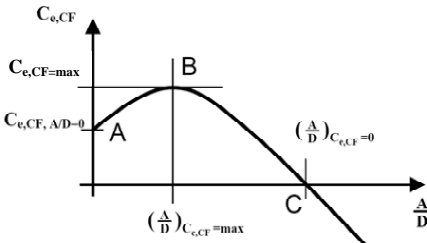
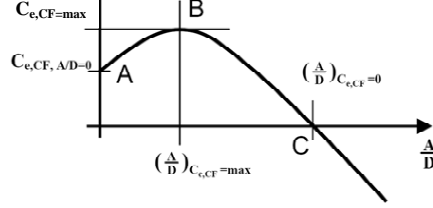
1. Non-linear static analysis of the structure by considering gravity, buoyancy, boundary condition and current.
2. Eigenvalue analysis using still water values for added mass.
3. Identification of possible excitation frequencies.
4. Iteration to find actual response frequencies, and frequency dependent added mass.
5. Identification of dominating and secondary response frequencies.
6. Calculation of CF response at all possible frequencies; calculation of IL response at twice the CF frequencies.
7. Calculation of fatigue damage by assuming concurrent response frequencies or time sharing and drag magnification.

2.6.2 Excitation force model

For pure CF VIV, VIVANA uses a excitation coefficient model based on Gopalkrishnan (1993) with some modifications from flexible beam tests.

It is seen from Figure 2.14a that at a given \hat{f} , $C_{e,CF}$ is a function of $(A/D)_{CF}$. Instead of using a two-parameter contour plot, VIVANA defines excitation coefficient curve with a set of parameters, which are functions of the non-dimensional frequency \hat{f} . Sketches of excitation coefficient curves are shown in Figure 2.18a (CF) and Figure 2.18b (IL). These curves are defined from three points and has the maximum value at point B. AB and BC are two 2^{nd} order polynomial, (Larsen et al., 2009).

- Point A gives the excitation coefficient value when there is no response, $C_{e,CF}|_{(A/D)_{CF}=0}$.
- Point B is defined by the maximum value of the excitation coefficient, $C_{e,CF,max}$ and corresponding amplitude ratio, $A/D|_{C_{e,CF,max}}$.
- Point C defines the A/D that gives zero excitation force for the actual non-dimensional frequency, $A/D|_{C_{e,CF}=0}$. This is the same amplitude that will occur for free, un-damped oscillations for the same flow condition.



(a) CF excitation force coefficient curve, for pure CF response. (b) IL excitation force coefficient curve, for pure IL response.

Figure 2.18: VIVANA built-in excitation force coefficient curves (Larsen et al., 2009).

Figure 2.19 shows the numerical values of coordinates of points A, B and C as a function of f for CFVIV (Larsen et al., 2009).

2.0.3 Time sharing in VIVANA

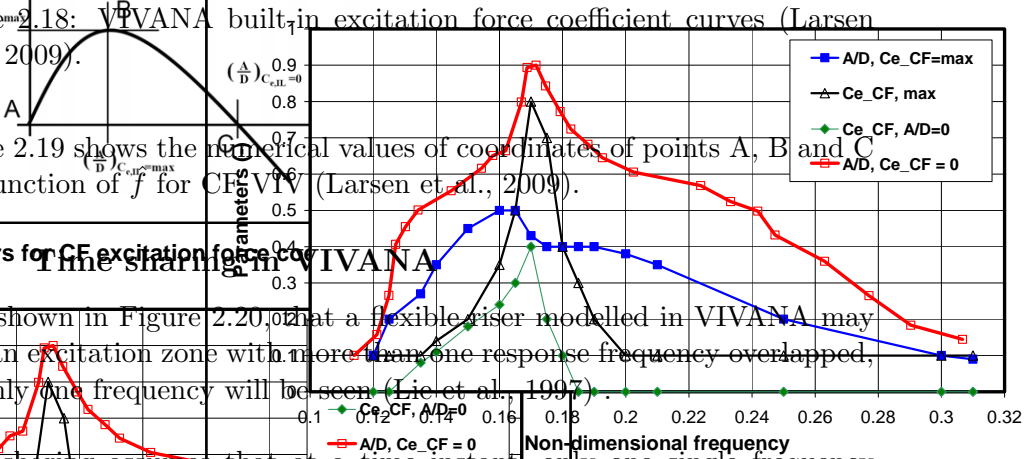
As is shown in Figure 2.20, that a flexible riser modelled in VIVANA may have an excitation zone with more than one response frequency overlapped, but only one frequency will be seen (Lie et al., 1997).

Time sharing assumes that at a time instant, only one single frequency responses is allowed. The relative duration of these response is found by ranking the response frequencies using the same excitation parameters when several frequencies are active simultaneously.

Two methods are coded:

1. Simultaneously active frequencies, no overlap of zones.
2. Consecutive response frequencies, with overlapping zones.

Parameters for CF excitation force coefficients



Non-dimensional frequency

$$\left(\frac{A}{D}\right)_{C_e,CF} = \max$$

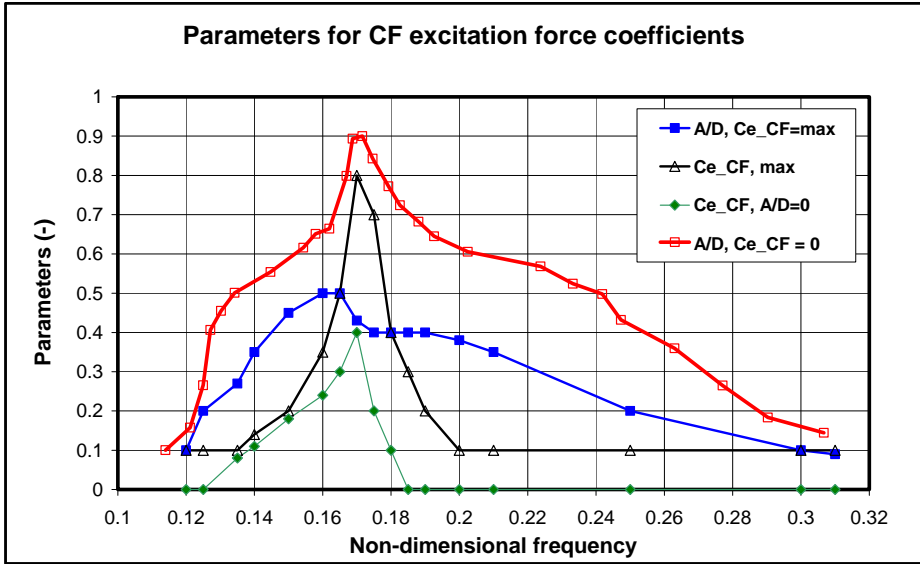


Figure 2.19: Parameters used to define specific CF excitation coefficient curves (Larsen et al., 2009).
 Vivan - Theory Manual
 Multi frequency response

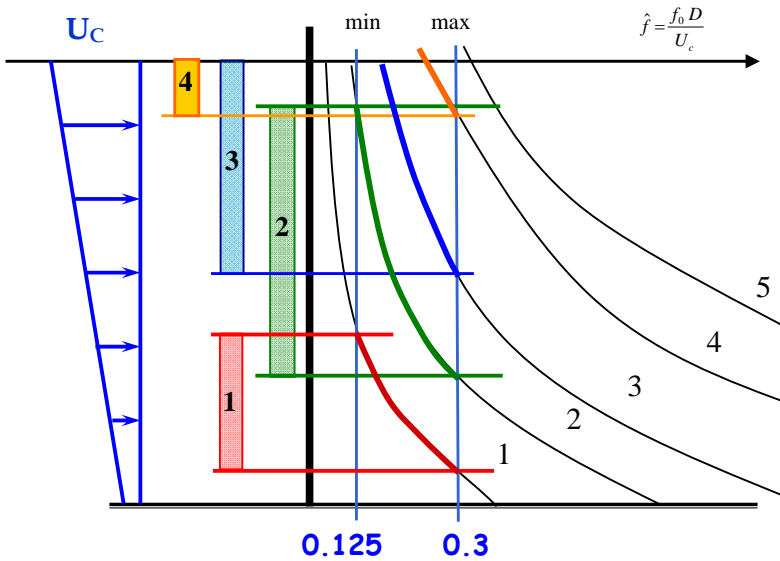


Figure 2.20: Overlapping excitation zones on riser with constant diameter and exposed to sheared current, from Larsen et al. (2009).

In order to define the priority among all possibly acting frequencies, an excitation parameter based on energy considerations have been defined:

$$E_i = \int_{L_{e,i}} U_N^3(s) D_H^2(s) \left(\frac{A}{D}\right)_{C_e=0} ds \tag{8.2}$$

The integral for the excitation parameter is taken over the excitation zone for each frequency.

2.7 A time-domain method

Besides classical frequency domain models, Mainçon (2010) developed a time domain model which may capture the IL/CF interaction, higher order frequency components, drag amplifications and structural non-linearities.

For each cross section of a slender structure model, recent history of the relative velocity is described as a combination of Laguerre polynomials (see Figure 2.21). The compressed information is further used to enter an interpolation function which can predict the instantaneous hydrodynamic force and thereby allow to conduct time domain dynamic analysis (Mainçon, 2010; *CeSOS Annual Report*, 2011). A large database of forces found from experiments with forced motions of a rigid cylinder must be available. The orbits should represent realistic motion pattern of flexible beams.

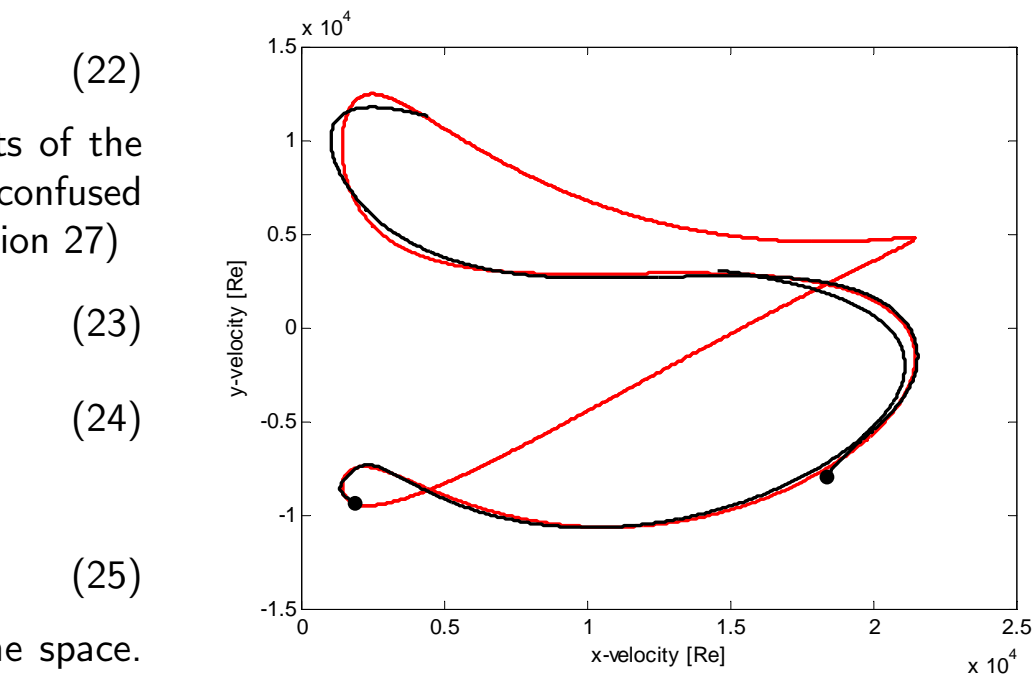


Figure 2.21: A comparison between measured relative velocity components (red line) and approximation by Laguerre polynomials (black line), from Mainçon (2010).
Figure 3: Example of Laguerre approximation for two components of a velocity history (arbitrary scaling). The red dot marks the present time. The red curve is the original cyclic signal and the black curves are Laguerre approximations for two different instants
 Figure 2.22 shows a comparison between measured force from forced motion (original cyclic signal) and the black curves are Laguerre approximations for two different instants

(26)

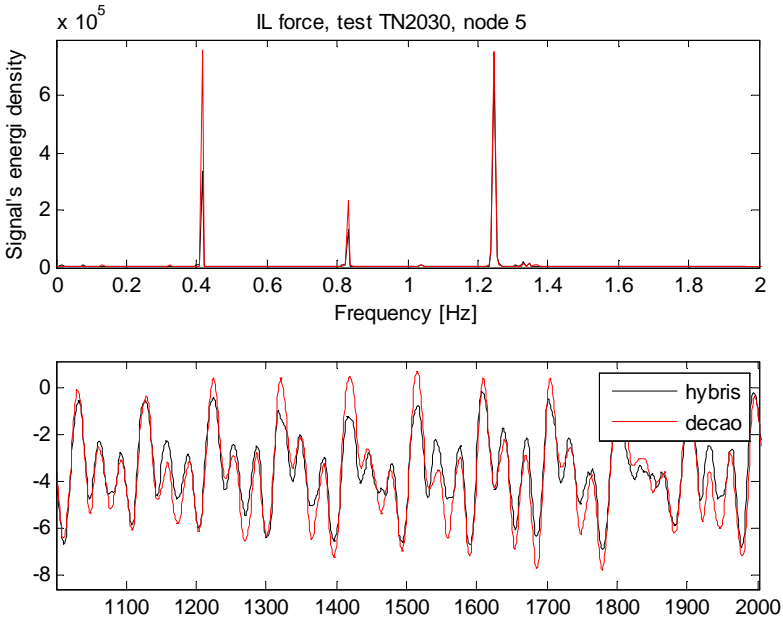
4.5 Differential equation for Laguerre co-

(27)

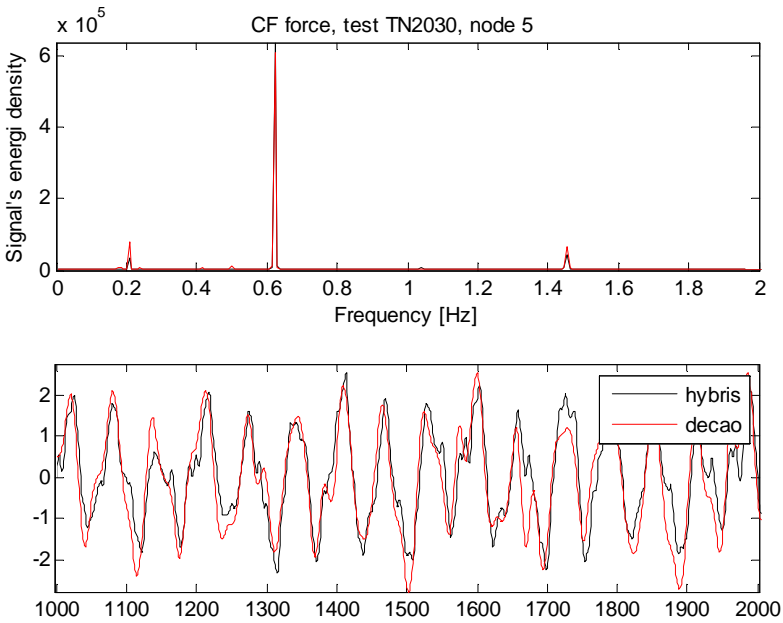
efficients

experiment and approximation by using Laguerre polynomials for one cross section of a flexible beam subjected to uniform current. Simultaneous force and displacement information at discrete points in a time history were used to establish the model, and the model can predict the whole time history, despite sometimes the prediction is not good enough.

This concept is promising, but more work is needed to understand orbit stability and related issues. In order to establish a more complete database, there is a call for more forced motion experiments of rigid cylinder section with measured motion orbits. It can be expected that with a more robust database, this time domain method can be used in prediction of any VIV response.



(a) IL force spectra and time history.



(b) CF force spectra and time history.

Figure 2.22: A comparison between measured force time history (red line) and force approximation given by Laguerre polynomials (black line), from Mainçon (2010).

2.8 Numerical methods

2.8.1 Basic equations

Equation of continuity

The equation of continuity is:

$$\frac{\partial \rho}{\partial t} + \nabla \cdot (\rho \vec{u}) = 0 \quad (2.43)$$

where ρ is the fluid density, $\vec{\nabla}$ is the vector gradient operator, (\cdot) is the vector dot product and \vec{u} is the velocity vector.

If the fluid is incompressible, the equation becomes

$$\nabla \cdot \vec{u} = 0 \quad (2.44)$$

Navier-Stokes Equations

The second order non-linear partial differential equations named after C.L.M.H. Navier (1785-1836) and Sir George G. Stokes (1819-1903) can be started as:

$$\frac{\partial(\rho u_i)}{\partial t} + \frac{\partial}{\partial x_j}(\rho u_i u_j) = \frac{\partial^2}{\partial x_j^2}(\mu u_i) - \frac{\partial p}{\partial x_i} - \rho g_i \quad (2.45)$$

where g_i is the gravity acceleration vector.

Regardless gravity, Eq. 2.45 can be written like:

$$\frac{\partial(\rho u_i)}{\partial t} + \frac{\partial}{\partial x_j}(\rho u_i u_j) = 2 \frac{\partial}{\partial x_j}(\mu S_{ij}) - \frac{\partial p}{\partial x_i} \quad (2.46)$$

where $S_{ij} = \frac{1}{2}(\frac{\partial u_i}{\partial x_j} + \frac{\partial u_j}{\partial x_i})$.

2.8.2 Turbulence modelling

Standard $k - \epsilon$ model

The transport equations of turbulence kinetic energy, k , and its rate of dissipation, ϵ , are:

$$\frac{\partial}{\partial t}(\rho k) + \frac{\partial}{\partial x_i}(\rho k u_i) = \frac{\partial}{\partial x_j}[(\mu + \frac{\mu_t}{\sigma_k}) \frac{\partial k}{\partial x_j}] + G_k + G_b - \rho \epsilon - Y_M + S_k \quad (2.47)$$

and

$$\frac{\partial}{\partial t}(\rho\epsilon) + \frac{\partial}{\partial x_i}(\rho\epsilon u_i) = \frac{\partial}{\partial x_j}[(\mu + \frac{\mu_t}{\sigma_\epsilon})\frac{\partial\epsilon}{\partial x_j}] + C_{1\epsilon}\frac{\epsilon}{k}(G_k + C_{3\epsilon}G_b) - C_{2\epsilon}\rho\frac{\epsilon^2}{k} + S_\epsilon \quad (2.48)$$

where G_k represents the turbulence kinetic energy generated by the mean velocity gradients; G_b is the turbulence kinetic energy generated by buoyancy; Y_m represents the fluctuating dilatation in compressible turbulence to the overall dissipation rate; $C_{1\epsilon}$, $C_{2\epsilon}$ and $C_{3\epsilon}$ are constants; σ_k and σ_ϵ are turbulent Prandtl numbers for k and ϵ respectively; S_k and S_ϵ are user-defined source terms.

The turbulence viscosity, μ_t , is computed as:

$$\mu_t = \rho C_\mu \frac{k^2}{\epsilon} \quad (2.49)$$

where the model constants have the following default values:

$$C_{1\epsilon} = 1.44, C_{2\epsilon} = 1.92, C_\mu = 0.09, \sigma_k = 1.0, \sigma_\epsilon = 1.3 \quad (2.50)$$

More details about standard $k-\epsilon$ model could be found in *ANSYS FLUENT User's Guide Release 13.0* (2010).

Large Eddy Simulation (LES)

The theory introduced in this section is based on White (2003), Pope (2000), *FLUENT 6.3 User's Guide* (2006) and *ANSYS FLUENT User's Guide Release 13.0* (2010).

Each transient fluid variable ϕ , could be described as:

$$\phi = \bar{\phi} + \phi' \quad (2.51)$$

where $\bar{\phi}$ is the large scale average component, which is called filtered variable, is directly solved by LES. ϕ' is small scale component, which describes the influence from small scale motions, also called subgrid-scale variable.

Filtered variable $\bar{\phi}$ can be obtained by:

$$\bar{\phi} = \int_D \phi G(x, x') dx' \quad (2.52)$$

where D is the fluid domain, $G(x, x')$ is the filter function that defines the scale of resolved eddies, which means that large scale eddies and small scale

eddies are solved separately. \mathbf{x} is the space coordinate in true fluid domain, while \mathbf{x}' is the space coordinate in the large scale space after filtering.

$$G(\mathbf{x}, \mathbf{x}') = \begin{cases} 1/V, & \mathbf{x}' \in V \\ 0, & \mathbf{x}' \notin V \end{cases} \quad (2.53)$$

where V is the volume of a computational cell.

After filtering process, The equation of momentum becomes

$$\frac{\partial}{\partial t}(\rho \bar{u}_i) + \frac{\partial}{\partial x_j}(\rho \overline{u_i u_j}) = \frac{\partial}{\partial x_j}[\mu(\frac{\partial \bar{u}_i}{\partial x_j} + \frac{\partial \bar{u}_j}{\partial x_i})] - \frac{\partial \bar{p}}{\partial x_i} \quad (2.54)$$

where \bar{p} is filtered pressure, $\overline{u_i u_j}$ is non-linear filtered advection term.

The filtered advection term can be split up as:

$$\rho \overline{u_i u_j} = \tau_{ij} + \rho \bar{u}_i \bar{u}_j \quad (2.55)$$

where τ_{ij} is the subgrid-scale stress (SGS). Then Eq.(2.46) becomes:

$$\frac{\partial}{\partial t}(\rho \bar{u}_i) + \frac{\partial}{\partial x_j}(\rho \bar{u}_i \bar{u}_j) = \frac{\partial}{\partial x_j}[\mu(\frac{\partial \bar{u}_i}{\partial x_j} + \frac{\partial \bar{u}_j}{\partial x_i})] - \frac{\partial \bar{p}}{\partial x_i} - \frac{\partial \tau_{ij}}{\partial x_j} \quad (2.56)$$

Smagorinsky-Lilly Model

The subgrid-scale turbulence models in *FLUENT 6.3 User's Guide* (2006) employ the Boussinesq hypothesis Hinze (1975), computing subgrid-scale turbulent stresses from

$$\tau_{ij} - \frac{1}{3}\tau_{kk}\delta_{ij} = -2\mu_t \bar{S}_{ij} \quad (2.57)$$

where τ_{kk} is the isotropic part of the subgrid-scale stresses. τ_{kk} is not modelled, but added to the filtered static pressure term. μ_t is the subgrid-scale turbulent viscosity. \bar{S}_{ij} is the rate-of-strain tensor for the resolved scale defined by

$$\bar{S}_{ij} = \frac{1}{2}(\frac{\partial \bar{u}_i}{\partial x_j} + \frac{\partial \bar{u}_j}{\partial x_i}) \quad (2.58)$$

In Smagorinsky-Lilly Model, the eddy-viscosity is modeled as:

$$\mu_t = \rho L_s^2 |\bar{S}| \quad (2.59)$$

where $|\bar{S}| = \sqrt{2\bar{S}_{ij}\bar{S}_{ij}}$. L_s is the mixing length for subgrid scales and in FLUENT is computed by:

$$L_s = \min(\kappa d, C_s V^{1/3}) \quad (2.60)$$

where κ is the von *Kármán* constant, d is the distance to the closest wall, C_s is the Smagorinsky constant, has a default value of 0.1 in FLUENT. V is the volume of the computational cell.

2.8.3 Research of forced motion of a rigid cylinder using LES

There is a large number of publications related to the use of CFD on VIV, since present study applies LES method on a rigid cylinder with forced motion, related works will be introduced herein.

When the Reynolds number is larger than the DNS capability, LES is considered to be the most accurate solution for the problem of a steady flow past a stationary circular cylinder (Al-Jamal and Dalton, 2004). Reynolds-averaged Navier-Stokes equations (RANS) based standard two-equation turbulence models ($k - \epsilon$ and $k - \omega$) can't predict turbulence flows accurately where the local isotropy of the turbulent stress play an important role, (Majumdar and Rodi, 1985).

Most recent solutions of steady flow past a fixed cylinder are Breuer (1998), Rocchi and Zasso (2002), Catalano et al. (2003), Fröhlich and Rodi (2004), Hansen and Forsythe (2004), Al-Jamal and Dalton (2004) (for the flow past a fixed cylinder), Young and Ooi (2007) and Cao et al. (2010). The Reynolds number varies from 60 to 10^6 .

Zhang and Dalton (1996) performed 2D LES study of a rigid cylinder oscillating freely in CF direction at the Reynolds number at 13,000. Lock-in was observed at the f_{st}/f_0 range from 1.0 to 1.3. $(A/D)_{CF} = 0.26$ and damping ratio of 0.02 was obtained.

Al-Jamal and Dalton (2004) did similar calculations with two mass ratios (1.67 and 7.85), with several damping ratios ($0.0 \leq \zeta \leq 0.1$) at Reynolds number of 8,000. For $0.555 < f_{st}/f_0 < 1.59$, expected response were shown. Beating phenomena was examined and was found to be decreased significantly when the damping ratio was increased to 0.1. What should be paid attention is that the wake response results disagreed with Williamson and co-authors. Reasons such as large fixed Reynolds number and non-harmonic oscillations were emphasized.

Tutar and Holdø (2000) modelled a circular cylinder with forced CF motions at $Re = 10,000$ to $100,000$ using Large Eddy Simulation (LES) based on a Smagorinsky Sub-Grid Scale (SGS) turbulence model. The comparison between 2D and 3D shows that 3D results match Bearman and Currie (1979)'s experimental results better than 2D results, and three dimensionality in the near wake flow were reflected by the deviations between 2D and 3D.

Atluri et al. (2009) applied 2D LES model to simulate a flow past a circular cylinder undergoing constant CF amplitude force oscillation with Re number in the range of 500 to 8000. By adjusting the oscillating frequency, non-periodic motions could be achieved. The 2D results shown a disagreement with the wake mode map in Williamson and Roshko (1988) except in the low Re and amplitude ratio range. Another finding was modulating the oscillating frequency affected the vortex shedding modes clearly.

Huang et al. (2009) used Large Eddy Simulation (LES) method to simulate a rigid cylinder undergoing 2D harmonic motion, and compared their results with Aronsen (2007). 3D vortex shedding modes were presented, and some hydrodynamic coefficients could be matched with experimental results.

Part II

Experimental Methods

Chapter 3

NDP High Mode VIV Tests

The experimental work in this thesis are based on measurements and selected results from the NDP High Mode VIV Tests (Braaten and Lie, 2005; Trim et al., 2005). This chapter presents the experimental set-up for these experiments; the riser model, instrumentation and calibration procedure. This set of tests was carried out by MARINTEK and all the raw data and reports were provided as data files to the author. The modal analysis was performed by Kristansen and Lie (2005), and this part is also described in Trim et al. (2005). Use of results from the NDP tests to define orbits for use in the second set of experiments was, however, carried out by the author, confer section 3.3.5.

3.1 Test set-up

3.1.1 MARINTEK Ocean Basin

The NDP tests were performed in the Ocean Basin at MARINTEK, Trondheim in 2003, see Figure 3.1. The Ocean Basin is 50 m wide and has a length of 80 m from the wave maker to intersection between beach and water surface. The depth of the basin itself is 10.0m, but it has an adjustable depth from 0.0 to 8.7m over an adjustable floor area ($48m \times 42m$). The basin is fitted with two sets of wave makers, but they were not used in the tests.

3.1.2 Test rig

A 40 m long riser was mounted in a rig and installed horizontally in the Ocean Basin (see Figure 3.2). The rig comprises:

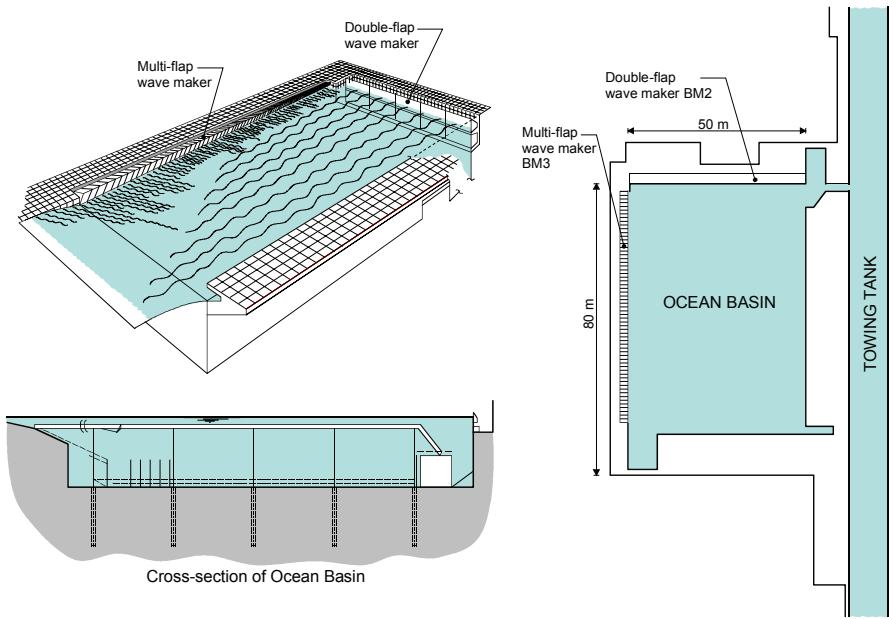


Figure 3.1: NDP high mode VIV setup (Braaten and Lie, 2005).

- Clump weights with springs at both ends to control motion and tension of the model
- An inclined pendulum arm connecting the clump weights to the gondola or crane
- A horizontal framework where the springs in the towing direction are connected to the test rig

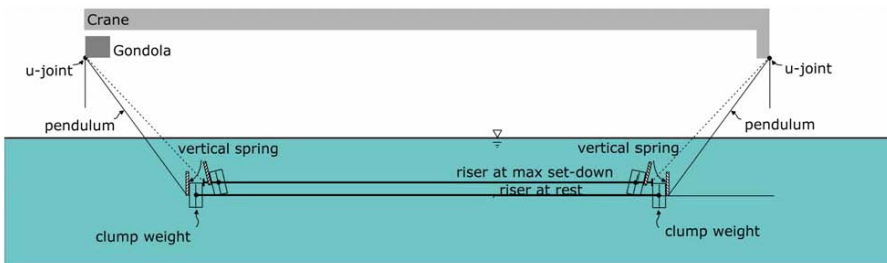
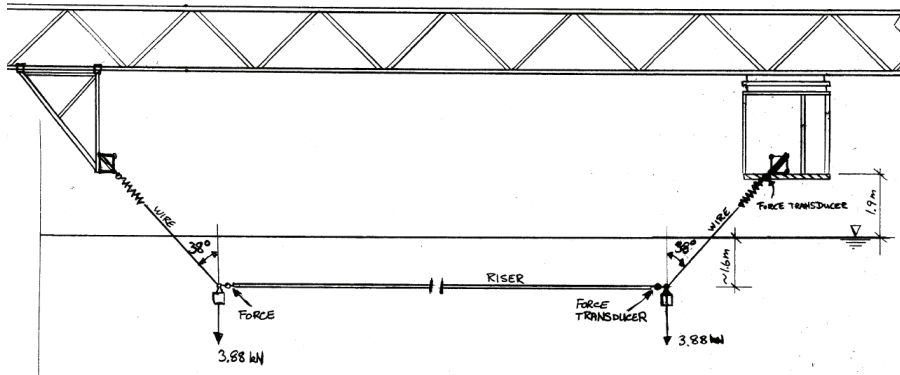


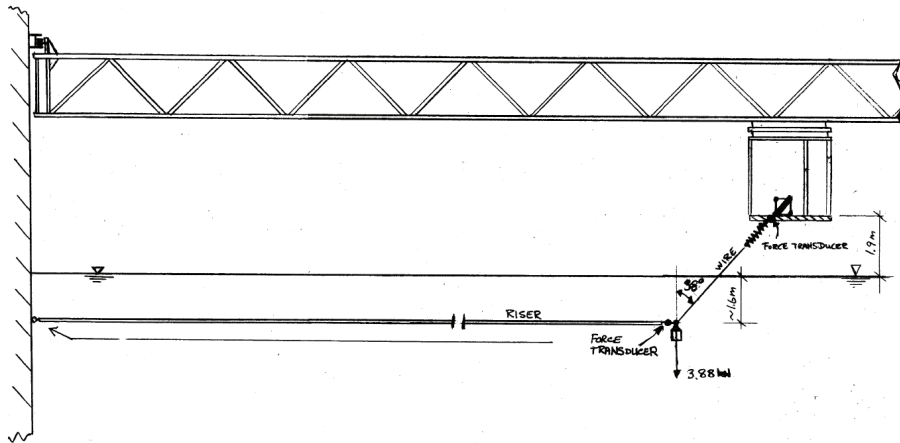
Figure 3.2: Principle sketch of the rig (Braaten and Lie, 2005).

The test set-up is presented in Figure 3.3. For the tests with uniform current, both ends of the riser were fixed to clump weights and the riser was

towed along the basin by use of the gondola and the transverse crane. For the case with triangular shear current the riser had a clump weight in one end, but the other end was connected to the wall of the basin. The free end was towed in a circular track by the gondola.



(a) Uniform flow.



(b) Triangular shear flow.

Figure 3.3: Principal sketch of test set-up in uniform and sheared flow (Braaten and Lie, 2005).

3.1.3 Riser model

The riser model was made from fiber-glass and was instrumented with about 80 transducers.

Table 3.1: Physical properties of bare riser model.

Parameter	Unit	Symbol	Dimension
Total length between pinned ends	[m]	L	38.0
Outer diameter	[mm]	D	27.0
Wall thickness of pipe	[mm]	t	3.0
Bending stiffness	[Nm^2]	EI	37.2
Young modulus for pipe	[N/m^2]	E	$3.62 \cdot 10^{10}$
Axial stiffness	[N]	EA	$5.09 \cdot 10^5$
Mass (air filled), measured	[kg/m]		0.761
Mass (water filled), estimated	[kg/m]		0.933
Mass ratio	[-]	m^*	1.62

Table 3.1 shows the physical properties of the riser model. The mass and the effective length of the riser model was between the centers of the universal joints at the ends (pin to pin). The riser model was flooded with water. An electrical pump was connected at one end of the riser to make sure that the riser was water filled during the testing period.

The riser was composed of 4 pipes. Two and two are glued together with both inside and outside sleeves. Then a special connection flange connected the two sections of the riser together.

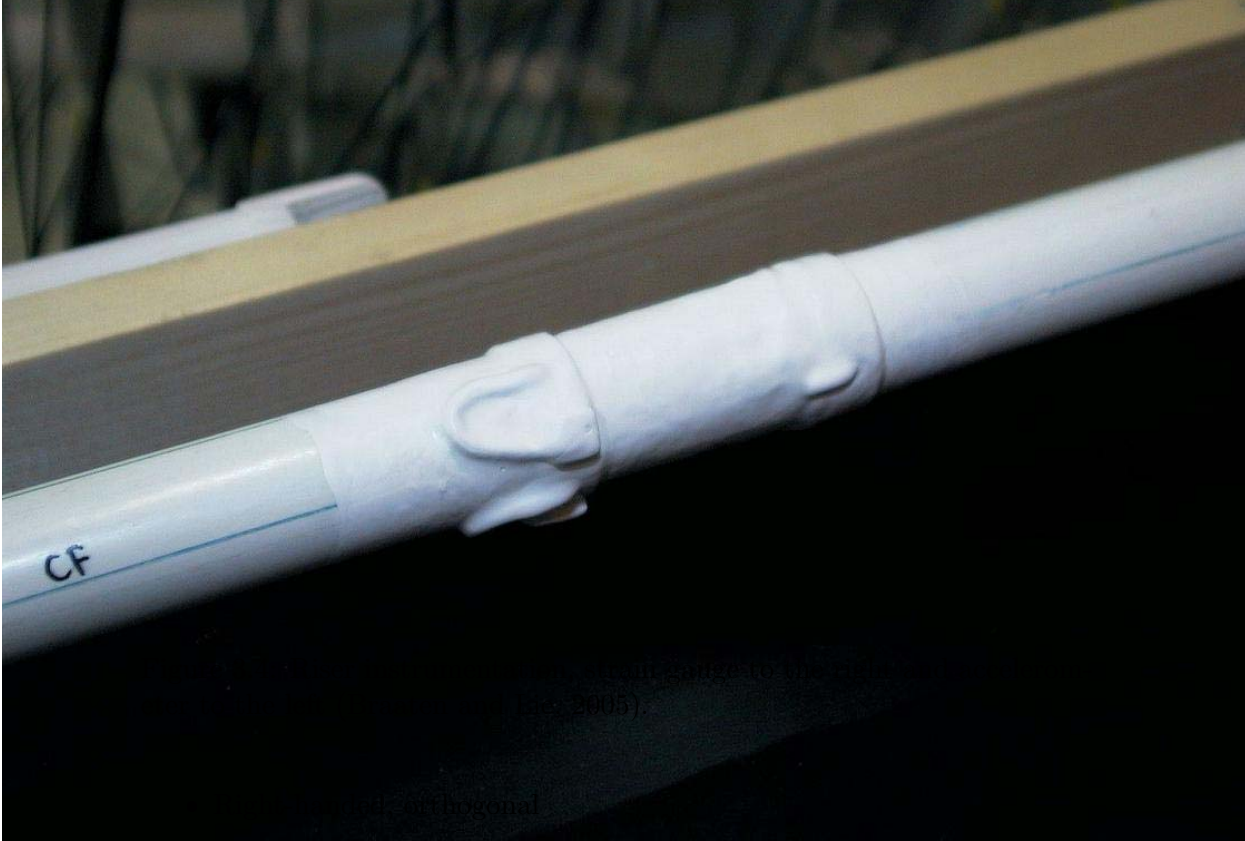
A fatigue test of a section of the model was performed for reliability and safety precautions. No visual damage was observed and the stiffness properties were found to be identical before and after the test.

Prior to the model test, the bare riser model was weighted both air-filled and water-filled in air. The mass ratio of the water-filled, bare riser, defined as the total mass flooded divided by the displaced mass. These data are also given in Table 3.1.

Since the strain gauges and the accelerometers were glued to the outside of pipe surface, the riser diameter was locally increased at the instrumented sections (bumps), see Figure 3.4.

3.1.4 Coordinate systems

The coordinate system was as follows (see Figure 3.5):



Picture 15 Riser instrumentation. Strain gauge to the right and accelerometer

- Origin at the centre of the universal joint in the bottom end (with zero velocity for shear flow cases) of the riser
- Positive z-axis pointing vertically out of paper
- Positive x-axis pointing in the towing direction.

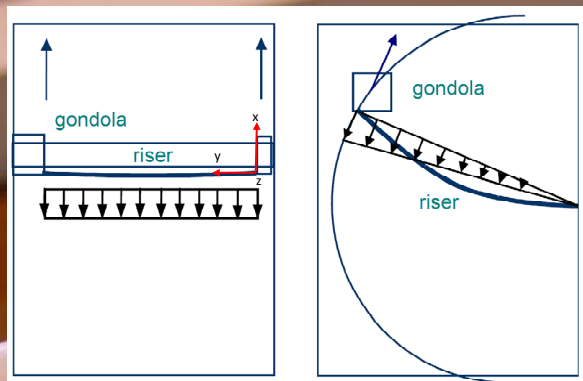


Figure 3.5: Test principals and coordinate system of NDP High Mode VIV Tests (Trim et al., 2005).

3.1.5 Instrumentation and measurements

The riser was instrumented by strain gages and accelerometers in both IL and CF directions. The number of transducers on the riser model is limited by the internal space of the riser model and the diameter of the instrument cables. Table 3.2 shows the instrumentation plan of the riser model.

Table 3.2: Instruments of riser model (Braaten and Lie, 2005).

Instruments	In-line	Cross-flow
Strain gauges	40	24
Accelerometers	8	8

In addition to the transducers on the riser model, the following response parameters were recorded:

Table 3.3: Additional instruments (Braaten and Lie, 2005).

Signal	Direction	Transducer
Accelerations of left clump weight	x, y and z	Linear accelerometers
Accelerations of right clump weight	x, y and z	Linear accelerometers
Riser force left end	x, y and z	Strain gauge transducer
Riser force right end	x, y and z	Strain gauge transducer
Towing velocity	x and y	Potentiometer

3.1.6 Data acquisition

One master MGCplus unit (A data acquisition system, HBM (2012)) and five slave units were connected with synchronization cables in a daisy chain. The master unit provide a clock signal for the slaves to synchronize data sampling. More details can be found in Braaten and Lie (2005). All signals were filtered with a 250 Hz Butterworth filter intrinsic to the MGCplus modules.

In order to prevent aliasing (folding of high frequency response (noise) onto the low frequency response), filter type, cut-off frequency and data sampling frequency were chosen with respect to the maximum expected response frequency. The data sampling frequency was 1200 Hz.

3.2 Test program and test procedures

3.2.1 Instrumentation verification and calibration tests.

In order to check the total instrument chain from the transducer to the printout, all force transducers and accelerometers on the clump weights were short-circuited or excited one by one.

3.2.2 Air and In-Water Decay Tests

Decay test in air were performed manually to record natural frequencies up to the fourth order. The measured value matched the theoretical eigenfrequencies well. Material damping of bare riser model has an value of 0.4% or less of critical damping.

Decay test of the risers were performed by exciting the riser manually in water also to determine the natural frequencies of riser model. Both naked and straked riser were tested. However, the tests were very difficult to analyse due to large hydrodynamic damping.

3.2.3 Riser VIV Tests

The complete test program can be found in Braaten and Lie (2005). In this thesis, only the ‘bare riser VIV test’ is used, including both uniform and triangular sheared flow cases. The total number of bare riser tests is 44. Table 3.4 shows the cases being used for this thesis.

Table 3.4: NDP test runs need to be calculated.

Velocity [m/s]	$Re(Re_{max})$	Uniform	Shear
0.50	12385	2030	
0.60	14190		2340
0.90	21285		2370
1.20	29724	2100	
1.50	35475		2430
1.80	44587	2160	

Re : Reynolds number of uniform flow cases;

Re_{max} : maximum Reynolds number of sheared flow cases.

3.3 Data processing and preparation to forced motion test

3.3.1 Time window

Selection of time window from the measurements to use in model analysis was based on the towing velocity. The velocity was increased from 0 to required test velocity, kept constant and then decreased to 0. Nominal start time was set to the instant when the towing velocity reached its maximum, and the end time to the instant when the towing velocity started to decrease. The period from nominal start time to stop time was denoted as nominal time window. In order to avoid transient effects and for simplicity and consistency, the last 2/3 of the nominal time window was chosen for all tests to be used for analysis, see Figure 3.6. Due to the computer memory capacity, the time window was further shortened for all tests with towing velocity less than 0.8 m/s (Kristansen and Lie, 2005).

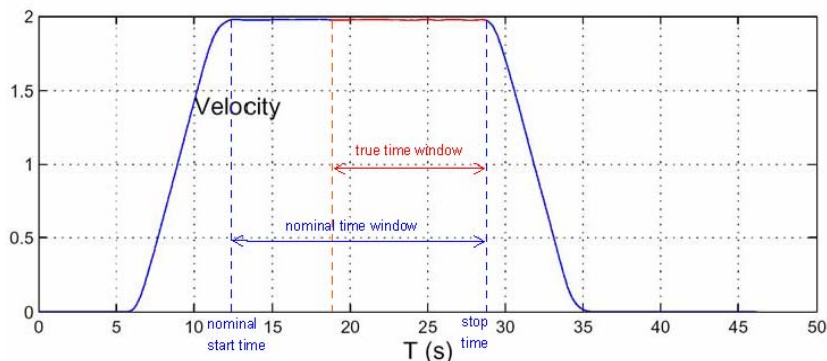


Figure 3.6: Time window selection of NDP high mode VIV tests (Braaten and Lie, 2005).

3.3.2 Band-pass filter

The raw signals were band-pass filtered to reduce the noise. Details regarding cut-off frequency and filter characteristics can be found in Appendix E of Kristansen and Lie (2005).

3.3.3 Modal analysis

Under the assumption that the deformed shape of a riser at any time could be expressed as a sum of eigenfunctions, modal analysis was conducted

by Kristansen and Lie (2005) using both signals from strain gauges and accelerometers along the beam.

Control Equation

The displacements along the riser for one direction can be written as:

$$x(z, t) = \sum_{n=0}^{\infty} w_n(t)\phi_n(z) \tag{3.1}$$

where $w_n(t)$ are the time-varying modal weights, and $\phi_n(z)$ are the eigenmodes which are functions of the position along the riser model (z). If we assume that the tension is constant and the beam is straight lined, the sinusoidal eigenmodes described by Eq. (2.6) can be applied.

Using both curvature and acceleration

Both strain and acceleration signals were used in the modal analysis. A linear system was established and solved in Fourier space by using the least squares method. In the end, modal weight factors were found for each mode as a function of time.

The first step was to convert the strain signals, ε , into curvature, κ , applying the following relation:

$$\kappa = \varepsilon/R \tag{3.2}$$

where R is the radius of the pipe cross section.

Then both the second spatial derivative ($\kappa = x''$) and second time derivative ($a = \ddot{x}$) of the displacement eigenfunctions were available, applying Eq. (3.1) with a finite number of modes, N :

$$\kappa(z, t) = \sum_{n=1}^N w_n(t)\phi_n''(z) \tag{3.3}$$

$$a(z, t) = \sum_{n=1}^N \ddot{w}_n(t)\phi_n(z) \tag{3.4}$$

Information about curvature and accelerations are only available at a finite number of locations along the riser, $z = z_i$ with $i = 1, 2, \dots, M_{a/k}^{IL/CF}$, where the subscript a denotes acceleration, and κ denotes the curvature. In NDP

tests, $M_a^{IL/CF} = 8$; $M_k^{IL} = 40$ and $M_k^{CF} = 24/23$ (naked uniform: 24; others: 23), also see Table 3.2. Then for a given instant in time, there were $M = M_k + M_a$ equations with N unknowns. To avoid un-determined system of equations, $N \leq M$ was required. When $N = M$, the system of equations has a single, unique solution; when $N < M$, the system may be solved by using the least squares method.

It is easy to solve this system in Fourier space, denoting the Fourier transform in time by $\hat{y} = F\{y\}$, and $F\{\ddot{y}\} = -\omega^2 \hat{y}$.

$$\hat{\kappa}(z, t) = \sum_{n=1}^N \hat{w}_n(\omega) \phi_n''(z) \quad (3.5)$$

$$\hat{a}(z, t) = -\omega^2 \sum_{n=1}^N \hat{w}_n(\omega) \phi_n(z) \quad (3.6)$$

The system might be described by a linear system:

$$A\hat{w} = \hat{b} \quad (3.7)$$

where the system matrix A contains the discrete eigenvectors and \hat{b} contains the measurements. In more detail:

$$A = \begin{bmatrix} \phi_1''^1 & \phi_2''^1 & \cdots & \phi_N''^1 \\ \phi_1''^2 & \cdot & \cdots & \cdot \\ \vdots & \cdot & \cdot & \cdot \\ \phi_1''^{M_k} & \phi_2''^{M_k} & \cdots & \phi_N''^{M_k} \\ \phi_1^1 & \phi_2^1 & \cdots & \phi_N^1 \\ \phi_1^2 & \cdot & \cdots & \cdot \\ \vdots & \cdot & \cdot & \cdot \\ \phi_1^{M_a} & \phi_2^{M_a} & \cdots & \phi_N^{M_a} \end{bmatrix} \quad \hat{w} = \begin{bmatrix} \hat{w}_1 \\ \hat{w}_2 \\ \vdots \\ \hat{w}_N \end{bmatrix} \quad \hat{b} = \begin{bmatrix} \hat{\kappa}_1 \\ \hat{\kappa}_2 \\ \vdots \\ \hat{\kappa}_{M_k} \\ -\frac{\hat{a}_1}{\omega^2} \\ -\frac{\hat{a}_2}{\omega^2} \\ \vdots \\ -\frac{\hat{a}_{M_a}}{\omega^2} \end{bmatrix} \quad (3.8)$$

where $\phi_n^i = \phi(z_i)$. $\hat{\kappa}_i$ is the complex Fourier component of the curvature signal at position z_i , and \hat{a}_i is the complex Fourier component of the acceleration signal at position z_i .

The modal weight factors become

$$\hat{w} = (A^T A)^{-1} A^T \hat{b} \quad (3.9)$$

and the solution of the system, the modal weight factor vector can be obtained by inverse Fourier transform, i.e. $w(t) = F^{-1}\{\hat{w}(\omega)\}$.

In order to eliminate the noise effect from the strain signals on low modes, the lowest participating mode N_{low} and total number of participating mode N_{tot} were selected, then highest participating mode is $N_{high} = N_{low} + N_{tot} - 1$. A modified system matrix A , denoted by \tilde{A} , is used to find the modal weights from weights from mode number N_{low} to N_{high} :

$$\tilde{A} = \begin{bmatrix} \begin{bmatrix} 0 \end{bmatrix} \\ \begin{bmatrix} \phi''_{N_{low}+N_0} & \cdots & \phi''_{N_{high}} \end{bmatrix} \\ \begin{bmatrix} \phi_{N_{low}} & \cdots & \phi_{N_{high}} \end{bmatrix} \end{bmatrix} \quad (3.10)$$

where the zero sub-matrix has dimensions $M_\kappa \times N_0$, where typically $N_0 \ll N - n + 1$. This technique provided improved modal analysis for the case with low modes participation. The modal weights factors are found by using least squares method :

$$\hat{w} = (\tilde{A}^T \tilde{A})^{-1} \tilde{A}^T \hat{b} \quad (3.11)$$

The above method is described in detail in Kristansen and Lie (2005), and can also be found in Trim et al. (2005).

The dominating and participating modes of selected cases are shown in Table 3.5.

Model weight factors of uniform current and shear current are shown in Figure 3.7a and 3.7b respectively.

Table 3.5: Dominating and participating modes, from Appendix E of Kristansen and Lie (2005).

Test No.	IL		CF	
	dominate	range	dominate	range
2030	7	1-15	4	1-10
2100	14	10-20	8	4-12
2160	20	10-20	9	9-12
2340	7	1-15	4	2-10
2370	10	2-20	6	2-12
2430	12	10-20	7	5-12

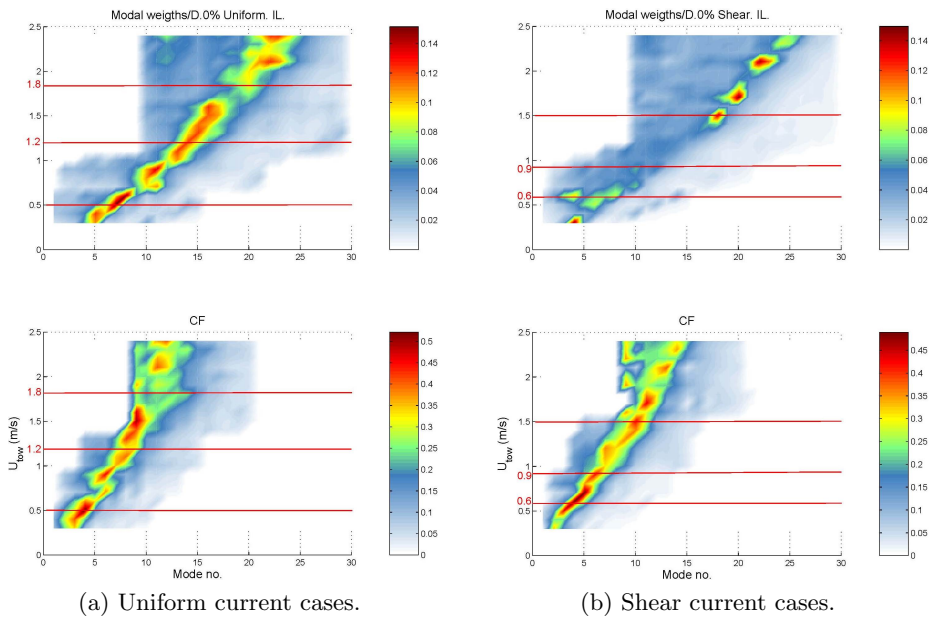


Figure 3.7: Contour plots of modal weights, from Appendix E of Kristansen and Lie (2005).

3.3.4 Choice of cases for forced motion tests

Red lines in Figure 3.7a and 3.7b indicate the cases chosen for the present study (see also Table 3.4). More sheared flow cases were initially chosen, but were not conducted due to the limitation of instruments in the laboratory.

The three uniform flow cases have different properties:

- Case 2030: Both IL and CF are dominated by low mode and modal weights are strong.
- Case 2100: IL has higher order modes and with medium strength modal weight; the dominating CF mode is not so distinct.
- Case 2160: Both IL and CF response show a large range of participating modes, but the modal weights are low for both directions.

The three linear sheared flow cases have these characteristics:

- Case 2340: IL has a broad band of participating modes, but CF has a clear dominating mode.
- Case 2370: IL does not have a strong dominating mode, and the dominating CF mode is not so strong as for case 2340.
- Case 2430: Both IL and CF response are dominated by high mode order.

3.3.5 Definition of periodic orbits

A consequence of the stochastic nature of VIV is that the CF/IL motion at a given position on the oscillating beam is not periodic. However, periodic orbits are required for identification of force coefficients. Periodic orbits were therefore defined by selecting two successive orbits and generate a smooth transition from the last part of the first cycle to the next. Figure 3.8 shows this process. In Figure 3.8a, the orbit for more than one cycle can be seen, there is an overlapped part. A number of points on each of the two orbits were used with a weight function to create a series of points between them (red line), and hence define a periodic orbit, see Figure 3.8b. The weight function is defined as:

$$x_{IL/CF,new,i} = \frac{i}{N}x_{IL/CF,C1,i} + \frac{N-i}{N}x_{IL/CF,C2,i} \quad (3.12)$$

where N is interpolating points within the overlapped part; i is the i^{th} point; $x_{IL/CF,new,i}$ is new displacement value of the i^{th} point of the red line; $x_{IL/CF,C1,i}$ is the displacement value of the i^{th} point of the overlapped part of the first cycle; $x_{IL/CF,C2,i}$ is the displacement value of the i^{th} point of the overlapped part of the second cycle.

Figure 3.8c shows the time varying observed orbits from flexible beam test, and illustrates the variability of the orbit during the test period.

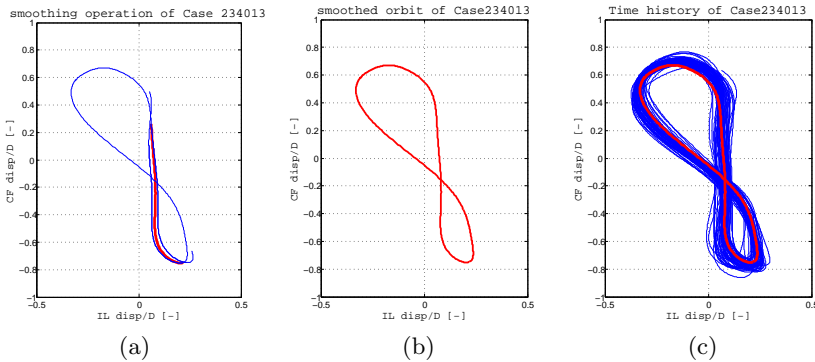


Figure 3.8: Smoothing process of a non-periodic orbit and time varying observed orbits of the same section (Yin and Larsen, 2010).

Chapter 4

Forced Motion Experiments

This chapter presents the experimental work of the thesis, including the experimental set-up, signal processing, a description of the test matrix and a summary of the PIV techniques. Except for the author's own main test matrix, all of the other experimental work, including calibration, set-up, and verification tests, was conducted in collaboration with Aglen (2012).

4.1 Test set-up

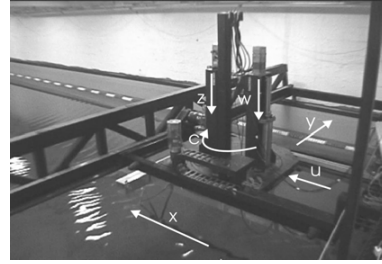
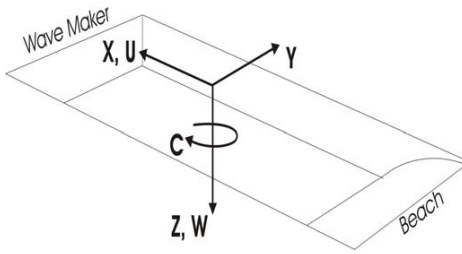
4.1.1 Facilities

The forced motion experiments took place in NTNU's Marine Cybernetics Laboratory (MCLab), (*MCLab Carriage Remote Control User Manual*, 2008). MCLab is equipped with a towing tank, which has dimensions of $40m \times 6.45m \times 1.5m$ (L×B×D) and an overhead towing carriage. Five degrees of freedom can be achieved by a computer-controlled simulator located on the main carriage. Figure 4.1 shows a sketch and photo of the rig.

The apparatus was designed and used by Aronsen (2007) and later used by Soni (2008). The test model used for the forced motion tests was a rigid cylinder with a 10 cm outer diameter and 2 m length, resulting in an L/D ratio of 20. The rig was attached to the simulator on the carriage by a yoke. Oscillatory motions were created by simultaneously moving the yoke horizontally (IL) and vertically (CF). All parameters needed to control the motions, such as carriage speed and the local positions (IL and CF) of the rig were input into a PC on the carriage. Initialisation of each test was controlled by a master input file on the same PC. The ends of the cylinder were capped to keep the cylinder air filled to keep its mass as low as possible.

X	Main Carriage (Gantry)	-15.5	8.5	± 20	0.5	2.0	0.5
Y	Transverse carriage	-2.4	2.4	± 5	0.2	1.0	1
U	small Carriage in X direction	-0.4?	0.4?	± 1	0.2	1.0	1
C	Rotation Table			$\pm 1^\circ$			
Z	Vertical Axis	-0.2?	0.2?	± 0.5	0.1	0.5	2
W	Vertical Axis	-0.2?	0.2?	± 0.5	0.1	0.5	2

Positive direction is based on a maneuvering type coordinates with Z and W positive downwards.



The limits on amplitude and frequency for harmonic oscillations are:
 Figure 4.1: MC Lab, taken from *MCLab Carriage Remote Control User Manual* (2008).

Table 4.1: Limits of apparatus in MC Lab (*MCLab Carriage Remote Control User Manual*, 2008).

Axis	Description	Min [m]	Max [m]	Pos Error [mm]	U_N [m/s]	U_{max} [m/s]	A_{max} [m/s ²]
X	Main Carriage	-15.5	8.5	± 20	0.5	2.0	0.5
U	small Carriage (IL)	-0.4	0.4	± 1	0.2	1.0	1.0
Z/W	vertical Axis (CF)	-0.2	0.2	± 0.5	0.1	0.5	2.0

Two end-plates ($7D \times 5D$) were installed to reduce three-dimensional end effects. A schematic description of the experimental set-up is shown in Figure 4.2.

4.1.2 Instruments

Force transducers

Two strain gauges were mounted orthogonally to measure the force in the IL and CF directions. The strain gauges were type PW2CMR/18kg, produced by Hottinger. Figure 4.3a shows a ‘cross’ of force strain gauges mounted on one end-plate. The forces on both sides were measured. The strain gauges were calibrated in three steps: individually, in a cross and in a cross on the cylinder. Details of the calibration process are given in Appendix A.

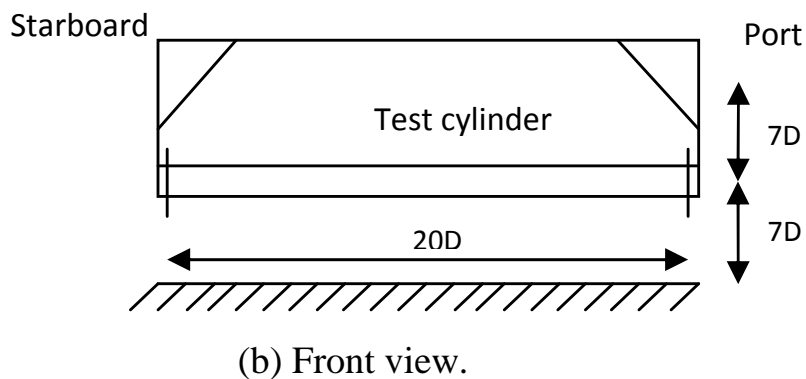
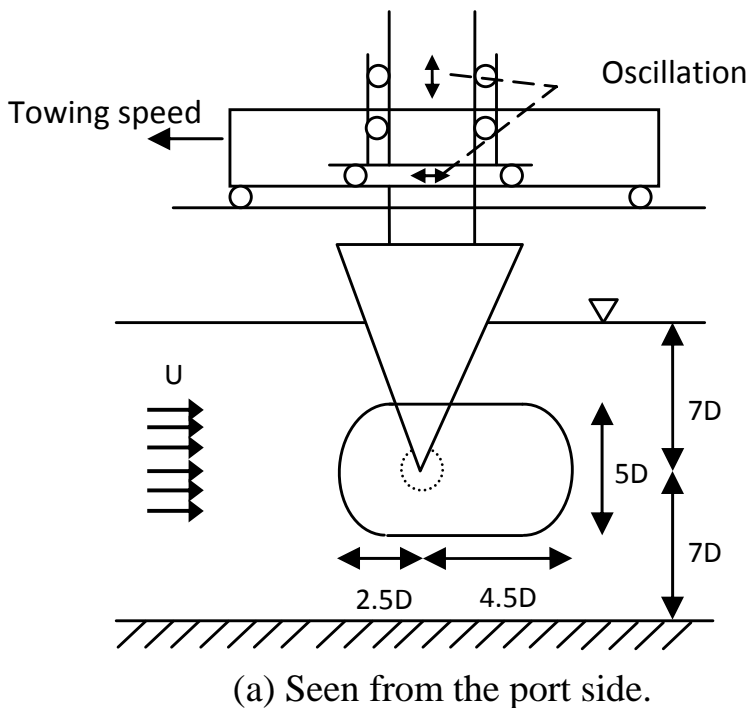
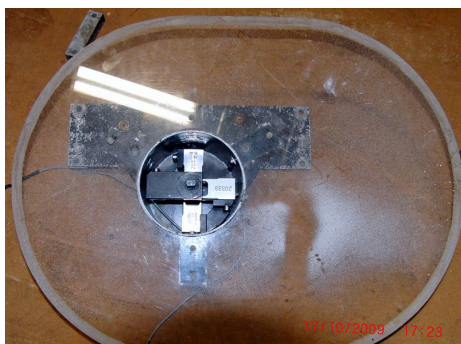


Figure 4.2: MC Lab setup.

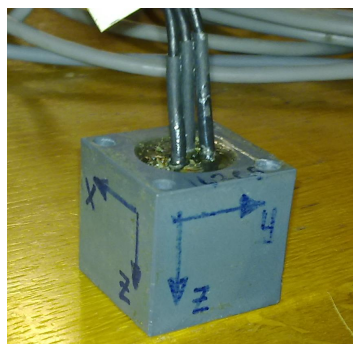
Accelerometers

Both 3D and 1D accelerometers were used during the experiments. Figure 4.3b shows one of the 3D accelerometers.

Two accelerometers that can measure acceleration in 3 dimensions (3D)



(a) ‘Cross’ of strain gauges mounted in one end-plate.



(b) A 3-D accelerometer.

Figure 4.3: Instruments used in forced motion experiments.

were mounted on the outside of the housing of the ‘cross’ strain gauges, which is also a part of the end-plate. As the motion of the end-plates is the same as the cylinder model, measured accelerations on the plate were used as the accelerations of the cylinder model. Only two of the three directions (x and z) were used to record acceleration signals in both the IL and CF directions. Two additional 1D accelerometers were mounted on the carriage to measure carriage vibrations. The recorded acceleration of the towing carriage can also be used to derive the towing velocity and displacement of the carriage.

String potentiometers

Two string potentiometers were used to record the IL and CF model displacement signals. The string potentiometer measuring the IL displacement was placed horizontally, with one end was clamped onto the carriage, and the other end was clamped on the yoke. The other string potentiometer was installed in a similar manner but oriented vertically.

Leveller

A leveller was used to ensure that the cylinder was mounted horizontally. Distances from both ends of the cylinder to a ‘base plane’ are measured and kept the same, in order to make sure the cylinder is perpendicular to the incoming flow.

PIV set-up

Particle-Image Velocimetry (PIV) is a technique that uses particles as markers, measuring the motion of a small region of the fluid field by observing the locations of the markers in the images at two or more times in succession, as described by Adrian (1991).

The experiment using PIV equipments used the same setup as Soni (2008). The experimental work related to PIV was performed with technical help from Visscher (2011).

94

CHAPTER 6. EXPERIMENTAL SET-UP: RIGID PIP

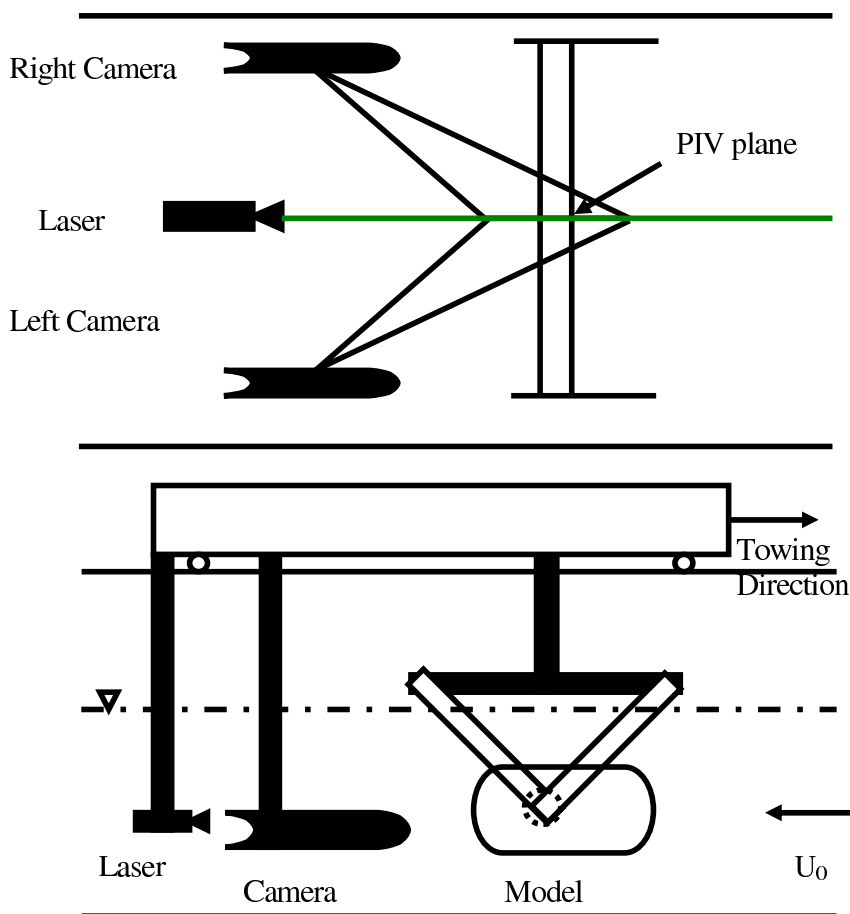


Figure 4.4: PIV setup (Soni, 2008).

Figure 6.2: Schematic presentation of the experimental set-up.

6.1 The apparatus

The PIV system was mounted downstream of the cylinder in order to capture the fluid field within the measuring frame. The entire system was composed of a 10 Hz double-pulse laser, two highly sensitive 10 Hz CCD cameras with $1,600 \times 1,200$ active pixels, light-sheet optics and tracer particles.

Several steel frames were mounted on the carriage platform. Tubes were mounted on the steel frames to support the laser and cameras installation. Two cameras were fastened in the underwater housings with glass windows. The observation area in this study is $5D \times 7D$, which is larger than that used by Soni (2008). Figure 4.4 shows the arrangement of equipments of the PIV equipment.

Particles were evenly mixed with water in a bucket, and then injected into the mid-section of the towing tank. After the water had settled, the lights in the towing tank were turned off, the laser was turned on, the carriage movement was started, and the laser was synchronised with the CCD cameras at two consecutive points in time. The particles were reflected in the light of the laser, and as their locations changed in the measurement field, they were captured by the cameras. Through processing of the pictures, the velocity flow field in the model was calculated, and a vorticity field was obtained.

Signals were recorded on 18 different channels, as shown in Table 4.2.

4.1.3 Coordinate system

The coordinate system is defined in Figure 4.5. The positive direction of the X-axis (IL) is opposite to the incoming flow, and the positive direction of the Z-axis (CF) is upwards. The Y-axis is not used in this thesis.

4.1.4 Definition of phase angle

Aronsen (2007) used the following two equations to describe harmonic motions with CF and IL components:

$$\begin{aligned} CF : x_{CF}(t) &= A_{CF} \cos(\omega_{osc} t) \\ IL : x_{IL}(t) &= A_{IL} \sin(2\omega_{osc} t + \theta) \end{aligned} \quad (4.1)$$

This thesis will follow the same definitions. There is another definition of the phase angle, which shows a phase shift from the present work ((Jauvtis

Table 4.2: Channels in MC Lab.

NO.	Parameter	Unit
1	IL acceleration, starborad side	$[m/s^2]$
3	CF acceleration, starborad side	$[m/s^2]$
4	IL force, starborad side	$[N]$
5	CF force, starborad side	$[N]$
6	IL force, port side	$[N]$
7	CF force, port side	$[N]$
8	IL acceleration, port side	$[m/s^2]$
9	CF acceleration, port side	$[m/s^2]$
11	IL displacement, string potentiometer	$[m]$
12	CF displacement, string potentiometer	$[m]$
13	IL acceleration, on carriage	$[m/s^2]$
14	CF acceleration, on carriage	$[m/s^2]$
15	IL displacement, U axis in carriage	$[m]$
16	CF displacement, Z axis in carriage	$[m]$
17	Carriage position	$[m]$
18	PIV trigger signal	$[V]$

and Williamson, 2004; Dahl, 2008; Wu, 2011) as follows:

$$\begin{aligned}
 CF : x_{CF}(t) &= A_{CF} \sin(\omega_{osc} t) \\
 IL : x_{IL}(t) &= A_{IL} \sin(2\omega_{osc} t + \theta)
 \end{aligned}
 \tag{4.2}$$

The phase angle between the hydrodynamic force (see section 4.5.4) and displacement in the IL direction is as follows:

$$\begin{aligned}
 \text{Hydrodynamic force} : F_{hydro,IL,2}(t) &= F_{hydro,IL,2,0} \sin(2\omega_{osc} t + \theta + \phi_X) \\
 \text{Displacement} : x_{IL}(t) &= A_{IL} \sin(2\omega_{osc} t + \theta)
 \end{aligned}
 \tag{4.3}$$

The phase angle between the hydrodynamic force and displacement in the

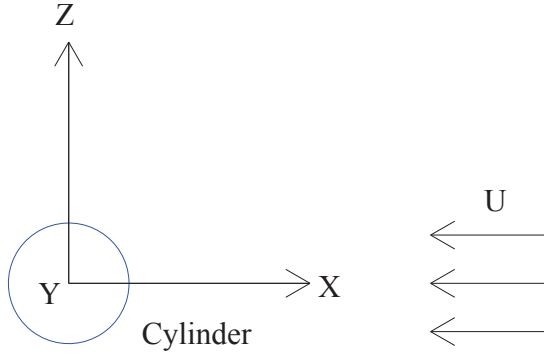


Figure 4.5: Coordinate system of forced motion tests in MCLab.

CF direction is as follows:

$$\begin{aligned} \text{Hydrodynamic force : } F_{hydro,CF,1}(t) &= F_{hydro,CF,1,0} \sin(\omega_{osc}t + \phi_Y) \\ \text{Displacement : } x_{CF}(t) &= A_{CF} \sin(\omega_{osc}t) \end{aligned} \quad (4.4)$$

Phase angle diagram

Figure 4.6a shows the definition of the phase angle between the IL and CF displacements. Figure 4.6b shows a sketch of both the phase angle between displacements and the phase angle between the displacement and hydrodynamic forces in each direction.

4.2 Modelling laws

The main test matrix for the tests performed at MCLab was based on the measurements of NDP high-mode VIV tests. Similarity rules were applied when scaling from the NDP model to the MCLab model, (Aarsnes and Steen, n.d.).

4.2.1 Geometric similarity

The scale factor between NDP tests and the MCLab forced motion experiment is as follows:

$$\lambda = \frac{D_{NDP}}{D_{MC}} = \frac{0.027}{0.1} = 0.27 \quad (4.5)$$

where D_{NDP} and D_{MC} are the diameters of the model in the NDP tests and MCLab tests respectively.

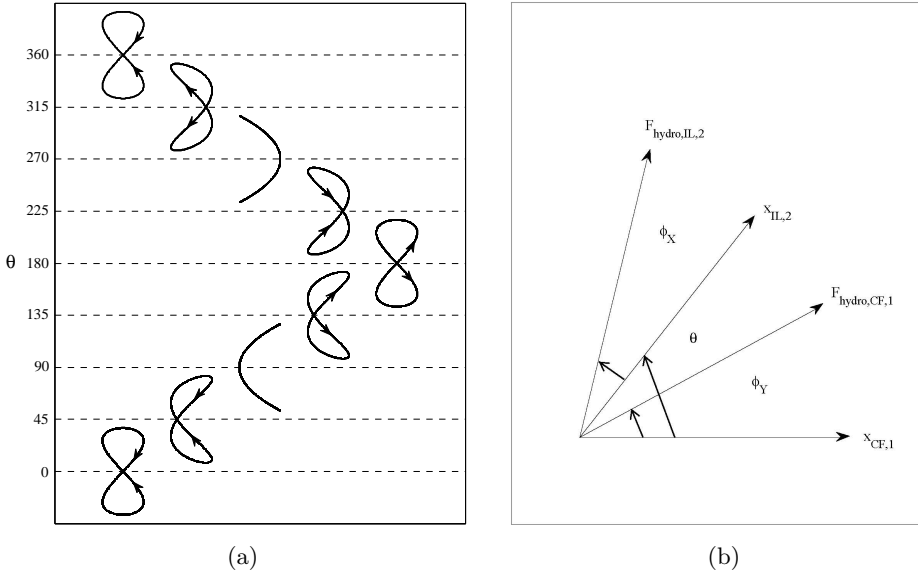


Figure 4.6: (a) Definition of phase angle θ between 1st CF harmonic displacement component and 2nd IL harmonic displacement component, the flow direction is from left to the right. (b) Definition of the phase angle ϕ between a harmonic hydrodynamic force component and harmonic displacement component in CF and IL directions.

4.2.2 Reynolds number

The Reynolds number was held constant to obtain the correct hydrodynamic forces, as shown below:

$$Re = \frac{U_{NDP} D_{NDP}}{\nu} = \frac{U_{MC} D_{MC}}{\nu} \quad (4.6)$$

where U_{NDP} is the velocity of the current selected section and U_{MC} is the towing velocity of the corresponding case. From this relationship, the towing velocity for the MCLab test is determined as follows:

$$U_{MC} = U_{NDP} \cdot \lambda \quad (4.7)$$

4.2.3 Non-dimensional frequency

The non-dimensional frequency defined by Eq. (2.19) was held constant between two experiments using the following relationship:

$$\hat{f} = \frac{f_{osc,NDP} D_{NDP}}{U_{NDP}} = \frac{f_{osc,MC} D_{MC}}{U_{MC}} \quad (4.8)$$

where $f_{osc,NDP}$ and $f_{osc,MC}$ are the oscillation frequencies of each test case.

Therefore, the oscillation frequency for the MCLab test cases can be calculated as follows:

$$f_{osc,MC} = f_{osc,NDP} \cdot \lambda^2 \quad (4.9)$$

4.2.4 Amplitude ratio

The IL and CF oscillating amplitude ratios were held constant between the NDP tests and MCLab tests using the following equations:

$$\left(\frac{A}{D}\right)_{CF/IL} = \frac{A_{CF/IL,NDP}}{D_{NDP}} = \frac{A_{CF/IL,MC}}{D_{MC}} \quad (4.10)$$

$$A_{CF/IL,MC} = \frac{A_{CF/IL,NDP}}{\lambda} \quad (4.11)$$

4.3 Test procedure

All of the tests numbers outside the author's own test matrix are mainly from Aronsen (2007), others are from Szwalek and Larsen (2009).

4.3.1 Decay tests

The decay tests (also named 'pluck tests', (Aronsen, 2007)) were conducted both in air and water to determine the eigenfrequencies and damping of the system.

Consider a one-degree-of-freedom damped system, see Eq. (2.31).

The critical damping is given by:

$$c_{kr} = 2m\omega_0 = 2\sqrt{mk} \quad (4.12)$$

where ω_0 is the natural frequency for an un-damped system.

The damping ratio is defined as follows:

$$\xi = \frac{c}{c_{kr}} = \frac{c}{2m\omega_0} \quad (4.13)$$

For real structures, the most common case is that the damping ratio $\xi \ll 1$. Free oscillation of a damped system will take place at a 'damped natural frequency' given by:

$$\omega_d = \omega_0 \sqrt{1 - \xi^2} \quad (4.14)$$

The method used to determine the damping in this thesis is to compare two amplitudes of the force signal with an interval of an integer number of periods: $T_d = 2\pi/\omega_d$.

$$\frac{u_i}{u_{i+n}} = e^{n\xi\omega_0 T_d} \quad (4.15)$$

here u_i represents force signal.

The logarithmic decrement Λ is defined as follows

$$\Lambda = \ln\left(\frac{u_i}{u_{i+n}}\right) = n\xi\omega_0 T_d = 2\pi n \frac{\xi}{\sqrt{1 - \xi^2}} \simeq 2\pi n\xi \quad (4.16)$$

The approximation is made based on the fact that ξ is typically a small number.

Then an approximate expression for the damping ratio is given by:

$$\xi \simeq \frac{1}{2\pi n} \ln\left(\frac{u_i}{u_{i+n}}\right) \quad (4.17)$$

Finally, the damped eigenfrequency can be calculated by Eq. (4.14). Details of this method can be found in Larsen (2007).

Alternatively, the damped frequency can be found directly in the frequency domain by using the FFT.

In air

Before the tank was filled with water, decay tests were performed manually in both the IL and CF directions. The measured natural frequency in air was above 30 Hz in both directions.

In water

When the tank was filled with water and ready for regular tests, decay tests were manually conducted again, both in the IL and CF directions. The measured damped eigenfrequency in water was higher than 6 Hz.

The natural frequency in both air and in water was much higher than the response frequency, which is smaller than 1Hz. Therefore, the noise caused by the system was filtered out.

4.3.2 Stationary tests

Stationary tests indicated that the cylinder was towed with constant speed, with no motion in the IL or CF directions. Table 4.3 shows the list of stationary tests performed.

In air

The stationary tests in air are conducted primarily to measure the noise of the system, and through analysis in the frequency domain, to determine the frequency range of the noise and filter it out.

In water

The same tests were performed in water, to determine the drag coefficient and Strouhal number with varying Re .

4.3.3 Harmonic forced motion tests

There are three different types of harmonic forced motion tests, as described in section 2.5.2. Harmonic motions were applied in the IL, CF and combined IL and CF directions before the tank was filled with water to estimate the capacity of the experimental system by using the tests with the maximum and minimum amplitude ratios. These tests were also used to judge the variability of the non-dimensional frequency.

Pure CF tests in air

Table 4.3 shows the results of the pure CF harmonic tests in air. All of the tests have the maximum $(A/D) = 1$. The non-dimensional frequencies were 0.143 and 0.220.

Pure IL tests in air

For pure IL tests, the amplitude was in the range of $[0.05, 0.175]$, and the non-dimensional frequency was in the range of $[0.524, 1.179]$, as shown in Table 4.3.

Combined IL and CF tests in air

The combined IL and CF tests in air have small amplitude ratios, as they were taken from Aronsen (2007). Aronsen's tests were performed with a constant amplitude ratio of 2 between the CF and IL directions, and

$(A/D)_{CF} = 0.3$. The two selected runs had different phase angles, as shown in Table 4.3.

Pure CF tests in water

The pure CF tests in water had the same Reynolds number $Re = 24000$. The amplitude ratio was 0.6 for all tests, and the non-dimensional frequency was in the range of [0.13, 0.2].

Pure IL tests in water

The amplitude ratio of the pure IL tests was held constant at 0.175, and the frequency range was [0.2, 0.45].

Combined IL and CF tests in water

Three ‘figure 8’ tests with different Re values and phase angles between the IL and CF directions were performed in water, as shown in Table 4.3.

Similar to the procedure of the harmonic tests in air, pure CF, pure IL and combined IL and CF tests were also performed in water, and the results were verified using the results obtained by Aronsen (2007).

4.3.4 Daily test

One stationary test and one ‘figure 8’ test were performed twice daily (before and after the main test matrix). Table 4.3 shows the properties of these two tests. The daily tests were important because the stationary tests were used to check the operation of all force transducers, connections and carriage equipment, and the ‘figure 8’ test was used to check the functioning of accelerometers and potentiometers.

4.3.5 Main test matrix

Definition of 19 sections of the NDP test model

For each NDP 38 m-long pipe, the provided displacement data is a matrix, which contains displacement time series of 200 discrete locations along the pipe in IL and CF directions.

Table 4.3: Test runs outside main test matrix.

Type	Test NO.	Re	$(A/D)_{CF}$	$(A/D)_{IL}$	\hat{f}	θ [°]
$S_{A/W}$	8900	10100				
	8901	18349				
	8902	24000				
	8903	27523				
	8904	32110				
	8905	36697				
	8906	38500				
	8907	41284				
	8908	45872				
CF_A	5060	10100	0.4		0.130	
	5064	10100	0.4		0.200	
	5090	10100	1.0		0.130	
	5094	10100	1.0		0.200	
IL_A	8060	24000		0.05	0.200	
	8065	24000		0.05	0.45	
	8084	24000		0.175	0.200	
	8089	24000		0.175	0.45	
$CF&IL_A$	8920	24000	0.3	0.15	0.163	0
	8925	24000	0.3	0.15	0.163	180
CF_W	5370	24000	0.6		0.130	
	5371	24000	0.6		0.145	
	5372	24000	0.6		0.160	
	5373	24000	0.6		0.175	
	5374	24000	0.6		0.200	
IL_W	8084	24000		0.175	0.200	
	8085	24000		0.175	0.250	
	8086	24000		0.175	0.300	
	8087	24000		0.175	0.350	
	8088	24000		0.175	0.400	
	8089	24000		0.175	0.450	
$CF&IL_W$	8921	10100	0.3	0.15	0.163	0
	8924	38500	0.3	0.15	0.100	0
	8925	24000	0.3	0.15	0.163	180
D_W	8902	24000				
	8924	38500	0.3	0.15	0.100	0

Type: S: stationary tests; CF: pure CF harmonic forced motion tests; IL: pure IL harmonic forced motion tests; $CF&IL$: combined CF and IL harmonic forced motion tests; D: daily tests. **Subscript:** A: in air; W: in water.

The following formula was used to select 19 sections from the ‘top end’ (where the velocity is maximum for sheared flow cases) to the ‘bottom end’:

$$l_i = (i \times 10 - 1)l \quad i = 1, 2, \dots, 19 \quad (4.18)$$

where l_i is the distance from the top end to section i and $l = 38/199 \text{ m}$.

The local velocity for shear flow cases is as follows:

$$U_i = U_{max} \cdot \left(1 - \frac{l_i}{38}\right) \quad i = 1, 2, \dots, 19 \quad (4.19)$$

To run each case in MCLab, the modelling laws described in section 4.2 were applied. The towing velocity and oscillating frequency were calculated, and the amplitude ratio was held constant.

Definition of different types of forced motion experiments

In section 2.5.2, ‘observed orbits’ were defined as the measured motion of a cross section of the flexible pipe. There are three applications of ‘observed orbits’:

1. Periodic tests: Select the displacement in one cycle, make the orbit close (see section 3.3.5), and apply it to the forced motion tests.
2. Filtered harmonic tests: Based on a periodic test orbit, using the FFT, filter out higher order frequency components, transform them back into a time series, and apply them to the forced motion tests.
3. Observed orbit tests: Select a displacement duration that has N cycles and apply it directly to the forced motion tests without smoothing.

Table 4.4 shows the main test matrix performed in MCLab. The PIV tests used the same orbit as the periodic tests, with PIV measuring equipments installed.

4.4 Execution of the experiment

Each test run was performed in MCLab as follows:

1. Load the input file with suffix *.mcl* into the *Mclc.vi* LabVIEW front panel. Synchronise the computer with the carriage.
2. Perform the zero settings of all channels.

Table 4.4: Main test matrix.

Type	Test NO.	Runs	Test NO.	Runs
Periodic	N2030x	19	N2340x	19
	N2100x*	19	N2370x*	19
	N2160x*	19	N2430x*	19
Periodic orbit variation			N23405	2
			N234018	2
			N23702	2
			N23707	2
Filtered harmonic			H23405	2
			H234018	2
Observed orbit	TN2030x	19	TN2340x	19
PIV	P2030x	3	P2340x	8
	P2100x*	4	P2370x*	8
	P2160x*	1	P2430x*	8
Total		84		112

$x = 1, 2, \dots, 19$.

Cases with superscript * has a modified oscillation frequencies due to the limit of experimental equipment, see section 4.1.1 and Appendix B.

3. Start logging data before starting the carriage.
4. Start the carriage. The carriage accelerates to the desired towing velocity and continues to run at this velocity for N oscillation periods.
5. The carriage decelerates from the towing velocity to zero: simultaneously, the oscillations stop.
6. Data logging continues for approximately 10 seconds after the carriage stops.
7. Stop logging data and save the data file in a binary format.

8. Drive the carriage back at a fixed velocity 0.5m/s to the original position for all test runs, and wait approximately 10 minutes for the water to calm, before the next test.

4.5 Signal processing procedure

The signal pre- and post-processor were developed based on the methods used by Aronsen (2007) and Soni (2008). As there are some differences between the present experiments and those performed in the previous studies, the processors are also different.

4.5.1 Time window

The length of each rigid cylinder test was between 50 seconds and 4 minutes, utilising the available length of the tank (20m). The data were sampled at 400 Hz. The cylinder started from rest, implying that the state at $t = 0$ was that of a stationary cylinder in still water. At $t > 0$ the cylinder oscillated at a prescribed motion. Simultaneously, the towing carriage accelerated to the desired velocity, maintained a constant towing speed, and then decelerated to zero speed at the end of the experiment. The time window to be used in data processing was chosen based on the following principles:

- Avoid the acceleration and deceleration sections with varying towing velocities.
- Avoid force/displacement transient effects.
- Find a period of an integer number of cycles by counting the up-crossing points in the CF motion signal (use the IL motion signal if IL is dominant). Calculate the oscillation frequency.

4.5.2 Carriage motion signals

- The towing velocity of the carriage was calculated by using the carriage position signal, and the Re number and non-dimensional frequency were calculated based on the towing velocity of the carriage.

4.5.3 IL and CF motion signals

- The mean values for the IL and CF displacements were subtracted from each displacement value to determine the maximum amplitude for each direction.

- In the frequency domain, the velocity and acceleration from the displacement signals were calculated using a MATLAB script as follows:
 1. FFT was used to transform the signal $x(t)$ to frequency domain, $X(\omega) = fft(x(t))$.
 2. A frequency vector with the same length as X was established. The vector had a range from 0 to the Nyquist frequency and then from a negative value of the Nyquist frequency to 0.
 3. Both low- and high-pass filtering was performed by setting the values of X outside the frequency band equal to 0.

4.5.4 Force signals

The force signals were processed in the following steps:

- The force signal was multiplied by the calibration factor and rotated by the skew angle (see Appendix A).
- The mean IL and CF force components were subtracted from the force signals.
- The mean drag coefficients were computed using the mean IL force.
- The inertia force component caused by the dry mass of the cylinder was subtracted from the result to obtain the net hydrodynamic force.

4.6 Hydrodynamic coefficients

There are two methods of calculating the hydrodynamic coefficients: using the Fourier series components of the displacements or filtering the displacement signals around each frequency component. These two methods will be introduced in the following sections.

4.6.1 Fourier series

The IL and CF displacement time series are defined as $x_{IL}(t)$ and $x_{CF}(t)$ respectively. They can be expressed in Fourier series to obtain the harmonic components as follows:

$$x_{IL/CF}(t) = \frac{a_{IL/CF,0}}{2} + \sum_{n=1}^{\infty} [a_{IL/CF,n} \cos(\frac{2n\pi}{T}t) + b_{IL/CF,n} \sin(\frac{2n\pi}{T}t)] \quad (4.20)$$

where

$$a_{IL/CF,n} = \frac{2}{kT} \int_t^{t+kT} x_{IL/CF}(\tau) \cos\left(\frac{2n\pi}{T}\tau\right) d\tau \quad (n = 0, 1, 2, \dots) \quad (4.21)$$

$$b_{IL/CF,n} = \frac{2}{kT} \int_t^{t+kT} x_{IL/CF}(\tau) \sin\left(\frac{2n\pi}{T}\tau\right) d\tau \quad (n = 1, 2, \dots) \quad (4.22)$$

and k is the number of oscillation cycles.

The IL and CF displacement time series of each frequency component $x_{IL/CF,n}(t)$ are:

$$x_{IL/CF,n}(t) = A_{IL/CF,n} \cos\left(\frac{2n\pi}{T}t - \theta_{IL/CF,n}\right) \quad (n = 1, 2, \dots) \quad (4.23)$$

where the amplitude of each frequency is:

$$A_{IL/CF,n} = \sqrt{a_{IL/CF,n}^2 + b_{IL/CF,n}^2} \quad (n = 1, 2, \dots) \quad (4.24)$$

and the phase angle is:

$$\theta_{IL/CF,n} = \arctan\left(\frac{b_{IL/CF,n}}{a_{IL/CF,n}}\right) \quad (n = 1, 2, \dots) \quad (4.25)$$

4.6.2 Band-pass filtering signal

Fourier series components can represent periodic orbits well. However, the experimental data indicated that there was a bandwidth around each frequency component of the hydrodynamic force. If the Fourier series components of the force are used to calculate the hydrodynamic coefficients, then the information beyond the discrete frequency value is lost.

To capture all of the important information of the hydrodynamic force, a band-pass filtering method was applied both to the displacement and force signals. For the n^{th} order response frequency $f_{osc,n} = n f_{osc}$, a frequency band $[f_{osc,n} - 0.2 f_{osc}, f_{osc,n} + 0.2 f_{osc}]$ was applied.

4.6.3 Hydrodynamic coefficients for each frequency component

The mean drag coefficient is defined as:

$$C_D = \frac{F_{IL,mean}(\tau)}{\frac{1}{2}\rho DLU^2} = \frac{\lim_{k \rightarrow \infty} \frac{\int_t^{t+kT} F_{IL}(\tau) d\tau}{kT}}{\frac{1}{2}\rho DLU^2} \quad (4.26)$$

where $F_{IL,mean}(\tau)$ is the force in the IL direction.

The dynamic excitation coefficient corresponding to the n^{th} harmonic component ω_n is defined as follows (Soni, 2008):

$$C_{e,IL/CF,n} = \frac{\frac{2}{x_{IL/CFn,0}\omega_n} \lim_{k \rightarrow \infty} \frac{\int_t^{t+kT} F_{hydro,IL/CF}(\tau) \cdot \dot{x}_{IL/CF,n}(\tau) d\tau}{kT}}{\frac{1}{2}\rho DLU^2} \quad (4.27)$$

The subscripts IL and CF on the hydrodynamic coefficients correspond to the IL and CF directions, and the subscript n corresponds to the n^{th} order frequency. $x_{IL/CFn,0}$ is the displacement amplitude at the n^{th} order frequency in IL or CF direction, see Eq. (4.23). The force coefficient defines the energy transfer between the fluid and cylinder for each harmonic component present in the time series. Positive coefficients indicate that energy is transferred from the fluid to the cylinder, while negative coefficients indicate energy dissipation through hydrodynamic damping.

The added mass coefficient represents the hydrodynamic force in phase with the acceleration and is defined as follows:

$$C_{a,IL/CF,n} = \frac{-\frac{2}{x_{IL/CFn,0}\omega_n^2} \lim_{k \rightarrow \infty} \frac{\int_t^{t+kT} F_{hydro,IL/CF}(\tau) \cdot \ddot{x}_{IL/CF,n}(\tau) d\tau}{kT}}{\frac{\pi D^2}{4} \rho L \omega_n^2 x_{IL/CFn,0}} \quad (4.28)$$

This coefficient explains the physics of added mass for each harmonic component.

The average power transfer, \bar{E} , during a period of time, kT , is defined as follows:

$$\bar{E}_{IL/CF} = \lim_{k \rightarrow \infty} \frac{\int_t^{t+kT} F_{hydro,IL/CF}(\tau) \cdot \dot{x}_{IL/CF,n}(\tau) d\tau}{kT} \quad (4.29)$$

Note that the integrals in Eqs. (4.27) to (4.29) must always be taken over an integer number of oscillation periods ($k = 1, 2, 3, \dots, N$).

The total dynamic force coefficient is defined as follows:

$$C_{t,IL/CF,n} = \frac{\sqrt{a_{IL/CF,n}^2 + b_{IL/CF,n}^2}}{\frac{1}{2}\rho DLU^2} \quad (4.30)$$

where

$$a_{IL/CF,n} = \frac{2}{kT} \int_t^{t+kT} F_{hydro,n,IL/CF}(\tau) \cos\left(\frac{2n\pi}{T}\tau\right) d\tau \quad (4.31)$$

$$b_{IL/CF,n} = \frac{2}{kT} \int_t^{t+kT} F_{hydro,n,IL/CF}(\tau) \sin\left(\frac{2n\pi}{T}\tau\right) d\tau \quad (4.32)$$

The IL or CF rms-coefficient, is defined by the total hydrodynamic force as follows:

$$C_{rms,IL/CF} = \frac{\sqrt{2 \cdot \frac{1}{n} \sum_{i=1}^n (F_{hydro,IL/CF,i} - \bar{F}_{hydro,IL/CF})^2}}{\frac{1}{2}\rho DLU_0^2} \quad (4.33)$$

4.7 Analysis of forced motion tests with observed orbits

4.7.1 Drawback of the Fourier transform

A time-domain signal can be represented by a sum of discrete frequencies using trigonometric functions with fixed amplitude. However, if we have a signal such as:

$$x(t) = A(t) \sin(\omega t + \theta) \quad (4.34)$$

where the amplitude is changing with time. To capture the variation of amplitude $A(t)$, more trigonometric functions are needed in addition to the trigonometric function at ω .

4.7.2 Envelope detection

Another method that might be more valid is called ‘Envelope detection’ (details described in ‘MATLAB HELP’). The main principle is to find the ‘envelope’ (outline) of a signal. Two methods can be used:

- Squaring and low-pass filtering
The input signal is first squared and then sent through a low-pass filter.
- Hilbert transform
*The **analytic signal** of the input is created using a Hilbert transform. The envelope of the signal can be found by taking the absolute value of the analytic signal.*

The analytic signal for a sequence x has a one-sided Fourier transform, that is, negative frequencies are 0. To approximate the analytic signal, the Hilbert transform calculates the FFT of the input sequence, replaces those FFT coefficients that correspond to negative frequencies with zeros, and calculates the inverse FFT of the result.

By applying the ‘Envelope detection’ technique to determine the amplitude envelop of a signal, together with the FFT to find the frequency components, such signals as that shown in Eq. (4.34) can be described accurately.

4.7.3 Statistical analysis

Both displacement and force signals from observed orbit tests are not stable; instead, they show a chaotic characteristic (Modarres-Sadeghi et al., 2011). Even for periodic tests, when the input motion is periodic, the force also exhibits amplitude variations. Therefore, a statistical analysis is required in those cases, and the first step is to compare statistical parameters between the periodic orbits and observed orbits. The goal is to find a model to represent the response and force.

Different probability models are used for comparison purposes, as shown in Table 4.5. Rayleigh distribution is related to individual maxima. Gumbel distribution, two-parameter and three-parameter Weibull distributions are extreme value distributions.

Table 4.5: Probabilistic models.

Model.	Density function	Cumulative distribution
Rayleigh	$f_Y(y) = \frac{y}{\sigma^2} \exp\{-\frac{1}{2}(\frac{y}{\sigma})^2\}$	$F_Y(y) = 1 - \exp\{-\frac{1}{2}(\frac{y}{\sigma})^2\}$
Gumbel	$f_Y(y) = \alpha \exp\{-\alpha(y-u) - e^{-\alpha(y-u)}\}$	$F_Y(y) = \exp\{e^{-\alpha(y-u)}\} - \infty \leq y \leq \infty$
Weibull (2)	$f_Y(y) = \frac{\lambda}{\sigma} (\frac{y}{\sigma})^{\lambda-1} \exp\{-(\frac{y}{\sigma})^\lambda\}$	$F_Y(y) = 1 - \exp\{-(\frac{y}{\sigma})^\lambda\}$
Weibull (3)	$f_Y(y) = \frac{\lambda}{\sigma} (\frac{y-\mu}{\lambda})^{\lambda-1} \exp\{-(\frac{y-\mu}{\sigma})^\lambda\}$	$F_Y(y) = 1 - \exp\{-(\frac{y-\mu}{\sigma})^\lambda\}$

4.8 Processing and analysis of PIV data

4.8.1 Basic equations

Velocity

The local velocity, \vec{u} , of a particle can be estimated as follows:

$$\vec{u}(\vec{x}, t) \doteq \frac{\Delta \vec{x}(\vec{x}, t)}{\Delta t} \quad (4.35)$$

where $\Delta \vec{x}$ is the displacement of a particle located at \vec{x} at time t over a short time interval, Δt .

Vorticity

The *vorticity* is defined as a measure of the rotational velocity of fluid elements (Blevins, 1990) as follows:

$$\omega = \frac{\partial v}{\partial x} - \frac{\partial u}{\partial y} \quad (4.36)$$

where ω is the sum of the rotational velocities of two adjacent sides of the fluid element.

4.8.2 PIV data post processing

Thousands of images were recorded during the PIV test runs. Commercial software, VidPIV (*VidPIV User Manual*, 2005), was used to map the images from two cameras, and velocity vectors were calculated. The wake behind the cylinder model was captured, and a file containing the data was saved. Then, MATLAB was used to process the data further to calculate the phase average and vorticity. The plan was to compare the vortex field measured with PIV to the CFD simulation results. But due to the particle-mixed water was not clear, the images recorded from the underwater cameras are too obscure to be processed. Only force measurements are used in this study.

Chapter 5

Uncertainty Analysis and Quality Control

This chapter presents the uncertainty analysis used for the forced motion test results. All of the error sources relevant to the hydrodynamic coefficients are discussed. The final results are given as a value with an error bar. For the cases performed twice (PIV tests), special attention is given to the stability of the force signals and the phase angle between the hydrodynamic force and displacement.

5.1 General description

If property data and experimentally determined information is used in an analytical solution, a quantitative estimate of the reliability of a measured or calculated value should be provided. This measure is the basis of uncertainty analysis. Here, a 95% confidence interval is used, i.e., the probability that the true value to be within this interval is 0.95 (Aronsen, 2007; Coleman and Steele, 1999).

5.1.1 Error and Uncertainty

The total measurement error is defined as the difference between the measured value and the true value. The total error (δ) is the sum of the systematic (bias) error and the random (precision) error. The bias error (β) is constant for a specific parameter and test procedure. The random component (ε) of the total error is also termed the repeatability or repeatability error. Uncertainty is the statistical estimate of the error (Coleman and

Steele, 1999; Aronsen, 2007).

Due to the change in precision error, the total error varies according to each measurement as follow:

$$\delta_i = \beta + \varepsilon_i \quad (5.1)$$

To understand the difference between bias and precision error, the calibration of a single force sensor is used as an example. During this process, the bias error is given by the possible error in the weight used to perform the calibration. The precision error is typically given by the variation in calibration coefficients found from different loading sequences (Aronsen, 2007).

Replication Level

When discussing errors and uncertainties in measurements, it is important to distinguish between repetition and replication. Repetition means that something is repeated. Replication level is defined by considering what is repeated when repeating an experiment. Three replication levels were defined by Aronsen (2007) and Coleman and Steele (1999):

0th order replication level The measured process is hypothesised to be absolutely steady, meaning that it is independent of time. Random errors arise only from the intrinsic variations in the the measuring system. An example is measuring the length and diameter of the test cylinder model.

1st order replication level In a time-dependent experiment, the time marches forward, while all instrument identities are fixed. The variability of the measurement is caused by the variables that vary with time during repeated trials. An example would be the measurements of force during the fixed-cylinder towing test.

Nth order replication level The uncertainty of these levels includes the random errors estimated by the first-order replication level together with all systematic errors influencing the measurements. This step requires performing a second test at a later time or performing a similar experiment in a different laboratory.

Without changing the set-up, repeating the test at another time is recognised as the 2^{nd} order replication level. The higher replication level relates to the PIV test phase in which the PIV equipment was mounted.

5.2 Data Reduction Equations (DRE)

Key results of this experimental work are the hydrodynamic coefficients derived from several variables. The propagation of elemental error related to each variable to the final result is captured by the data reduction equation (Coleman and Steele, 1999). A description of this equation and how it is used in the uncertainty analysis is provided below.

5.2.1 General

The general data reduction equation is:

$$r = r(X_1, X_2, \dots, X_N) \quad (5.2)$$

where r is an experimental result that is a function of n measured variables X_i .

For a large-sample experiment (the number of degrees of freedom n of the result r is 9 or more), the 95% confidence uncertainty analysis recommended for use is:

$$U_r^2 = B_r^2 + P_r^2 \quad (5.3)$$

where U_r , B_r and P_r are overall uncertainty, systematic uncertainty, and random uncertainty respectively. The DRE is used to calculate B and P individually.

$$B_r^2 = \sum_{i=1}^N \theta_i^2 B_i^2 + 2 \sum_{i=1}^{N-1} \sum_{k=i+1}^N \theta_i \theta_k B_{ik} \quad (5.4)$$

where B_i is the systematic uncertainty of the variables X_i in Eq. (5.2), B_{ik} is the covariance estimator for the systematic errors in X_i and X_k , and

$$\theta_i = \frac{\partial r}{\partial X_i} \quad (5.5)$$

which is called the *absolute sensitivity coefficient*, defines how the results are influenced by one specific measurement.

If the measurements of different variables are independent of each other, the covariance terms are zero and Eq. (5.4) becomes

$$B_r^2 = \left(\frac{\partial r}{\partial X_1} B_1 \right)^2 + \left(\frac{\partial r}{\partial X_2} B_2 \right)^2 + \dots + \left(\frac{\partial r}{\partial X_N} B_N \right)^2 \quad (5.6)$$

where for the N th variable, X_N , if there are J significant elemental bias error sources and the corresponding systematic uncertainties are estimated as $(B_N)_1, (B_N)_2, \dots, (B_N)_J$, the systematic uncertainty of the measurement of X_N is calculated as the root-mean-square combination of the elemental systematic uncertainties as follows:

$$B_N = \left[\sum_{k=1}^J (B_N)_k^2 \right]^{1/2} \quad (5.7)$$

and

$$P_r^2 = \sum_{i=1}^N \theta_i^2 P_i^2 \quad (5.8)$$

$$= \left(\frac{\partial r}{\partial X_1} P_1 \right)^2 + \left(\frac{\partial r}{\partial X_2} P_2 \right)^2 + \dots + \left(\frac{\partial r}{\partial X_N} P_N \right)^2 \quad (5.9)$$

where P_i is the random uncertainty of the variables X_i in Eq. (5.2). This relation applies when it is assumed that the large-sample equation applies and that the random uncertainty for each measured variable is determined from a data set with $N_i \geq 10$.

It is the degrees of freedom of the result, not the degrees of freedom of the separate uncertainty sources, that dictates whether the large-sample approximation is appropriate. If there are several variables with only a few degrees of freedom, their combination in the calculation of the degrees of freedom of the result will often show that the large-sample approximation can be used to obtain a 95% confidence estimate of the total uncertainty (Coleman and Steele, 1999).

The uncertainty in the result is given by

$$U_r^2 = \left(\frac{\partial r}{\partial X_1} \right)^2 U_{X_1}^2 + \left(\frac{\partial r}{\partial X_2} \right)^2 U_{X_2}^2 + \dots + \left(\frac{\partial r}{\partial X_n} \right)^2 U_{X_n}^2 = \sum \theta_i^2 U_{X_i}^2 \quad (5.10)$$

By dividing each term in Eq. (5.10) by r^2 and multiplying each term on the right-hand side by $(X_i/X_i)^2$, which equals 1, Eq. (5.10) becomes

$$\frac{U_r^2}{r^2} = \left(\frac{X_1}{r} \frac{\partial r}{\partial X_1} \right)^2 \left(\frac{U_{X_1}}{X_1} \right)^2 + \left(\frac{X_2}{r} \frac{\partial r}{\partial X_2} \right)^2 \left(\frac{U_{X_2}}{X_2} \right)^2 + \dots + \left(\frac{X_n}{r} \frac{\partial r}{\partial X_n} \right)^2 \left(\frac{U_{X_n}}{X_n} \right)^2 \quad (5.11)$$

The term $\frac{X_i}{r} \frac{\partial r}{\partial X_i}$ on the right side of Eq. (5.11) is the uncertainty magnification factor (UMF). The UMF for a given X_i indicates the influence of the

uncertainty in that particular variable on the uncertainty in the final result. A UMF value greater than 1 indicates that the influence of the uncertainty in the variable is magnified as it propagates through the data reduction equation to the result, and vice versa. For simplicity, UMF was assumed to be 1, which means that the uncertainty of each variable is neither magnified nor diminished during the propagation process. Then, Eq. (5.11) can be simplified as follows:

$$\frac{U_r^2}{r^2} = \left(\frac{U_{X_1}}{X_1}\right)^2 + \left(\frac{U_{X_2}}{X_2}\right)^2 + \dots + \left(\frac{U_{X_n}}{X_n}\right)^2 \quad (5.12)$$

In this thesis, Eq.(5.10) is used as the DRE, while bias error and precision error are taken into account through Eq.(5.6) and Eq.(5.9), and total uncertainty is calculated by Eq.(5.3).

5.2.2 DRE for the hydrodynamic coefficients

In this section, the absolute sensitivity coefficients for the three hydrodynamic coefficients are determined.

Drag coefficient C_D

$$\left(\frac{U_{C_D}}{C_D}\right)^2 = \left(\frac{U_{F_{IL,mean}}}{F_{IL,mean}}\right)^2 + \left(\frac{U_D}{D}\right)^2 + \left(\frac{U_L}{L}\right)^2 + \left(\frac{2U_{U_0}}{U_0}\right)^2 \quad (5.13)$$

For the dynamic excitation coefficient, C_e , and the added mass coefficient, C_a , the coefficients can have a value of zero. Thus, Eq. (5.12) cannot be used because the denominator cannot be zero.

The CF and IL hydrodynamic excitation and added mass coefficients are calculated from the hydrodynamic force in phase with the respective velocity and acceleration components of the oscillating cylinder model. To obtain these two components of the hydrodynamic force, the two following integrations on k motion periods were computed:

$$I_{C_e} = \lim_{k \rightarrow \infty} \frac{\int_t^{t+kT} F_{hydro,IL/CF}(\tau) \cdot \dot{x}_{IL/CF,n}(\tau) d\tau}{kT} \quad (5.14)$$

$$I_{C_a} = \lim_{k \rightarrow \infty} \frac{\int_t^{t+kT} F_{hydro,IL/CF}(\tau) \cdot \ddot{x}_{IL/CF,n}(\tau) d\tau}{kT} \quad (5.15)$$

where each part of the above equations is explained in Eqs. (4.27) and (4.28).

During the experiment, k cannot approach infinity, so Eqs. (5.14) and (5.15) become:

$$I_{C_e} = \frac{\int_t^{t+kT} F_{hydro,IL/CF}(\tau) \cdot \dot{x}_{IL/CF,n}(\tau) d\tau}{kT} \quad (5.16)$$

$$I_{C_a} = \frac{\int_t^{t+kT} F_{hydro,IL/CF}(\tau) \cdot \ddot{x}_{IL/CF,n}(\tau) d\tau}{kT} \quad (5.17)$$

The dynamic excitation coefficient (C_e) is defined by Eq. (4.27). The uncertainty in C_e is calculated as follows:

$$(U_{C_e})^2 = (\theta_{I_{C_e}})^2 (U_{I_{C_e}})^2 + (\theta_{x_{IL/CF,n,0}})^2 (U_{x_{IL/CF,n,0}})^2 + (\theta_{\omega_n})^2 (U_{\omega_n})^2 + (\theta_{\rho})^2 (U_{\rho})^2 + (\theta_D)^2 (U_D)^2 + (\theta_L)^2 (U_L)^2 + (\theta_{U_0})^2 (U_{U_0})^2 \quad (5.18)$$

where the absolute sensitivity coefficients are given by:

$$\theta_{I_{C_e}} = \frac{\partial C_e}{\partial I_{C_e}} = \frac{4}{x_{IL/CF,n,0} \omega_n \rho D L U_0^2} \quad (5.19)$$

$$\theta_{x_{IL/CF,n,0}} = \frac{\partial C_e}{\partial x_{IL/CF,n,0}} = -\frac{4I_{C_e}}{x_{IL/CF,n,0}^2 \omega_n \rho D L U_0^2} \quad (5.20)$$

$$\theta_{\omega_n} = \frac{\partial C_e}{\partial \omega_n} = -\frac{4I_{C_e}}{x_{IL/CF,n,0} \omega_n^2 \rho D L U_0^2} \quad (5.21)$$

$$\theta_{\rho} = \frac{\partial C_e}{\partial \rho} = -\frac{4I_{C_e}}{x_{IL/CF,n,0} \omega_n \rho^2 D L U_0^2} \quad (5.22)$$

$$\theta_D = \frac{\partial C_e}{\partial D} = -\frac{4I_{C_e}}{x_{IL/CF,n,0} \omega_n \rho D^2 L U_0^2} \quad (5.23)$$

$$\theta_L = \frac{\partial C_e}{\partial L} = -\frac{4I_{C_e}}{x_{IL/CF,n,0} \omega_n \rho D L^2 U_0^2} \quad (5.24)$$

$$\theta_{U_0} = \frac{\partial C_e}{\partial U_0} = -\frac{8I_{C_e}}{x_{IL/CF,n,0} \omega_n \rho D L U_0^3} \quad (5.25)$$

The added mass coefficient (C_a) is defined by Eq. (4.28), and the uncertainty in C_a is:

$$(U_{C_a})^2 = (\theta_{I_{C_a}})^2 (U_{I_{C_a}})^2 + (\theta_{x_{IL/CF,n,0}})^2 (U_{x_{IL/CF,n,0}})^2 + (\theta_{\omega_n})^2 (U_{\omega_n})^2 + (\theta_D)^2 (U_D)^2 + (\theta_{\rho})^2 (U_{\rho})^2 + (\theta_L)^2 (U_L)^2 \quad (5.26)$$

where the absolute sensitivity coefficients are given by:

$$\theta_{I_{C_a}} = \frac{\partial C_a}{\partial I_{C_a}} = -\frac{8}{x_{IL/CF,n,0}^2 \omega_n^4 \pi \rho L D^2} \quad (5.27)$$

$$\theta_{x_{IL/CF,n,0}} = \frac{\partial C_a}{\partial x_{IL/CF,n,0}} = \frac{16 I_{C_a}}{x_{IL/CF,n,0}^3 \omega_n^4 \pi \rho L D^2} \quad (5.28)$$

$$\theta_{\omega_n} = \frac{\partial C_a}{\partial \omega_n} = \frac{32 I_{C_a}}{x_{IL/CF,n,0}^2 \omega_n^5 \pi \rho L D^2} \quad (5.29)$$

$$\theta_{\rho} = \frac{\partial C_a}{\partial \rho} = \frac{8 I_{C_a}}{x_{IL/CF,n,0}^2 \omega_n^4 \pi \rho^2 L D^2} \quad (5.30)$$

$$\theta_L = \frac{\partial C_a}{\partial L} = \frac{8 I_{C_a}}{x_{IL/CF,n,0}^2 \omega_n^4 \pi \rho L^2 D^2} \quad (5.31)$$

$$\theta_D = \frac{\partial C_a}{\partial D} = \frac{16 I_{C_a}}{x_{IL/CF,n,0}^2 \omega_n^4 \pi \rho L D^3} \quad (5.32)$$

For each hydrodynamic coefficient, the uncertainty of each error source was estimated. Then, the absolute sensitivity coefficient corresponding to each error source was calculated. Finally, Eqs. (5.18) and (5.26) were applied to calculate the uncertainties of the excitation coefficient and added mass coefficient respectively.

5.3 Individual uncertainties in the DRE

In this section the individual uncertainties, U_i , in the DRE are addressed. Both bias and precision errors, which are denoted as B and P respectively, are addressed.

5.3.1 Uncertainty in water density

Water density varies with temperature, as shown in Table 5.1. The towing tank was filled with fresh water, and during the test, the water temperature was measured several times at one side of the tank. In addition, during the experiments with the PIV equipment, the water density may have changed because of the particles added to the water, this effect was considered as an additional bias of 0.1.

The mean value and precision error of the water temperature can be calculated from the measurements in Table 5.1. By interpolating the densities of

Table 5.1: Mass density (ρ) and kinematic viscosity (ν) of fresh water. (Faltinsen, 1990)

Temperature	$\rho(kg \cdot m^{-3})$	$\nu \cdot 10^6(m^2s^{-1})$
0 °C	999.8	1.59
5 °C	1000.0	1.52
10 °C	999.7	1.31
15 °C	999.1	1.14
20 °C	998.2	1.00

Table 5.2: Measured temperature and estimated error of water density.

Date (2010)	<i>Jan20th</i>	<i>Jan21st</i>	<i>Jan23rd</i>	<i>Jan24th</i>
Reading temperature °C	14.1	13.4/13.5	12.5/12.9	12.8
Mean temperature °C			13.2	
STD. temperature °C			0.58	
t- value			2.571	
Mean density $kg \cdot m^{-3}$			999.32	
Density error $B_\rho(kg \cdot m^{-3})$			0.5	

different temperatures in Table 5.2, the corresponding water density can be determined. A constant density was used for all of the experiments. Thus, the density variation was treated as a bias error.

5.3.2 Uncertainty in the cylinder diameter and length

In this study, the same rigid cylinder model as Aronsen (2007) was used. The coating of the cylinder was repainted prior to the experiment. The uncertainties in the cylinder diameter and length were taken as bias errors and the values used in Aronsen (2007) were accepted as valid (see Table 5.3).

5.3.3 Uncertainty in the cylinder mass

The mass of the cylinder model was measured five times by an electronic weight. All five readings were unchanged and equal to 9.775 kg. The error in

Table 5.3: Error in cylinder diameter, U_D , and length, U_L .

D [mm]	$B_D[mm]$	L[mm]	$B_L[mm]$
100.0	0.1	2000	5

cylinder mass was treated as a bias error of 0.01 kg to account for potential uncertainty.

5.3.4 Uncertainties in the IL and CF displacements

The precision errors of the calibration factors of the IL and CF potentiometers cause bias errors in the IL and CF displacements, respectively. As the velocities and accelerations are derived from potentiometer measurements, these errors propagate to the velocity and acceleration calculations. The error is included through the use of Eqs. (5.16) and (5.17).

5.3.5 Uncertainty in towing velocity

The towing velocity, U , is derived from the towing carriage position measurements. The instantaneous velocity vector (the derivative of the displacement signal) was calculated to estimate the precision error, and the average velocity (given by averaging the instantaneous velocity) was calculated and used in the force coefficient calculation.

The bias error in the towing velocity is related to the calibration factor used in the motion control system and can be estimated by the signals under zero velocity. In this thesis, the bias used by Aronsen (2007), $B_U/U = 0.01$, was applied. The precision error was the variation over N oscillation cycles, $P_U = 2 \cdot S_U/\sqrt{N}$.

5.3.6 Uncertainty in drag force

The drag coefficient is calculated from the mean drag force, which was measured in a time window of an integer number of oscillation periods.

The errors in the calibration factors and IL/CF cross talk contributed to the bias error of the drag force. The precision error can be calculated from the variations of the mean drag force of each cycle.

5.3.7 Uncertainty in the decomposed force

Several elemental error sources contribute to the uncertainty of the decomposed force:

Bias errors

- Error in the calibration factors for the IL/CF force transducers.

- Error in the cross-talk angle between the IL and CF force transducers.
- Error from the Fourier decomposing or filtering of the displacement signal, as well as the derivation of the velocity and acceleration signal.

Precision errors

- Variation of the mean force in the IL and CF directions.
- Error due to the numerical calculation of the integration.

1. Error in the calibration factors and cross-talk angle

The calibration procedure is described in Appendix A. Each calibration factor used in the data processing program used an average of 8 values measured during the calibration process. This procedure caused a precision error for each calibration factor, as shown in Table A.1.

2. Error in the rotation angle

The rotation angle, found in Step III of the force transducer calibration, is discussed in detail in Appendix A. The error was estimated based on 40 values on each side, as shown in Table A.1. The errors in the calibration factors and rotation angles propagate into the force signal through the following equations:

$$F_{IL,A} = F_{20332} \cdot \cos(\alpha_A) - F_{20333} \cdot \sin(\alpha_A) \quad (5.33)$$

$$F_{CF,A} = F_{20332} \cdot \sin(\alpha_A) + F_{20333} \cdot \cos(\alpha_A) \quad (5.34)$$

$$F_{IL,B} = F_{20335} \cdot \cos(\alpha_B) - F_{20334} \cdot \sin(\alpha_B) \quad (5.35)$$

$$F_{CF,B} = F_{20335} \cdot \sin(\alpha_B) + F_{20334} \cdot \cos(\alpha_B) \quad (5.36)$$

where the subscript number 2033x is the serial number of strain gauge used in the experiment; $F_{2033x} = S_{2033x} \cdot f_{c2033x}$, $x = 2, 3, 4, 5$; S_{2033x} are the volt values from the channels of the force transducers, F_{2033x} is the preliminary force signal after multiplying the volt values with the calibration factor, f_{c2033x} is the calibration factor and α_A and α_B are the rotation angles on the A and B sides, respectively. The bias error of the force caused by these two parameters can be calculated by Eq. (5.6). An additional bias error comes from the cross talk between the IL and CF transducers, resulting in 2% bias error, as shown in Appendix A.

3. Error in the derivation of velocity and acceleration from the Fourier component or filtered motion signal

The displacement signals recorded from the string potentiometers in both the IL and CF directions are used to derive the cylinder oscillation velocity and acceleration. The following two methods are used to calculate $x_{IL/CF,n}(\tau)$.

- The IL and CF motion signals are decomposed into Fourier components as a combination of sinusoidal signals (see section 4.6.1). If the response or the hydrodynamic force has a frequency component that is not a multiple of the oscillation frequency, the Fourier decomposition process will fail, as it only takes discrete-frequency values into account.
- The motion signals are band-pass filtered with an FFT to determine the displacement component around each frequency. If there is a time-varying amplitude, this method will produce better results. The bandwidth will have an influence on the filtering results. A bandwidth of 0.4 times the oscillation frequency was chosen for this analysis.

Precision error of the decomposed force

The precision error of Eqs. (5.16) and (5.17) were estimated by the integral of each oscillation period. The numerical errors of the filtered hydrodynamic force component, velocity or acceleration signal and oscillation period contribute to the precision error of the integral.

5.4 Additional Error Sources

5.4.1 Residual flow

Between tests, the carriage was towed back to the start position. There was a waiting time of 10 minutes (Aronsen, 2007) before the next test started. There may have been residual flow that influenced the towing velocity.

Ersdal (2004) suggested an empirical equation to estimate the residual flow level based on far wake theory as follows:

$$\frac{u_1}{U} = 1.2 \left(\frac{Ut}{C_D D} \right)^{-\frac{1}{2}} \quad (5.37)$$

Relatively large residual flow makes the true flow velocity different from given velocity, this introduces uncertainties of the hydrodynamic coefficients.

5.4.2 Cylinder end conditions

To avoid ant 3D end effects from the finite length of the model, two end plates designed by Aronsen (2007) were mounted on both ends of the cylinder. These end plates consisted of Plexiglas and were structurally attached to the housing of the force sensors. There was a small gap between the housing and the edge of the cylinder ends to avoid touching the cylinder and influencing the force measurement .

5.4.3 Blockage effect

Zdravkovich (2002) defined the blockage effect as the confining effect on the model induced by the walls in wind or water tunnels. The water surface can also be a blockage effect source.

The blockage ratio is defined as the diameter of the cylinder divided by the water depth. The blockage ratio in our experiments was less than 0.1 and the Re number varied from 10^3 to 10^5 . Therefore, the blockage effect was negligible in this experiment.

5.4.4 Effective towing tank length

The number of oscillation cycles for each run is limited by the towing velocity and the length of the towing tank. The test rig at MCLab has an effective length of 21 m. The start and end of each time history were deleted to eliminate the transient effects, and work with an integer number of cycles of steady oscillations.

The effective time duration can be simply calculated as L/U , where L is the effective length of the towing tank and U is the towing velocity. Assuming that the oscillations are stable, at least N stable cycles (T_{osc}) are needed:

$$\frac{L}{U} \geq NT_{osc} \quad (5.38)$$

where $T_{osc} = 1/f_{osc}$, and the following limitation is obtained:

$$\frac{f_{osc}}{U} \geq \frac{N}{L} \quad (5.39)$$

5.5 Uncertainty analysis results

The bias errors and precision errors of the drag coefficient, excitation coefficient and added mass coefficient were calculated for each test case using the DRE for the uncertainty analysis. The contribution of the error of each element was compared to determine the most important error source. As the forces were measured at both sides of the cylinder, the correlation of the forces at both sides is examined. For the tests conducted once or twice a day, the repeatability was also analysed.

5.5.1 Residual flow

The waiting time between two test runs (10 min) was established based on the experimental work of Aronsen (2007). The relative velocity of the residual flow was calculated by Eq. (5.37), and the results are shown in Figure 5.1a. It can be seen that there is less than 10% of residual flow after 10 min of waiting when the towing velocity is larger than $0.05m/s$. When the towing velocity nears zero, the relative residual flow velocity increases dramatically. The cases with such low towing velocity correspond to the cross sections near the bottom end of a flexible beam exposed to shear current.

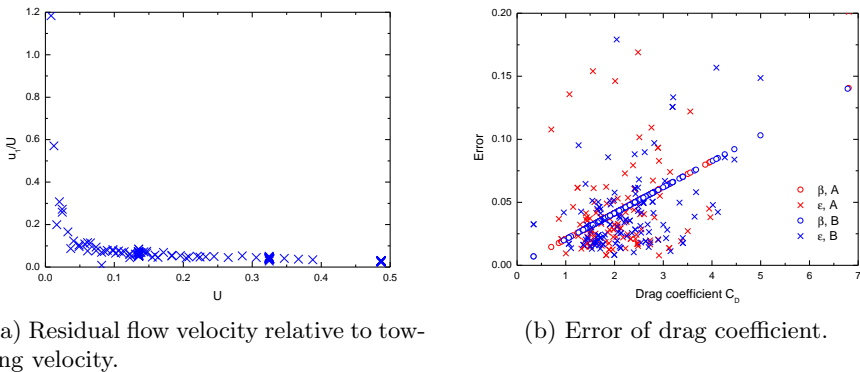


Figure 5.1: Residual flow relative velocity and error of drag coefficients. β : bias error; ϵ : precision error. A and B represent starboard and port sides of cylinder model.

5.5.2 Drag coefficient

The bias error and precision error of the drag coefficients are presented in Figure 5.1b. The bias error of the drag coefficient arises from the mean IL force, towing velocity, water density and cylinder properties (L and D). The first two terms are the main contributors. The bias errors in the calibration factor of the IL and CF strain gauges and the IL and CF interactions (see Table A.1) result in a bias error in the mean IL force. A relative bias error of 0.01 was used for the towing velocity. The variations in the mean drag force and towing velocity in each oscillation period result in precision errors in the drag coefficient. The bias error increases linearly with the drag coefficients, and the precision error is scattered, with most of the values below 0.1.

5.5.3 Excitation coefficient

Figures 5.2a and 5.2b show the errors in the excitation coefficients at the dominating frequencies in the CF and IL directions. Generally, in both directions, the bias error caused by the water density and cylinder properties is negligible. The bias errors of the integration and the towing velocity are significant. In the integration (Eq.5.16), the bias error of the force calibration factors (see Table A.1) plays a more important role than the error in the IL and CF cross talk. Figure 5.2a shows that the bias error increases with increasing magnitude of the CF excitation coefficient. The precision error arises from the numerical calculation process. The precision errors for the zero excitation coefficients in the CF and IL directions are 0.08 and 0.04, respectively.

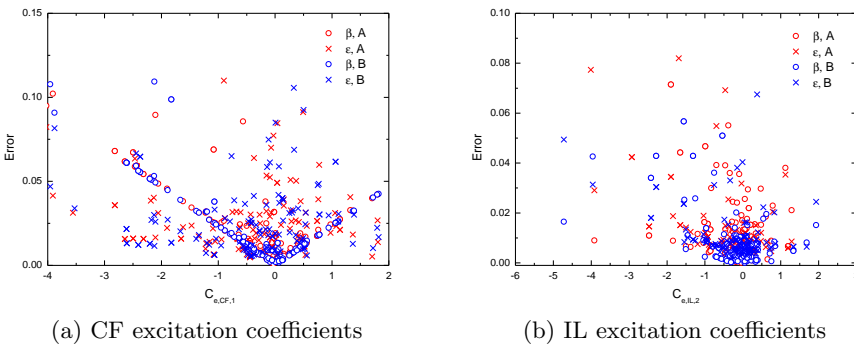


Figure 5.2: Error of excitation coefficients. β : bias error; ϵ : precision error. A and B represent starboard and port sides of cylinder model.

5.5.4 Added mass coefficient

The uncertainties of the added mass coefficients are calculated by Eq. (5.26). The results are shown in Figures 5.3a and 5.3b. The integration and amplitude errors contribute most to the bias error. In the integration (Eq. 5.17), the bias errors in the force calibration factors (see Table A.1) are primary error source; in addition, the errors in accelerations derived from displacement signals are also significant. Figure 5.3a shows that the bias error increases with increasing magnitude of the added mass coefficients.

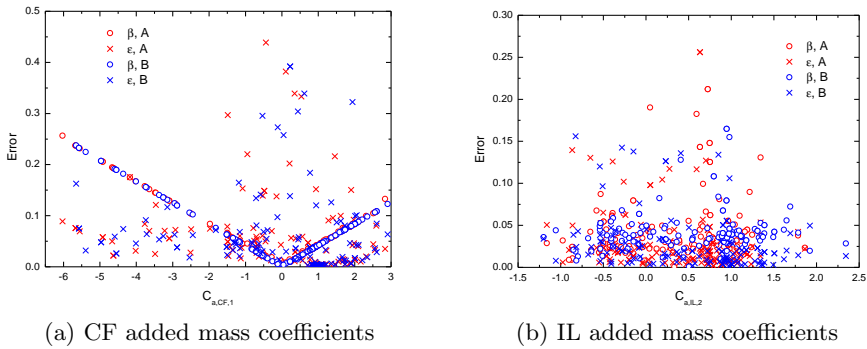


Figure 5.3: Error of added mass coefficients. β : bias error; ε : precision error. A and B represent starboard and port sides of cylinder model.

5.5.5 Repeatability

One stationary test and one ‘figure 8’ test were run before and after the main test matrix every experimental day to ensure that the connections of every transducer were unchanged and that they were working properly.

The period without PIV equipment installed is ‘Phase I’, which is comprised of 32 runs, and the period with PIV equipment is ‘Phase II’, which is comprised of 14 runs. A and B represent the starboard and port sides, respectively.

Stationary tests

The results of the stationary tests are presented in Table 5.4. The B side has a higher mean drag coefficient than the A side in both phases. Compared to the phase I tests, the phase II tests have higher $C_{rms,CF}$ and $C_{rms,IL}$

Table 5.4: Results from stationary tests. μ : mean value; σ : standard deviation

Phase	C_D		S_t		$C_{rms,CF}$		$C_{rms,IL}$	
	μ	σ	μ	σ	μ	σ	μ	σ
I, A	1.265	0.034	0.188	0.002	0.667	0.344	0.480	0.234
I, B	1.346	0.030	0.187	0.003	0.644	0.331	0.696	0.338
II, A	1.279	0.039	0.189	0.002	0.768	0.162	0.709	0.080
II, B	1.317	0.020	0.188	0.002	0.729	0.212	0.930	0.068

C. Norberg / Journal of Fluids and Structures 17 (2003) 57–96

59

values, but the B side has higher $C_{rms,IL}$ values than the A side.

The Reynolds number of the stationary tests is $2.4 \cdot 10^4$, and the Strouhal number agrees well with the results in Norberg (2003), as shown in Figure 5.4a. The rms lift coefficient is defined by Eq. (4.33), which is $\sqrt{2}$ times of the R.M.S lift coefficient in Figure 5.4b. Phase I agrees well with the results in Norberg (2003), but the lift coefficients for phase II are on the upper boundary in Figure 5.4b.

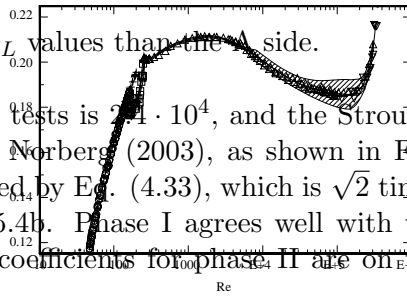


Fig. 1. Strouhal number versus Reynolds number: ∇ , Bearman (1969); Norberg (1987a, 1994); \circ , laminar shedding; \square , wake transition; Δ , turbulent shedding; ---, Barkley and Henderson (1996), 2-D; \times , Kwon and Choi (1996), 2-D; +, Posdziech and Grundmann (2000), 2-D; —, formulas in Appendix A. Shaded region corresponds to the bandwidth (-3 dB) of the shedding peak frequency.

C. Norberg / Journal of Fluids and Structures 17 (2003) 57–96

59

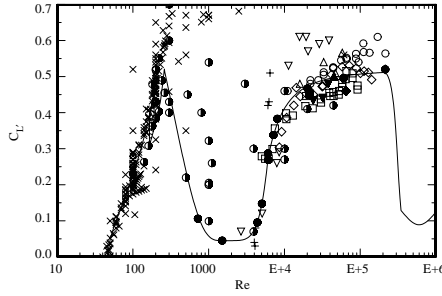
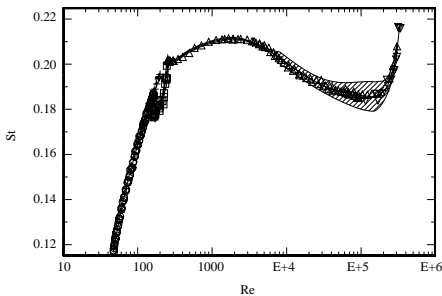


Fig. 2. R.m.s. lift coefficient versus Reynolds number: \square , Keefe (1962); +, Leehey and Hanson (1971); \blacktriangle , Sonnevile (1973); Δ , Mohr transition; \triangle , turbulent shedding; ---, Barkley and Henderson (1996), 2-D; \times , Kwon and Choi (1996), 2-D; +, Posdziech and Grundmann (2000), 2-D; —, formulas in Appendix A. Shaded region corresponds to the bandwidth (-3 dB) of the shedding peak frequency.

Figure 5.4: Strouhal number and rms lift coefficient, from Norberg (2003)

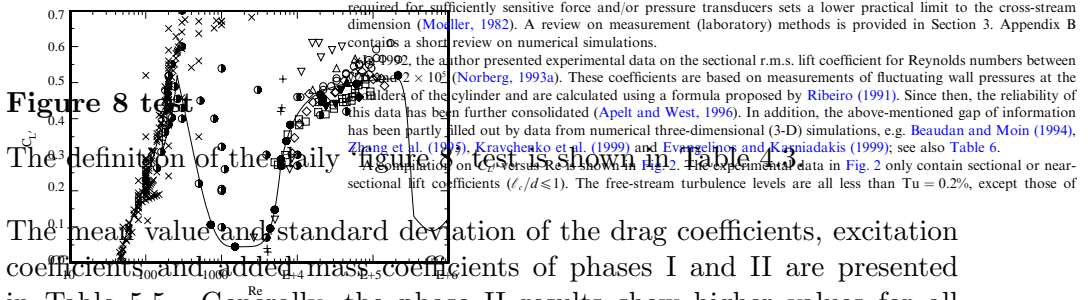


Fig. 2. R.m.s. lift coefficient versus Reynolds number: \square , Keefe (1962); +, Leehey and Hanson (1971); \blacktriangle , Sonnevile (1973); Δ , Mohr (1981); ∇ , Moeller and Leehey (1984); \blacksquare , Gartshore (1984); \diamond , Szepessy and Bearman (1992); \circ , West and Apelt (1993); \blacklozenge , Sakamoto and Haniu (1994); \times , 2-D; half-filled circle, 3-D; \bullet , present; —, formulas in Appendix A.

cylinder; the sectional lift force has to be sensed on a short segment of the cylinder span and the necessary space required for sufficiently sensitive force and/or pressure transducers sets a lower practical limit to the cross-stream dimension (Moeller, 1982). A review on measurement (laboratory) methods is provided in Section 3. Appendix B contains a short review on numerical simulations.

In 1992, the author presented experimental data on the sectional r.m.s. lift coefficient for Reynolds numbers between 720 and 2×10^5 (Norberg, 1993a). These coefficients are based on measurements of fluctuating wall pressures at the shoulders of the cylinder and are calculated using a formula proposed by Ribeiro (1991). Since then, the reliability of this data has been further consolidated (Apelt and West, 1996). In addition, the above-mentioned gap of information has been partly filled out by data from numerical three-dimensional (3-D) simulations, e.g. Beaudan and Moin (1994), Zhang et al. (1995), Kravchenko et al. (1999) and Evangelinos and Karayiannis (1999); see also Table 6.

Table 5.5: Results from figure 8 tests. μ : mean value; σ : standard deviation

Phase	C_D		$C_{e,CF}$		$C_{e,IL}$	
	μ	σ	μ	σ	μ	σ
I, A	1.353	0.020	0.333	0.082	-0.180	0.009
I, B	1.478	0.020	0.371	0.083	-0.211	0.009
II, A	1.390	0.036	0.370	0.072	-0.193	0.009
II, B	1.473	0.014	0.376	0.080	-0.217	0.010

Phase	$C_{a,CF}$		$C_{a,IL}$	
	μ	σ	μ	σ
I, A	-3.216	0.498	-0.392	0.022
I, B	-3.496	0.505	-0.337	0.025
II, A	-3.422	0.408	-0.399	0.025
II, B	-3.517	0.512	-0.347	0.028

coefficients for both the A and B sides. The A-side results show smaller values for all of the coefficients than the B side except for the IL added mass coefficient.

5.5.6 2^{nd} order replication

Verification test results

A series of pure IL and pure CF tests were performed before running the test matrix. The results were compared to previous experiments by Aronsen (2007) and Szwalek and Larsen (2009), with $Re = 24000$. A detailed description of the tests is provided in Table 4.3.

The excitation coefficient, added mass coefficient and drag coefficient were plotted against non-dimensional frequency, as shown in Figures 5.5 to Figure 5.7. Most of the results agree well with those of Aronsen (2007), except the excitation coefficient of the pure IL tests. The results calculated from the A- and B-side measurements agree with each other, except that the B-side drag coefficients are slightly higher than those of the A side.

PIV repeat tests

Thirty-two test cases were repeated with the PIV equipment installed; they are in the 2^{nd} replication level. The relative error of each hydrodynamic coefficient is defined as follows:

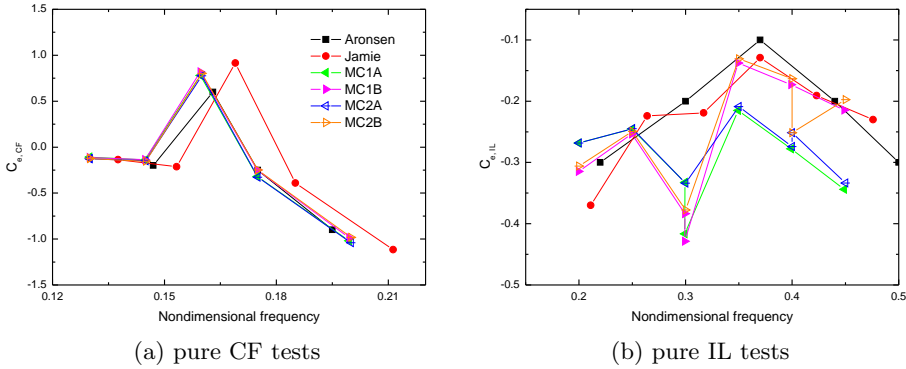


Figure 5.5: Excitation coefficients of verification tests.

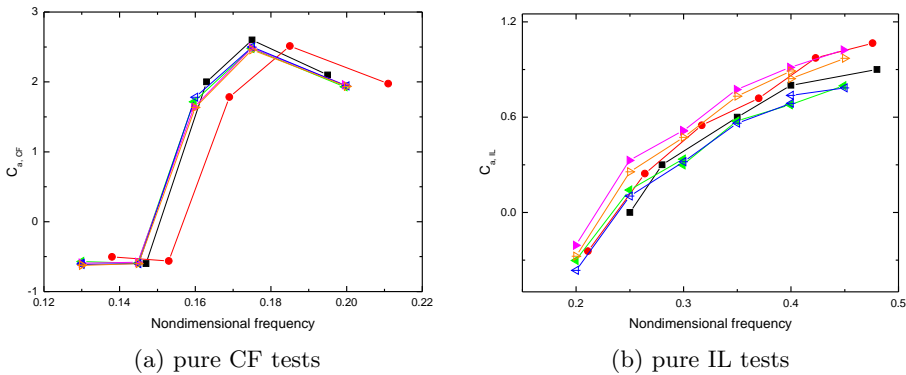


Figure 5.6: Added mass coefficients of verification tests.

$$e = \frac{x_{PIV} - \bar{x}}{\bar{x}} \quad (5.40)$$

where x_{PIV} is the hydrodynamic coefficient calculated from the PIV run and \bar{x} is the average value between two runs for the same coefficient.

Figures D.1a and Figure D.1b (Appendix D) show the relative error of the hydrodynamic coefficients in the CF and IL directions, respectively. In each figure, the x-axis is the sequence number of the 32 PIV cases, and the y-axis is the relative error of the coefficient. The two blue lines are the lower and upper limits (10%) of the error, and the red stars are the relative error of each test run. The cases with a relative error falling between the lower and

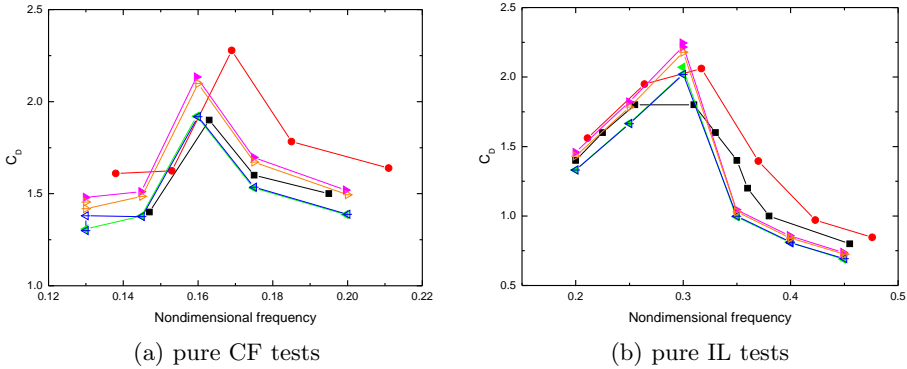


Figure 5.7: Drag coefficients of verification tests.

upper limit were considered ‘stable’; otherwise, they were considered ‘unstable’. The errors of the A- and B-side excitation coefficients and added mass coefficients for the cylinder model are presented for the CF and IL directions. The test run without a data point of relative error shown in the figure implies that the absolute value of the relative error is larger than 0.5.

Table D.1 shows the number of each coefficient at either side, among the 32 test cases, that have a relative error within 0.1. It also shows the percentage in each range.

Among the 32 PIV runs, there were three different types of ‘force-coefficient’ relationships. Three representative test runs were selected for discussion. In Figure D.1, they are marked with green frames, and the corresponding NDP test numbers are marked at the bottom of each frame.

Figures D.2 to D.4 (Appendix D) show the filtered force component of ω_1 to ω_4 in both the CF (a) and IL (b) directions. In each sub-figure, the upper and lower rows show the time history of the force signal with and without the PIV installed, respectively. The maximum values in each time history are marked with red circles. The mean value and standard deviation of the maxima are shown in Tables D.2 to D.4. Phase A occurred from October to December in 2010 without PIV equipment installed, and Phase B occurred in January in 2011.

Stable force-stable results

As shown in Figure D.1 (Appendix D), in Case 21002, all of the coefficients have a relative error less than 0.1. Figure D.2 and Table D.2 (Appendix D) show that the filtered force components are nearly identical for the two runs.

Stable force-unstable results

Case 24307 also has stable filtered force signals, but the hydrodynamic coefficients show large discrepancies between the two runs, as shown in Figure D.1. This observation must be caused by the phase between the displacement and force.

Unstable force-unstable results

Figure D.4 shows that Case 23407 has different force time histories for the two runs, and in each run itself, the signal is clearly unstable, particularly in the CF direction. From Table D.4, large differences can also be observed when comparing the mean values. The standard deviation is also large.

The three selected cases imply that when using the results of forced motion experiments with a short, rigid cylinder, the force signals, as well as the coefficients, should be checked for stability. The instability of force signals is a reflection of the wake around the cylinder, and PIV measurements are necessary to check the wake and vortex pattern.

Part III

Numerical Method

Chapter 6

CFD numerical calculation

The flow close to an oscillating cylinder has been calculated by use of several commercial programs based on CFD. The purpose of this chapter is to describe the applied methods.

6.1 Pre-processing: computational model & mesh generation

The pre-processing software package GAMBIT was used to create the model and generate the mesh of the computing domain. Gambit is a pre-processor to FLUENT. It provides both structural and non-structural meshes in 2D and 3D (*FLUENT 6.3 User's Guide*, 2006; *ANSYS FLUENT User's Guide Release 13.0*, 2010).

Two models were used during the calculation. The first model was modified based on Huang et al. (2009), and a second mesh was developed from Huang's 2D structured mesh, which is not published yet.

6.1.1 Mesh generation

Mesh strategy A

Figure 6.1 shows mesh A and the boundary conditions of the computational domain. The computational domain has dimensions of $L(\text{length}) \times B(\text{width}) \times H(\text{height}) = 45D \times 30D \times 8D$, where D is the diameter of the cylinder. The front region is a semi-circular shape with a radius of $15D$. The length of the cylinder model is $8D$. A circle with a radius of $8D$ moves rigidly with the cylinder model, including the mesh inside, and the mesh

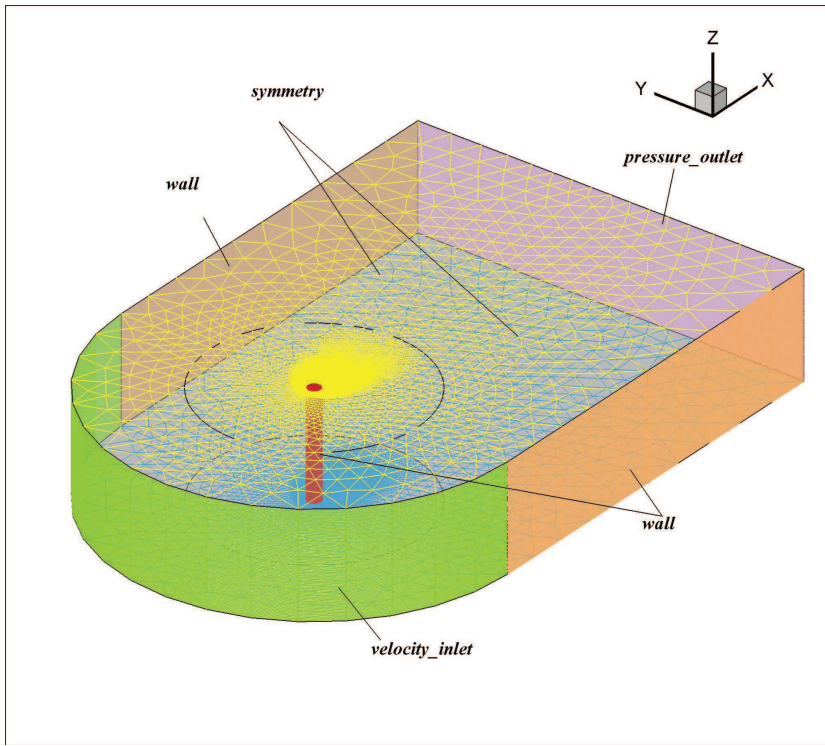


Figure 6.1: Mesh A generation and boundary conditions.

outside the circle deforms according to the movement of the circle. Inside the circle, a semi-elliptical domain, $a \times b = 7.5D \times 4D$, had a finer mesh around the cylinder and wake region to capture details of the flow domain. A 2D X-Y plane view of the mesh is shown in Figure 6.2a.

In the X-Y plane, a non-structural triangular mesh was used, as shown in Figure 6.2a. In the X-Z and Y-Z planes, structural rectangular meshes were used. The resulting 3D elements consist of triangular prisms.

Mesh strategy B

The second model is cylindrical, as shown in Figure 6.3. In the X-Y plane, the computational domain has a radius of $20D$ (where D is the diameter of the cylinder model), as shown in Figure 6.4, and in the Z direction, the length of the cylinder is $10D$. A circle with a radius of $8D$ moves rigidly with the cylinder model, including the mesh inside, and the mesh inside is denser than that outside, particularly in the wake area behind the cylinder.

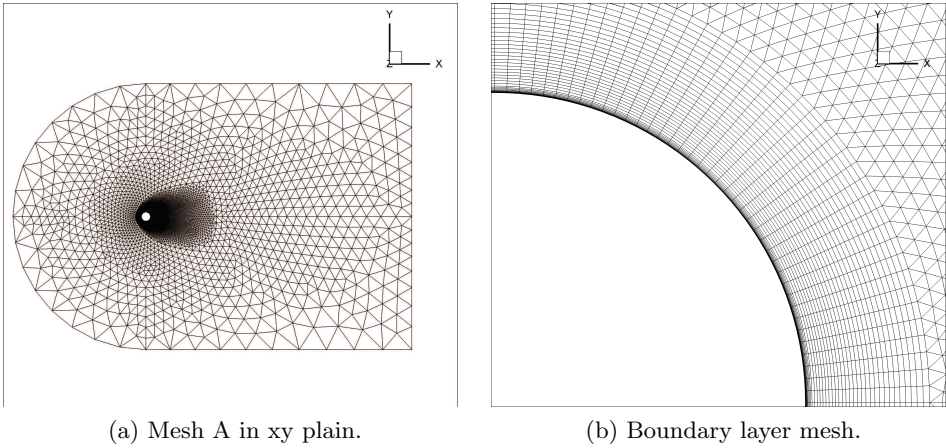


Figure 6.2: Mesh A in xy plain and detail mesh around the cylinder.

Table 6.1: Two mesh generation strategies.

Mesh	Nodes	Elements	N_c	N_t	N_z
A	1338553	1989400	160	40*	100
B	8568180	8467200	360	225	100

N_c : Number of nodes in the cylinder circumferential direction.

N_t : Number of nodes in the cylinder wall normal direction.

N_z : Number of nodes in the cylinder length direction.

Table 6.1 summarises the two mesh strategies.

6.1.2 Boundary conditions

As is shown in Figures 6.1 and 6.3, the boundary conditions are as follows:

Cylinder: Wall

Port/Starboard: Wall

Up/down (model ends): Symmetry

Inlet: Velocity inlet

Outlet: Pressure outlet

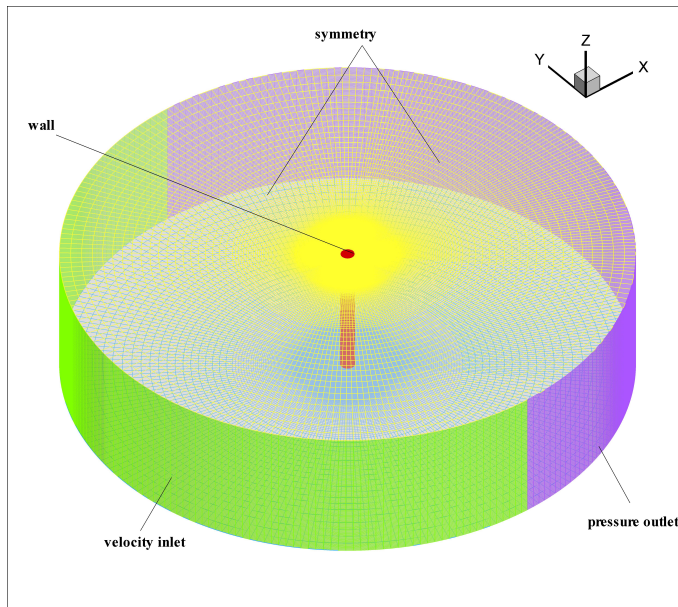


Figure 6.3: Mesh B generation and boundary conditions.

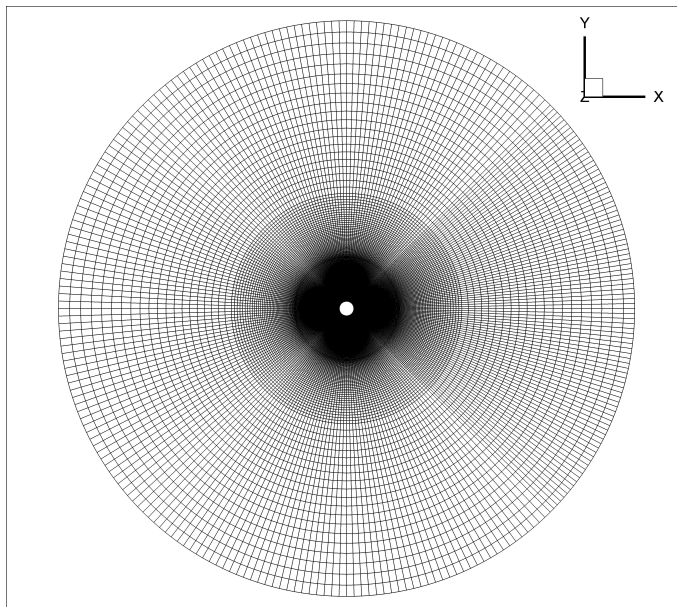


Figure 6.4: Mesh B in xy plain.

6.1.3 Time step

The time step Δt in all of the simulations was held constant at 0.005s. The dimensionless time step is defined as follows:

$$\frac{U \cdot \Delta t}{D} \quad (6.1)$$

6.1.4 Boundary layer

The non-dimensional wall distance (y^+) is defined as follows:

$$y^+ = \frac{u_* y}{\nu} \quad (6.2)$$

where u_* is the friction velocity, y is the distance between the first-layer mesh to the cylinder wall, and ν is the local kinematic viscosity of the fluid.

In the present study, the y^+ value was assumed to be unity. The boundary layer settings are shown in Table 6.2, and the boundary layer mesh is shown in Figure 6.2b.

Table 6.2: Detail boundary layer setting.

First row	Growth factor	Number of rows
0.0005	1.2	10

6.1.5 Mesh independence test

A mesh independence test of Mesh A was performed by Huang et al. (2009), in which the grid density in the Z direction was increased by a factor of 4. However, the span-wise (Z direction) resolution is significant for LES (and DNS) flow problems, as discussed by Breuer (1998). For $Re = 3900$, Breuer suggested the number of grid points of 64 in the span-wise direction with πD length. Dong and Karniadakis (2005) performed DNS of flow past a stationary cylinder at $Re = 10000$ with a cylinder length of πD . Dong and Karniadakis discovered that ‘*drag coefficients, base pressure (base suction) coefficients, and the Strouhal number from the simulations were in good agreement with the experimental results for various grid numbers in the spanwise direction (from 16 to 128), indicating that these physical quantities are generally not very sensitive to grid resolution. The lift coefficient, however, demonstrates a higher sensitivity to grid resolution.*’

Based on the above findings, the mesh applied in this thesis is not considered to have high resolution. So the present numerical results should not be used to explain the detail physics of the flow field.

6.2 FLUENT solver

The CFD calculations in this thesis were performed using the commercial fluid dynamic software package FLUENT. Tecplot 360 and MATLAB were used to analyse the results.

6.2.1 Turbulence model

For the 2D simulations, the standard $k - \varepsilon$ 2-equation model was applied.

For 3D simulations, LES was applied, as described in section 2.8.2.

6.2.2 Dynamic mesh

For mesh strategy A, which is described in section 6.1.1, a circular region with diameter $15D$ was defined to move with the cylinder without distortion, and the mesh outside the circle deformed according to the motion of the cylinder and the fixed outer boundaries (Huang et al., 2009). A combination of a smoothing and re-meshing dynamic mesh strategy was applied to simulate the vibrating cylinder with imposed motion in both the IL and CF directions.

As all the computational cases were subjected to forced motion, a dynamic mesh strategy was needed. The meshes inside the circle around the cylinder model with radius $8D$ had exactly the same motion as the cylinder. The motion is defined by the time-varying velocity vectors (IL and CF), which was saved as *.txt* files. These were read into the model by a UDF executing file.

The meshes outside the rigid moving circular area deformed according to a certain rule. The *2.5D Surface Remeshing Method* for a 3D model was used for the deformation.

The model in this study is 3D, but the motion is 2D. The *2.5D Surface Remeshing Method* marks the faces on a deforming boundary, and then, the marked faces are remeshed and smoothed on one side based on face skewness and the minimum and maximum length scales. Finally, the changes

are extruded along the Z axis (cylinder span direction) to the opposite side. Rigid body motion is applied to the moving face zones (circle outside the cylinder), while the triangular extrusion surface is assigned to a deforming zone with remeshing and smoothing enabled. The opposite side of the triangular mesh is also assigned to a deforming zone, with only smoothing enabled (*ANSYS FLUENT User's Guide Release 13.0*, 2010).

6.2.3 User Defined Functions (UDF)

ANSYS FLUENT allows users to embed user-defined functions (UDF) into a computational model. A UDF was written in the C programming language and defined using the DEFINE macros provided by ANSYS FLUENT.

In the present study, a UDF was used to read the velocity vectors saved in the *.txt* file, apply them to the model, record the transient velocity, displacement and force signals and save the results in another *.txt* file.

6.2.4 Parallel Computing

The parallel solver of ANSYS FLUENT is able to compute a solution by using multiple processes that may be executing on the same computer or different computers in a network.

The parallel processing is shown in Figure 6.5. It uses the interactions between ANSYS FLUENT, a host process and a set of compute-node processes. ANSYS FLUENT interacts with the host process and the collection of compute nodes using a utility named *cortex* which manages the user interface of ANSYS FLUENT and basic graphical functions (*ANSYS FLUENT User's Guide Release 13.0*, 2010).

High Performance Computing (HPC) at NTNU in Trondheim was used as a platform to conduct the calculation.

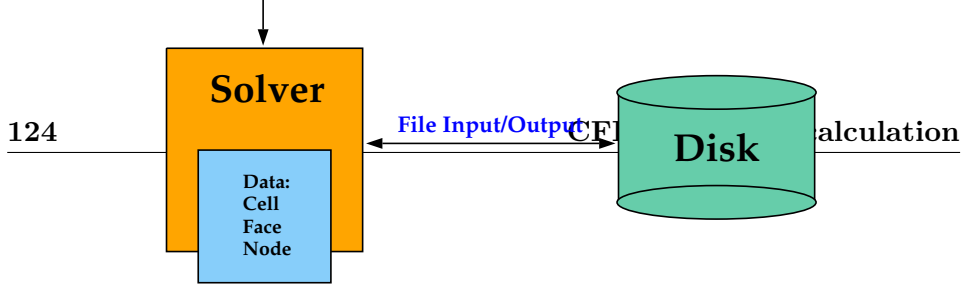


Figure 31.1.1: Serial FLUENT Architecture

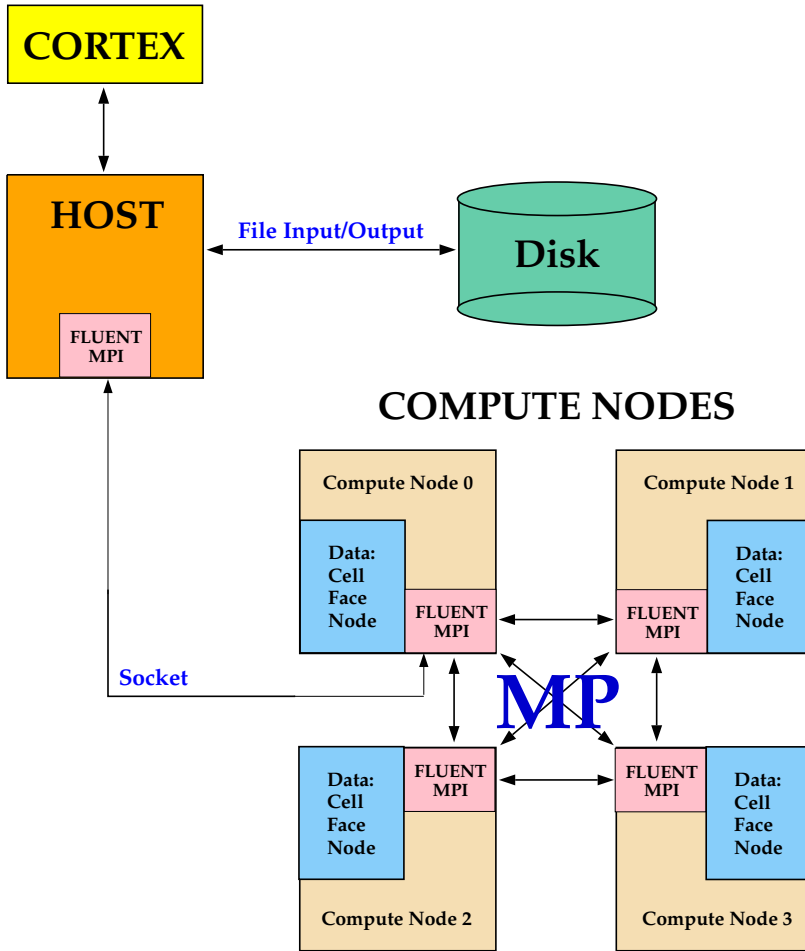


Figure 6.5: Parallel FLUENT Architecture (ANSYS FLUENT User's Guide Release 13.0, 2010).

Part IV

Results

Chapter 7

Observations & Discussions

This chapter presents the results of both experiments and numerical simulation. It contains three parts: Part 1 presents some results from the NDP high mode VIV tests, and the results of the forced motion experiments are shown in part 2. Part 3 presents the results of both 2D and 3D CFD simulations.

7.1 Results of the NDP High Mode VIV Tests

The author was not involved in the NDP High Mode VIV Test program. However, because the forced motion experimental work in this thesis is strongly linked to the NDP tests, some important results will be presented herein. The key results can be found in Braaten and Lie (2005), Kristansen and Lie (2005), and Trim et al. (2005). The results without a reference in this thesis are the work performed by the author based on the displacement data from the NDP tests provided by Trygve Kristiansen.

7.1.1 Global responses of a flexible beam

Figure 7.1 shows the RMS values of the response amplitudes along the flexible beam for the NDP cases used in this thesis. The stars show the locations of 19 cross sections selected for analysis (see also Appendix B), and the blue and red colours represent the CF and IL directions, respectively. The values in the figures are calculated from the displacement data provided by Trygve Kristiansen. Figures 7.1a, 7.1b and 7.1c show the responses of three uniform cases. Figures 7.1d, 7.1e and 7.1f show responses of three sheared flow cases in the NDP test.

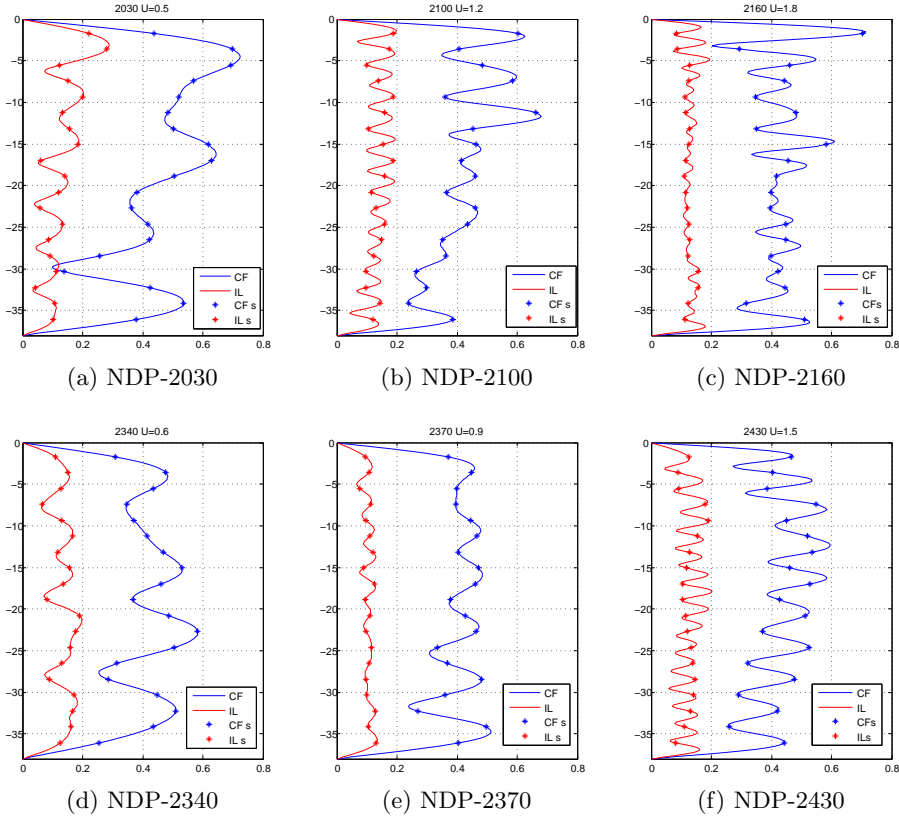


Figure 7.1: RMS values of response amplitudes of flexible beam of different NDP cases.

The contour plots of the displacements along the entire pipe as they vary with time are given in Figure 7.2 for Case 2030, which is plotted in the same manner as Fig 10(a) in Modarres-Sadeghi et al. (2011). The maximum current velocity is found at $z = 0$; the plots for the other cases used in this thesis are shown in Appendix E. These plots illustrate the influence of standing and travelling waves, and the dominating modes in the CF and IL directions.

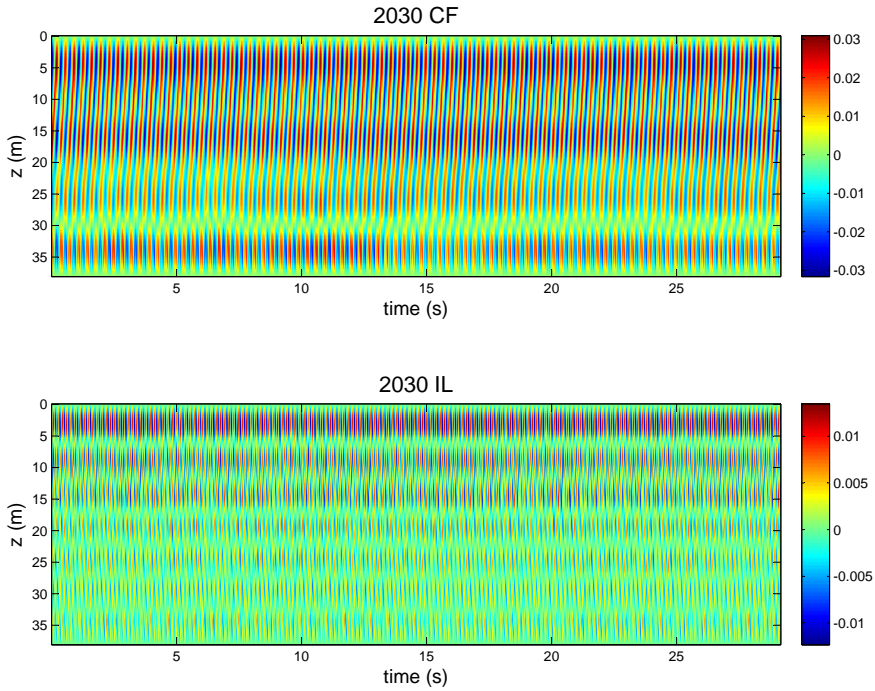


Figure 7.2: CF & IL displacements in time and space for NDP uniform flow case 2030, $U = 0.5 \text{ m/s}$.

7.1.2 Local response: Characterisation of response types

CF response

Based on the data from the NDP tests, Modarres-Sadeghi et al. (2011) divided the responses of the cross-sections of a flexible pipe in the CF direction into three categories:

- The entire signal is quasi-periodic (Type-I).
- Quasi-periodic signal (Type-I) interrupted by bursts of chaotic oscillations (Type-II).
- Entirely chaotic signal (Type-II) and even the smallest sub-signals (the signal in a very small time window) confirm the chaotic features.

Figures 7.3a and 7.3b summarise the characteristics of the CF responses at one specific location ($z \simeq 4 \text{ m}$) along the beam under uniform and sheared

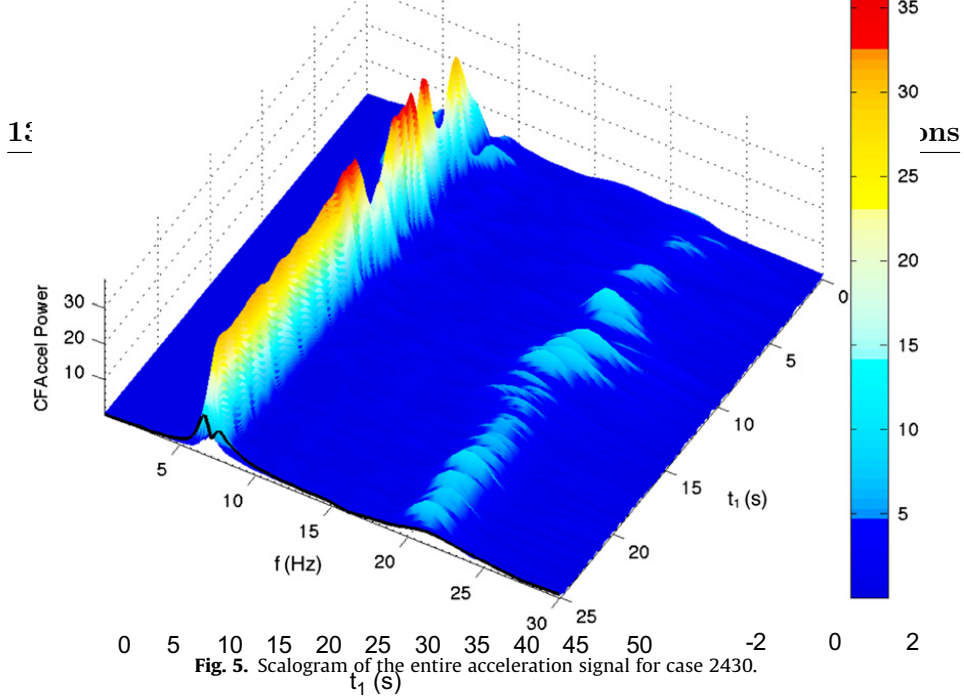
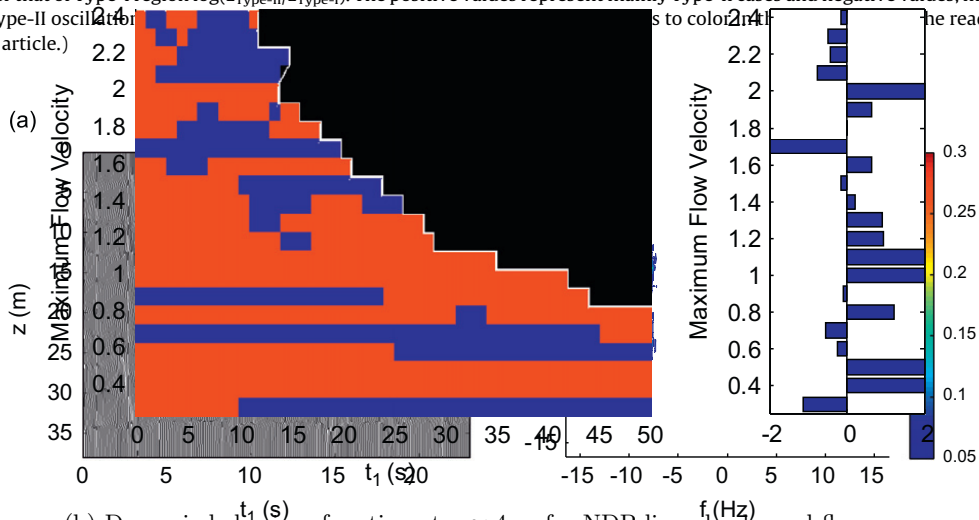


Fig. 5. Scalogram of the entire acceleration signal for case 2430.

1. (a) Dynamical behavior of a point at $z \sim 4$ m for all NDP uniform flow cases; red: Type-II; blue: Type-I; black: no results. (b) The logarithm of overall length of Type-II region over that of Type-I region $\log(L_{Type-II}/L_{Type-I})$. The positive values represent mainly Type-II cases and negative values, mainly Type-I, while 2 presents purely Type-II oscillation. (c) 2D Fourier transform of the reconstructed signal. For the interpretation of the references to color in this figure legend, the reader is referred to the web version of this article.)



2. (a) Reconstructed cross-flow displacement in time and space for a uniform flow case (2430) and (b) 2D Fourier transform of the reconstructed signal. The positive values represent mainly Type-II cases and negative values, mainly Type-I, while 2 presents purely Type-II oscillation. For the interpretation of the references to color in this figure legend, the reader is referred to the web version of this article.)

Type-II riser response. The positive values represent mainly Type-II cases and negative values represent mainly Type-I cases. For example, the third harmonic component of the strain for case 2480, a sheared flow case with $U_{max}=2$ m/s, is 0.05 of the first harmonic component. One could then argue that because this is a negligible higher harmonic component, we can consider only the first harmonic component of a signal as small, the quasi-periodic (Type-I) oscillation does not show the periodicity of the strain. However, the resulting fatigue life will be over predicted by 70%, as the first harmonic component of the strain is 1.37×10^{-4} versus the actual fatigue life is 4.1×10^{-4} versus Type-II. It is not safe to use the first harmonic component of the strain in order to calculate the fatigue life, even when the first harmonic component is large (as in case 2340), there are still other components of the strain that contribute to the fatigue life, which is now a higher strain harmonic and small, because the signal is of Type-II. The difference between fatigue life calculated using a filtered VIV signal and the actual fatigue life is large when the signal is of Type-II. The difference between fatigue life calculated using a filtered VIV signal and the actual fatigue life is large when the signal is of Type-II. The difference between fatigue life calculated using a filtered VIV signal and the actual fatigue life is large when the signal is of Type-II.

Effect of filtering bandwidth on fatigue calculation

A major difference between the fatigue calculation of a Type-I and a Type-II signal is the impact of filtering: A fatigue calculation for a Type-I response is practically independent of the filter used, since most energy is concentrated around the

Most of the cases are dominated by chaotic responses. As described earlier, the quasi-periodic response can be interrupted by the chaotic response (Type-II), for instance, the NDP Case 2370 with a maximum flow velocity of 0.9 m/s in Figure 7.3b; however, a chaotic signal can also change into a quasi-periodic response. See the case in the same figure with a maximum flow velocity of 0.6 m/s (NDP Case 2340).

As described in section 3.3.5, nearly all of the periodic forced motion tests apply smoothed orbits selected from a time window with quasi-periodic oscillations. The forced motion experiments with measured orbits from NDP cases 2370 and 2430 have chaotic responses in the CF direction.

Combined IL and CF responses

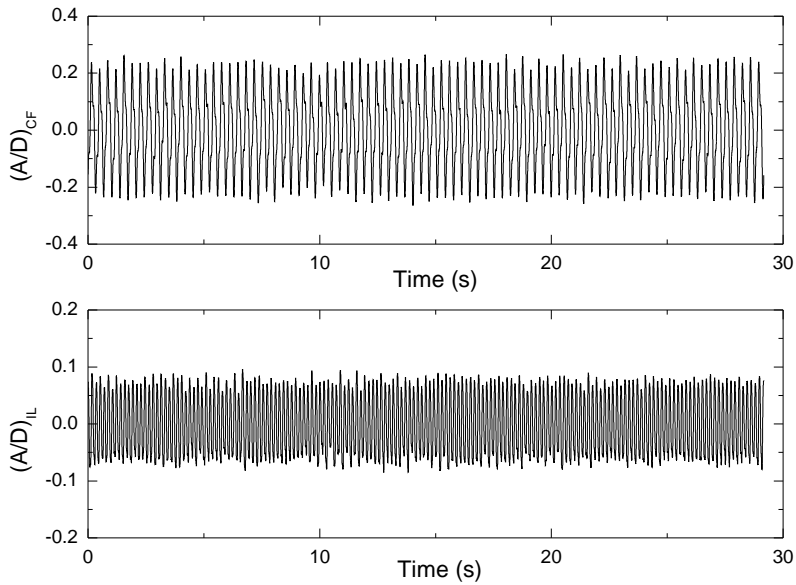
The CF and IL responses interact with each other, and thus, the responses in both directions should be considered simultaneously.

Figures 7.4 and 7.5 show 4 different response types of combined IL and CF responses from NDP tests (2030: uniform flow. 2370, 2450, 2470: sheared flow). Both signals are taken from a position of $z = 9.5\text{ m}$ from the top end ($z = 0\text{ m}$) and normalised by the diameter. Figure 7.4a shows that both the CF and IL responses are fairly stable, which corresponds to a Type-I response. In Figure 7.4b, the CF response exhibits quasi-periodic characteristics while the IL response shows a distinct amplitude modulation during the entire time duration. In the time section from 0 s to 12 s of Figure 7.5a, a similar response type to Figure 7.4b is observed, while both CF and IL exhibit a chaotic response (Type-II) thereafter. The CF response could be classified as a combination of Type-I and Type-II responses. Figure 7.5b shows chaotic responses in both the CF and IL directions (Type-II).

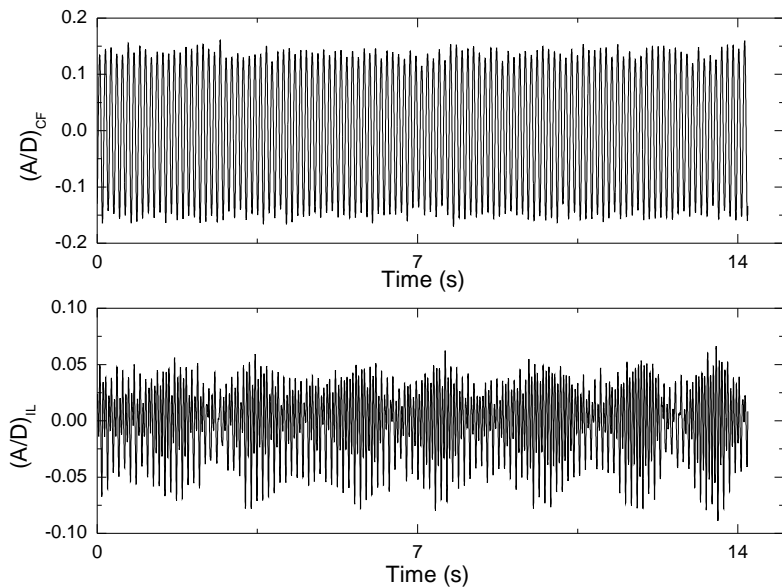
The IL response in Figure 7.4b has a modulated amplitude, where amplitude modulation can be described as the low-frequency modulation of a signal with a constant carrying frequency. This type of response can not be classified as quasi-periodic or chaotic. However, the CF response is still quasi-periodic and apparently not influenced by the regular modulation of the IL response. On the contrary, quasi-periodic IL and amplitude-modulated CF responses are rarely observed in NDP tests.

VIV can also show the ‘beating’ of responses at two slightly different frequencies, where the difference between the two frequencies is small relative to the response frequency. The response contains both the sum and the difference

of two close frequencies. Beating has been observed by Alexander (1981), Grosenbaugh et al. (1991) and others. This phenomenon was explained in Gopalkrishnan (1993). Given a long, flexible riser in a sheared current, the variation of the flow velocity will lead to a variation in the vortex shedding frequency along the riser. Each cross section responds primarily to the local hydrodynamic force at the local vortex shedding frequency. This response may create a travelling wave that will propagate in both directions along the beam and damp out within several wavelengths. In this way, the response at each cross section is not only dominated by the local vortex shedding frequency but also affected by other frequency components from adjacent cross sections along the riser. In addition, dynamic tension variations will adjust the eigenfrequencies and thereby lead to amplitude modulation.

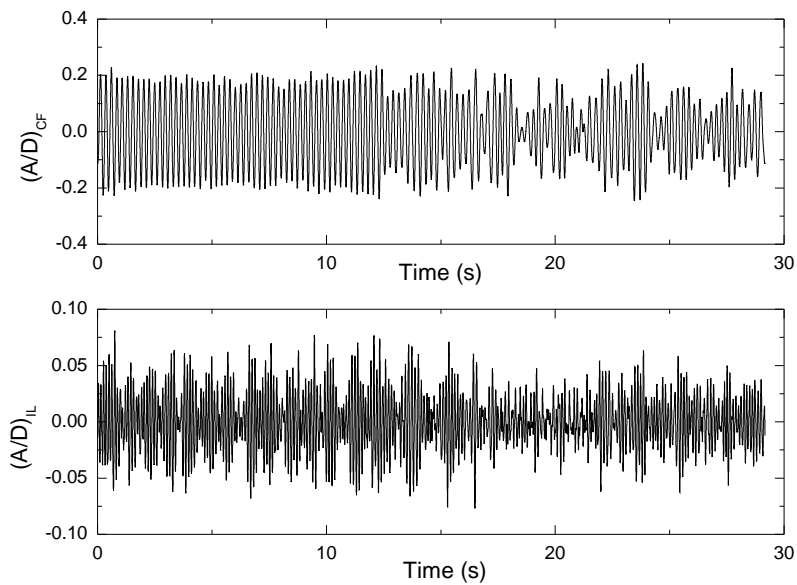


(a) Case 2030.

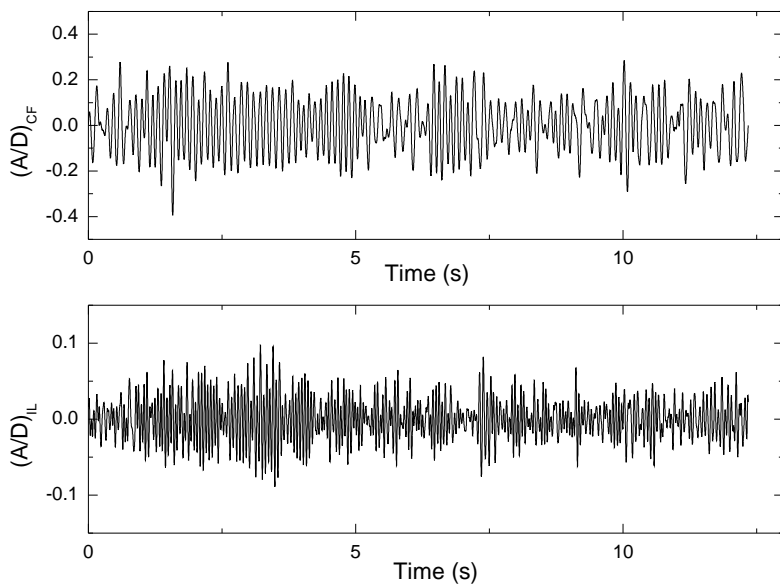


(b) Case 2450.

Figure 7.4: CF and IL responses of a cross section from NDP riser model, Yin and Larsen (2012).



(a) Case 2370.



(b) Case 2470.

Figure 7.5: CF and IL responses of a cross section from NDP riser model, Yin and Larsen (2012).

7.2 Results of the forced motion experiments

In this section, the results of the different types of forced motion tests described in Chapter 4 are presented. Some important observations and conclusions from other researchers are also introduced. As shown in Figure 2.17, there are a number of different types of forced motion experiments, and a comparison is performed step by step to approach a complete understanding of the hydrodynamic forces extracted from forced motion experiments.

7.2.1 Stationary: Drag coefficient and Strouhal number

Prior to the forced motion tests, the cylinder was towed without oscillatory motions at different velocities. These stationary tests were conducted twice with the opposite towing directions ('Run 1' and 'Run 2'). The Strouhal number and the drag coefficients from the starboard side (A) and the port side (B) are shown in Figure 7.6. They are compared with the values from Schewe (1983) and Szwalek and Larsen (2009), and results at two other fixed Re are shown in Table 7.1.

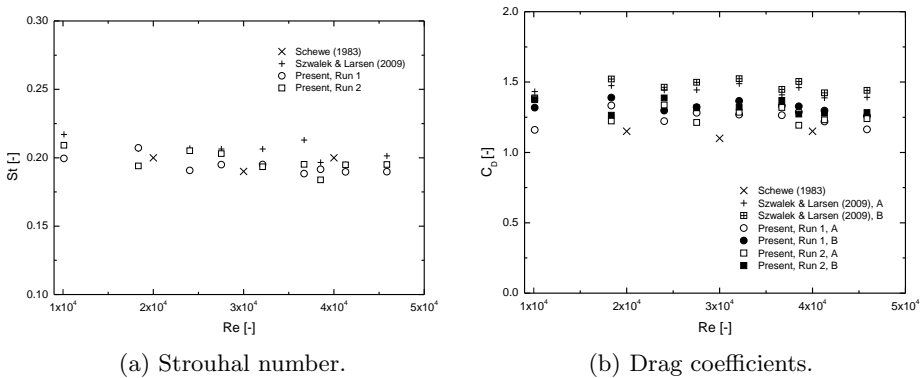


Figure 7.6: Strouhal number and drag coefficients of stationary tests.

Table 7.1: Stationary test results at two Re .

Re	St	C_D	Author
10000	0.193	1.186	Gopalkrishnan (1993)
24000	0.188	1.325*	Aronsen (2007)

* From starboard.

Generally, the Strouhal number agrees well with the values from other experiments; the calculated drag coefficients fall between those of Schewe (1983) and Szwalek and Larsen (2009). Szwalek and Larsen (2009) used the same set-up as that for these experiments but had higher drag coefficients.

7.2.2 Harmonic: IL & CF vs. pure CF

The contour plots of the excitation coefficients and the added mass coefficients from the pure CF harmonic forced motion experiments performed by Gopalkrishnan (1993) are shown in Figure 2.14. The Reynolds number was fixed at 10,000.

Aronsen (2007) conducted both pure CF and combined IL and CF harmonic forced motion tests at four non-dimensional frequencies: 0.147, 0.163, 0.175, and 0.195. The Reynolds number was fixed at 24,000. He showed that the shape of the orbit, which is defined by a phase angle between IL and CF (see Eq. 4.1) can affect the coefficients significantly. For a non-dimensional frequency of 0.147, distinct branches are observed at a phase angle of 70° , while a general trend in this critical phase angle was not observed.

Another finding by Aronsen (2007) is that the 3^{rd} harmonic forces in the CF direction are attributed to IL motions, and the maximum 3^{rd} harmonic force observed is proportional to $(A/D)_{IL}$. Moreover, this higher order force is significantly lower in the pure CF forced motion test, which confirms the influence of the IL motion.

Dahl (2008) conducted a large number of forced vibration experiments at two Reynolds numbers: 8760 and 6860. By fixing the reduced velocity and analysing the zero power contours, he found that the maximum $(A/D)_{CF}$ increases when the reduced velocity increases while the phase angle (see Eq. 4.2) decreases.

Dahl (2008) discovered that the combination of a small $(A/D)_{CF}$ and a large $(A/D)_{IL}$ with a phase of 135° (Eq. 4.2) lead to small 3^{rd} harmonic forces in the CF direction. With the exception of this region, the 3^{rd} harmonic forces tend to increase with increasing $(A/D)_{IL}$, which was the conclusion drawn by Aronsen (2007).

7.2.3 Harmonic: IL & CF vs. pure IL

Aronsen (2007) also compared the coefficients in the IL direction calculated

from the combined IL and CF forced motion tests with the results of the pure IL test. A general trend was not found. However, the importance of the phase angle between the IL and CF motions was clear, and the 3rd harmonic forces in the CF direction were comparable between the pure IL test and the combined IL and CF forced motion test.

The main work presented in this thesis involves the forced motion experiments in which the orbits observed in the NDP tests with a flexible beam are applied. The following sections will present the results from these tests.

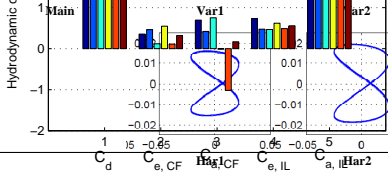
7.2.4 Periodic: Sensitivity of orbits

Because the orbits used for periodic forced motion tests were obtained by smoothing the observed motions of the cross sections of a flexible beam (see Figure 3.8), the choice of time window will influence the shape of the orbit and thus the estimated coefficients.

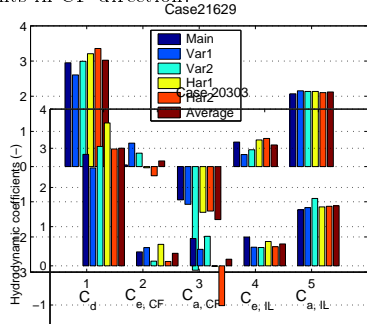
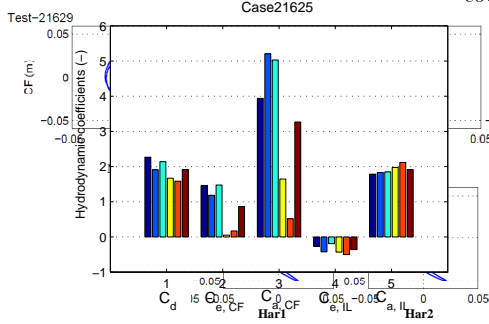
Soni (2008) investigated the variation of periodic orbits and compared them to filtered harmonic orbits. His Test-21629 and Test-21625 are selected for illustration. For each test, three periodic orbits were selected with the use of different time windows, and two harmonic orbits were used to represent the orbits (Var1 and Var2) with one harmonic component in each direction. Figure 7.7a and Figure 7.7c show all orbits that were used for each test.

The results in terms of the drag, the excitation and the added mass coefficients of each orbit and the average values are shown in Figures 7.7b and 7.7d. The added mass coefficients in the IL direction have almost the same values for all cases, but the CF added mass coefficients are more sensitive to the shape of the orbit. The CF and IL excitation force coefficients vary significantly. The overall trend found by comparing the results from the observed orbits and the harmonic orbits is that harmonic orbits may give reasonable values for many cases, especially for the cases with orbits close to harmonic orbits (Test-21629), but some significant discrepancies can also be observed for the case with a strong higher order displacement component (Test-21625) (Soni, 2008).

A similar comparison was conducted by Yin and Larsen (2011). The ‘best-fit orbit’ and two alternative orbits similar to the main orbit were tested. For Case 23405 and Case 234018, two harmonic orbits defined by the IL and CF harmonic components of the two alternative periodic orbits were

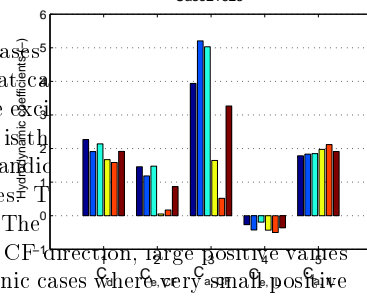
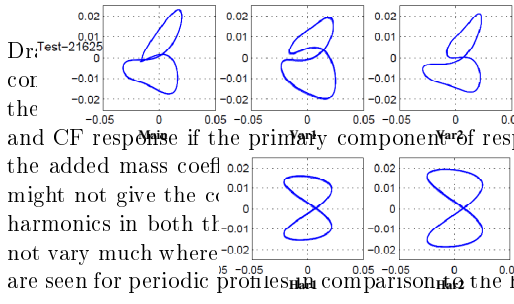


loop was tested. The examples are shown in Figure 7.14. The purpose of harmonic loops is to gain some experience regarding the feasibility of using harmonic tests in an empirical model for combined IL and CF response. In terms of hydrodynamic coefficients presented statistically in Table 7.9, histograms in Figure 7.15. The deviation of added mass coefficient in IL direction is very small for all cases when compared with the harmonic profiles. For other coefficients, no significant deviation in values is observed, but for coefficients in CF direction.



(a) Alternative orbits from time history for test-21625. The hydrodynamic coefficients are compared by histograms for periodic and harmonic profiles

(b) Coefficients from alternative orbits for test-21629. The hydrodynamic coefficients are compared by histograms for periodic and harmonic profiles



(c) Alternative orbits from time history for test-21629. The hydrodynamic coefficients are compared by histograms for periodic and harmonic profiles

(d) Coefficients from alternative orbits for test-21625. The hydrodynamic coefficients are compared by histograms for periodic and harmonic profiles

Figure 7.7: Comparison between orbits and corresponding coefficients (Soni, 2008). Drawing a conclusion based only on a few number of cases is not an easy task. Considering the 19 profiles analyzed, the conclusion that can be drawn is that the response as harmonic gives reasonable values for the excitation coefficient and CF response if the primary component of response is the dominating one. The added mass coefficient in IL direction is a stable candidate, but the added mass coefficient in CF direction, large positive values are seen for periodic profiles in comparison to the harmonic cases where very small positive values are seen.

also tested; see Figure 7.8. The coefficients are shown as histograms in Figure 7.9. Case 23403 should be the best case to use in a discussion of the validity of the hydrodynamic coefficients from harmonic orbits. According to Figure 7.9a, the harmonic orbits give much higher $C_{e,CF}$ values than the periodic orbits, and the first harmonic orbit shows a lower $C_{a,CF}$ than the other orbits. The $C_{a,IL}$ value found using two harmonic orbits is close to the result of the main orbit, but the results using two other periodic orbits vary significantly, which is also shown in Figure 7.9c and Figure 7.9d.

The deviation of $C_{a,IL}$ is very small for Case 234018 when comparing the harmonic orbits with the periodic ones. A similar observation was found by Soni (2008). For Case 234018, large discrepancies were found for C_d , $C_{e,IL}$ and $C_{e,CF}$. The most probable reason is that this case applies the

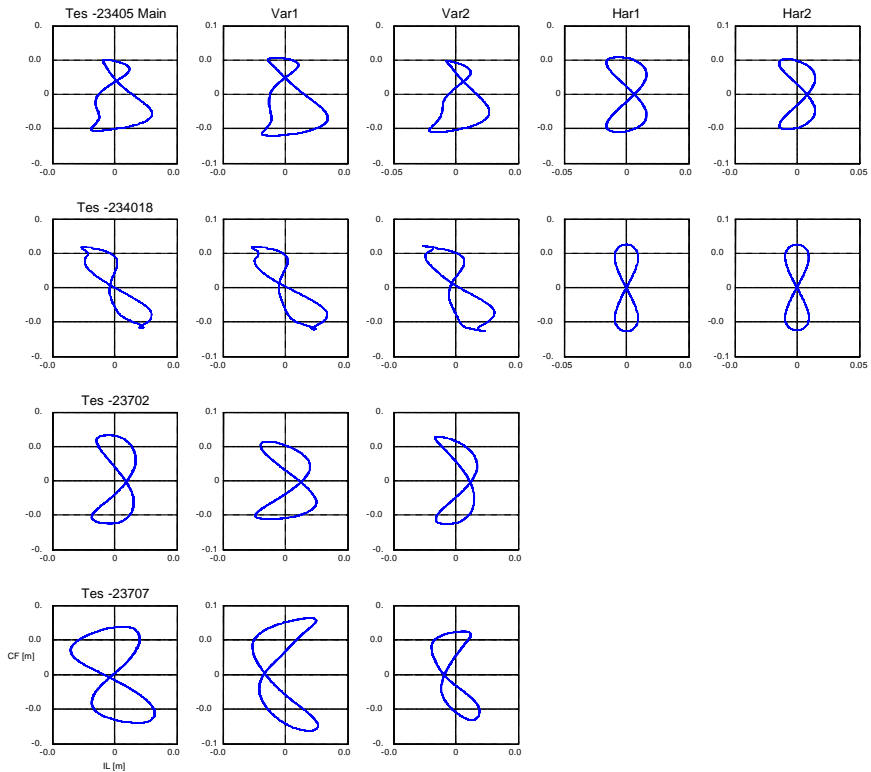
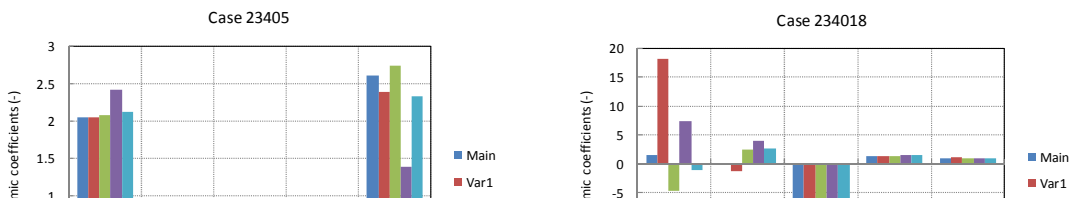


Figure 7.8: Alternative orbits for the same test. (Yin and Larsen, 2011).

Figure 9 Different tested trajectories for comparison.

The coefficients are showed as histograms in Figure 10. Case 23405 should be the best case to use in a discussion on the validity of hydrodynamic coefficients from harmonic trajectories. From Figure 10 (a), it is easy to observe that harmonic trajectories give much higher $C_{e,CF}$ values than the natural loops, and the first harmonic loop shows a lower $C_{a,CF}$ than the others. It is interesting to see that $C_{a,IL}$ found from two harmonic trajectories are close to the result from the main loop, but the results from two other realistic trajectories vary significantly. This can also be seen from Figure 10 (c) (d). In summary, on one hand, the comparison between alternative periodic orbits and the result from the main loop is sensitive to the shape of the orbit; on the other hand, the comparison between periodic orbits and harmonic orbits shows that there are discrepancies between the results. It is reasonable to believe that the discrepancy depends on the scale of the higher order displacement component.



for the others. It is interesting to see that $C_{a,IL}$ found from two harmonic trajectories are close to the result from the main loop, but the results from two other realistic trajectories vary significantly. This can also be seen from Figure 10 (c) (d).

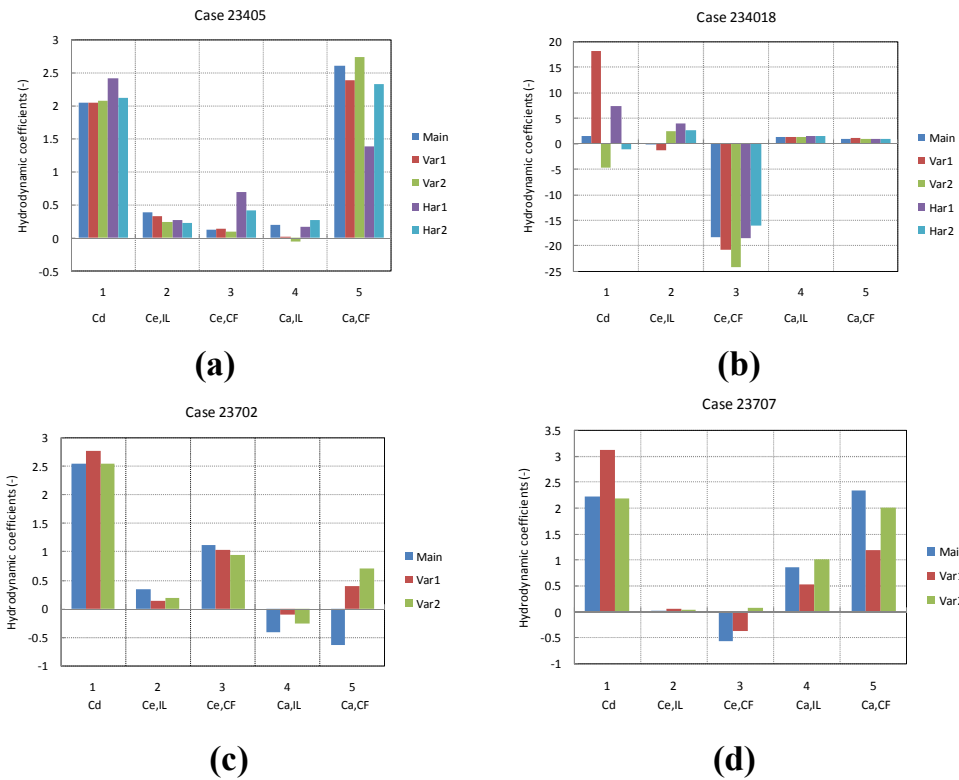


Figure 7.9: Hydrodynamic coefficients comparison by histograms for periodic and harmonic orbits (Yin and Larsen, 2011).

Figure 10 Hydrodynamic coefficients comparison by histograms for periodic and harmonic profiles.

7.2.5 Periodic: Contour Plots

The deviation of $C_{a,IL}$ is very small for case 234018 when comparing the harmonic trajectories with periodic ones. Similar observation was found by Soni (2008). For case 234018, large discrepancies were found for C_d , $C_{e,IL}$ and $C_{e,CF}$. The most probable reason is that this case applies the trajectory from a

The coefficients and the added mass coefficients are presented as Contour Plots in Figure 7.10 and 7.12. The coefficients are calculated by using Eqs. (4.27) and (4.28), and the filtered amplitude ratios are defined by Eq. (4.24). The drag coefficients are plotted with non-dimensional frequency and amplitude ratio in CF in Figure 7.13.

In the three shear flow NDP cases, the results for the hydrodynamic coefficients are sensitive to imperfect measurements because the four cross sections close to the fixed end are exposed to very low flow velocities. The values found for these positions are therefore not included in this thesis.

factor
and p
cons
IL di

flexi
same
appr

ampl
Figur
param
The
dotted
indic
value
trend
trend
(A/D
same
and a
while

is th
coeff
param
group

CF excitation coefficient

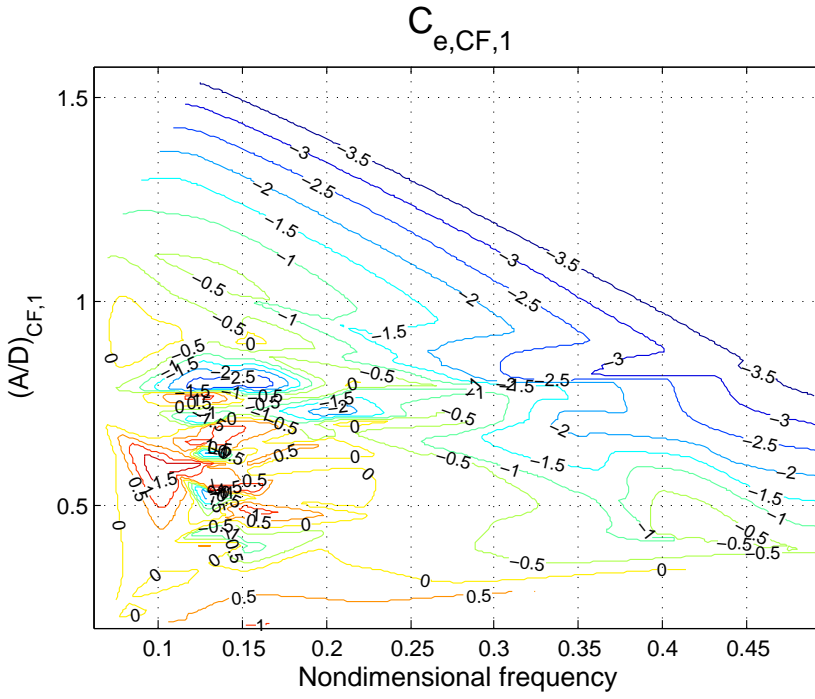
The pure CF excitation coefficient contour plot by Gopalkrishnan (1993) (see Figure 2.14a) contains two *excitation regions*. Inside the excitation region, the energy is transferred from the fluid to the structure and vice versa outside. Comparing Figure 7.10a with Figure 2.14a, the first excitation region is present, and the second region appears in the high non-dimensional frequency-low $(A/D)_{CF}$ area. The zero contour lines define the CF response amplitude for a rigid cylinder on a spring without mechanical damping. In Figure 2.14a, the first excitation region covers the non-dimensional frequency range of $[0.12, 0.18]$, with a maximum $(A/D)_{CF}$ at approximately 0.85. While the result of this study shows a wider excitation region and the maximum $(A/D)_{CF}$ can reach as high as 1, this result is close to the finding of Soni (2008). Similar to Soni (2008), there are also ‘*islands*’ with negative values inside the excitation region.

It is important to note that the excitation for high non-dimensional frequency was also found by Chasparis et al. (2009) and Wu et al. (2010). The results may thus be correct and will support an extension of the excitation zone for structures in sheared flow when the non-dimensional frequency is beyond 0.3, which is often used as an upper value today.

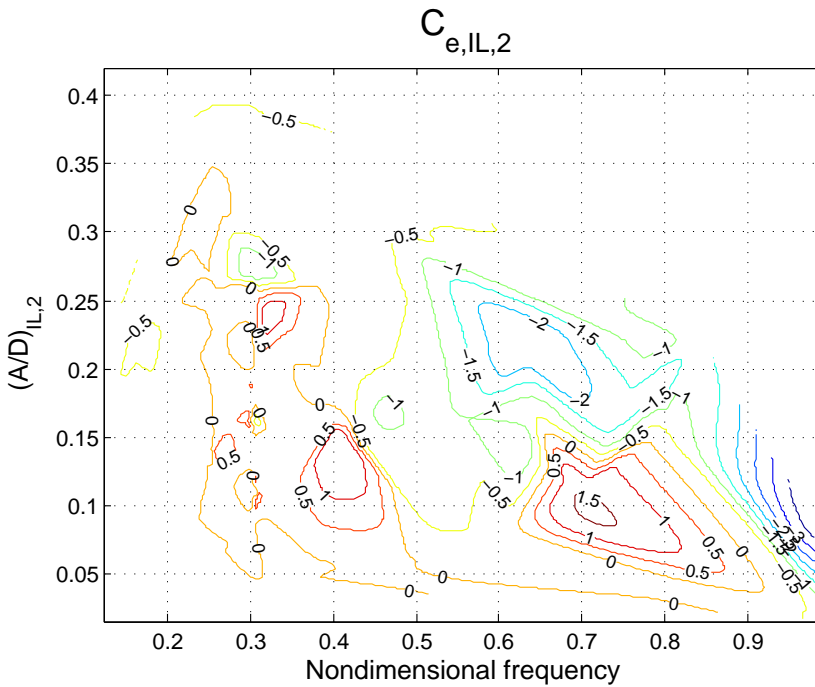
IL excitation coefficient

Aronsen (2007) produced contour plots based on his pure IL forced motion experiments, and he refers to the area surrounded by the zero contour lines as ‘*instability regions*’, see Figure 2.16a. He defines the first instability region with a non-dimensional frequency ranging from 0.375 to 0.76, and the maximum $(A/D)_{IL}$ is 0.13. The non-dimensional frequency of the second instability region ranges from 0.27 to 0.375, and the maximum $(A/D)_{IL}$ is 0.11. To prevent confusion, this study defines the 1st instability region as having a higher non-dimensional frequency range than the 2nd instability region. Figure 7.10b shows that the 1st instability region ranges from 0.62 to 0.91 and that it has a maximum $(A/D)_{IL}$ at approximately 0.15; the 2nd instability region ranges from 0.2 to 0.5 and has a maximum $(A/D)_{IL}$ at approximately 0.15. These two regions are equivalent to those found by Aronsen (2007).

However, this study also found a third instability region around the amplitude ratio of 0.25. These amplitudes are not present for the pure IL response, but they are often found for the combined IL and CF cases. The



(a) CF.



(b) IL.

Figure 7.10: Contour plots of excitation coefficients from periodic tests.

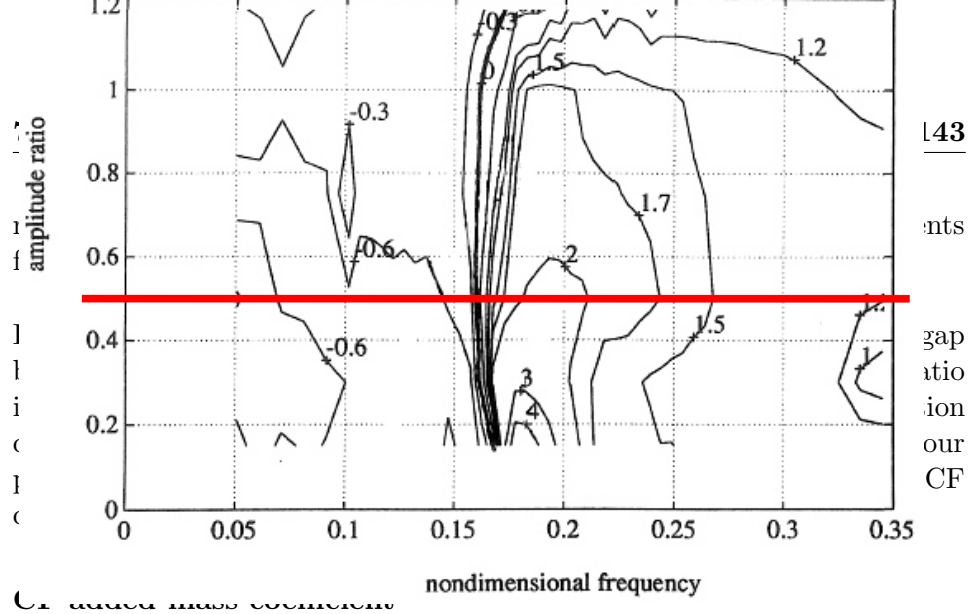


Figure 7.10 The Contour plot of the CF added mass coefficient based on forced harmonic motions. From Gopalkrishnan (1993). This figure shows that the added mass coefficient is almost independent of the amplitude ratio. By taking the values at $(A/D)_{CF} = 0.5$, Larsen et al. (2009) employed the added mass model shown in Figure 7.11. This study also shows that the added mass coefficients in the CF direction due to periodic motions are less independent of the amplitude ratio. The non-dimensional frequency range from 0.1 to 0.15 is occupied by negative values; see Figure 7.12a.

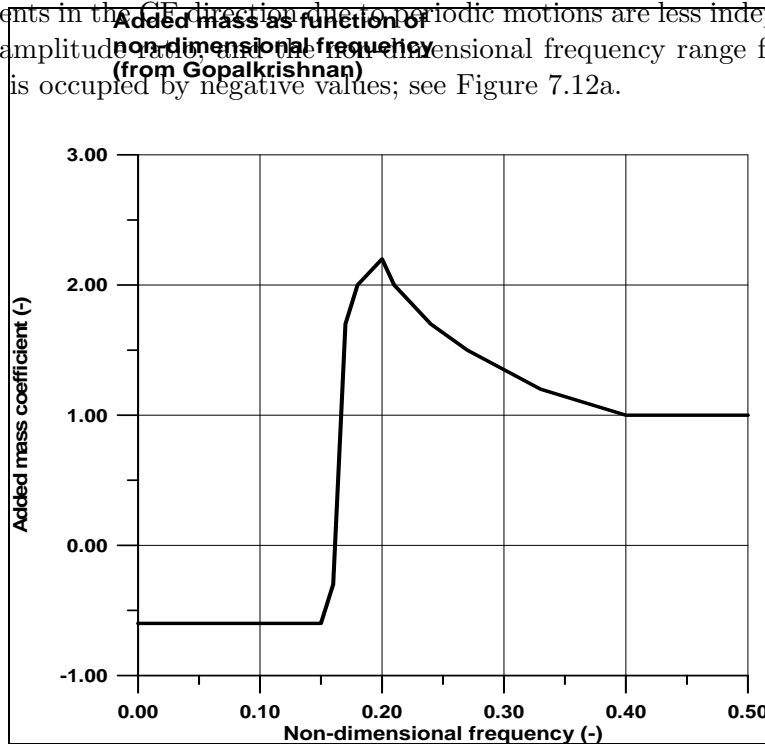


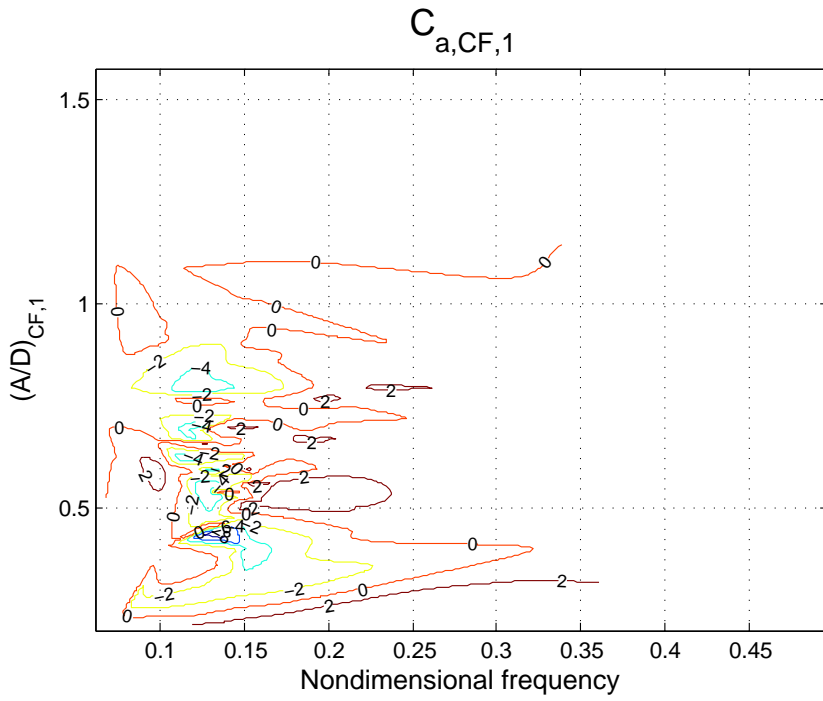
Figure 7.11: Added mass coefficient curve embedded in VIVANA, from Larsen et al. (2009). The VIVANA model for added mass as function of non-dimensional frequency for cross-flow VIV.

IL added mass coefficient

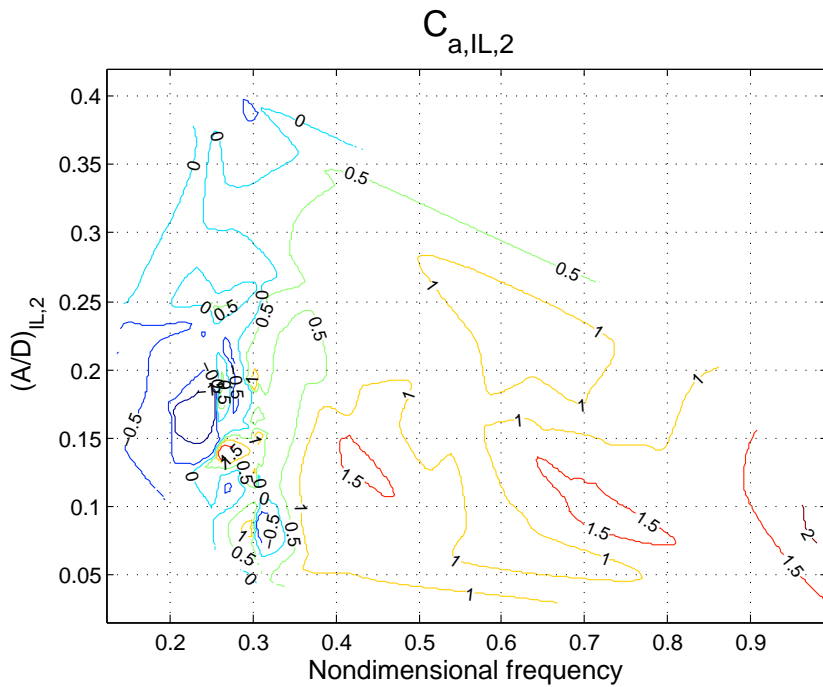
The added mass coefficients in the IL direction are shown in Figure 7.12b. This coefficient is less influenced by the amplitude ratio compared with the non-dimensional frequency. In general, it tends to increase with increasing non-dimensional frequency, which complies with the pure IL added mass coefficients found by Aronsen (2007); see Figure 2.16b.

Drag coefficient

The drag coefficients from the periodic motion tests are presented in Figure 7.13. As introduced in section 2.4.5, the drag coefficient is amplified if there is motion in the CF direction. According to Figure 7.13a, an increasing trend with $(A/D)_{CF}$ seems to exist while the contour plot with $(A/D)_{IL}$ is disordered; see Figure 7.13b.



(a) CF.



(b) IL.

Figure 7.12: Contour plots of added mass coefficients from periodic tests.

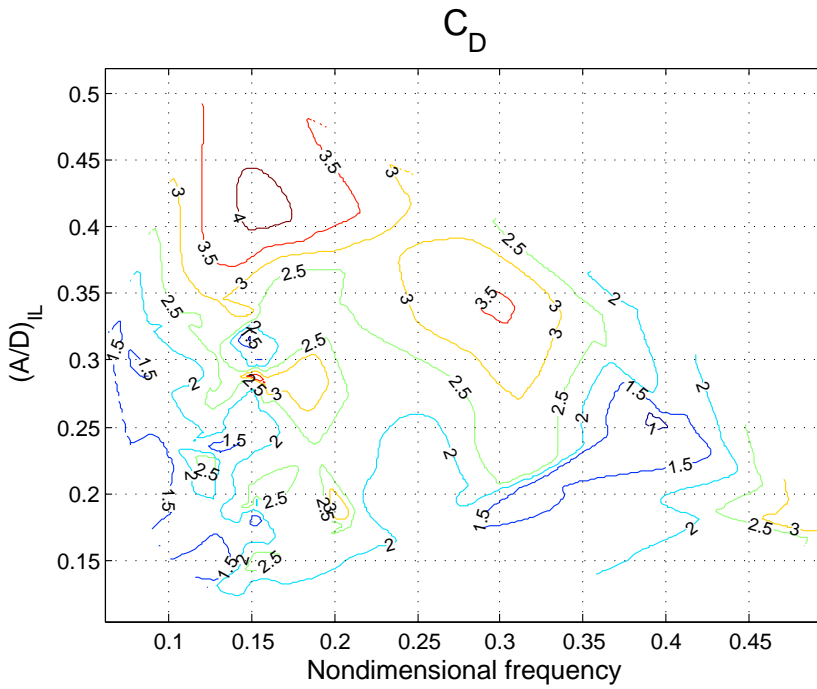
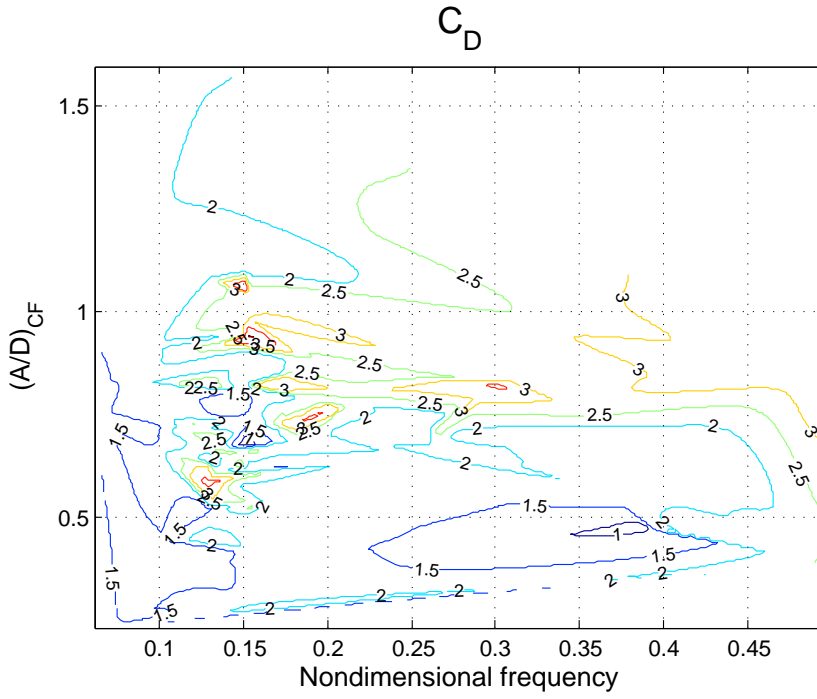


Figure 7.13: Contour plots of drag coefficients from periodic motion tests.

Excitation coefficient amended with the relative velocity

Two harmonic orbits with phase angles of 0 and 180 degrees (see Figure 4.1) were tested by Aronsen (2007). Given the coefficients and the results from the PIV experiment, he discovered that the orbital direction can influence the results significantly. Huang et al. (2009) performed numerical simulations of these two cases and investigated the influence from the orbital direction.

To include this orbital direction effect, the *relative velocity* is introduced; see Figure 7.14. The IL velocities of the oscillating cylinder at the maximum and minimum CF amplitudes are defined as $u_{IL} |_{(\frac{A}{D})_{CF,max}}$ and $u_{IL} |_{(\frac{A}{D})_{CF,min}}$, respectively. For harmonic orbits, they are equal, while periodic orbits are not symmetric. In this case, their mean values are used to define the relative velocity u_r :

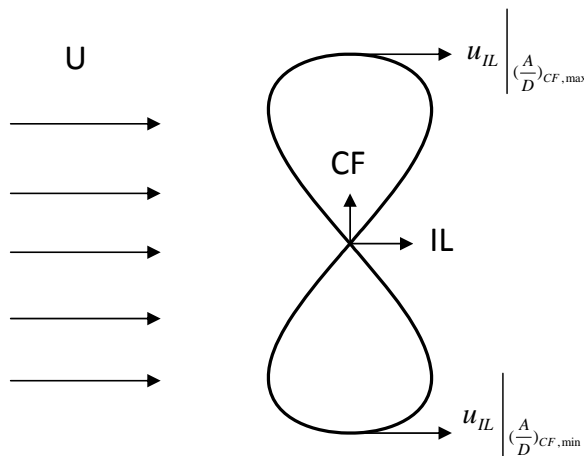


Figure 7.14: Illustration of relative velocity.

Travel Report of OMAE 2011

$$u_r = U - \frac{1}{2} \left[u_{IL} |_{(\frac{A}{D})_{CF,max}} + u_{IL} |_{(\frac{A}{D})_{CF,min}} \right] \quad (7.1)$$

The relative velocity is used to calculate the non-dimensional frequency, and the amended non-dimensional frequency is defined as

I attended OMAE 2011 held in Rotterdam from June 19th to 24th, The Netherland this summer. The full program can be found in <http://www.asmeconferences.org/OMAE2011/> and all of the papers can be found in the CD at library.

$$\frac{f}{u_r} = \frac{f}{U} \cdot \frac{U}{u_r} \quad (7.2)$$

There were 13 Symposia and I mainly attended the CFD & VIV symposia. I presented my paper OMAE2011-49438 'Experimental and numerical analysis of forced motion of a circular cylinder.' I got several questions from the audience.

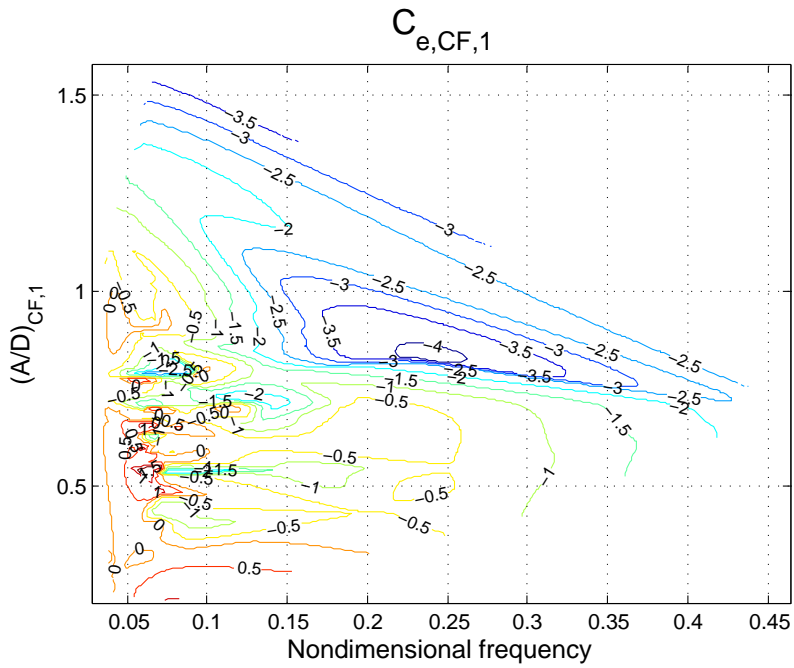
There was call for the benchmark study of both experimental work and numerical calculation related to VIV. From experimental point of view, there is still a lack of Particle Image Velocimetry (PIV) data, which can give more information of the wake after a circular cylinder directly. On the other hand, there was a discussion about the validation and verification of CFD work, which will form a workshop in OMAE2012.

The contour plots of the excitation coefficients using \hat{f}_r are shown in Figure 7.15.

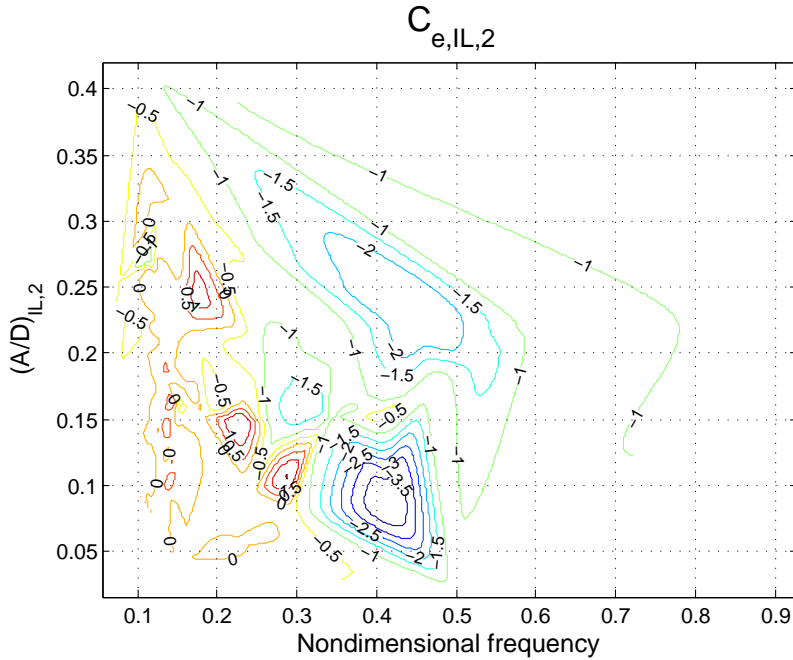
According to a comparison of Figure 7.15 with Figure 7.10, the non-dimensional frequency range of the excitation regions generally decreases. In the CF direction, the \hat{f}_r ranges from 0.04 to 0.1 approximately. In the IL direction, the first instability region disappears while \hat{f}_r of the 2nd instability region ranges from 0.1 to 0.3.

To summarise this section, contour plots are used to present the excitation coefficients, the added mass coefficients and the drag coefficients. Several aspects require attention:

1. Data from periodic motion tests with varying Re were used to produce the plots.
2. Periodic motions have higher order displacement components.
3. The phase angle between $(A/D)_{CF,1}$ and $(A/D)_{IL,2}$ was not considered here; see Figure B.2.



(a) CF.



(b) IL.

Figure 7.15: Contour plots of excitation coefficients from periodic tests.

7.2.6 Periodic: Higher order components

The higher order harmonic force components were found in harmonic forced motion experiments with IL motions (Aronsen, 2007; Dahl, 2008) and in a field test by Vandiver et al. (2006). Higher order harmonic force components are important because their high frequency can cause significant fatigue damage to the vibrating structure.

One difference between this study and other rigid cylinder forced oscillation experiments is that the orbits are not harmonic and thus contain higher order displacement components. As a consequence, it is more difficult to interpret the higher order force components because they are coupled with higher order displacement components. However, for the forced motion experiments using harmonic orbits, the higher order harmonic force component is irrelevant to the higher order displacement components simply because there are no higher harmonic displacement components in the orbits.

Higher order displacement components

The displacements in the IL and CF directions are filtered around multiple times with frequency up to ω_6 ; the filtered amplitudes are presented in Figure F.1 and Figure F.2 (Appendix F) for the uniform and shear flow NDP cases, respectively.

Generally, there are more higher order displacement components in the IL direction than in the CF direction. For the shear flow cases, $(A/D)_{IL,1}$ becomes relatively larger as the length to the top end (with maximum current velocity) increases. However, as the Re increases, this influence becomes smaller; see Figure F.2b, F.2d and F.2f (Appendix F).

Higher order force components

Figure F.3 and Figure F.4 (Appendix F) show the total hydrodynamic force coefficients normalised by the $C_{rms,CF/IL}$. The relative magnitudes of the hydrodynamic force at ω_1 to ω_6 are illustrated.

The third-order harmonic total hydrodynamic force coefficients $C_{t,CF,3}$ are presented in Dahl (2008). It is shown that $C_{t,CF,3}$ is related to several parameters: $(A/D)_{CF}$, $(A/D)_{IL}$, θ , V_r ($1/\hat{f}$) and Re. The $(A/D)_{IL}$ is a key parameter: when other parameters are fixed, $C_{t,CF,3}$ increases with increas-

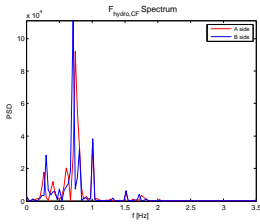
ing $(A/D)_{IL}$. In addition, the phase angle θ between IL and CF and V_r also has an influence on $C_{t,CF,3}$, but the influence is much weaker.

This study contains more parameters than the harmonic motion experiments because there are higher order displacement components in the orbits; see Figure F.1 and Figure F.2 (Appendix F). The phase angle θ is varying; see Figure B.2 (Appendix B). Re is not fixed, and thus, there are insufficient data to create a plot similar to that in Dahl (2008).

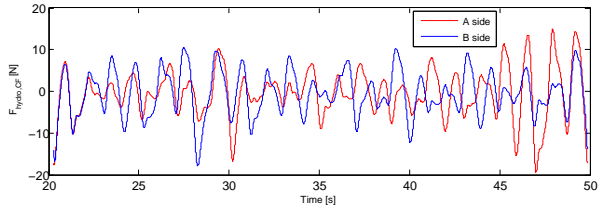
7.2.7 Periodic: Broad band and frequency drift

Some periodic oscillation tests do not produce stable periodic hydrodynamic forces; see Figure 7.16 and Figure 7.17. In each figure, the force spectrum and the time series are shown in both the CF and IL directions. Test N216010 has a stable IL hydrodynamic force, but in the CF direction, the force is unstable and has a broad frequency band, and the dominant frequency is not at the oscillation frequency, which is 0.5 Hz. Test N216011 also has an oscillation frequency of 0.5 Hz, but both the CF and IL forces are unstable. The force spectrum shows that the frequency components are not at multiples of the oscillation frequency. Therefore, the total hydrodynamic force coefficients calculated around multiple oscillation frequencies are much smaller.

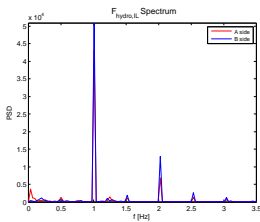
By checking the parameters of these two tests and comparing them with Figure 2.15, it is clear that both tests have λ^* values of approximately 9.8 and $(A/D)_{CF}$ less than 0.8. In the contour plots of Figure 2.15, these values are located in the area with no synchronised vortex shedding pattern. Even these two tests have higher Re numbers than the contour plots in Morse and Williamson (2009), who compared contour plots between $Re = 4000$ and $Re = 12000$, but the general conclusions are quite similar.



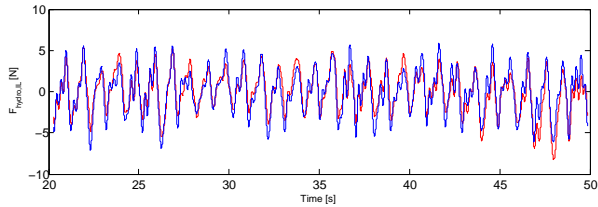
(a) CF Force spectrum



(b) CF Force time series

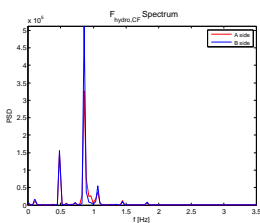


(c) IL Force spectrum

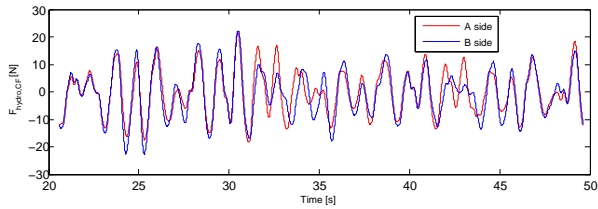


(d) IL Force time series

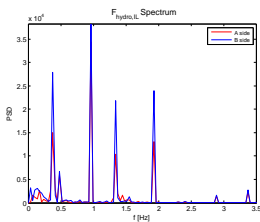
Figure 7.16: IL and CF hydrodynamic force time series and power spectra of test 216010.



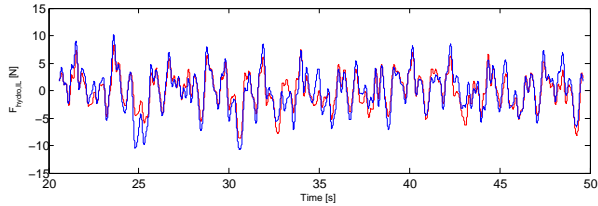
(a) CF Force spectrum



(b) CF Force time series



(c) IL Force spectrum



(d) IL Force time series

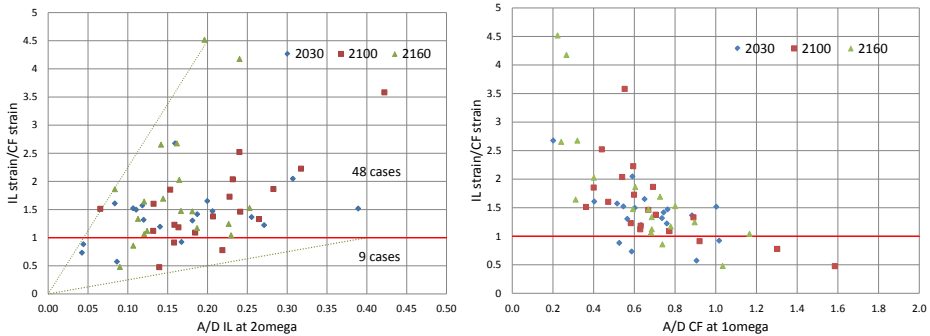
Figure 7.17: IL and CF hydrodynamic force time series and power spectra of test 216011.

7.2.8 Periodic tests of uniform flow cases

Orbits taken from three uniform NDP cases are shown in Figure B.3, Figure B.4 and Figure B.5 (see Appendix B). Their Re numbers are shown in Table 3.4. The smallest IL and CF amplitude ratios are approximately 0.1 and 0.25, respectively, while the largest IL amplitude ratio is 0.4, and the largest CF amplitude is above 1.5.

Because the rigid pipe apparatus places limitations on the towing speed and the orbital accelerations, the orbits from NDP cases 2100 and 2160 could not be tuned to the correct non-dimensional frequencies. By adjusting the non-dimensional frequency by a factor (see Table B.2, Appendix B), the tests could be conducted in an acceptable way.

Figure 7.18 shows the relative strain of the IL and CF directions for all uniform flow cases, which is defined by Eq. (2.22). The horizontal red line indicates equal strain from CF and IL. Among the 57 uniform cases, there are 48 cases with a higher IL strain than CF strain, which indicates that the IL response contributes more to fatigue damage than the CF response.



(a) Relative strain from CF and IL vibrations as function of $(A/D)_{IL,2}$.

(b) Relative strain from CF and IL vibrations as function of $(A/D)_{CF,1}$.

Figure 7.18: Relative strain of uniform flow cases.

Figure 7.19 shows the excitation coefficients at primary frequencies in the CF and IL directions. All three cases have a visual trend of decreasing with increasing A/D , which has been recognised as leading to the self-limiting feature of VIV. However, for almost the same amplitude ratio (Figure 7.19a, data points A, B and C, and Figure 7.19b, data points D, E and F), we have almost identical CF and IL amplitudes for the primary frequencies, while

the excitation coefficients vary significantly. This variation will be discussed in detail later.

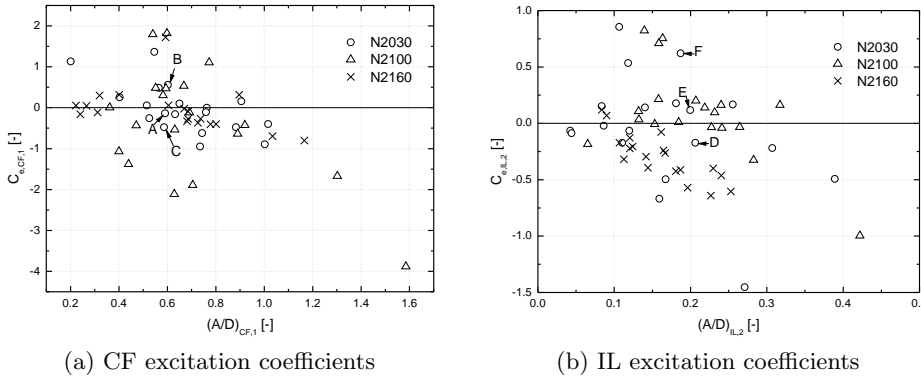


Figure 7.19: Excitation coefficients for CF and IL directions of periodic forced motion tests, corresponding to uniform cases in NDP.

Figure 7.20a and b show the added mass coefficients in the CF and IL directions, respectively. The coefficients are scattered for both the IL and CF directions. However, they tend to converge to zero with increasing amplitude ratio.

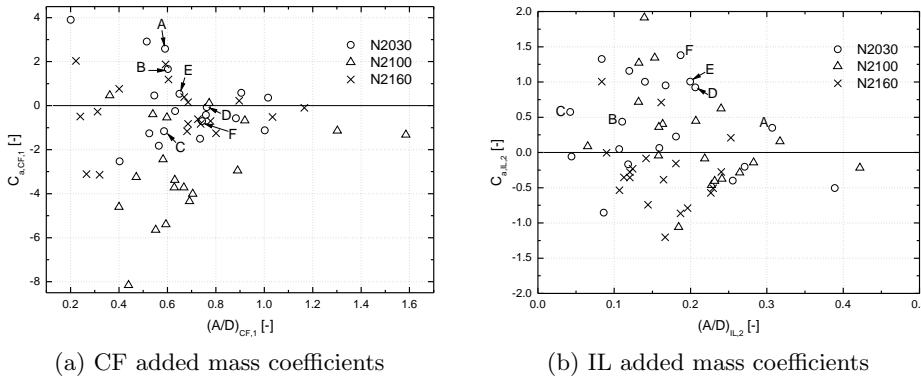


Figure 7.20: Added mass coefficients for CF and IL directions of periodic forced motion tests, corresponding to uniform flow cases in NDP.

The orbits of the six cases marked in Figure 7.19 are shown in Figure 7.21. The X and Y axes are the IL and CF amplitude ratios, respectively. The blue lines are the periodic orbits found in the NDP tests and then applied as

	$C_{e,CF,1}$	$C_{e,IL,2}$	$C_{a,CF,1}$	$C_{a,IL,2}$	$C_{t,CF,1}$	$C_{t,CF,3}$	$C_{t,CF,5}$	$C_{t,IL,2}$	$C_{t,IL,4}$	$C_{t,IL,6}$	$C_{t,CF,2}$
A	-0.138	-0.220	2.582	0.349	2.258	0.991	0.575	0.669	0.780	1.127	
B	0.560	-0.173	1.662	-0.437	1.562	2.430	1.033	0.330	0.278	9.165	155
C	-0.478	-0.065	-0.478	0.573	1.165	0.747	0.106	0.165	1.241	0.373	
D	-0.005	-0.173	-0.074	0.923	0.080	0.533	0.373	1.072	0.420	4.664	0.758
E	0.099	0.631	0.006	1.006	0.934	0.264	0.264	0.127	1.127	1.127	
F	-0.621	0.620	-0.709	1.379	0.975	2.690	0.349	1.596	1.378	4.375	

7.2. Results of the forced motion experiments

the forced motion in the rigid cylinder tests. The red lines are the harmonic orbits, created by filtering the periodic loops with a small bandwidth around ω_1 in the CF direction and ω_2 in the IL direction.

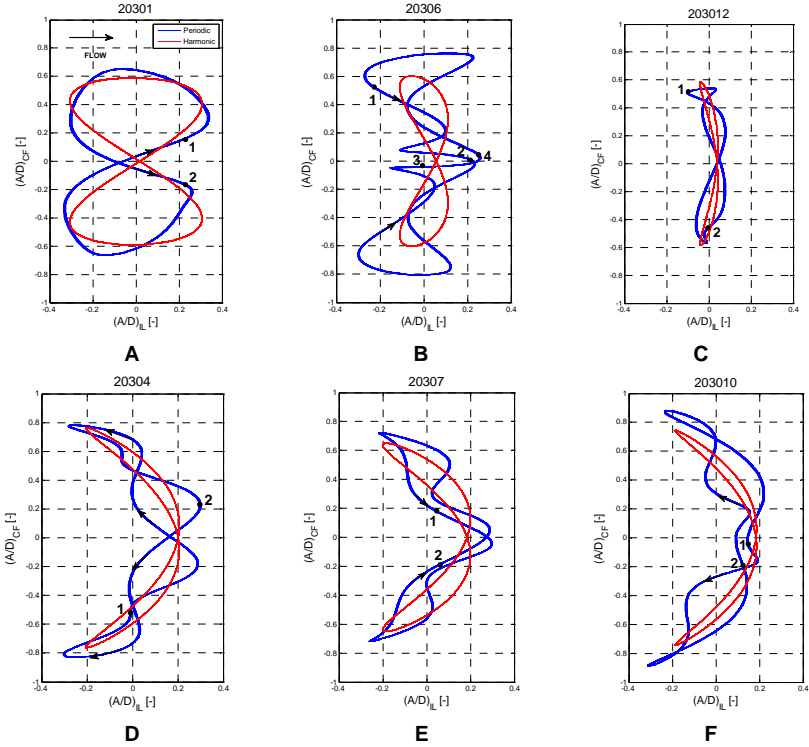


Figure 12 Periodic and harmonic trajectories of the six cases.

Figure 7.21: Periodic and harmonic orbits of six locations on the same flexible pipe subjected to uniform current, case 2030 (Yin and Larsen, 2011).

Three cases for Group 1 (A, B, C) have similar $(A/D)_{CF}$ at ω_1 , which is at approximately 0.6. Case A has the largest $(A/D)_{IL}$, while Case C has the smallest IL motion; B has the greatest higher order amplitudes in both the CF and IL directions. Significant IL motion components are found at ω_4 and even for ω_6 . For Group 2 (D, E and F), three cases have a main $(A/D)_{IL}$ of approximately 0.2. Their CF amplitudes show minor variability. F has the highest value of 0.89, and E has the lowest value of 0.726; all three of these cases have a strong higher-motion component in the IL direction.

Figure 7.22 shows the relationship between the influence factors (which dom-

inate the amplitude ratios, the higher amplitude ratios and the phase angle) and the hydrodynamic coefficients. Here, we only consider the hydrodynamic coefficients at ω_1 in CF and ω_2 in the IL direction.

ANNEX B

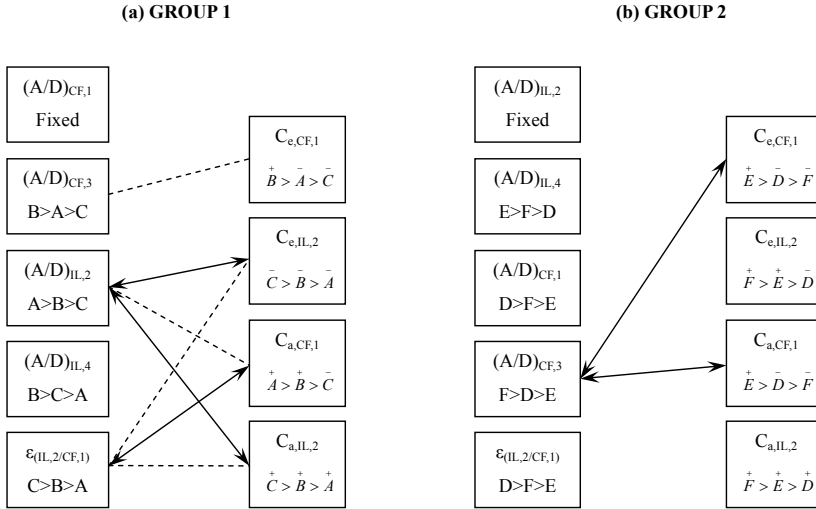


Figure 7.22: Schematic overview of the relationship between hydrodynamic coefficients and motion parameter. Dotted line: Coefficient is seen to increase for increasing parameter; Solid line: Coefficient is seen to decrease for increasing parameter (Yin and Larsen, 2011).

Non-dimensional frequency

All six of the cases discussed above belong to the same flexible beam case with a uniform current. Hence, they have the same non-dimensional oscillation frequency, which is approximately 0.15.

IL/CF components of forces and displacements

To evaluate the influence of the variation of the CF amplitude, the amplitude in the IL direction should be fixed, and vice versa. Figure 7.22 illustrates the influence of the motion parameters on the hydrodynamic coefficients in a qualitative way. A dotted line between a motion parameter and a coefficient indicates that the coefficient increases when the value of the parameter increases while a solid line indicates the opposite trend. The absence of a connecting line indicates that no clear trend is observed. Figure 7.22a shows almost the same $(A/D)_{CF,1}$, while the other factors vary.

Only $C_{e,CF,1}$ follows the same trend as $(A/D)_{CF,3}$. The hydrodynamic excitation coefficients and the added mass coefficients decrease with increasing $(A/D)_{IL,2}$, while $C_{a,CF,1}$ increases with increasing IL amplitude ratio.

In Figure 7.22b, $(A/D)_{IL,2}$ is fixed. The only obvious trend is that the hydrodynamic excitation coefficient and the added mass coefficient decrease with increasing $(A/D)_{CF,3}$. The other parameters have a weak influence. Because the CF amplitude for this group has a smaller variation than that for Group 1, one may conclude that this is the main reason for the difference between the trends.

Phase angle

Another influencing factor is the phase angle between the IL and CF motions at the dominant frequencies, which is defined by Eq. (4.2) and shown in Table 7.2. An interesting observation is found: if $(A/D)_{CF,1}$ is fixed (A,B,C), the phase angle decreases with increasing $(A/D)_{IL,2}$; however, the phase angle increases with increasing $(A/D)_{CF,1}$ if $(A/D)_{IL,2}$ is fixed. It is too early to conclude that the phase is controlled by the CF amplitude rather than the IL amplitude in nature, but at least these samples indicate such a trend.

Table 7.2: Phase angle and total dynamic force coefficients of six tests.

	θ [°]	$C_{t,CF,1}$	$C_{t,CF,3}$	$C_{t,CF,5}$	$C_{t,IL,2}$	$C_{t,IL,4}$	$C_{t,IL,6}$
A	183.3	2.258	0.991	0.575	0.669	0.780	1.127
B	210.8	1.562	2.430	1.033	0.330	0.278	9.165
C	294.2	1.165	0.747	0.106	0.165	1.241	0.373
D	294.8	0.080	0.533	0.373	1.072	0.420	4.664
E	237.8	0.516	0.934	0.264	1.185	1.344	4.127
F	257.4	0.975	2.690	0.349	1.596	1.378	4.375

Higher order forces

Table 7.2 shows the total dynamic coefficients of the six cases. These coefficients are linked to the IL and CF directions and the frequency components and are defined by Eqs. (4.30), (4.31) and (4.32).

Aronsen (2007) found that the main higher order force components are at ω_3 in the CF direction and ω_4 in the IL direction. He also showed that the

force at ω_3 in the CF direction is approximately 30% of the force at the primary frequency ω_1 for cases with significant IL displacements. His results were based on tests with harmonic orbits and a constant ratio between $(A/D)_{IL}$ and $(A/D)_{CF}$ of 0.5.

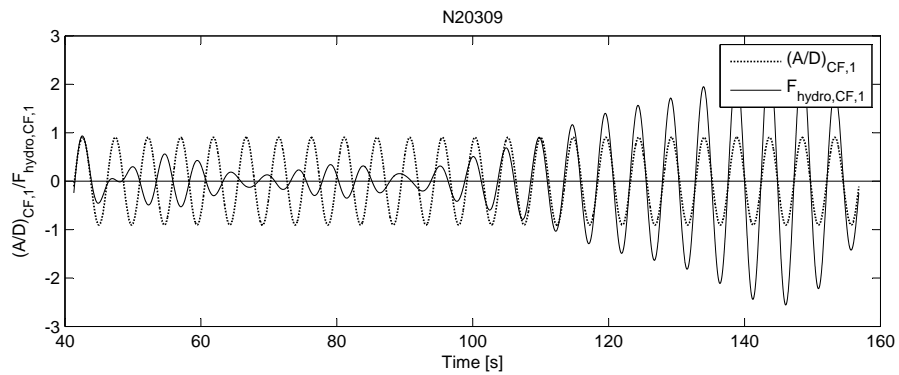
Among the six tests considered, only A has an IL/CF amplitude ratio close to 0.5. Table 7.2 shows that the dynamic force at ω_3 for this case is 44% of the force at ω_1 , which is close to the finding of Aronsen (2007). B and F have the highest CF force at ω_3 . B also has a considerable force component at ω_5 . B, D, E and F have large dynamic forces at ω_6 in the IL direction.

7.2.9 Periodic: Self-excited transition

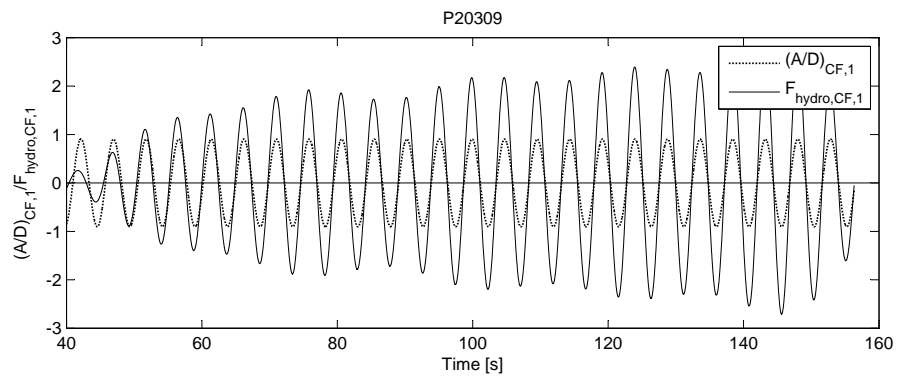
Periodic case 20309 was conducted twice: once with a PIV measurement and again without it. The forced oscillation orbits were the same for these two runs; however, measured forces were unstable and different from each other. Figure 7.23 shows the filtered hydrodynamic force and the normalised displacement signals on the dominating frequency in the IL and CF directions.

Figure 7.23 shows the normalised displacement and the hydrodynamic force in the CF direction for both runs. Figure 7.23a shows that there is a transition of the hydrodynamic force magnitude and a phase shift between the force and the displacement in the CF direction. Figure 7.23b shows that this transition occurs at the very beginning of the time window. Before the transition, the hydrodynamic force is out of phase with the displacement, but it becomes in phase after the transition and also more stable than before the transition. This transition also occurs to IL signals but at a later time point; see Figure 7.24.

A similar observation was reported in Carberry et al. (2005) from the results of controlled oscillation experiments. Carberry et al. (2001) first defined this phenomenon as a *self-excited transition*: it is reflected by a jump in the phase and the amplitude of the lift coefficient, which corresponds to a change in the vortex shedding mode and phase. This transition can occur to both varying oscillation frequencies and a constant oscillation frequency. Figure 7.25 shows the lift coefficient from a pure CF forced oscillation case at a constant frequency, and the vortex shedding mode changes from ‘2P’ to ‘2S’ as the ‘low-frequency state’ shift to ‘high-frequency state’. There is an obvious increase of the lift coefficient, and the phase between force and

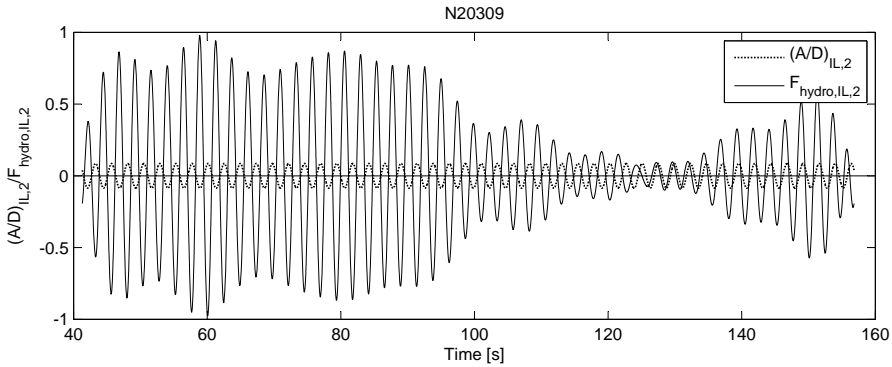


(a) CF N20309

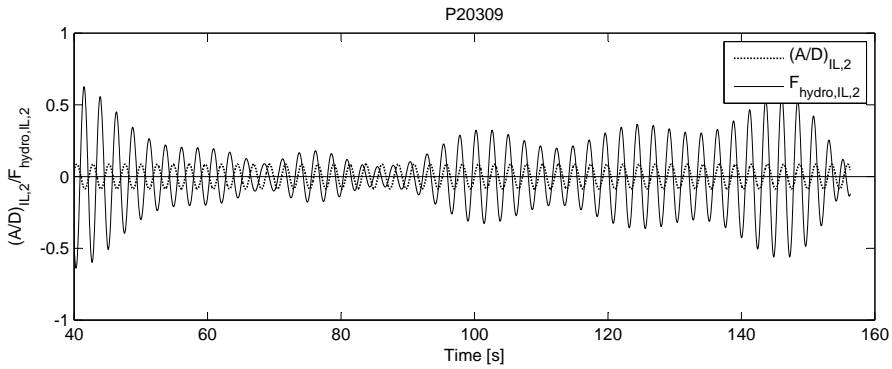


(b) CF P20309

Figure 7.23: CF dominating displacement and hydrodynamic force of periodic case 20309.



(a) IL N20309



(b) IL P20309

Figure 7.24: IL dominating displacement and hydrodynamic force of periodic case 20309.

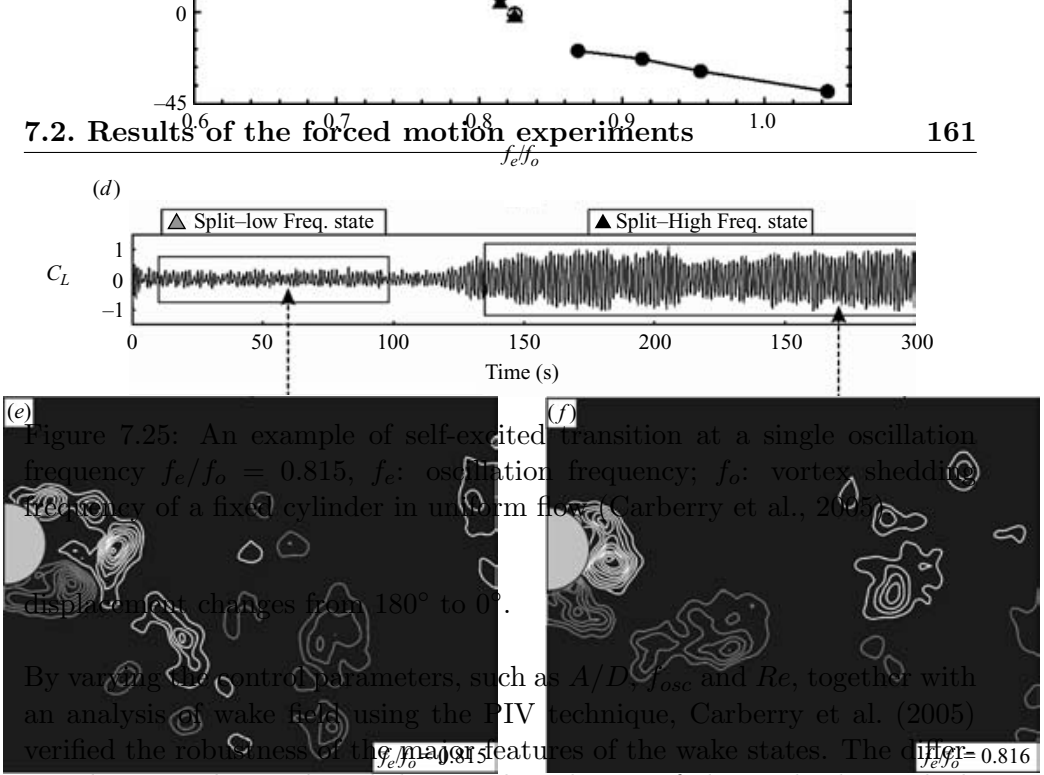


Figure 7.25: An example of self-excited transition at a single oscillation frequency $f_e/f_o = 0.815$, f_e : oscillation frequency; f_o : vortex shedding frequency of a fixed cylinder in uniform flow (Carberry et al., 2005).

displacement changes from 180° to 0° .

By varying the control parameters, such as A/D , f_{osc} and Re , together with an analysis of wake field using the PIV technique, Carberry et al. (2005) verified the robustness of the major features of the wake states. The difference between this work and their work is the use of observed orbits, which contain both IL and CF motions and higher order components, in contrast to harmonic forced motions. This difference introduces many influencing factors, and it is natural to ask whether the self-excited transition in this type of experiment will have different characteristics.

7.2.10 Energy transfer for Case N2340, periodic motions

The energy transfer rate between the fluid and the oscillating beam can be found by using Eq. 4.29. The amplitude ratios of all cross sections for the NDP flexible beam Case 2340 are shown in Figure 7.26.

Figure 7.27 shows the average energy transfer rate in the CF and IL directions, respectively (see Eq. 4.29). Positive values indicate that energy is transferred from the fluid to the cylinder, while negative values indicate damping. The maximum flow velocity is at $x = 0\text{ m}$, while the velocity is zero at $x = 38\text{ m}$. The energy transfer is determined by measurements with the motion-controlled rigid cylinder and not from the flexible beam tests.

The IL and CF energies shown in Figure 7.27a and 7.27b contain the primary and secondary frequencies in both directions. The energy is transferred from the fluid to the beam at high flow velocities. It is also easy to observe that large amplitudes lead to damping, which illustrates the well-known self-limiting feature of VIV.

FIGURE 4. For caption see facing page.

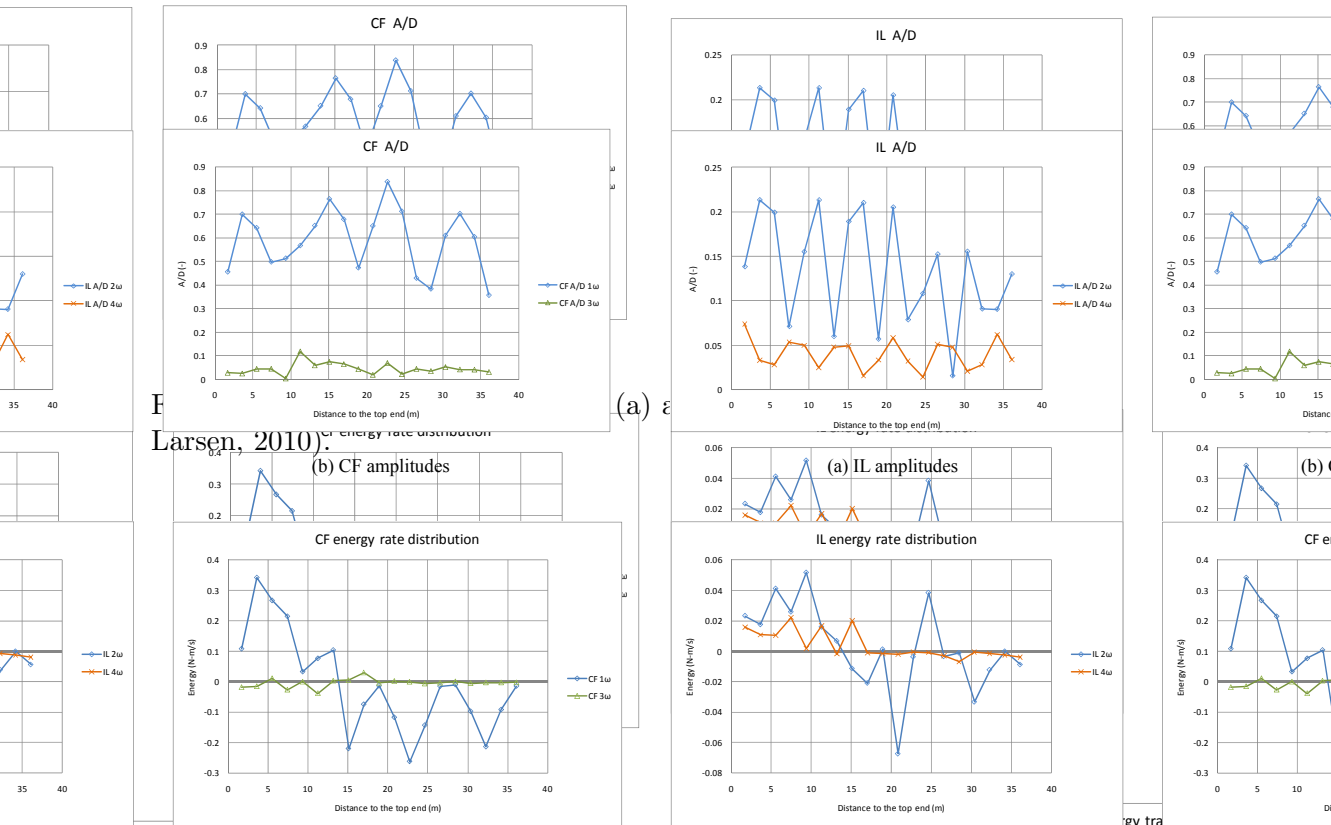


Figure 7.27: Average energy transfer rate of CF (a) and IL (b) for Case 2340 (Yin and Larsen, 2010).

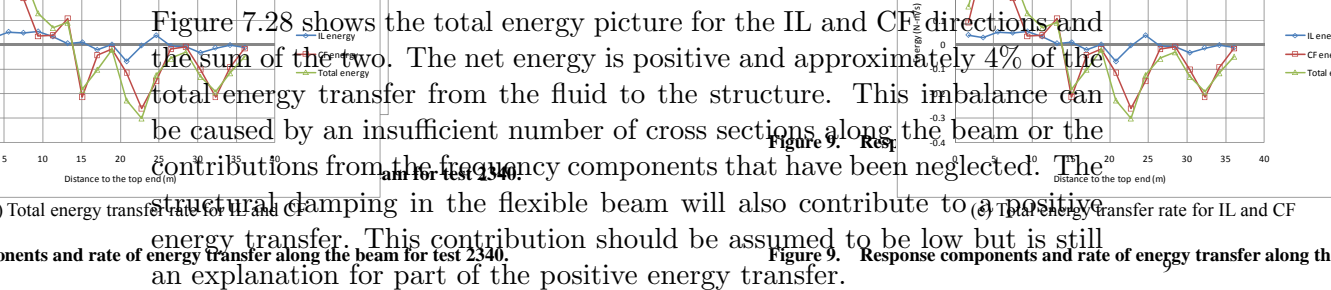
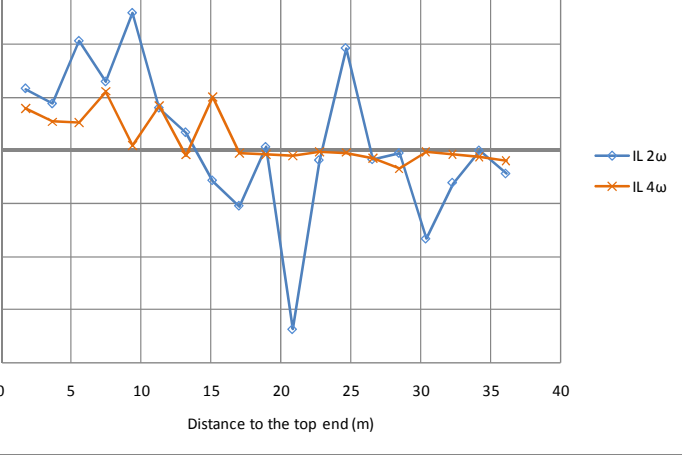
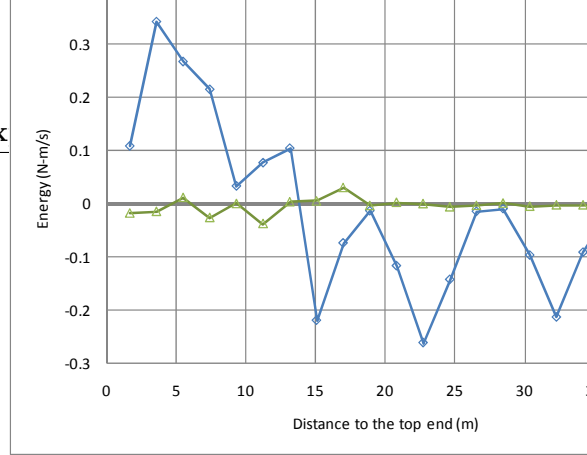


Figure 7.28 shows the total energy picture for the IL and CF directions and the sum of the two. The net energy is positive and approximately 4% of the total energy transfer from the fluid to the structure. This imbalance can be caused by an insufficient number of cross sections along the beam or the contributions from the frequency components that have been neglected.

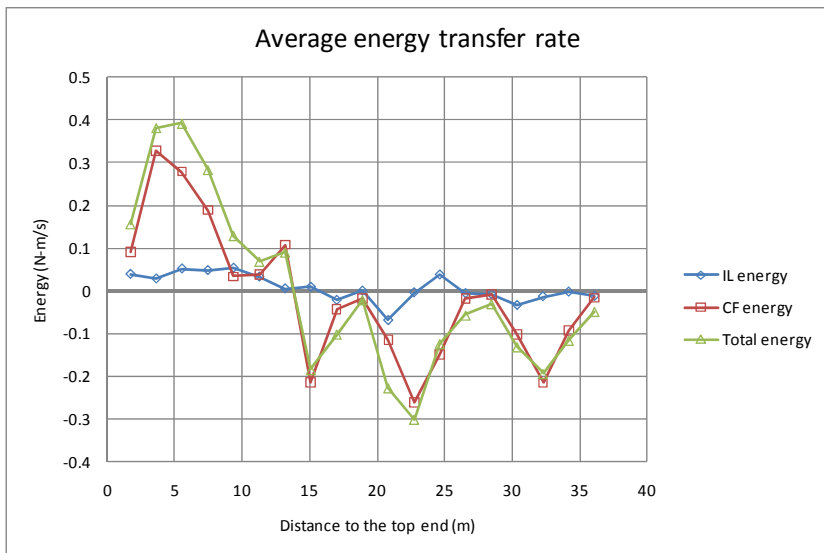
The structural damping in the flexible beam will also contribute to a positive energy transfer. This contribution should be assumed to be low but is still an explanation for part of the positive energy transfer.



(c) Energy transfer rate, IL ω_2 and ω_4



(d) Energy transfer rate, CF ω_1 and ω_2



(e) Total energy transfer rate for IL and CF

Figure 7.28: Total energy transfer rate for Case 2340 (Yin and Larsen, 2010)

Figure 9. Response components and rate of energy transfer along the beam for test 2340

7.2.11 Non-periodic: Observed orbit experiments

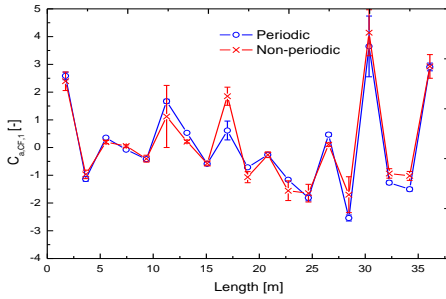
A cross section of the flexible beam will not have a perfectly periodic motion. The frequency will be close to constant, but the IL and CF amplitudes and the phase between them will show some variations (see Figure 3.8). We may therefore ask the question: Do the selected periodic orbits represent the real oscillations adequately? One way of testing this question is to use the non-periodic observed orbits for cross section motions as forced motions for the rigid cylinder and compare the average coefficient from this test to the coefficients found in the periodic orbit test. One NDP uniform flow case (2030) and two shear flow cases (2340 and 2370) were selected for comparison. The hydrodynamic excitation coefficients and the added mass coefficients are presented in Figure 7.29, Figure 7.30 and Figure 7.31, respectively. The primary and first higher order frequency components in both directions (ω_1 and ω_3 for CF, ω_2 and ω_4 for IL) are included.

According to Figure 7.29 and Figure 7.30, most of the coefficients from periodic tests agree well with the results of non-periodic observed motion tests, except that the higher order added mass coefficients have relatively larger discrepancies. In general, non-periodic results have larger uncertainties.

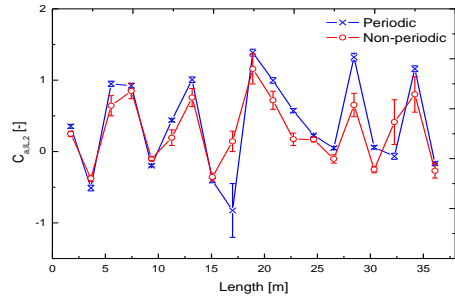
The good agreement is attributed to the fact that both the CF and IL non-periodic observed motions exhibit quasi-periodic characteristics (Type-I) for cases 2030 and 2340; see Figure 7.2, Figure E.3 (Appendix E), Figure B.9 and Figure B.10 (Appendix B).

For Case 2370, only $C_{e,CF,1}$, $C_{e,IL,2}$ and $C_{a,CF,1}$ are comparable for the first half-span of the flexible beam (the high-velocity region). The other coefficients deviate between the periodic and non-periodic tests. The reason is that the response type of case 2370 is quasi-periodic (Type-I) plus chaotic (Type-II); see Figure E.4 (Appendix E) and Figure 7.5a. All of the periodic orbits were selected from a time window with quasi-periodic responses; though the non-periodic observed motion tests started from a time instant within the quasi-periodic time window, where it ended depended on the local velocity. Because it is a shear flow case, the regions with high velocities required less running time in MCLab than the low-velocity regions, which included less chaotic responses because, as it approaches the low-velocity region, the running time in MCLab increases and presents increasingly chaotic responses; see Figure E.4 (Appendix E) and Figure B.11 (Appendix B).

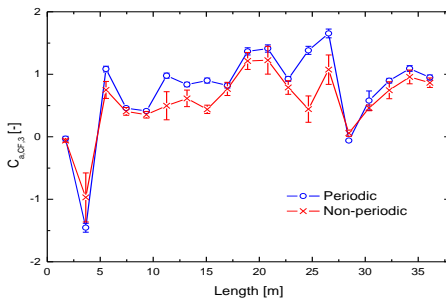
In summary, the comparison between the results from periodic and non-



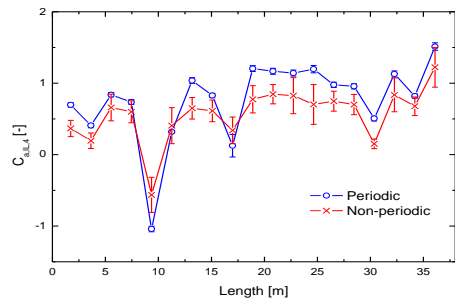
(a) CP2030CACF1



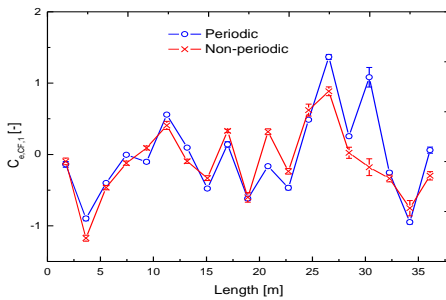
(b) CP2030CAIL2



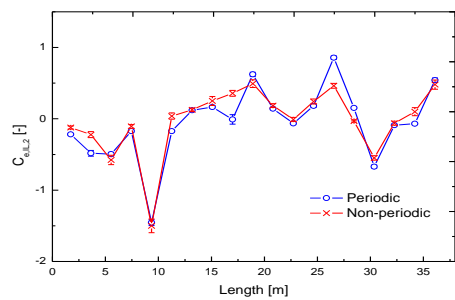
(c) CP2030CACF3



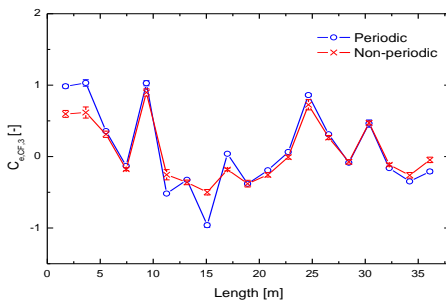
(d) CP2030CAIL4



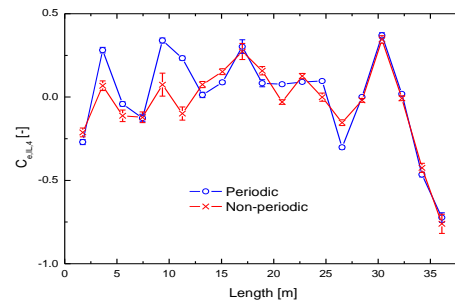
(e) CP2030CECF1



(f) CP2030CEIL2

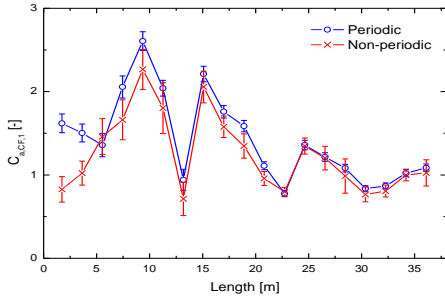


(g) CP2030CECF3

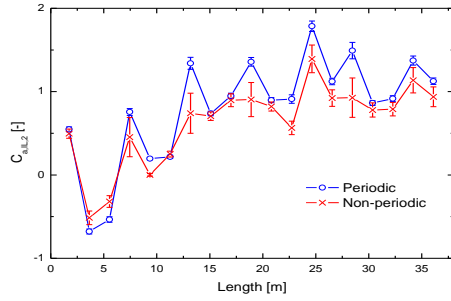


(h) CP2030CEIL4

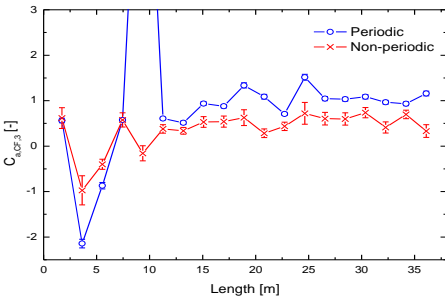
Figure 7.29: Comparison of hydrodynamic coefficients between periodic and non-periodic orbits, Case 2030, Yin and Larsen (2012).



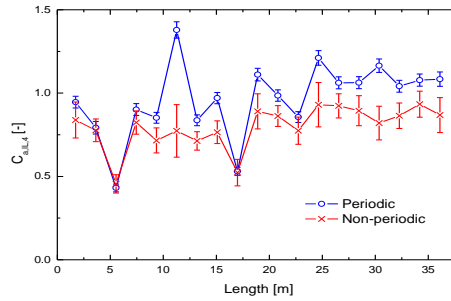
(a) CP2340CACF1



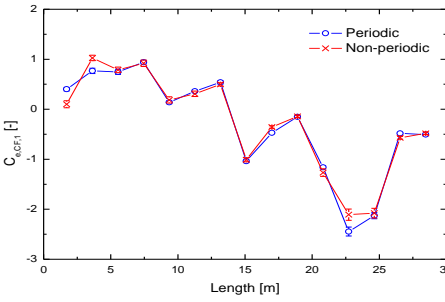
(b) CP2340CAIL2



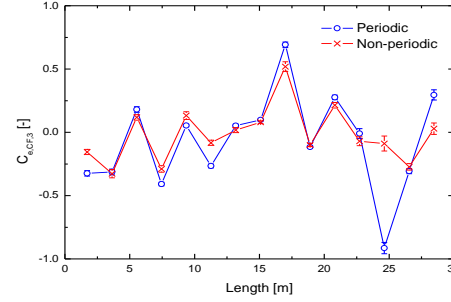
(c) CP2340CACF3



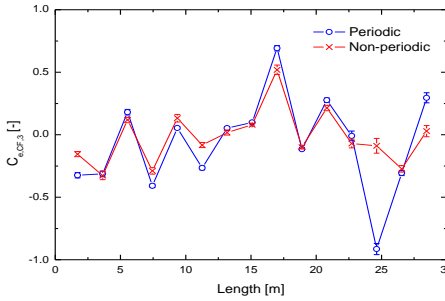
(d) CP2340CAIL4



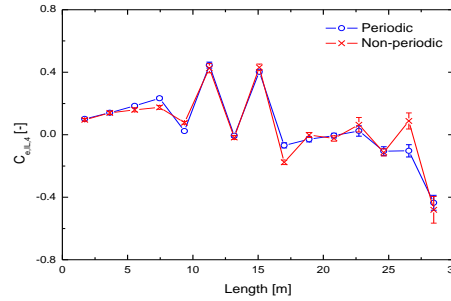
(e) CP2340CECF1



(f) CP2340CEIL2

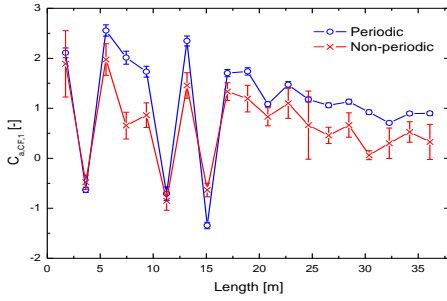


(g) CP2340CECF3

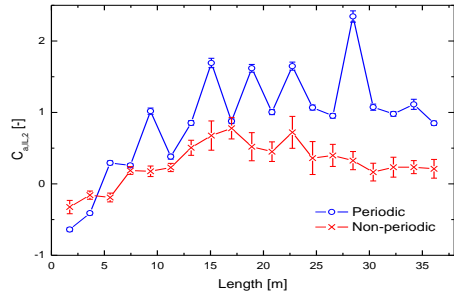


(h) CP2340CEIL4

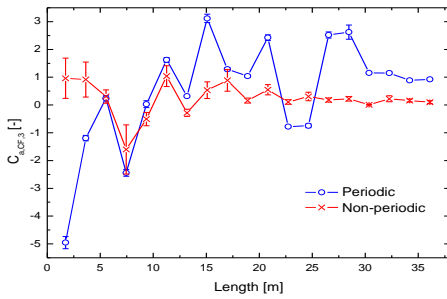
Figure 7.30: Comparison of hydrodynamic coefficients between periodic and non-periodic orbits, Case 2340, Yin and Larsen (2012).



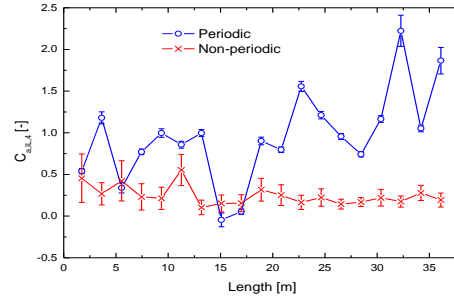
(a) CP2370CACF1



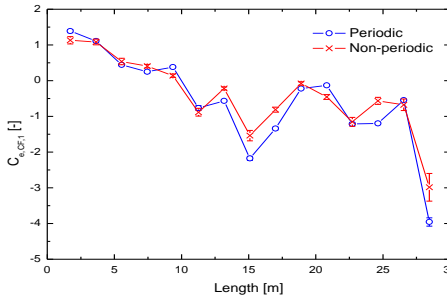
(b) CP2370CAIL2



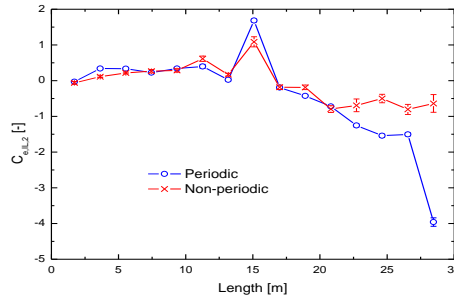
(c) CP2370CACF3



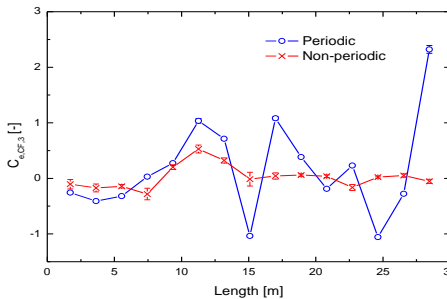
(d) CP2370CAIL4



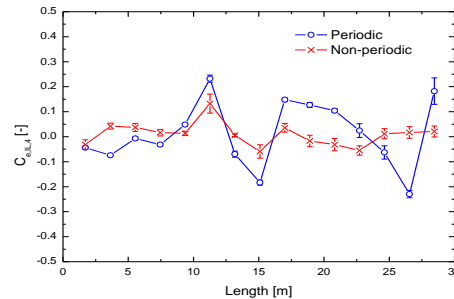
(e) CP2370CECF1



(f) CP2370CEIL2

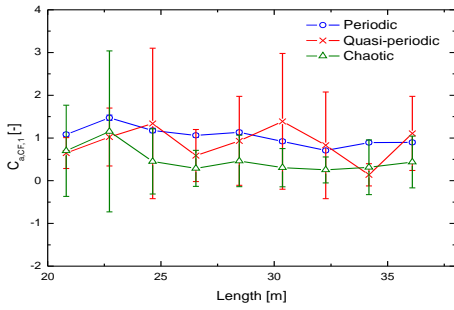


(g) CP2370CECF3

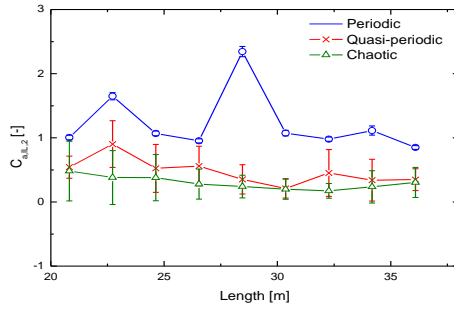


(h) CP2370CEIL4

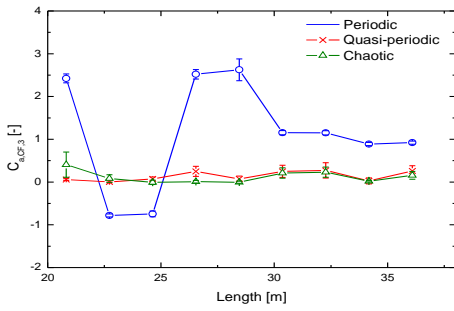
Figure 7.31: Comparison of hydrodynamic coefficients between periodic and non-periodic orbits, Case 2370, Yin and Larsen (2012).



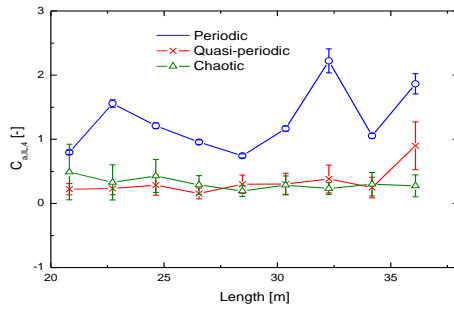
(a) PQC2370CACF1



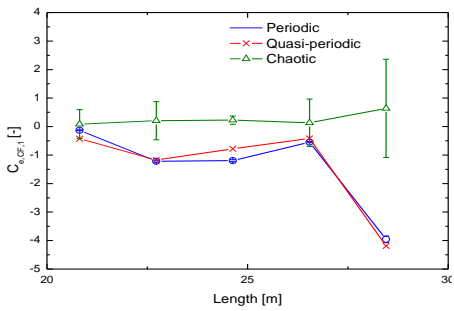
(b) PQC2370CAIL2



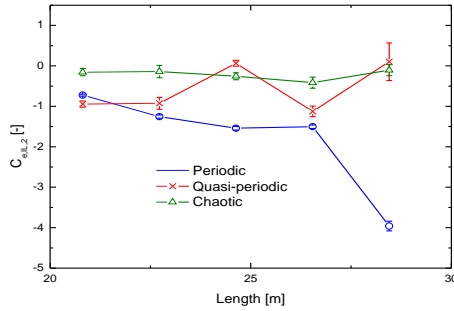
(c) PQC2370CACF3



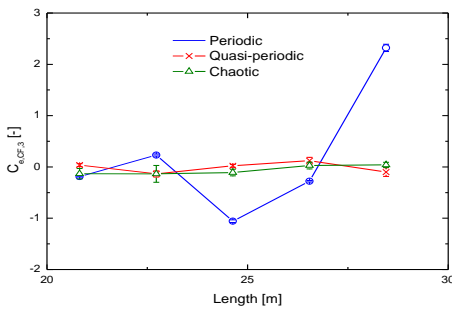
(d) PQC2370CAIL4



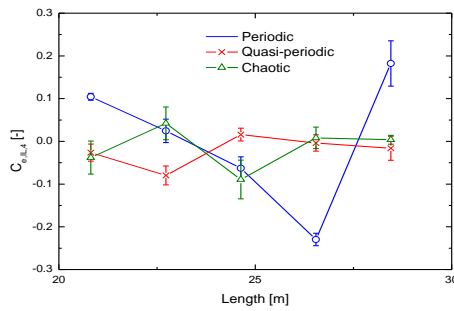
(e) PQC2370CECF1



(f) PQC2370CEIL2



(g) PQC2370CECF3



(h) PQC2370CEIL4

Figure 7.32: Comparison of hydrodynamic coefficients between periodic, quasi-periodic and chaotic orbits, Case 2370.

periodic motion tests shows that results from the flexible beam with quasi-periodic responses in both the IL and CF directions shows that the periodic tests are adequate to obtain satisfactory results. However, the more chaotic the response is, the larger the disagreement between the periodic and non-periodic motion tests is. An alternative might be to apply statistical methods to estimate the fatigue damage due to these responses.

7.3 Numerical simulation results

Both two-dimensional (2D) and three-dimensional (3D) numerical simulations were performed. The methods are described in Chapter 6. The results of the numerical simulations are presented in this section.

7.3.1 Two-dimensional analysis of Case N2030

The hydrodynamic coefficients for six cross sections from NDP uniform case 2030 with a uniform flow were presented in section 7.2.8. To understand the variability of the coefficients, two-dimensional simulations were conducted by using the commercial software FLUENT (*FLUENT 6.3 User's Guide*, 2006). The standard $k - \epsilon$ turbulence model was applied to resolve the Navier-Stokes equations. The dimensionless time step $U \cdot \delta t / D$ was 0.0065 for all simulations. The computational domain and mesh are shown in Figure 6.2a and Figure 6.2b, respectively. The details of the mesh generation and dynamic mesh strategy can be found in section 6.1.1.

Figure 7.33 shows the vortex shedding pattern at typical time instants. The corresponding positions on the orbits are marked with black dots and numbers in Figure 7.21. The notations of the vortex shedding patterns are referred to in Figure 2.4.

In Group 1, A and C have a ‘2P’ vortex shedding pattern, which means that a pair of vortices is shed into the wake during each half cycle. B has a ‘2T’ vortex shedding pattern: in each half cycle, after a pair of vortices has been shed, there is another single vortex shed into the wake. This vortex pattern is linked to the large higher order motion component in the IL direction for these cases; see Figure 7.21. The result shows large higher order dynamic force components both in the CF and IL directions (see Table 7.2).

In Group 2, D has a ‘P+T’ vortex shedding mode. When the cylinder moves downwards, a pair of vortices is shed into the wake, while 3 vortices are shed when the cylinder moves upwards. E has a ‘2T’ vortex pattern, which is also the case for F. In this group, a strong higher order component in the IL direction is observed, which induces the larger dynamic force components at ω_3 in the CF direction and at ω_6 in the IL direction.

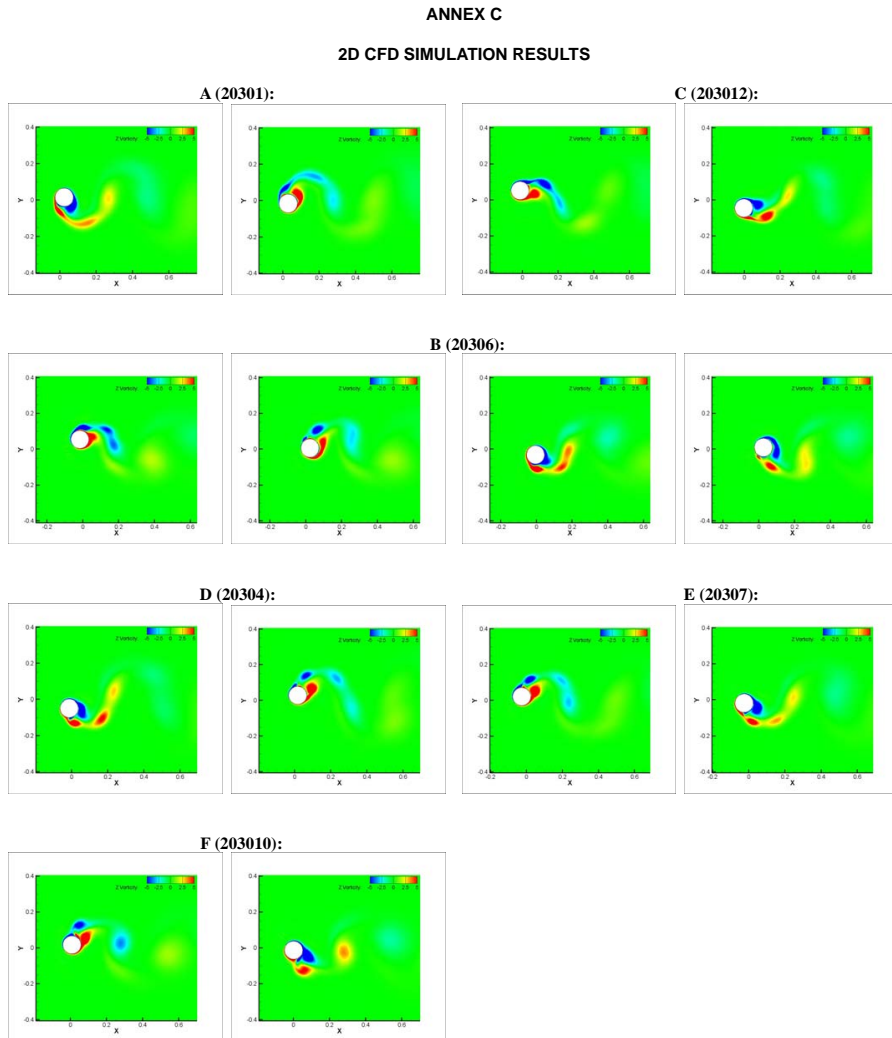


Figure 7.33: Vorticity contour plots of six cross sections of NDP 2030.

7.3.2 3D analysis of harmonic ‘Figure 8’ orbits

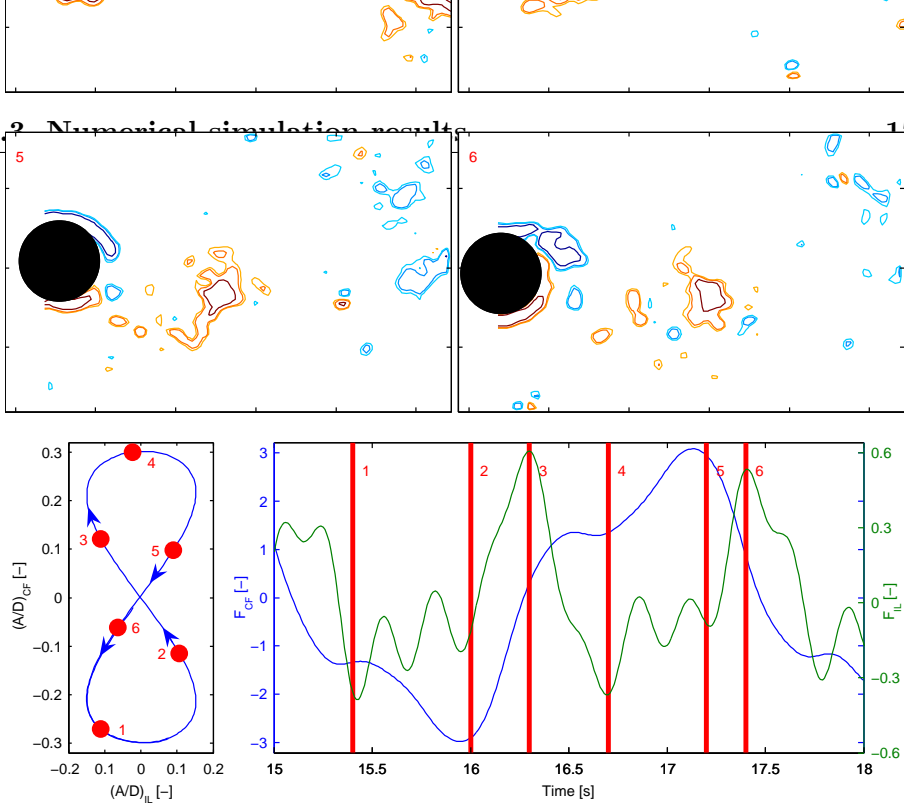
Two ‘figure 8’ orbits with phase angles of 0 and 180 degrees were compared by Aronsen (2007), and the hydrodynamic force coefficients were found to be different for these two orbits with opposite directions. Huang et al. (2009) performed a 3D LES simulation of these two cases, using a method that was the basis for the present study. In this section, the hydrodynamic forces obtained from these three studies are presented and discussed.

$\theta = 0^\circ$

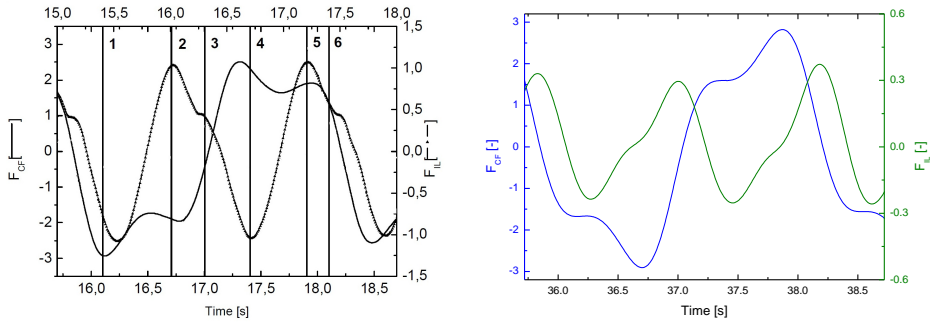
The ‘figure 8’ orbit with phase angle 0 and the corresponding hydrodynamic forces measured by Aronsen (2007) are shown in Figure 7.34a. His PIV results show that $\theta = 0^\circ$ case has a ‘2C’ vortex shedding mode. In Figure 7.34b, the hydrodynamic force in the CF direction is seen to have the same magnitude as that obtained experimentally, but the force in the IL direction is significantly higher than the corresponding experimental result. Figure 7.34c shows the numerical results from the present study. The hydrodynamic force in the CF direction is modelled very well, but the IL force is slightly smaller than the experimental result. However, the higher order IL hydrodynamic forces are not seen in any of the numerical results. By compare Figure 7.34b and Figure 7.34c, a improvement of numerical results is seen, which is due to denser grid in the span-wise direction of the cylinder.

$\theta = 180^\circ$

The ‘figure 8’ orbit with phase angle 180 and the corresponding hydrodynamic forces measured by Aronsen (2007) are shown in Figure 7.35a. His PIV results show that $\theta = 0^\circ$ case has a ‘2T’ vortex shedding mode. The results obtained by Huang et al. (2009) also correspond well with the experimental results, except for the higher order IL hydrodynamic forces (see Figure 7.35b). Figure 7.34c shows that within each half cycle, the first peak of the CF hydrodynamic force becomes even higher than the second peak value. In contrast to experimental results, the higher order IL forces present do not appear in present numerical study.

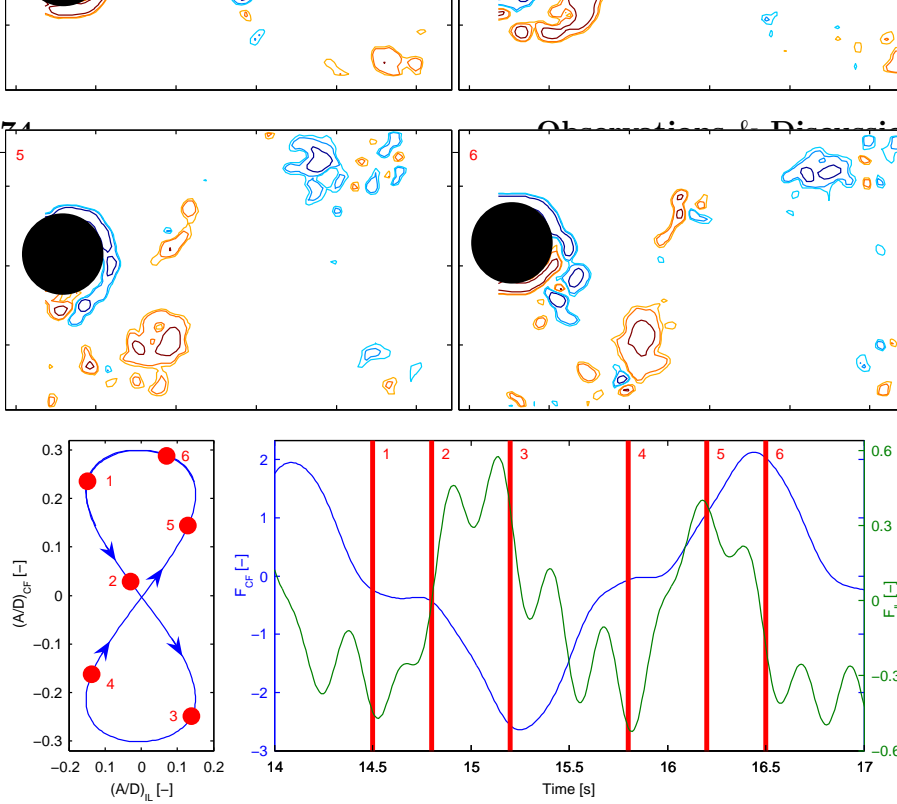


(a) Experimental measurements from Aronsen (2007).
 Figure 8.11: PIV results for $\alpha=0$, $J_{CF}=0.163$ and $(A/D)_{CF}=0.3$.

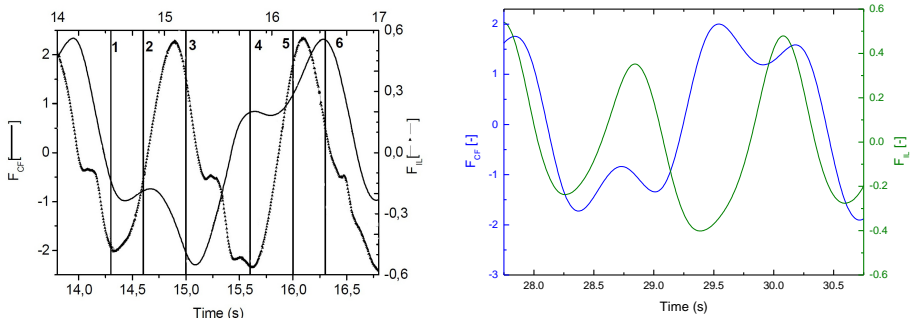


(b) Numerical results from Huang et al. (2009). (c) Numerical results from this study.

Figure 7.34: Comparison of hydrodynamic forces between experimental measurement, previous numerical results and present numerical results, $\theta = 0^\circ$, $Re = 24000$, $\hat{f} = 0.163$, $(A/D)_{CF} = 0.3$, $(A/D)_{IL} = 0.15$, current from the left to the right.



(a) Experimental measurements from Aronsen (2007).
Figure 8.12: PIV results for $\alpha=180$, $J_{CF}=0.163$ and $(A/D)_{CF}=0.3$.



(b) Numerical results from Huang et al. (2009). (c) Numerical results from this study.

Figure 7.35: Comparison of hydrodynamic forces between experimental measurement, previous numerical results and present numerical results, $\theta = 180^\circ$, $Re = 24000$, $\hat{f} = 0.163$, $(A/D)_{CF} = 0.3$, $(A/D)_{IL} = 0.15$, current from the left to the right.

7.3.3 3D simulation of Case N2340: Drag coefficients

The drag coefficients calculated from the IL forces of the 3D CFD simulations were compared with the experiment results; see Figure 7.36 and Figure 7.37. The drag coefficients are plotted against Re . Most of the CFD results match the experimental results. The experimental results also show that, as Re decreases, the uncertainty of the drag coefficient increases.

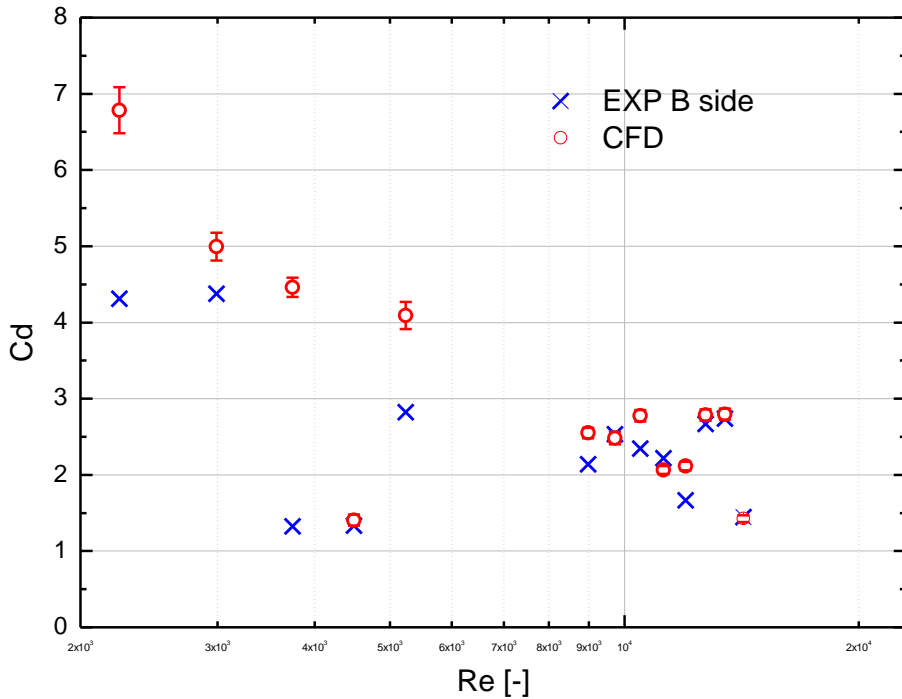


Figure 7.36: Drag coefficients vs Reynolds number, both experimental and numerical results of Case N2340.

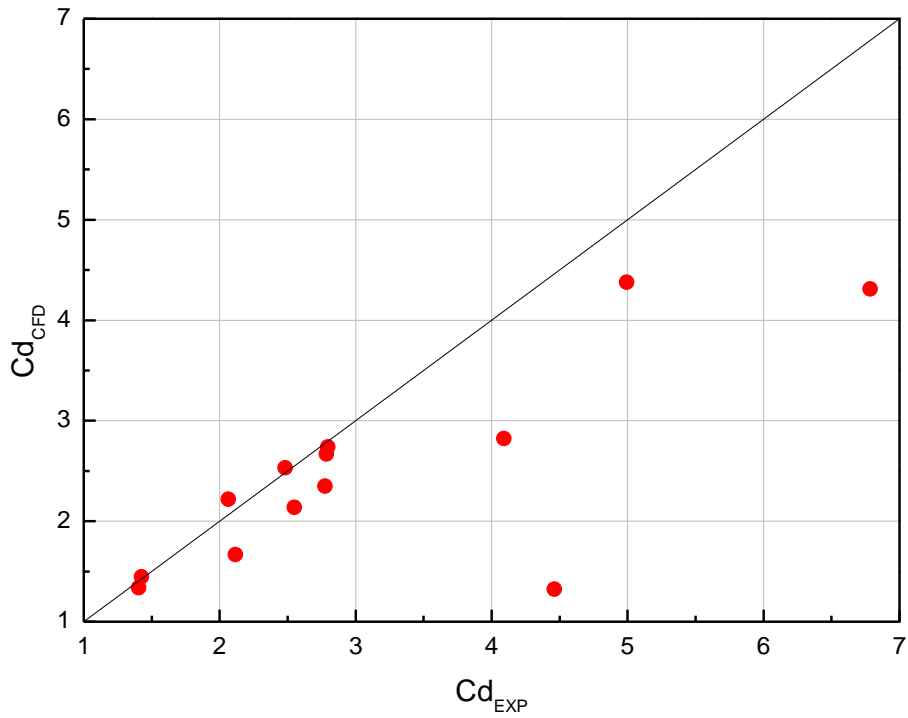


Figure 7.37: Comparison of drag coefficients between forced motion experiments and CFD simulation, selected cases of 2340.

7.3.4 3D simulation of Case N2340: Vortex shedding modes contour plot

Numerical simulations using LES were performed for 19 selected cross sections of Case N2340. The key parameters of cross sectional orbits are listed in Table 7.3.

There has so far been no systematic comparison between results from 3D LES simulations and the experiments for the combined IL and CF forced motion tests. Based on the pure CF controlled harmonic forced motion tests, Morse and Williamson (2009) published vortex shedding mode contour plots, such as Figure 2.15. This study attempts to relate the current numerical simulations and the experimental results to this contour plot.

Table 7.3: Key parameters of 19 cross sectional orbits of Case N2340.

NO.	λ^*	Re	$\frac{A_{CF,max}}{D}$	$\frac{A_{IL,max}}{D}$	$\frac{A_{CF,1}}{D}$	$\frac{A_{IL,2}}{D}$
23401	7.82	14222	0.521	0.235	0.456	0.138
23402	7.47	13470	0.696	0.289	0.700	0.213
23403	7.20	12721	0.655	0.288	0.642	0.199
23404	6.78	11983	0.577	0.163	0.497	0.071
23405	6.15	11223	0.531	0.304	0.513	0.155
23406	5.84	10477	0.749	0.365	0.567	0.213
23407	5.30	9730	0.690	0.232	0.651	0.060
23408	5.05	8981	0.876	0.328	0.764	0.189
23409	4.65	8236	0.785	0.268	0.679	0.210
234010	4.12	7483	0.517	0.141	0.473	0.057
234011	3.72	6737	0.720	0.422	0.650	0.205
234012	3.33	5986	0.820	0.340	0.838	0.078
234013	2.87	5237	0.771	0.328	0.712	0.108
234014	2.52	4493	0.472	0.340	0.429	0.152
234015	2.00	3745	0.389	0.163	0.384	0.016
234016	1.69	2991	0.708	0.336	0.609	0.155
234017	1.26	2244	0.698	0.307	0.702	0.091
234018	0.82	1499	0.593	0.299	0.604	0.090
234019	0.41	748	0.396	0.286	0.357	0.130

λ^* , normalized wavelength, $\frac{\lambda}{D} = \frac{U}{f_{osc}D}$.

To illustrate how the vortex shedding pattern may influence the forces found in the present CFD analyses, the following attempt was made: regardless

of the IL displacement component, the CF amplitude ratios of 19 orbits from Case N2340 are plotted in the same way as in Figure 2.15; see Figure 7.38. It is important to mention that neglecting IL components is a great simplification because the influence of the IL component is significant. This situation was discussed in section 7.2.8. However, there is no contour plot similar to Figure 2.15, which relates the vortex shedding modes with the amplitude ratio and the non-dimensional wavelength, except for the pure CF forced motion experiments in Morse and Williamson (2009).

In addition to the IL amplitude component, Re is another factor that must be considered. Case 2340 is a shear flow case, where Re decreases from section 1 to 19. Figure 2.15 has a unique Re of 12000, and Morse and Williamson (2009) also made a similar plot with $Re = 4000$. They suggested that ‘*the same general conclusions made in their paper remain valid over a whole range of the Reynolds number*’.

7.3.5 3D simulation of Case N2340: Comparison of force time histories

Figure 7.39 to Figure 7.45 show the comparison between the total hydrodynamic force according to experimental measurements and CFD simulations. The comparison in the CF and IL directions are shown in two figures for each case. The non-dimensional displacement and the hydrodynamic forces are plotted for three oscillation cycles. The orbits of these cases can be found in Figure B.6 (Appendix B).

A comparison between the experimental results and the numerical simulation is shown in Figure 7.39. Both the CF and IL hydrodynamic forces are in phase with the displacements, which tells that the excitation force is much smaller than the force linked to added mass, and that added mass is negative. The force amplitudes measured in the experiment are slightly higher than that found in the simulation.

The comparisons of cases N23402 and N23403 are shown in Figure 7.40 and Figure 7.41, respectively. Both cases have distinct CF and IL displacements at primary frequencies without large higher order components. There is a small phase lag between the displacement and the hydrodynamic force in the CF direction. A generally good comparison between the experiment and the simulation is observed. In the IL direction, the force is almost in anti-phase with the displacement, but it seems that the numerical simula-

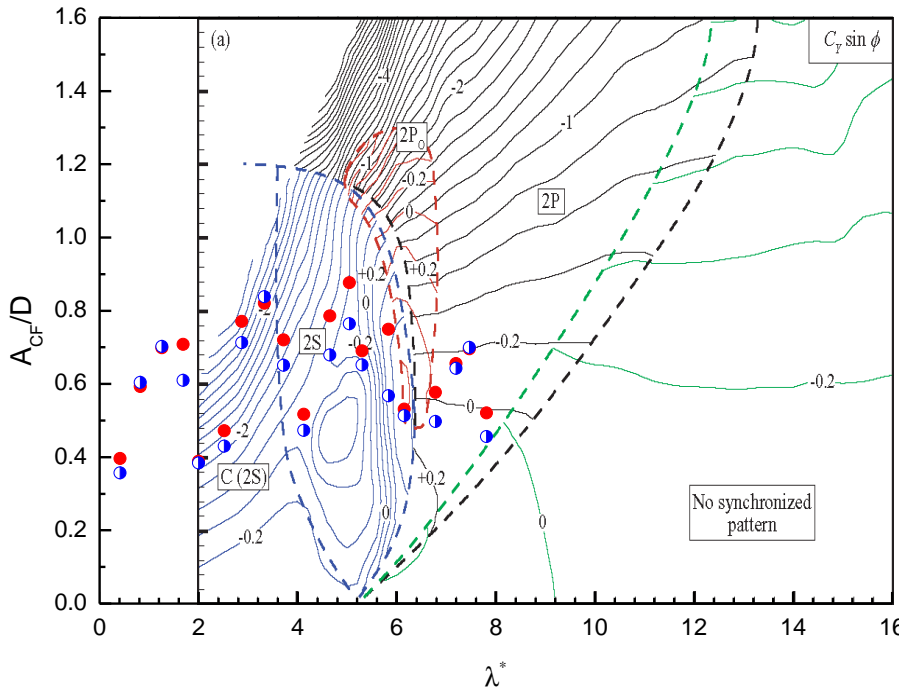


Figure 7.38: Maps of vortex shedding patterns, pure CF tests Morse and Williamson (2009); total and primary CF amplitude ratios of Case N2340 from present study, see Table 7.3. ●: total CF amplitude ratio; ●: primary CF amplitude ratio.

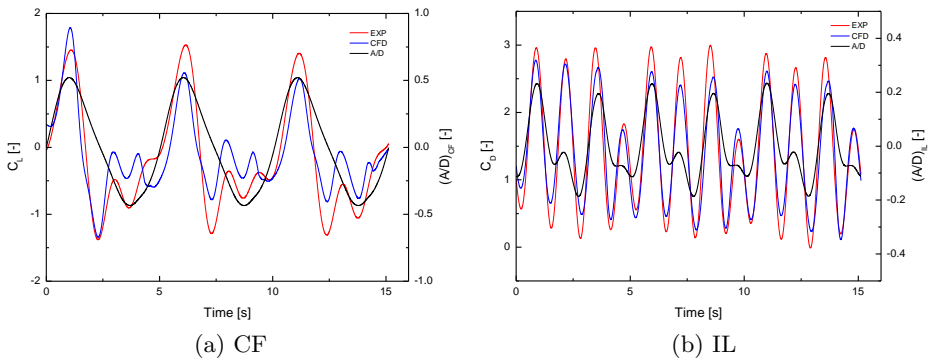


Figure 7.39: Hydrodynamic force comparison, Case N23401.

tion fails to quantify the higher order force components for both cases; see Figures 7.40b and 7.41b.

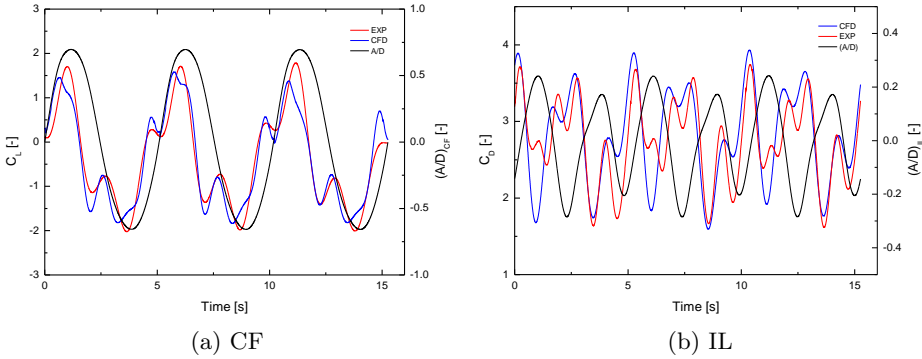


Figure 7.40: Hydrodynamic force comparison, Case N23402.

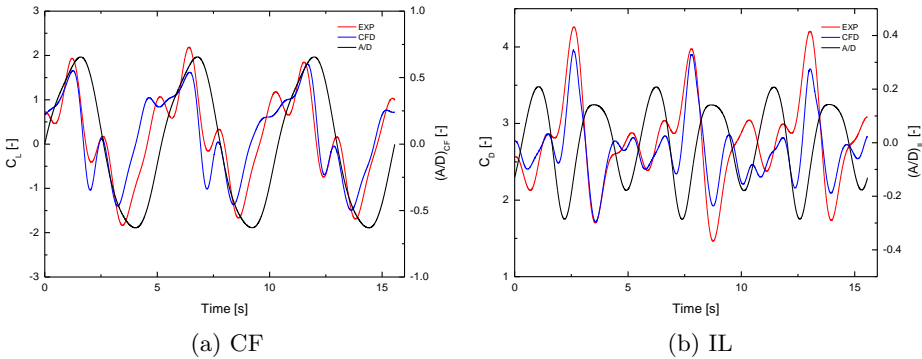


Figure 7.41: Hydrodynamic force comparison, Case N23403.

A mismatch between the experiment and the numerical simulation for Case N23404 is shown in Figure 7.42, especially in the CF direction; see Figure 7.42a. The hydrodynamic forces calculated from CFD are much smaller than the experimental measurements. According to Figure 7.38, case 23404 has $\lambda^* = 6.78$ and $\frac{A}{D_{max}} = 0.577$ and is located close to the boundary between the 2P and $2P_O$ vortex shedding modes. It might be the case that the experiment has a 2P mode and the CFD simulation has $2P_O$ modes or vice versa, in which ‘*the secondary vortex in each pair is much weaker than the*

primary vortex', according to Morse and Williamson (2009). The reason for the mismatch of forces is not obvious.

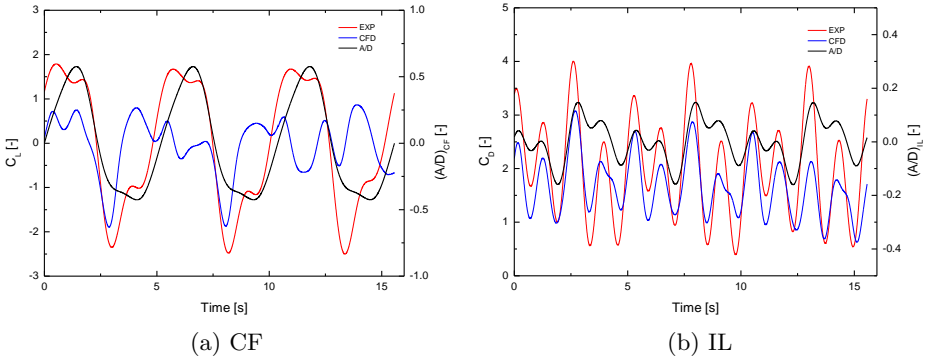


Figure 7.42: Hydrodynamic force comparison, Case N23404.

For case 23406, Figure 7.43a shows a good match in the CF direction. For the IL direction, however, CFD gives much larger IL forces than the experiments, and there is also a phase lag; see Figure 7.43b. According to Figure 7.38, this case has $\lambda^* = 5.84$, and it is also located close to the boundary between the $2P$ and $2P_O$ vortex shedding modes.

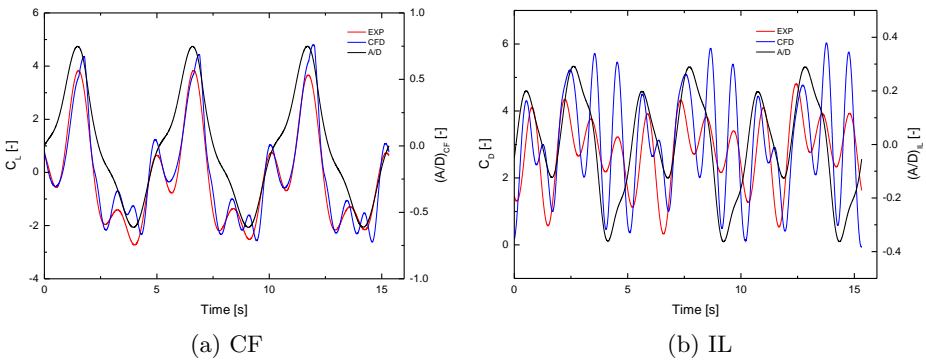


Figure 7.43: Hydrodynamic force comparison, Case N23406.

Case N234010: The hydrodynamic forces predicted by CFD are in good agreement with the experimental measurements; see Figure 7.44. A detailed discussion is in section 7.3.6.

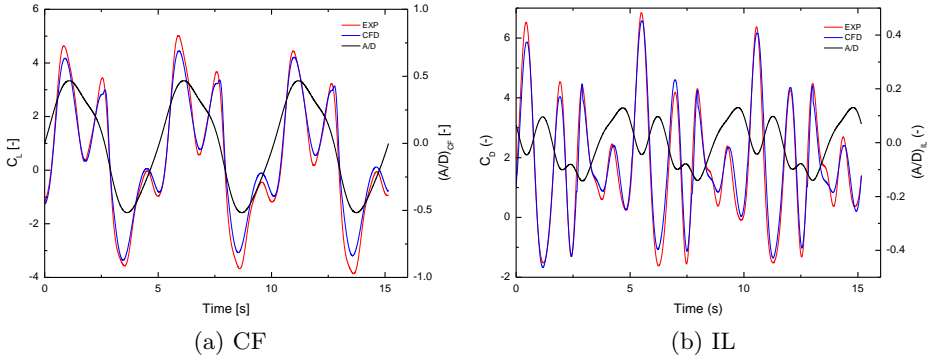


Figure 7.44: Hydrodynamic force comparison, Case N234010.

Cases N234015 to N234019 are the last five cross sections along the pipe, which have the lowest velocities (Re) and smallest normalised wave length λ^* ; see Table 7.3 and Figure 7.38. The hydrodynamic force comparison for Case 234015 is shown in Figure 7.45. Comparisons for Cases N234016 to N234019 are shown in Appendix G. In general, for these low Re cases (780 to 4000), the CFD simulation yields forces that are in agreement with the results from the experiments except for the IL force of Case N234019 (see Figure G.8b in Appendix G).

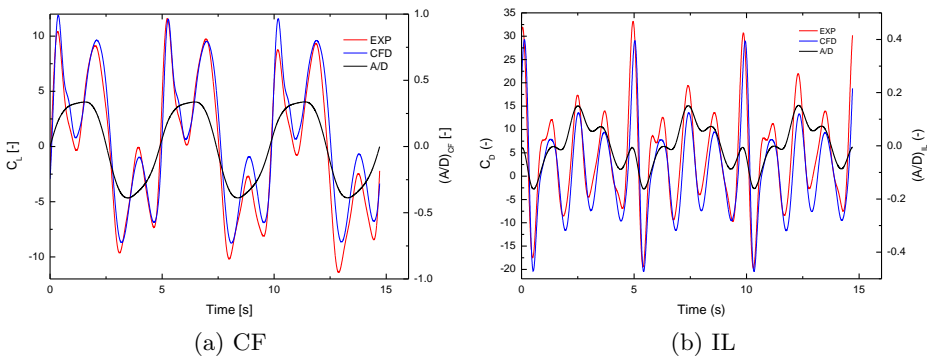


Figure 7.45: Hydrodynamic force comparison, Case N234015.

7.3.6 3D simulation of Case N2340: Transient z vorticity

In this section, the time history of hydrodynamic forces and the normalised displacement are shown in Figures 7.46, 7.49 and 7.52, respectively. Time instances for vorticity pictures are also included.

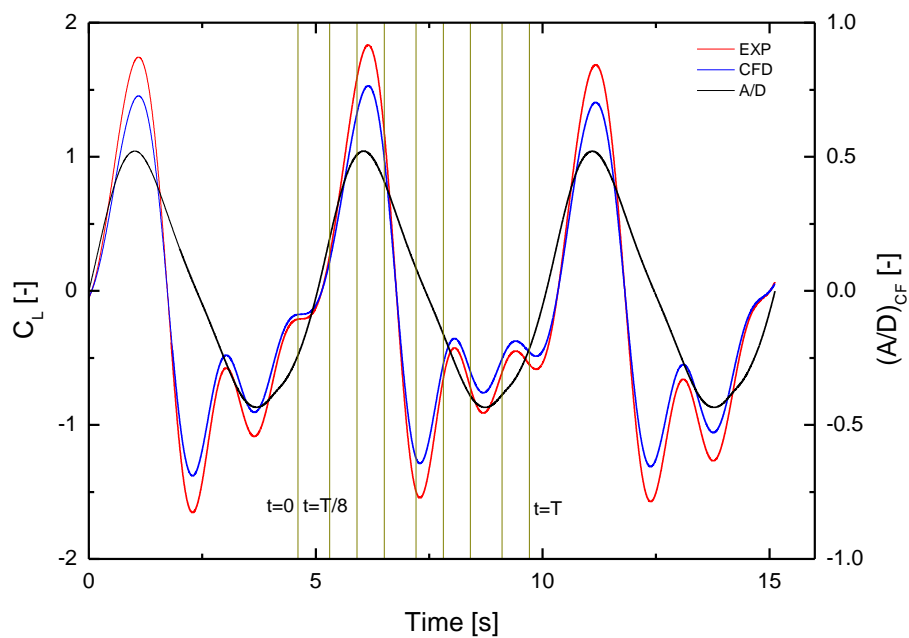
The 3D vorticity iso-surfaces in the z direction for cases N23401, N23405 and N234010 are presented. Figures 7.47, 7.48, 7.50, 7.51, 7.53, and 7.54 show the vorticity iso-surfaces behind the oscillating cylinder at the nine time instances during one complete oscillating cycle. The orbits and the positions of the cylinder along the orbits at the actual time instances are also shown in the figures.

N23401

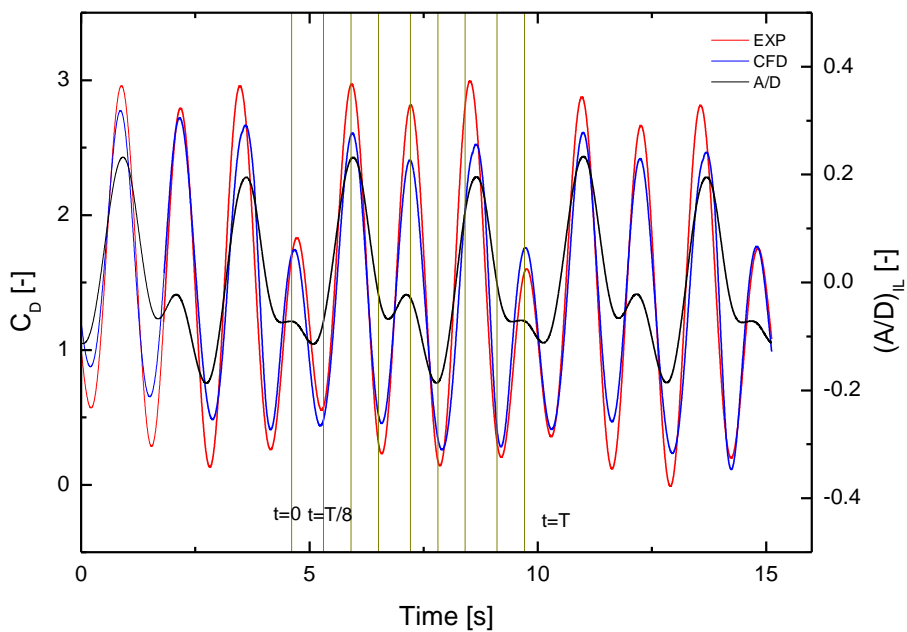
Case N23401 has $\lambda^* = 7.82$ and $Re=14222$, which is in the sub-critical regime (see Table 7.3). From Figure 7.38 it is seen that this case is located close to the lower boundary of ‘2P’ vortex shedding region.

The hydrodynamic forces are in phase with motions in both the IL and CF directions, see Figure 7.46. Numerical results are slightly smaller than experimental results.

Figure 7.47 shows strong 3D effect along the cylinder: the vortices shed in the first half oscillation cycle are very disordered, vortices with opposite directions couple with each other. However, in the second half cycle, distinct vortex tube is seen in Figure 7.48, but the vortex shedding mode is difficult to identify.



(a) CF



(b) IL

Figure 7.46: Comparison of hydrodynamic forces, Case N20301.

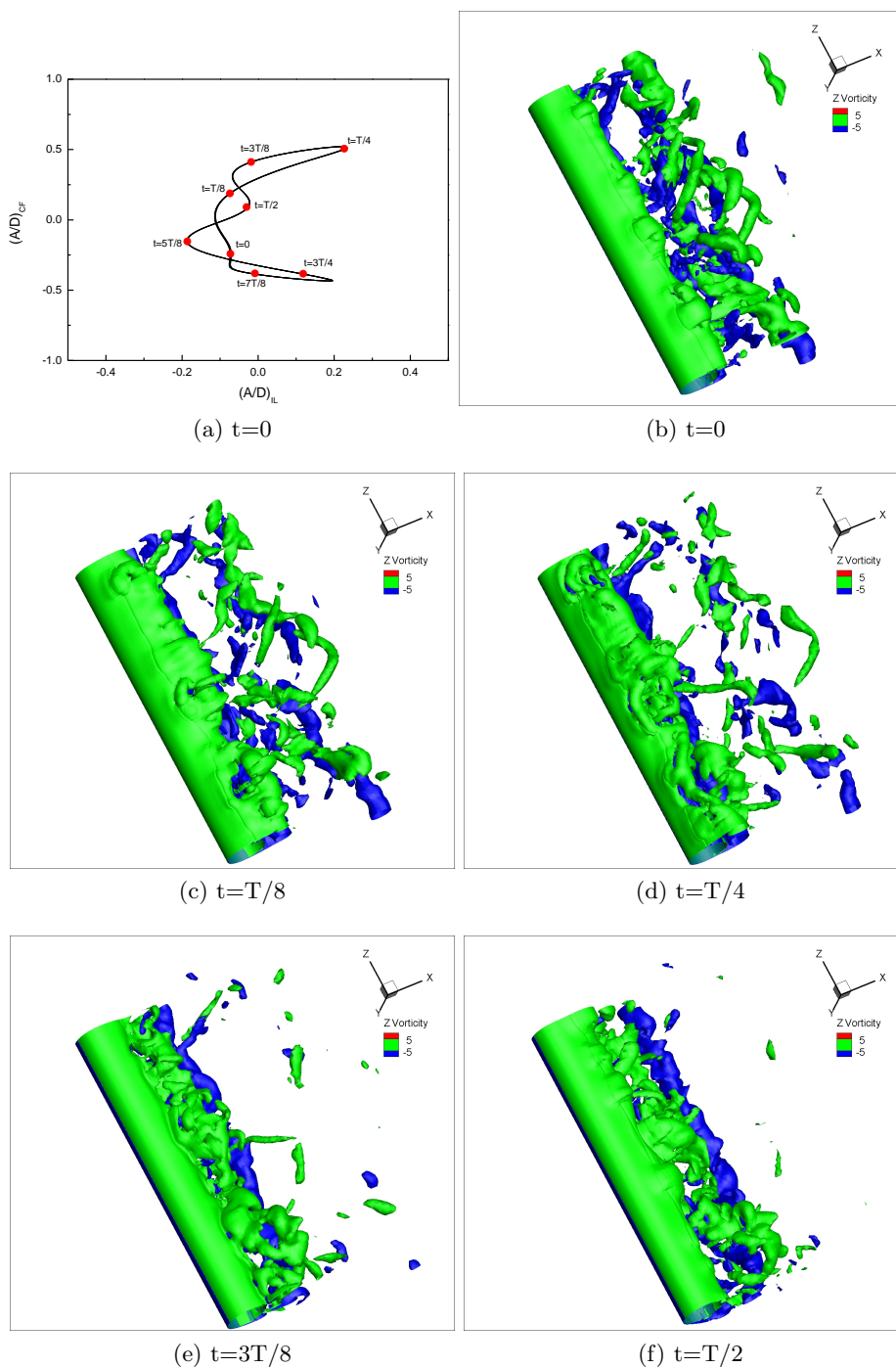


Figure 7.47: N23401 3D simulation (1).

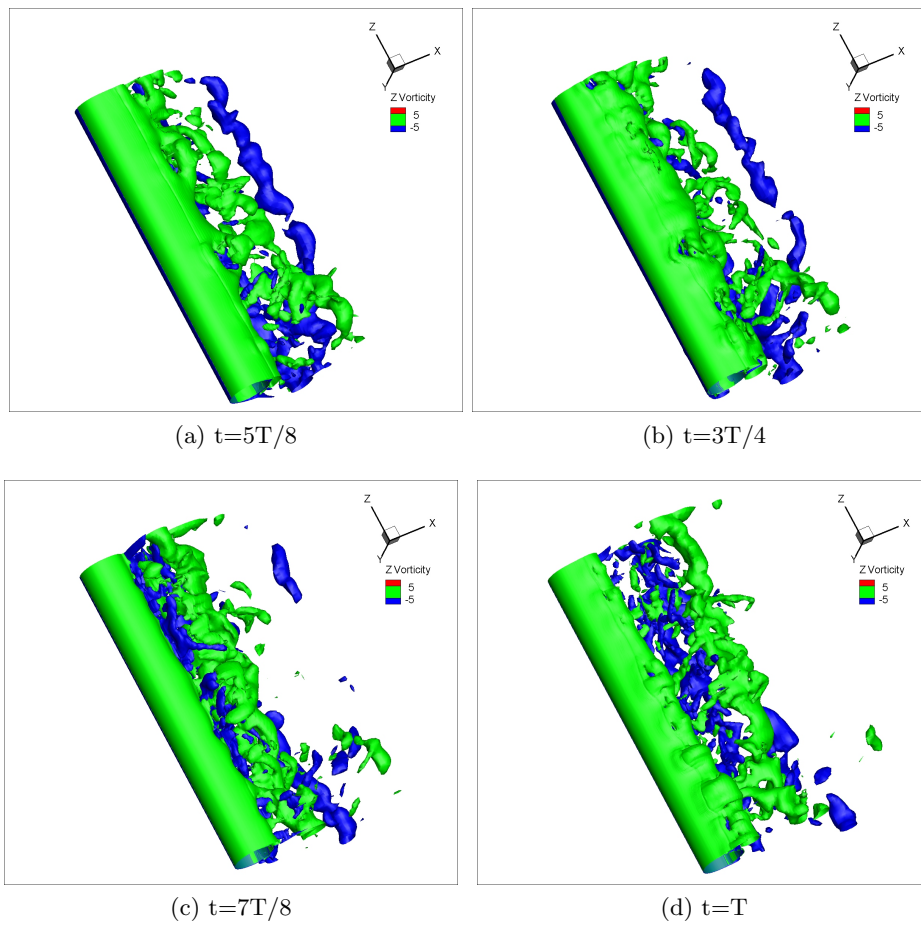


Figure 7.48: N23401 3D simulation (2).

N23405

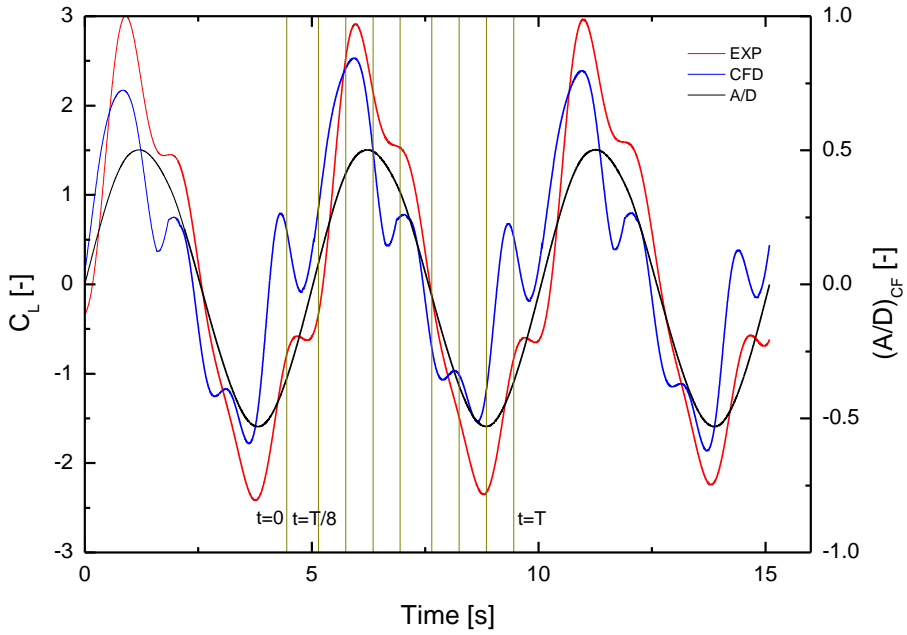
Case N23405 has $\lambda^* = 6.15$ and $\text{Re}=11223$, which is in the sub-critical regime (see Table 7.3). It is in the left boundary of the ‘ $2P_O$ ’ vortex shedding region in Figure 7.38.

The hydrodynamic forces presented in Figure 7.49 are roughly in phase with the displacements. In the CF direction, the hydrodynamic force calculated numerically is slightly lower than the experimental result, and the higher order force is significantly stronger than the experimental results. In the IL direction, the hydrodynamic force are modelled well.

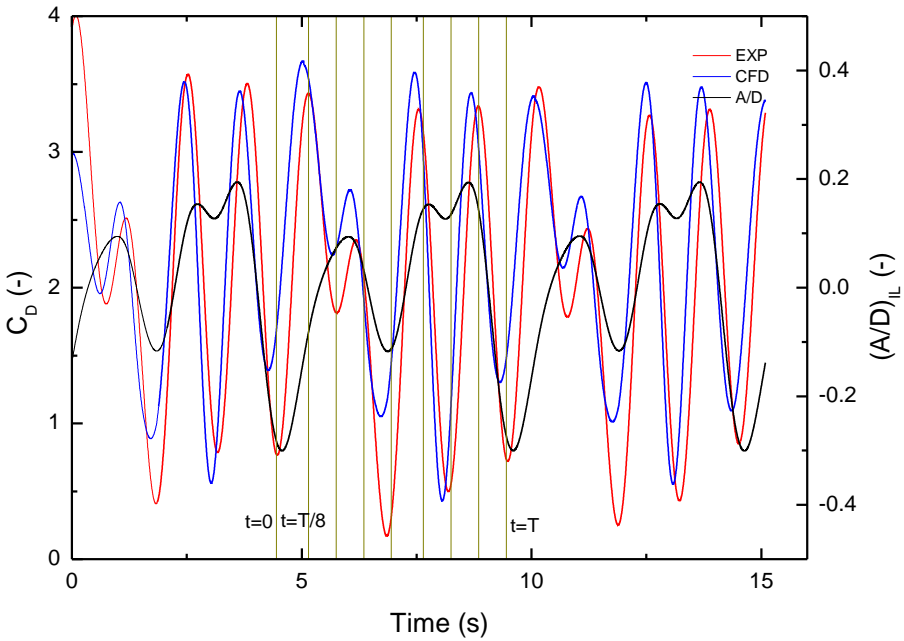
At $t = 0$, one green vortex tube (clockwise) is nearly dissipated, and one blue vortex tube (anti-clockwise) reaches a maximum magnitude, one clockwise vortex tube appears (see Figure 7.50b). From $t = T/8$ to $T/2$, the anti-clockwise vortex tube dissipates, the clockwise vortex tube develops, and another vortex tube in the same direction appears (see Figure 7.50).

At $t = 5T/8$, two anti-clockwise vortex tubes develop and shed into the wake. The tubes couple together, and one of them dissipates rather quickly (see Figure 7.51a). At $t = T$, a vortex tube in the clockwise direction begins to shed into the wake (see Figure 7.51d).

In each half cycle, there appears to be a triplet of vortices shed into the wake, and the vortex shedding mode is close ‘2T’.



(a) CF



(b) IL

Figure 7.49: Comparison of hydrodynamic forces, Case N20305.

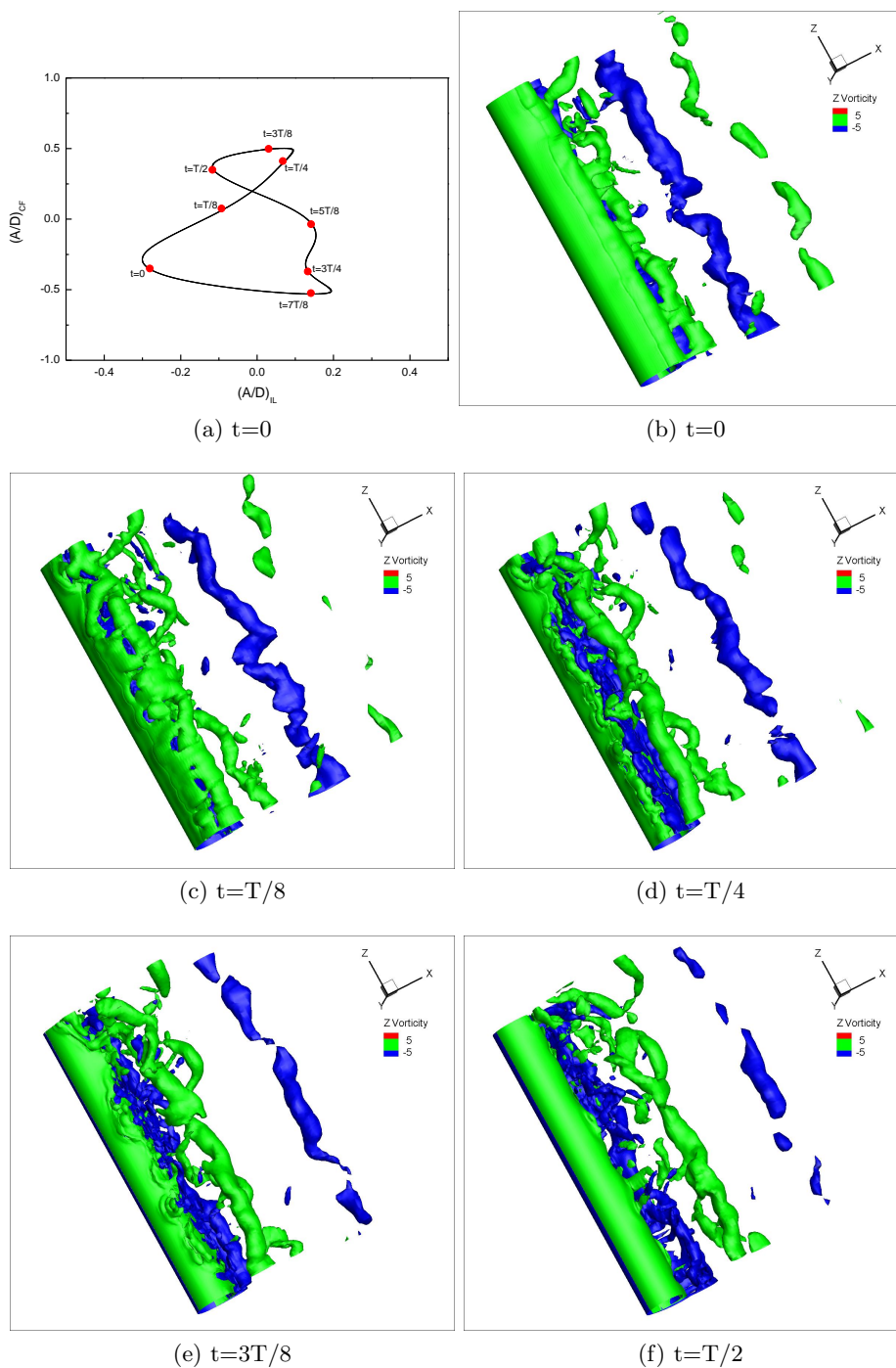


Figure 7.50: N23405 3D simulation (1).

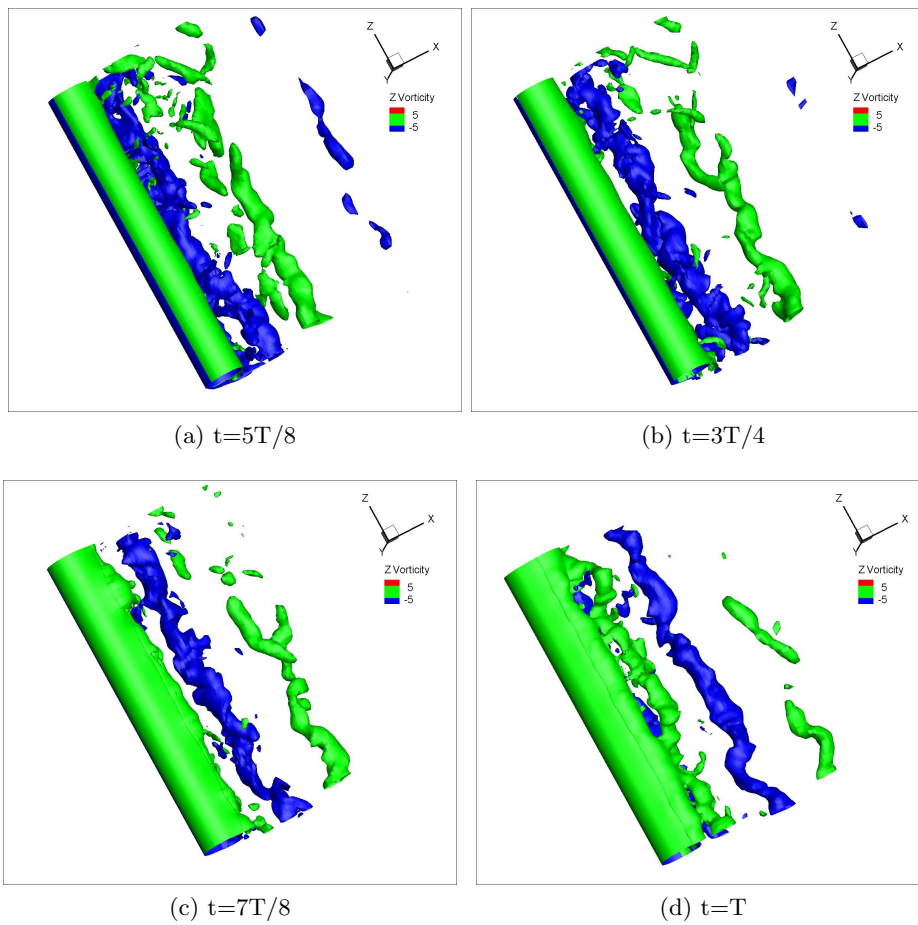


Figure 7.51: N23405 3D simulation (2).

N234010

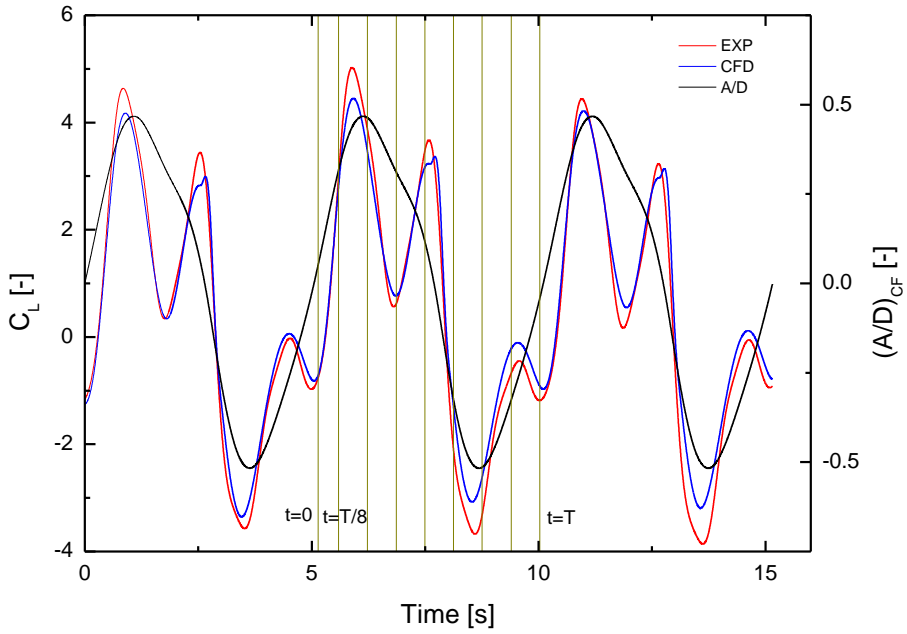
Case N234010 has $\lambda^* = 4.12$ and $Re=7483$, which is also in the sub-critical regime (see Table 7.3). Figure 7.38 shows that it is in the ‘2S’ vortex shedding region.

The hydrodynamic forces predicted numerically are compared with experimental results (see Figure 7.52). It shows that numerical results are in good agreement with the experimental results for this case. In the CF direction, hydrodynamic force has two peaks in each half cycle.

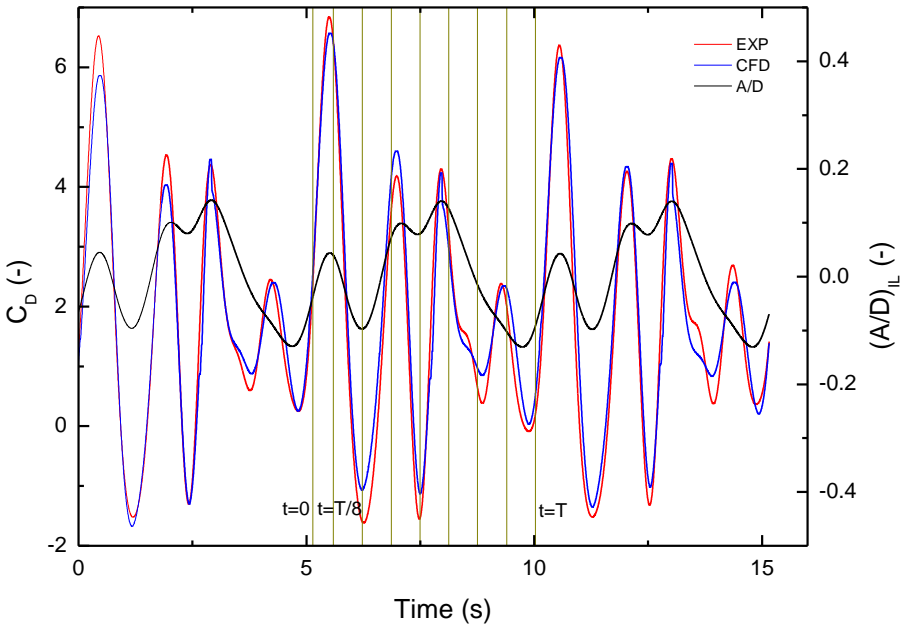
A large number of small scale vortices is seen in Figure 7.53 and 7.54. Strong 3D effect is shown along the cylinder, see the curved vortex tube marked with green colour.

Figure 7.53 shows the vortex shedding process of the first half cycle. The curved clockwise vortex tube loses its energy, following by a vortex tube with opposite sign; another clockwise vortex tube forms and sheds into the wake, all three vortex tubes forms a triplet. In Figure 7.53e and 7.53f, a pair of vortex tubes with opposite directions forms just after the first triplet. Then in Figure 7.53, the new-formed clockwise vortex tube dissipates quickly, and another anti-clockwise vortex tube forms and sheds from the cylinder (see Figure 7.54c and 7.54d). So, for this case, the vortex shedding mode is also ‘2T’.

In summary, the hydrodynamic forces predicted numerically are comparable to the experimental results for some Re values and orbits. The identified vortex shedding modes are clearly different from the map of Morse and Williamson (2009), which illustrates the influence of IL motion and higher order CF motion.



(a) CF



(b) IL

Figure 7.52: Comparison of hydrodynamic forces, Case N234010.

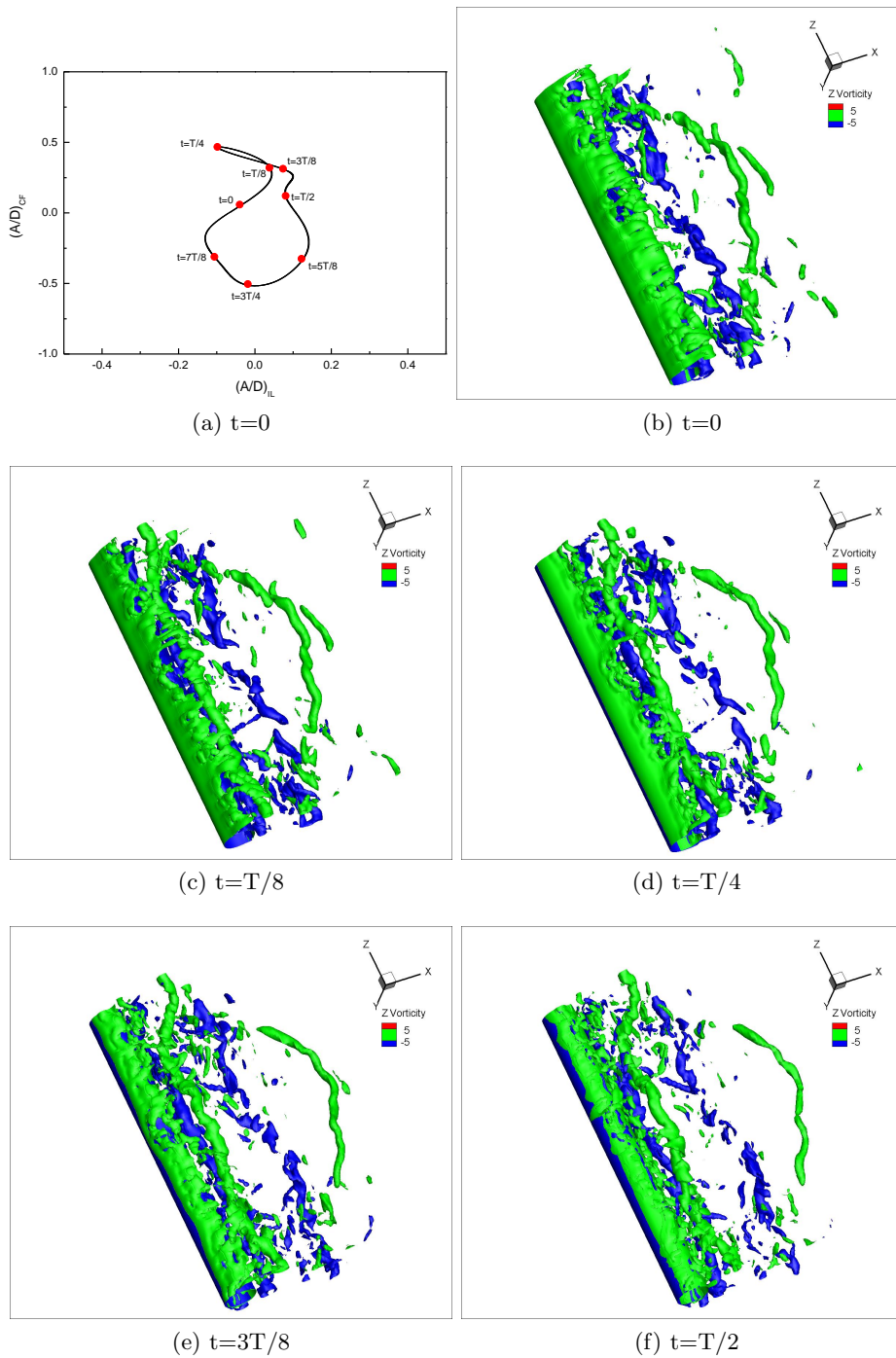


Figure 7.53: N234010 3D simulation (1).

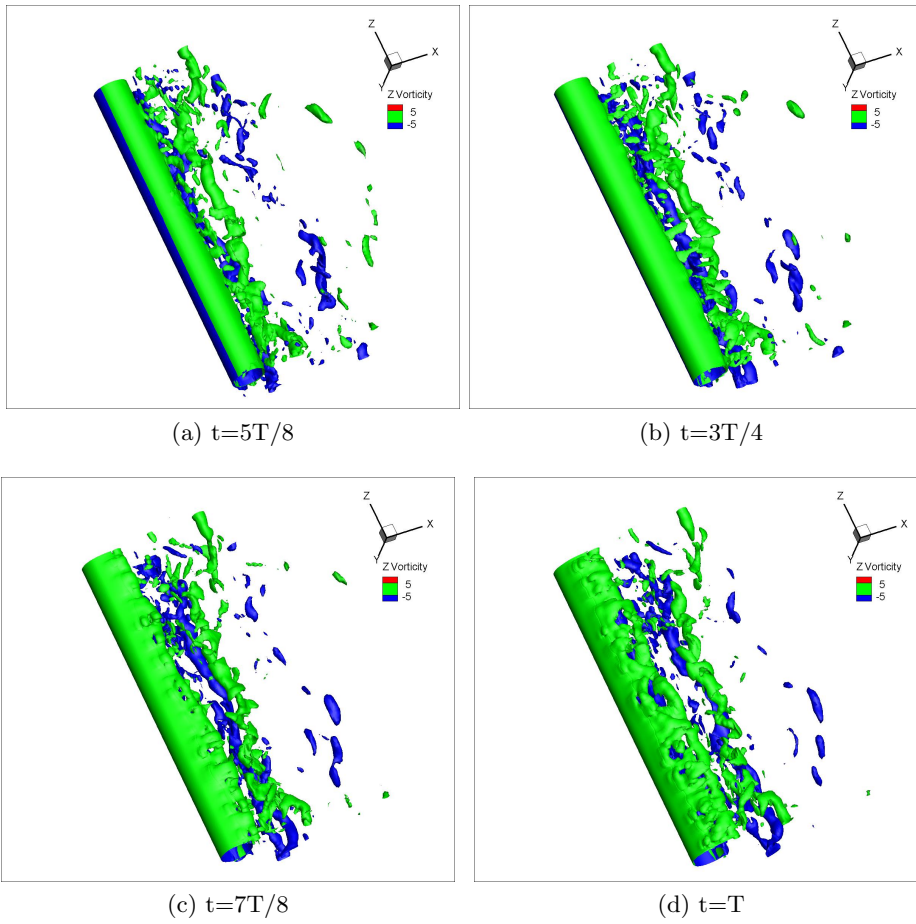


Figure 7.54: N234010 3D simulation (2).

Part V

Conclusions & Future work

Chapter 8

Conclusions

8.1 Principle Contributions

8.1.1 Forced motion experiments

A series of forced motion experiments were conducted in MCLab of NTNU, Trondheim. In addition to conventional harmonic motions, periodic, non-harmonic motions and measured motions were used in the experiment.

The periodic motions were taken from cross sections of a flexible pipe in NDP high mode VIV test:

- Periodic orbits were achieved from two successive cycles of measured motions based on a set of weighted points. For quasi-periodic responses, the periodic orbits can be considered representative of the responses within a certain time window.
- The existing response type classification has been made from the pure CF response. A more detail classification was performed for the combined IL and CF VIV response.

An uncertainty analysis of the experiment and data processing was performed to investigate the validity of the final results.

Periodic motion tests

Hydrodynamic coefficients were calculated from experiments using forced motions of a rigid cylinder section. The general trend of the coefficients for the CF components is similar to the results of the pure CF tests, while a comparison of the IL coefficients and the results of the pure IL tests indicate

that the pure IL response is significantly different from the response for IL in combination with CF. Both response amplitudes and coefficients are significantly greater in the combined case than in the pure IL case.

Periodic motion tests: Sheared flow cases

The IL motion component is a crucial factor affecting the force from vortex shedding, and higher order displacements are often larger in IL direction than in CF direction.

Higher order IL motion components were observed to cause larger higher order hydrodynamic forces in both the IL and CF directions.

Observed motion tests

An experimental method with forced natural orbits has been applied to a set of cases where the orbits are found from a flexible beam test with uniform and sheared currents.

Selected combined IL and CF response types were presented and discussed. Responses with IL amplitude modulation were investigated, and it was observed that the IL amplitude modulation can introduce higher order hydrodynamic forces in the CF direction.

The following conclusions can be made by comparing the hydrodynamic coefficients:

- Periodic orbits can be used to represent time-varying orbits when the responses are quasi-periodic (Type-I).
- When the responses are partly or fully chaotic, hydrodynamic coefficients calculated from tests with selected periodic orbits have larger uncertainty or fail to represent the entire time history.
- In general, higher order hydrodynamic coefficients have larger uncertainties than the primary frequency.

In general, hydrodynamic coefficients based on harmonic orbits will fail to describe forces on cross sections with observed orbits, particularly for the excitation coefficient in the CF direction.

Periodic orbit results can be used to predict excitation coefficients instead of the true time history oscillation to a certain extent. The added mass

coefficients obtained from these two methods differ significantly.

The present study will enrich the database of empirical models, particularly for improving our understanding of the interactions between the IL and CF responses and for quantifying the significance of higher order frequency components.

This thesis presents results in terms of coefficients, but to date, it has not been possible to find general trends between actual parameters that could help to establish an empirical model for the combined IL and CF response or higher order response components. Further testing and analysis of the results from this work should be performed to improve empirical methods used in VIV analyses.

8.1.2 2D and 3D CFD simulation

2D simulation

2-D CFD analyses were performed to identify the vortex shedding patterns for orbits of six cross sections from a pipe under uniform current. The results showed that the observed force components are clearly linked to vortex shedding patterns. The combined use of observed orbits and CFD analyses can help us to better understand VIV and the appearance of higher order force components in particular.

3D simulation

3D CFD analyses were performed for a oscillating rigid cylinder under uniform current, the orbits are from cross sections of a flexible pipe subject to sheared current, and the LES method was applied through a large Re variation. The simulated hydrodynamic forces corresponded well with the experimental results. The 3D vortex shedding modes are different from pure CF forced motion, which emphasis the importance of the IL motion and higher order displacements.

In some cases, there were large discrepancies, which can be attributed to the model optimisation, Re dependence, vortex shedding mode transition, and orbit shape.

The present study attempts, for the first time, to make a comparison of this type of experiment for engineering purpose. The preliminary results

encourage further research on this topic.

8.2 Recommendations for Future Work

Due to the limitations of the laboratory equipment, some cases could not be investigated. Upgrading of the equipment might be carried out in the future in order to conduct forced motion tests with higher Re number, large oscillation amplitude and frequency. In addition, longer length of the towing tank can increase the number of effective oscillation cycles for observed motion tests.

Particle Imaging Velocimetry (PIV) equipment should be applied more often for selected cases of the forced motion tests. These pictures will give detailed information of the vortex shedding pattern behind the cylinder. The same cases will also be analysed by use of numerical methods, PIV results can be used to calibrate CFD simulation. This effort will give valuable information about the vortex shedding process and also about the capability of numerical methods to handle VIV problems.

More effort should be put on CFD optimization. Different CFD models with optimized mesh, time step and turbulence model should be established according to different Re, oscillation amplitude and frequency. A detail validation and verification should be done before large sets of analyses are carried out. Further use of CFD may help to develop empirical models for combined IL and CF response including higher order frequency components.

Systematic parameter studies are recommended to understand the influence from various parameters. The present study applies observed orbits from flexible pipe experiments, so that several parameters are varying simultaneously, which makes it difficult to compare with other research results and identify trends. If any orbit can be described by a set of parameters in a systematic way, then it is much easier to define trends and also apply the results in empirical models.

Time domain solution for the VIV problem can be an alternative, which needs a large database from controlled motion experiments. A good classification of response types and orbits can reduce this work significantly.

Bibliography

(2012), Website: [Last accessed: 19.12.2012].

URL: <http://www.hbm.com>

10th International Ship and Offshore Structures Congress (ISSC) (1988).

8th International Ship and Offshore Structures Congress (ISSC) (1982).

Aarsnes, J. V. and Steen, S. (n.d.), Experimental methods in marine hydrodynamics. Lecture notes.

Adrian, R. J. (1991), ‘Particle imaging techniques for experimental fluid mechanics’, *Annu. Rev. Fluid Mech* **23**, 261–304.

Aglen, I. M. (2012), VIV in Free Span Pipelines, PhD thesis, Norwegian University of Science and Technology.

Al-Jamal, H. and Dalton, C. (2004), ‘Vortex induced vibrations using large eddy simulation at a moderate reynolds number’, *Journal of Fluids and Structures* **19**, 73–92.

Alexander, C. M. (1981), ‘The complex vibrations and implied drag of a long oceanographic wire in cross-flow’, *Ocean Engineering* **8**, 379–406.

ANSYS FLUENT User’s Guide Release 13.0 (2010).

Aronsen, K. H. (2007), An Experimental Investigation of In-line and Combined In-line and Cross-flow Vortex Induced Vibrations, PhD thesis, NTNU.

Atluri, S., Rao, V. and Dalton, C. (2009), ‘A numerical investigation of the near-wake structure in the variable frequency forced oscillation of a circular cylinder’, *Journal of Fluids and Structures* **25**, 229–244.

- Baarholm, G. S., Larsen, C. M. and Lie, H. (2006), 'On fatigue damage accumulation from in-line and cross-flow vortex-induced vibrations on risers', *Journal of Fluids and Structures* **22**, 109–127.
- Bearman, P. W. (1984), 'Vortex shedding from oscillating bluff bodies', *Annu. Rev. Fluid Mech* **16**, 195–222.
- Bearman, P. W. and Currie, I. G. (1979), 'Pressure-fluctuation measurements on an oscillating circular cylinder', *Journal of Fluid Mechanics* **91**, 661–677.
- Bishop, R. and Hassan, A. (1964), 'The lift and drag forces on a circular cylinder oscillating in a flowing fluid'.
- Blevins, R. D. (1990), *Flow-Induced Vibration*, 2 edition edn, Krieger Publishing Company, Kriegerdrive, Florida.
- Braaten, H. and Lie, H. (2005), NDP Riser High Mode VIV Tests - Main Report, Technical report, MARINTEK, Trondheim, Norway.
- Breuer, M. (1998), 'Numerical and modeling influences on large eddy simulations for the flow past a circular cylinder', *International Journal of Heat and Fluid Flow* **19**, 512–521.
- Brika, D. and Laneville, A. (1993), 'Vortex-induced vibration of a long flexible circular cylinder', *Journal of Fluid Mechanics* **250**, 481–508.
- Brunn, H. H. and Davies, P. (1975), 'An experimental investigation of the unsteady pressure forces on a circular cylinder in a turbulent cross flow', *Journal of Sound and Vibration* **40**, 535–559.
- Cao, S., Ozono, S., Tamura, Y., Ge, Y. and Kikugawa, H. (2010), 'Numerical simulation of reynolds number effects on velocity shear flow around a circular cylinder', *Journal of Fluid Structures* **26**, 685–702.
- Carberry, J., Sheridan, J. and Rockwell, D. (2001), 'Forces and wake modes of an oscillating cylinder', *Journal of Fluids and Structures* **15**, 523–532.
- Carberry, J., Sheridan, J. and Rockwell, D. (2005), 'Controlled oscillations of a cylinder: forces and wake modes', *Journal of Fluid Mechanics* **538**, 31–69.
- Catalano, P., Wang, M., Iaccarino, G. and Moin, P. (2003), 'Numerical simulation of the flow around a circular cylinder at high reynolds numbers', *International Journal of Heat and Fluid Flow* **24**, 463–469.

- CeSOS Annual Report* (2011), Technical report, CeSOS.
- Chaplin, J., Bearman, P. W., Cheng, Y., Fontaine, E., Graham, J. M. R., Herfjord, K., Huera-Huarte, F. J., Isherwood, M., Lambrakos, K., Larsen, C. M., Meneghini, J. R., Moe, G., Pattenden, R. J., Triantafyllou, M. S. and Willden, R. H. J. (2005), 'Blind predictions of laboratory measurements of vortex-induced vibrations of a tension riser', *Journal of Fluids and Structures* **21**, 25–40.
- Chasparis, F., Sadeghi, Y., Hover, F. S., Triantafyllou, M. S., Constantinides, Y. and Mukundan, H. (2009), VIV hydrodynamic data extraction from field data, *in* '28th International Conference on Ocean, Offshore and Arctic Engineering'.
- Coleman, H. W. and Steele, W. G. (1999), *Experimentation and Uncertainty Analysis for Engineers*, 2nd edition edn, John Wiley & Sons, Inc.
- Dahl, J. M. (2008), Vortex-Induced Vibration of a Circular Cylinder with Combined In-line and Cross-flow Motion, Doctor of philosophy, Center for Ocean Engineering, Department of Mechanical Engineering, MIT, Webb Institute, Glen Cove, NY, USA.
- Dahl, J. M., Hover, F. S. and Triantafyllou, M. S. (2006), 'Two degree-of-freedom vortex induced vibrations using a force assisted apparatus', *Journal of Fluids and Structures* **22**, 807–818.
- DNV-OS-F201 Dynamic risers* (2010).
- DNV-RP-C205 Environmental conditions and environmental loads* (2009).
- DNV-RP-F105 Free spanning pipelines* (2006).
- Dong, S. and Karniadakis, G. (2005), 'Dns of flow past a stationary and oscillating cylinder at $re=10000$ ', *Journal of Fluids and Structures* **20**, 519–531.
- Drescher, H. (1956), 'Messung der auf querongestromte Zylinder ausgeubten seitlich veranderten Drucke', *Zeitschrift f'ur Flugwissensschaft* **4**, 17–21.
- El Baroudi, M. (1960), Measurement of two-point correlations of velocity near a circular cylinder shedding a karman vortex street, Technical report, University of Toronto Institute of Aerophysics.
- Ersdal, S. (2004), Error analysis of experiments. Lecture note.

- Faltinsen, O. M. (1990), *Sea Loads on Ships and Offshore Structures*, Cambridge University Press.
- Feng, C. (1968), The measurement of vortex induced effects in flow past stationary and oscillating circular and d-section cylinders., Master's thesis, University of British Columbia.
- FLUENT 6.3 User's Guide* (2006).
- Fröhlich, J. and Rodi, W. (2004), 'LES of the flow around a circular cylinder of finite height', *International Journal of Heat and Fluid Flow* **25**, 537–548.
- Gerlach, C. R. and Dodge, F. T. (1970), An engineering approach to tube flow induced vibrations, in 'Flow-Induced Vibrations in Reactor System Components, Argonne National Laboratory', pp. 205–225.
- Gopalkrishnan, R. (1993), Vortex Induced Forces on Oscillating Bluff Cylinders, PhD thesis, MIT, Dep. of Ocean Engineering.
- Grosenbaugh, M. A., Yoerger, D. R., Hover, F. S. and Triantafyllou, M. S. (1991), 'Drag forces and flow-induced vibrations of a long vertical tow cable-part ii: Unsteady towing conditions.', *ASME Journal of Offshore Mechanics and Arctic Engineering* **113**, 199–204.
- Halse, K. H. (1997), On Vortex Shedding and Prediction of Vortex Induced Vibration of Circular Cylinders, PhD thesis, NTNU, Norway.
- Hansen, R. P. and Forsythe, J. (2004), 'A grid convergence study of a highly separated turbulent flow', *Computing in Science and Engineering* .
- Hinze, J. O. (1975), *Turbulence*, McGraw-Hill Publishing Co.
- Huang, Z. Y., Larsen, C. M. and Cui, W. C. (2009), 3-D LES study on a forced oscillating circular cylinder following the figure of eight movement, in 'Hydroelasticity in Marine Technology', University of Southampton, UK.
- Humphreys, J. S. (1960), 'On a circular cylinder in a steady wind at transition reynolds numbers', *Journal of Fluid Mechanics* **9**, 603–612.
- Huse, E. (2004), In-line VIV excitation and mass coefficients, Technical report, MARINTEK.

- Huse, E., Kleiven, G. and Nielsen, F. (1998), Large scale model testing of deep sea risers, *in* ‘Offshore Technology Conference’.
- Iida, A., Otaguro, T., Kato, C. and Fujita, H. (1997), Prediction of aerodynamic sound spectra from a circular cylinder, *in* C. E. o. J. S. of Instrument, ed., ‘5th Triennial International Symposium on Fluid Control, Measurement and Visualization (FLUCOME ‘97)’, Vol. 1, pp. 126–131.
- Jauvtis, N. and Williamson, C. H. K. (2004), ‘The effect of two degrees of freedom on vortex-induced vibration at low mass and damping’, *Journal of Fluid Mechanics* **509**, 23–62.
- Jeon, D. and Gharib, M. (2001), ‘On circular cylinders undergoing two-degree-of-freedom forced motions’, *Journal of Fluids and Structures* **15**, 533–541.
- Johansen, T. (2004), Hydrodynamiske koeffisienter for virvelinduserte svingninger i strømmens retning., Master’s thesis, Norwegian University of Science and Technology.
- Kacker, S. C., Pennington, B. and Hill, R. S. (1974), ‘Fluctuating lift coefficient for a circular cylinder in cross-flow’, *Journal of Mechanical Engineering Science* **16**, 215–224.
- Khalak, A. and Williamson, C. H. K. (1999), ‘Motions, forces and mode transitions in vortex induced vibrations at low mass-damping’, *Journal of Fluid and Structures* **13**, 813–851.
- Kristansen, T. and Lie, H. (2005), NDP Riser High Mode VIV Tests, Modal Analysis, Technical report, MARINTEK.
- Larsen, C. M. (2000), Vortex induced vibration. Lecture notes in NTNU.
- Larsen, C. M. (2007), Marine dynamics. Lecture notes in NTNU.
- Larsen, C. M. (2008), Aspects of marine riser analysis-an incomplete and preliminary collection of lecture notes and papers. Lecture notes in NTNU.
- Larsen, C. M. and Lie, H. (2008), On hydrodynamic coefficients for combined cross-flow and in-line vortex induced vibrations, *in* ‘27th International Conference on Ocean, Offshore and Arctic Engineering’, number OMAE2008-57569, Estoril, Portugal.

- Larsen, C. M., Lie, H., Passano, E., Yttervik, R., Wu, J. and Baarholm, G. (2009), *VIVANA Theory Manual v3.7*, v3.7 edn, MARINTEK.
- Larsen, C. M., Vikestad, K., Yttervik, R. and Passano, E. (2001), Empirical model for analysis of vortex induced vibrations theoretical background and case studies, in '20th International Conference on Ocean, Offshore and Arctic Engineering', number OMAE2001/OFT-1203.
- Larsen, C. M., Yttervik, R. and Aronsen, K. H. (2007), Calculation of in-line vortex induced vibrations of free span pipelines, in 'OMAE'.
- Leehey, P. and Hanson, C. (1971), 'Aeolian tones associated with resonated vibration.', *Journal of Sound and Vibration* **13**, 465–483.
- Lie, H. and Kaasen, K. (2006), 'Modal analysis of measurements from a large-scale viv model test of a riser in linearly sheared flow', *Journal of Fluid and Structures* **22**, 557–575.
- Lie, H., Larsen, C. M. and Vandiver, J. K. (1997), 'Vortex induced vibrations of long marine risers: Model test in a rotating rig', *OMAE* **1-B**, 241–252.
- Mainçon, P. (2010), 'A Wiener-Laguerre model of VIV forces given recent cylinder velocities', *Mathematical Problems in Engineering* .
- Mainçon, P., Barnardo, C. and Larsen, C. M. (2008), VIV force estimation using inverse FEM, in '28th International Conference on Ocean, Offshore and Arctic Engineering', number OMAE2008-57325, Estoril, Portugal.
- Majumdar, S. and Rodi, W. (1985), Numerical calculations of flow past circular cylinder, in 'Proceedings of 3rd Symposium on Numerical and Physical Aspects of Aerodynamic Flows.'
- MCLab Carriage Remote Control User Manual* (2008).
- Mercier, J. (1973), Large Amplitude Oscillations of a Circular Cylinder in a Low-speed Stream, PhD thesis, Stevens Institute of Technology.
- Modarres-Sadeghi, Y., Chasparis, F., Triantafyllou, M. S., Tognarelli, M. and Beynet, P. (2011), 'Chaotic response is a generic feature of vortex-induced vibrations of flexible risers', *Journal of Sound and Vibration* **330**, 2565–2579.
- Modarres-Sadeghi, Y., Mukundan, H., Dahl, J. M., Hover, F. S. and Triantafyllou, M. S. (2010), 'The effect of higher harmonic forces on fatigue life of marine risers', *Journal of Sound and Vibration* **329**, 43–55.

- Moe, G. and Wu, Z. J. (1990), 'The lift force on a cylinder vibrating in a current', *Journal of Offshore Mechanics and Arctic Engineering* **112**, 297–303.
- Morse, T. L. and Williamson, C. H. K. (2009), 'Prediction of vortex-induced vibration response by employing controlled motion.', *Journal of Fluid Mechanics* **634**, 5–39.
- Nielsen, P. (1992), *Costal Bottom Boundary Layers and Sediment Transport*, Vol. 4 of *Advanced Series on Ocean Engineering*, World Scientific.
- Norberg, C. (2003), 'Fluctuating lift on a circular cylinder: review and new measurements', *Journal of Fluids and Structures* **17**, 57–96.
- Novak, M. and Tanaka, H. (1975), Pressure correlations on a vibrating cylinder, in K. J. Eaton, ed., '4th International Conference on Wind Effects on Buildings and Structures', Cambridge University Press, pp. 227–232.
- Ottesen Hansen, N.-E. (1982), Vibrations of pipe arrays in waves, in 'Proceedings of BOSS'82'.
- Pope, S. B. (2000), *Turbulent flows*, Cambridge University Press.
- Reynolds, O. (1883), 'An experimental investigation of the circumstances which determine whether the motion of water shall be direct or sinuous, and of the law of resistance in parallel channels', *Philosophical Transactions of the Royal Society of London* **174**, 935–982.
- Rocchi, D. and Zasso, A. (2002), 'Vortex shedding from a circular cylinder in a smooth and wired configuration: comparison between 3d les simulation and experimental analysis', *Journal of Wind Engineering and Industrial Aerodynamics* **90**, 475–489.
- Sarpkaya, T. (1978), 'Fluid forces on oscillation cylinders', *Journal of the Waterway, Port, Coastal and Ocean Division, Proceedings of the American Society of Civil Engineers* **104**, 275–290.
- Sarpkaya, T. (1979), 'Vortex induced oscillations', *Journal of Applied Mechanics* **46**, 241–258.
- Sarpkaya, T. (1995), 'Hydrodynamic damping, flow-induced oscillations, and biharmonic response', *ASME Journal of Offshore Mechanics and Arctic Engineering* **117**, 232–238.

- Sarpkaya, T. (2004), 'A critical review of the intrinsic nature of vortex-induced vibrations', *Journal of Fluids and Structures* **19**, 389–447.
- Sarpkaya, T. and Isaacson, M. (1981), *Mechanics of wave forces on offshore structures*, Van Nostrand Reinhold Co. (New York).
- Schewe, G. (1983), 'On the force fluctuations acting on a circular cylinder in crossflow from subcritical up to transcritical reynolds numbers', *Journal of Fluid Mechanics* **133**, 265–285.
- Skaugset, K. B. (2003), On the Suppression of Vortex Induced Vibrations of Circular Cylinders by Radial Water Jets, PhD thesis, NTNU, Norway.
- Skop, R. A., Griffin, O. M. and Ramberg, S. E. (1977), Strumming predictions for the season II experimental mooring, in 'Offshore Technology Conference'.
- Soni, P. K. (2008), Hydrodynamic Coefficients for Vortex-Induced Vibrations of Flexible Beams, PhD thesis, Department of Marine Technology, NTNU, Norway.
- Soni, P. K., Larsen, C. M. and Wu, J. (2009), Hydrodynamic coefficients for vortex induced vibrations of slender beams, in '28th International Conference on Ocean, Offshore and Arctic Engineering', number OMAE2009-79797.
- Sonneville, P. (1976), 'Étude de la structure tridimensionnelle des écoulements autour d'un cylindre circulaire', *Bulletin de la Direction des Etudes et Recherches* **A**.
- Stokes, G. (1851), 'On the effect of the internal friction of fluids on the motion of pendulums', *Transactions of the Cambridge Philosophical Society* **9**, 8–106.
- Sumer, B. M. and Fredsøe, J. (1997), *Hydrodynamic around cylindrical structures*, Vol. 12 of *Advanced series on Ocean Engineering*, World Scientific, London.
- Szwalek, J. L. and Larsen, C. M. (2009), Reynolds number effects on hydrodynamic coefficients for pure in-line and pure cross-flow vortex induced vibrations, in '28th International Conference on Ocean, Offshore and Arctic Engineering', number OMAE2009-79399, Honolulu, Hawaii.

- Trim, A. D., Braaten, H., Lie, H. and Tognarelli, M. A. (2005), ‘Experimental investigation of vortex-induced vibration of long marine risers’, *Journal of Fluids and Structures* **21**, 335–361.
- Tutar, M. and Holdø, A. (2000), ‘Large eddy simulation of a smooth circular cylinder oscillating normal to a uniform flow’, *ASME Journal of Fluids Engineering* **122**, 694–702.
- Vandiver, J. K. (1983), Drag coefficients of long flexible cylinders, in ‘Off-shore Technology Conference’.
- Vandiver, J. K. (1993), ‘Dimensionless parameters important to the prediction of vortex-induced vibration of long, flexible cylinders in ocean currents’, *Journal of Fluids and Structures* **7**, 423–455.
- Vandiver, J. K., Jaiswal, V. and Jhingran, V. (2009), ‘Insights on vortex induced, traveling waves on long risers’, *Journal of Fluids and Structures* **25**, 641–653.
- Vandiver, J. K., Swithenbank, S. B., Jaiswal, V. and Jhingran, V. (2006), Fatigue damage from high mode number vortex induced vibration, in ‘25th International Conference on Ocean, Offshore and Arctic Engineering’, number OMAE2006-92409, Hamburg, Germany.
- VidPIV User Manual* (2005).
- Vikestad, K. (1998), Multi-frequency response of a cylinder subjected to vortex shedding and support motions, PhD thesis, Department of Marine Technology, NTNU, Norway.
- Visscher, J. H. (2011), Application of Particle Image Velocimetry on turbulent marine flows, PhD thesis, Norwegian University of Science and Technology.
- White, Frank, M. (2003), *Fluid Mechanics*, 5th edn, The McGraw-Hill Companies, Inc.
- Williamson, C. H. K. and Govardhan, R. (2004), ‘Vortex induced vibrations’, *Annu. Rev. Fluid Mech* **36**, 413–455.
- Williamson, C. H. K. and Jauvtis, N. (2004), ‘A high-amplitude 2T mode of vortex-induced vibration for a light body in XY motion’, *European Journal of Mechanics B/Fluids* **23**, 107–114.

- Williamson, C. H. K. and Roshko, A. (1988), 'Vortex formation in the wake of an oscillating cylinder', *Journal of Fluids and Structures* **2**, 355–381.
- Wu, J. (2011), Hydrodynamic Force Identification from Stochastic Vortex Induced Vibration Experiments with Slender Beams, PhD thesis, NTNU.
- Wu, J., Larsen, C. M. and Lie, H. (2010), Estimation of hydrodynamic coefficients for VIV of slender beam at high mode orders, *in* '29th International Conference on Ocean, Offshore and Arctic Engineering', Shanghai, China.
- Yin, D. and Larsen, C. M. (2010), On determination of VIV coefficients under shear flow condition, *in* '29th International Conference on Ocean, Offshore and Arctic Engineering', number OMAE2010-20306, Shanghai, China.
- Yin, D. and Larsen, C. M. (2011), Experimental and numerical analysis of forced motion of a circular cylinder, *in* '30th International Conference on Ocean, Offshore and Arctic Engineering', number OMAE2011-49438, Rotterdam, The Netherlands.
- Yin, D. and Larsen, C. M. (2012), Forced motion experiments with measured motions from flexible beam tests under uniform and sheared flows, *in* '31st International Conference on Ocean, Offshore and Arctic Engineering', number OMAE2012-83160, Rio de Janeiro, Brazil.
- Young, M. E. and Ooi, A. (2007), Comparative assessment of LES and URANS for flow over a cylinder at a Reynolds number of 3900, *in* '16th Australasian Fluid Mechanics Conference'.
- Zdravkovich, M. M. (2002), *Flow Around Circular Cylinders, Vol 1: Fundamentals*, Oxford University Press.
- Zhang, J. and Dalton, C. (1996), 'Interaction of vortex-induced vibrations of a circular cylinder and a steady approach flow at a Reynolds number of 13000', *Computers and Fluids* **25**, 283–294.

Appendix A

Calibration

The calibration procedure utilized in this work was first used by Aronsen (2007), and afterwards the same procedure was applied by Soni (2008) and Szwalek and Larsen (2009). From the calibration, calibration factors of force transducers, accelerometers and string potentiometers were found and later used in the post-processing of the experimental data.

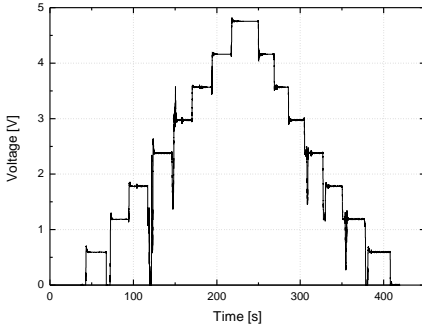
A.1 Calibration of force sensors

The calibration of the force sensors consisted of 3 steps. First, each strain gauge was calibrated individually to find the calibration coefficient (in N/V). Secondly, two and two sensors were mounted together to form a 'cross' in order to measure forces in two perpendicular directions. The 'cross' sensors were then calibrated to investigate if there was a force transfer between orthogonal directions. The last step was conducted when the cylinder was mounted in the test rig. Loads were applied on the cylinder to see whether the two sensor crosses were rotated when installed, and if so, find the cross-talk angle.

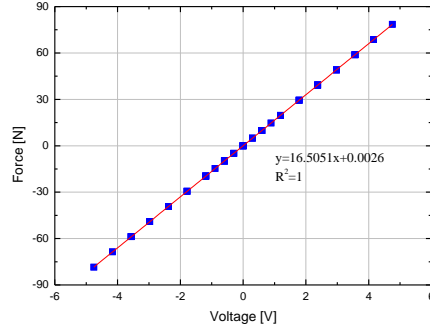
Step I, individual strain gauge calibration

Individual force sensor calibration was carried out for two times, before installation and after all runs completed.

The first step of force sensor calibration is to find the calibration factors for each force sensor, which was done by applying known weights and recording the output voltage.



(a) Calibration time series.



(b) Calibration results of 20333.

Figure A.1: Step I, force calibration results.

Before installation, weights were applied in the following sequence: 1, 2, 3, 4, 5, 6, 7, 8, 6, 4, 2 and 1kg. After all runs done, the sequence was changed to: 0.5, 1, 1.5, 2, 3, 4, 5, 6, 4, 2, 1.5, 1 and 0.5kg. A typical time series is shown in Figure A.1a. The load sequence was repeated two times in both positive and negative direction. Four load sequences were performed in each direction and the slope was estimated for every sequence. A standard deviation for the slope was then estimated based on a mean value of 1.0. The estimated relative error in the force coefficient was taken as $t_{95\%}$ times the estimated standard deviation, see Eq.(A.5). Calibration results for strain gauge 20333 is shown in Figure A.1b.

Linear Regression

In Figure A.1b the calibration coefficient is estimated by linear regression. The general expression for a linear regression is:

$$Y(X) = mX + c \quad (\text{A.1})$$

where m is the slope and c is the y -axis intercept. In the calibration procedure X represents the output voltage and Y is the gravity force (N) given by the applied weight.

The standard error (deviation) of the slope from the curve fit is given by (Coleman and Steele, 1999, chap. 7):

$$S_m = \sqrt{\frac{S_Y^2}{S_{XX}}} \quad (\text{A.2})$$

$$S_Y = \left[\frac{\sum_{i=1}^N (Y_i - mX_i - c)^2}{N - 2} \right]^{1/2} \quad (\text{A.3})$$

$$S_{XX} = \sum_{i=1}^N X_i^2 - \frac{(\sum_{i=1}^N X_i)^2}{N} \quad (\text{A.4})$$

S_m is an estimate of the standard deviation of Y , as no uncertainty is connected to X_i . The criteria is not completely met for these results as there are uncertainties related to the applied weights. However, the uncertainties are found to be negligible.

The confidence interval for the mean value of the slope is given by:

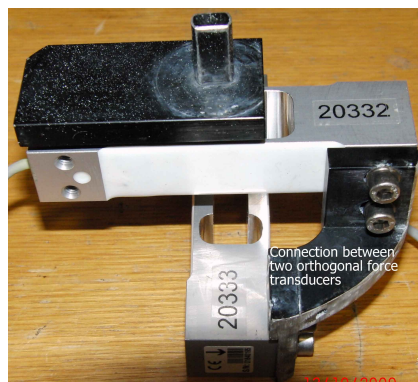
$$m - t_{95\%} S_m \leq \mu \leq m + t_{95\%} S_m \quad (\text{A.5})$$

In the post-processing of experimental data, the measured voltage is multiplied by the inverse of the slope m . The estimated uncertainty in the calibration coefficient is treated as a bias error in the force measurements. Calibration factors and estimated bias errors for the four force sensors are shown in Table A.1.

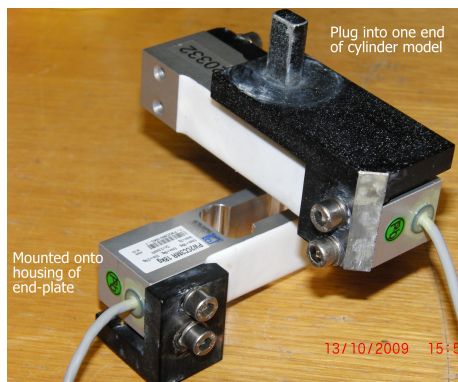
Step II, ‘cross’ strain gauges calibration

In step II, two and two force sensors were mounted together orthogonally, a metal accessory manufactured specially was used to connect two sensors, see Figure A.2a. Besides this connection accessory, two other metal accessories were mounted onto each of two force sensors respectively. One metal accessory has a tenon and can plug into the mortise in the end of the cylinder model; the other metal piece has 3 holes for bolts connecting the end-plate with the force sensor, see Figure A.2b.

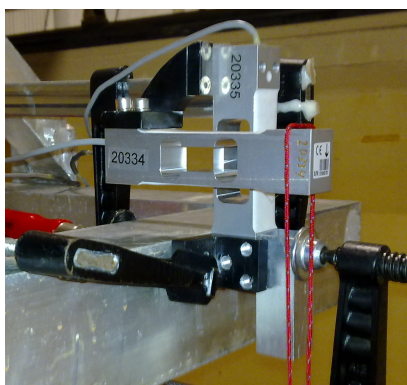
Loads were applied on the sensor cross in four directions to check whether the two sensors mounted orthogonally so that they could measure the IL and CF force correctly. If force was applied on one sensor, there was measurement from the other sensor, which is so called ‘cross-talk’, then the cross



(a) Connection between two orthogonal force sensors



(b) Another viewpoint of a 'cross'



(c) Step II, calibration of a 'cross'.



(d) A load 'cross' mounted on one endplate

Figure A.2: Connection and calibration of a load 'cross'.

should be demounted and assemble again.

Figure A.2c shows the calibration setup. When calibration was performed on one force sensor of the cross, the other force sensor was clumped onto a vertical surface, a gradienter to ensure the surface was perfectly vertical. Gravity force of the load was applied on one force sensor by a string (see the red string in Figure A.2c).

The result for one sensor cross is shown in Figure A.3a. It could be seen from the figure that when applying a force in CF direction, there was also a small force component in IL direction. This could not be avoid and might

be attributed to the way the two sensors are connected, see Figure A.2a. A force in CF direction cause a moment that has to be taken up by the IL sensor. The error seems to be linear and the two sensor crosses give similar results, see Table A.1. This was taken as bias error in the uncertainty analysis.

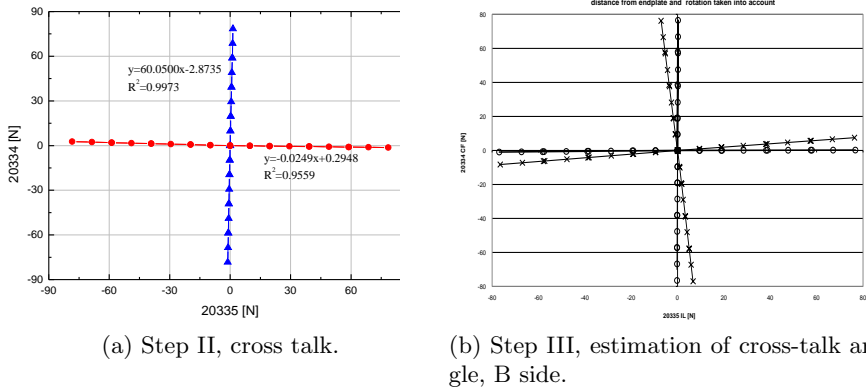


Figure A.3: Step 2 and step 3 of calibration.

Step III, installed strain gauges calibration

When two ‘sensor crosses’ were calibrated, they were mounted onto end-plates, see Figure A.2d; then the end-plates together ‘sensor crosses’ were installed onto the rig, see Figure A.4. Calibration was carried out again when all equipments were set up: first, check whether there was contact between ‘sensor cross’ and end-plate, if so, demount and modify; secondly, investigate if the ‘sensor cross’ has been rotated during installation and find the rotation angle; finally, correct the force with rotation angle and compare with applied load force.

The first condition was checked in this way: first, one side of the sensor crosses was mounted onto the end-plates, see Figure A.2d. A piece of paper was put between the edge of the cross and housing of the end-plate to see whether they contact each other. Then the end-plates and the cylinder were installed on the rig. A series of increasing loads were applied on each direction (similar to Step I), the maximum load was larger than the estimated maximum IL and CF force, see Figure A.4. Measured forces were plotted together, see Figure A.3b. A linear line proves that there is no contact between the cylinder and the housing; If the curve is not linear, the position

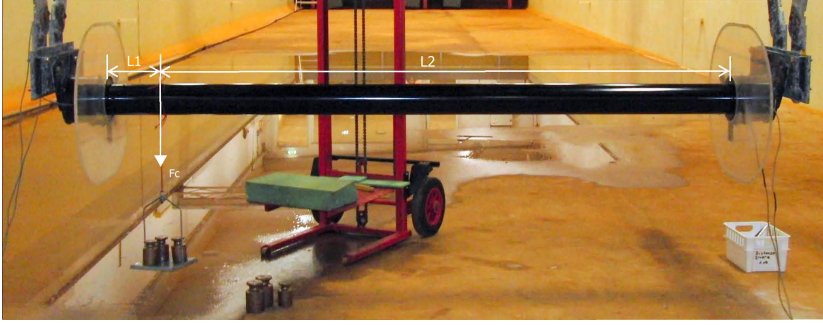


Figure A.4: Calibration step III when the set-up was completed.

Table A.1: Summary of force calibration factors.

Step	Parameter	Mean Value	Uncertainty 95%
I	f_{c20332} , IL SB	16.4613	$6.66 \cdot 10^{-4}$
	f_{c20333} , CF SB	-16.5039	$8.32 \cdot 10^{-4}$
	f_{c20335} , IL Port	16.6743	$9.48 \cdot 10^{-4}$
	f_{c20334} , CF Port	-16.5260	$5.52 \cdot 10^{-4}$
II	IL CF interaction (SB)	1.64%	0.22%
	IL CF interaction (Port)	1.84%	0.25%
III	Rotation angle (SB)	-0.6316 [deg]	2.4075
	Rotation angle (Port)	-5.4708 [deg]	0.7551

of the sensor cross needed to be modified.

The second condition was investigated by checking whether the measured force point fall onto X or Y axis (IL or CF). If it does not, the angle between the axis and linear line is the rotation angle during installation. When post-processing the experimental data, this angle was taken into account. Figure A.4 shows the calibration in negative CF direction at one end. The force taken by the closer end should be $F_c L1 / (L1 + L2)$, if the 'cross' was perfectly orthogonal, while rotated during installation, the rotation angle could be calculated from the measured CF force at closer end. Figure A.3b shows an example of the results. Crosses represent results from the calibration and circles represent the same results after correction for cross-talk angle.

Calibration coefficients of single load cells and cross talk angles with estimated uncertainties for the two sides are listed in Table A.1.

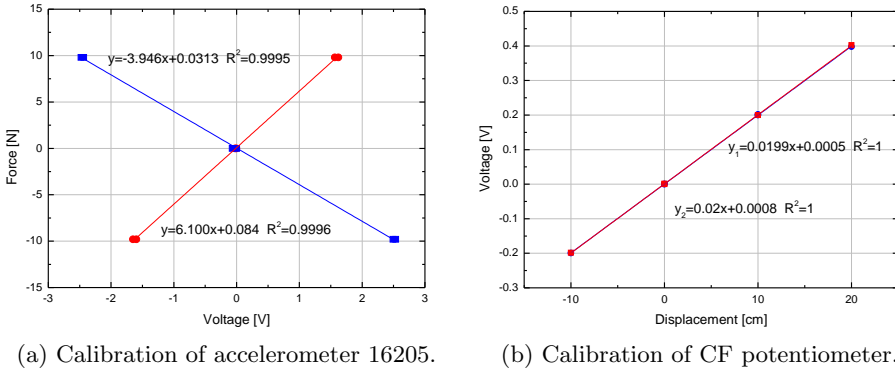


Figure A.5: Calibration of accelerometer and potentiometer.

A.2 Calibration of motion sensors

Two types of sensors were used, accelerometer and string potentiometer.

Accelerometer calibration

The accelerometers were calibrated by using the gravity acceleration, $g = 9.81m/s^2$. The accelerometers were calibrated by rotating the accelerometer so that the axis of interest would be horizontal ($acc=0$), vertical point down ($acc=-g$), and vertical point up ($acc=g$). Calibration coefficients and uncertainty were estimated in the same way as for the force sensors. One example of the assembled results is given in Figure A.5a. The results are given in Table A.2.

Table A.2: Calibration factors for accelerometers.

Accelerometer IL number	16217x	16217z	16205x	16205z
Mean value	4.385	-6.386	6.100	-3.946
Uncertainty, 95%	0.010	0.008	0.012	0.002

String potentiometer calibration

The string potentiometers were factory calibrated. The calibration coefficients were verified by use of a folding ruler in this way: first, the string was pulled out 10 cm and zero setting was performed; then the length was varied between 0 cm and 35 cm. The calibration factors of IL and CF potentiometers are shown in Table A.3, and results of CF potentiometer is shown

in Figure A.5b. The calibration factors were implemented into I/O settings.

Table A.3: Calibration factors for string potentiometers.

	IL	CF
Mean value	0.0041	0.02
Uncertainty, 95%	$1.08 \cdot 10^{-5}$	$6.93 \cdot 10^{-5}$

After installation on the carriage, the string potentiometers were calibrated again by adjusting the position of the cylinder, it was showed that the string potentiometer in IL direction over predicted the displacement by 5%. This was discovered by comparing the input and output displacement signals, and then corrected.

As the ruler had not been calibrated, an uncertainty value of 2% (95% confidence interval) was used (Aronsen, 2007).

Appendix B

Orbits applied in forced motion experiments

Figure B.1 illustrates the selected 19 sections with sheared flow case in NDP tests. Table B.1 shows the exact position of each cross section. Z axis has the direction along the riser and origin at top end which has maximum velocity for shear flow cases. For all orbits shown from Figure B.3 to Figure B.11, the flow direction is from left to right.

Due to the limitation of MCLab, forced motion tests with most of the orbits from NDP case 2100 and 2160 could not be carried out with $f_{osc,MC}$. The oscillation frequencies were scaled in order to run these cases. The scale factors (w) are shown in Table B.2. The actual oscillation frequencies are $f_{osc,MC}/w$, where $f_{osc,MC}$ is the calculated oscillation frequency from Eq. (4.8).

Phase angle calculated by Eq. (4.1) of all periodic orbits selected from 19 cross sections of NDP flexible beam are shown in Figure B.2. The legend

Table B.1: Positions of 19 cross sections along 38 m riser model.

NO.	Z (m)	NO.	Z (m)	NO.	Z (m)	NO.	Z (m)
S1	1.719	S6	11.266	S11	20.814	S16	30.362
S2	3.628	S7	13.176	S12	22.724	S17	32.271
S3	5.538	S8	15.085	S13	24.633	S18	34.181
S4	7.447	S9	16.995	S14	26.543	S19	36.090
S5	9.357	S10	18.905	S15	28.452		

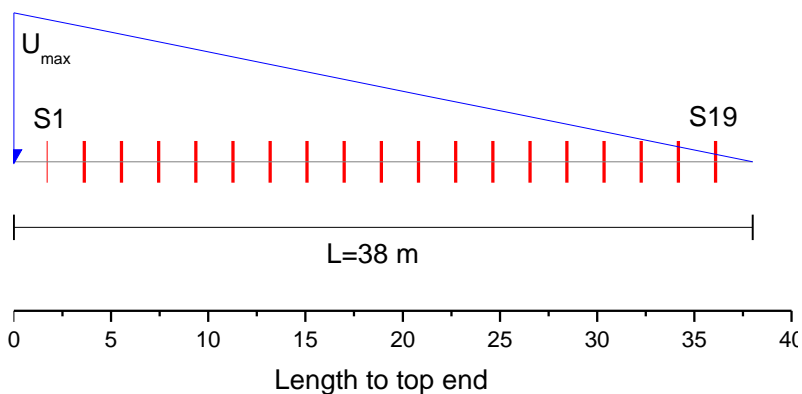


Figure B.1: Selected 19 cross sections along 38 m riser in NDP tests.

Table B.2: Scale factors on the oscillation frequencies of NDP case 2100 and 2160.

Sec. NO.	2100	2160	Sec. NO.	2100	2160
1	1.15	1.20	11	1.00	1.50
2	1.15	1.00	12	1.15	1.50
3	1.15	2.00	13	1.15	2.00
4	1.15	1.50	14	1.30	1.80
5	1.15	1.80	15	1.00	1.50
6	1.15	1.50	16	1.15	1.00
7	1.00	2.00	17	1.00	2.50
8	1.15	2.00	18	1.15	1.80
9	1.15	1.50	19	1.15	1.50
10	1.15	1.50			

of the Figure is corresponding case number in NDP High Mode VIV Tests, see Table 3.5.

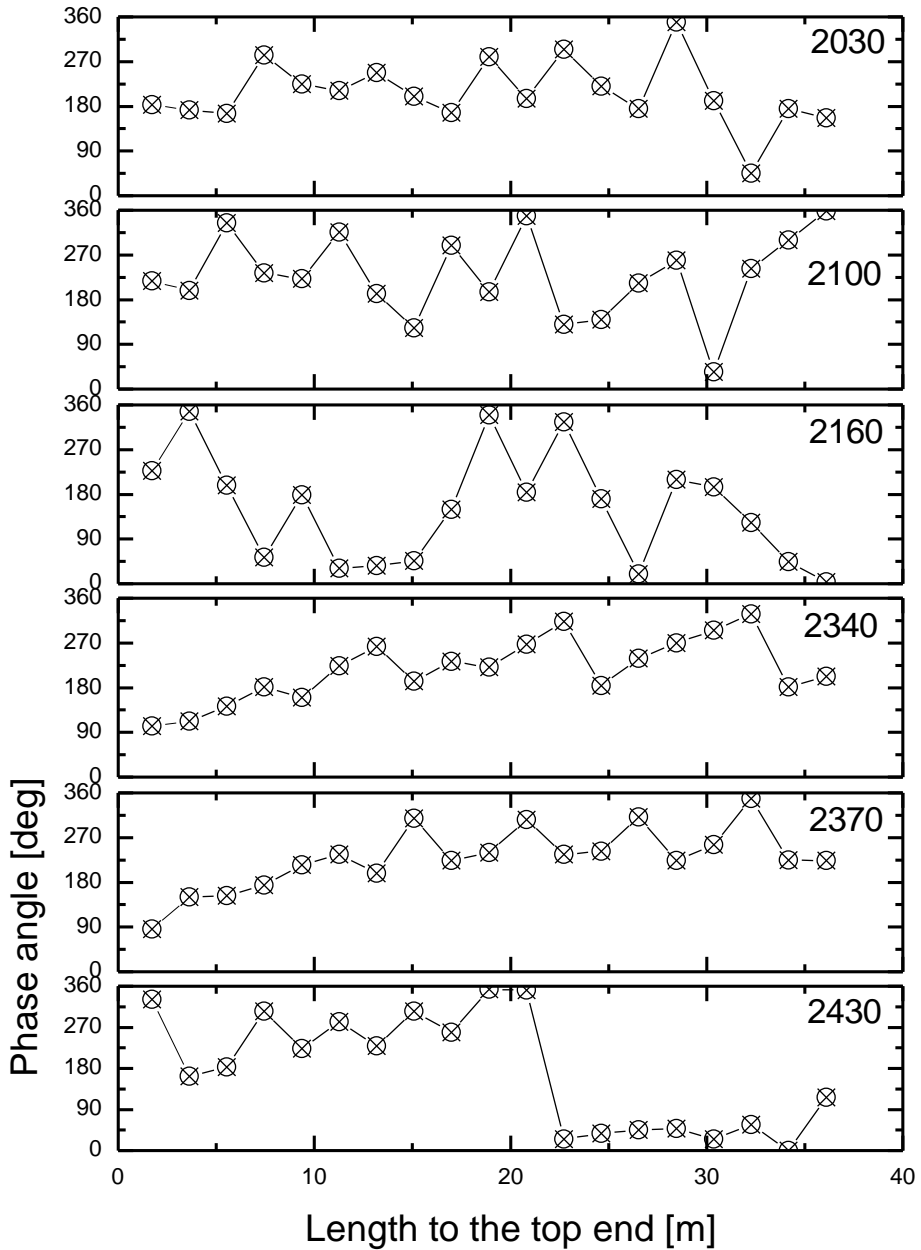


Figure B.2: Phase angle between $(A/D)_{CF,1}$ and $(A/D)_{IL,2}$ of periodic orbits. \otimes represent the phase angle of 19 selected cross sections.

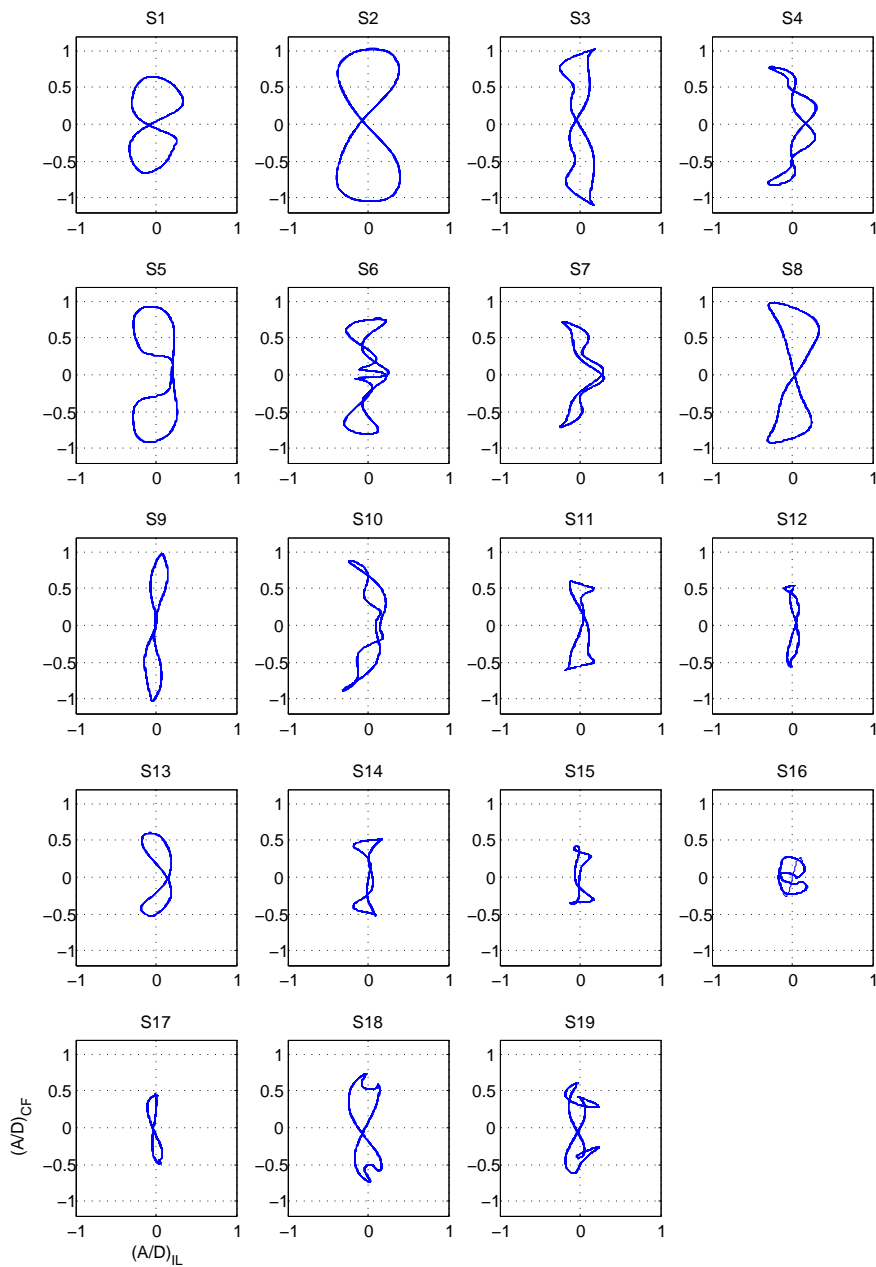


Figure B.3: Periodic orbits of 19 cross sections for NDP case 2030.

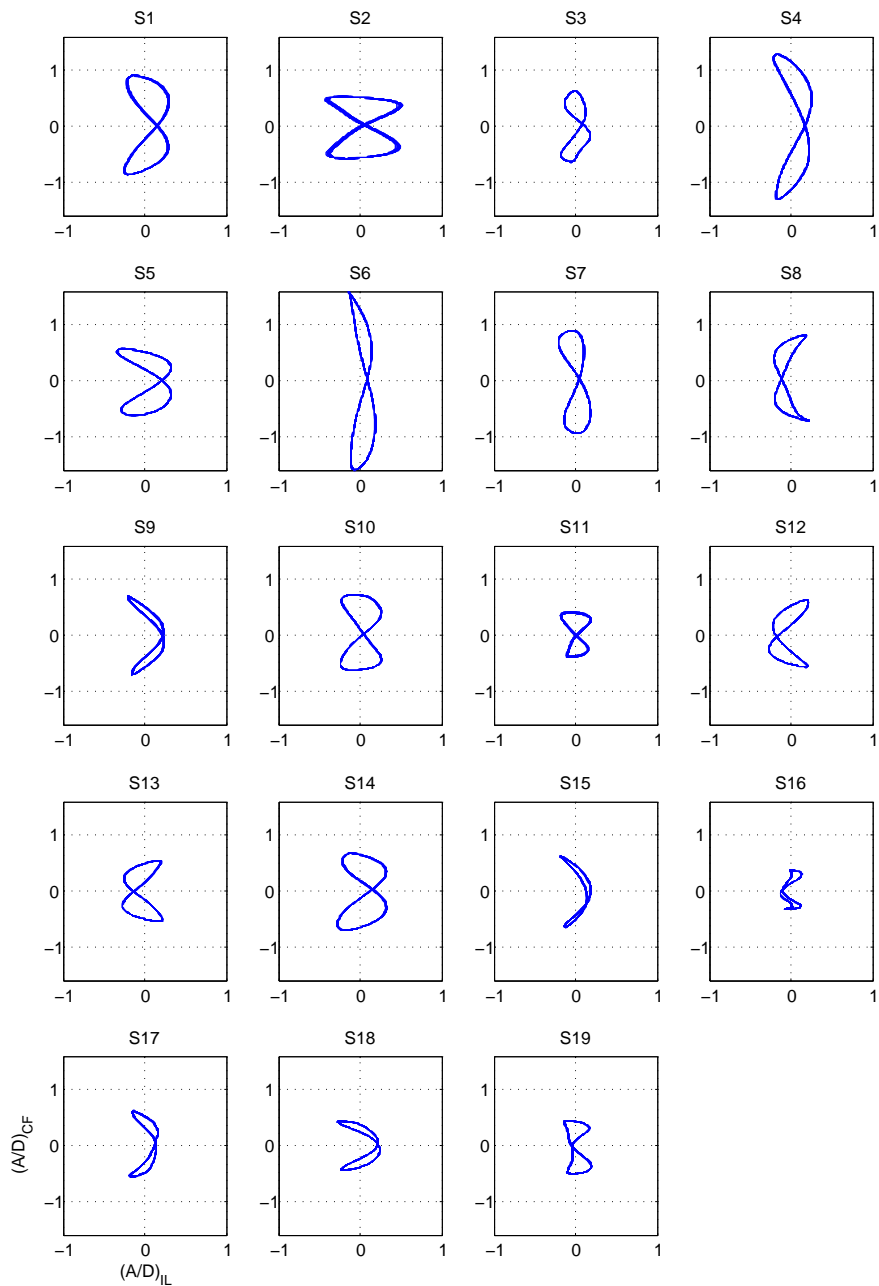


Figure B.4: Periodic orbits of 19 cross sections for NDP case 2100.

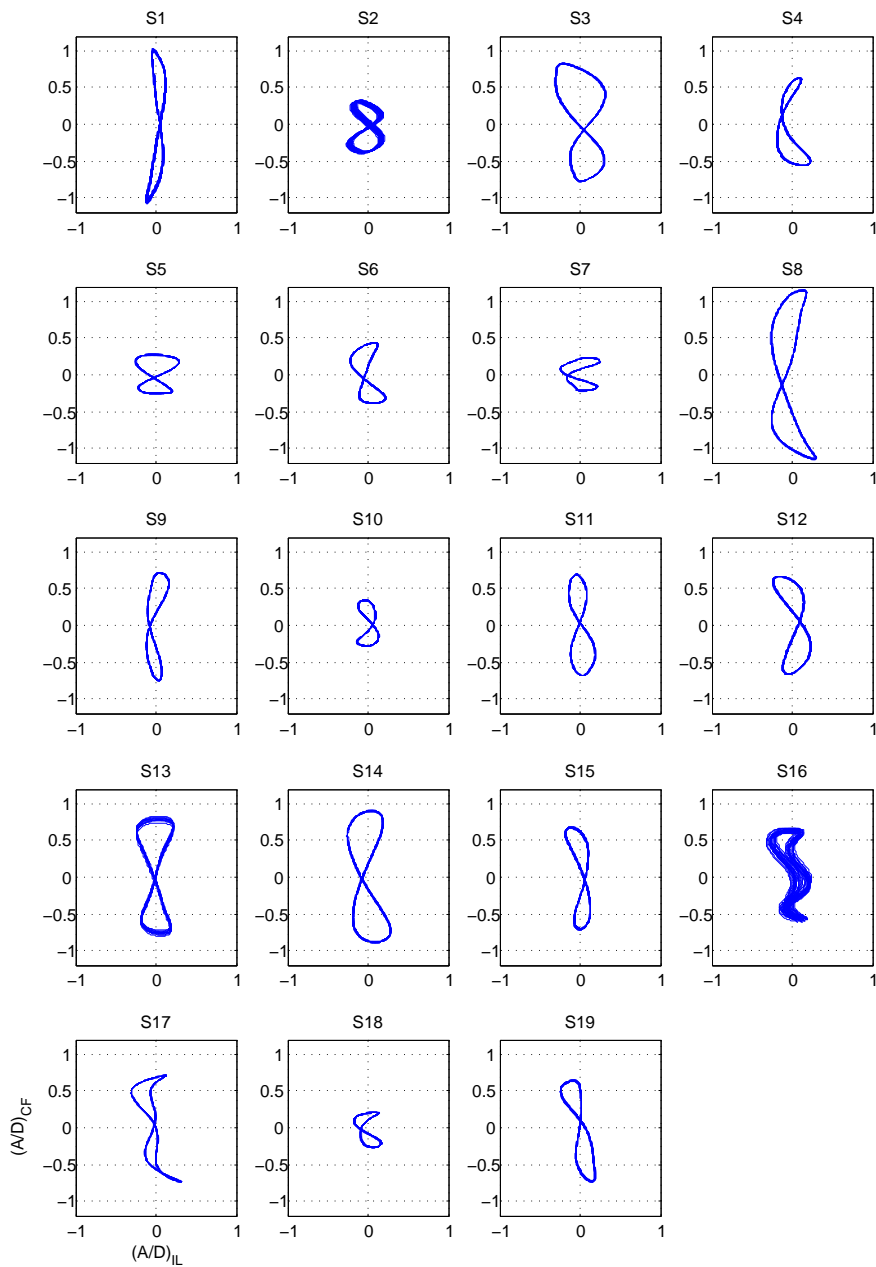


Figure B.5: Periodic orbits of 19 cross sections for NDP case 2160.

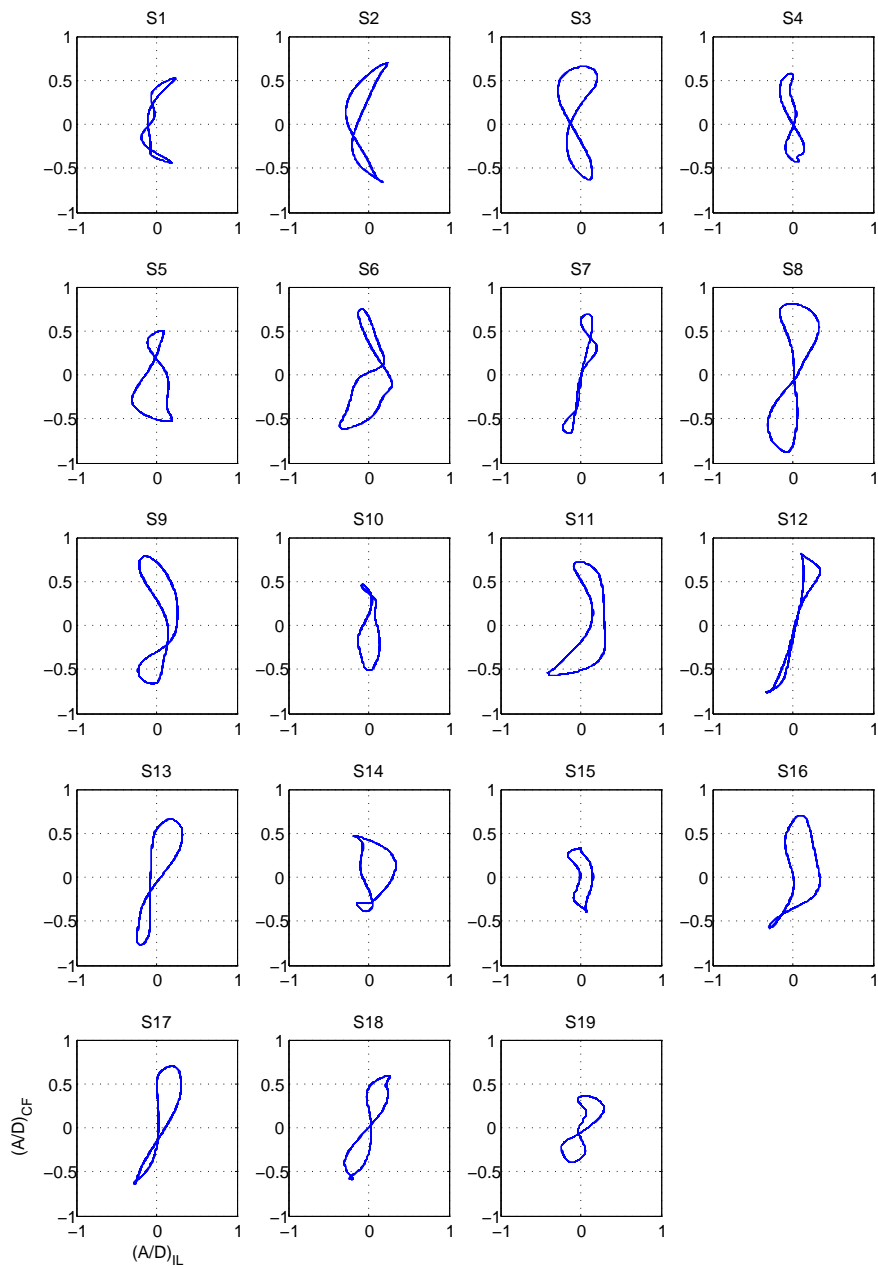


Figure B.6: Periodic orbits of 19 cross sections for NDP case 2340.

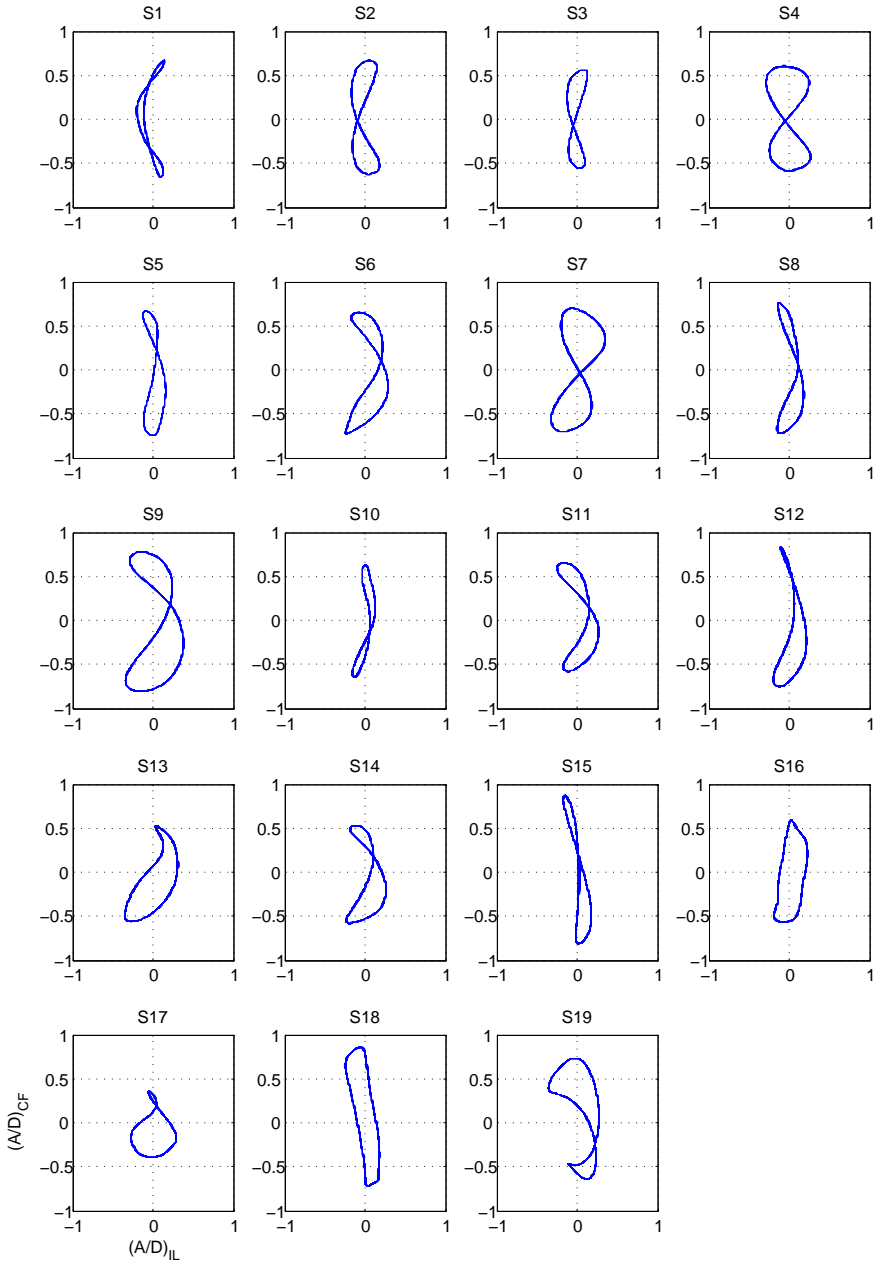


Figure B.7: Periodic orbits of 19 cross sections for NDP case 2370.

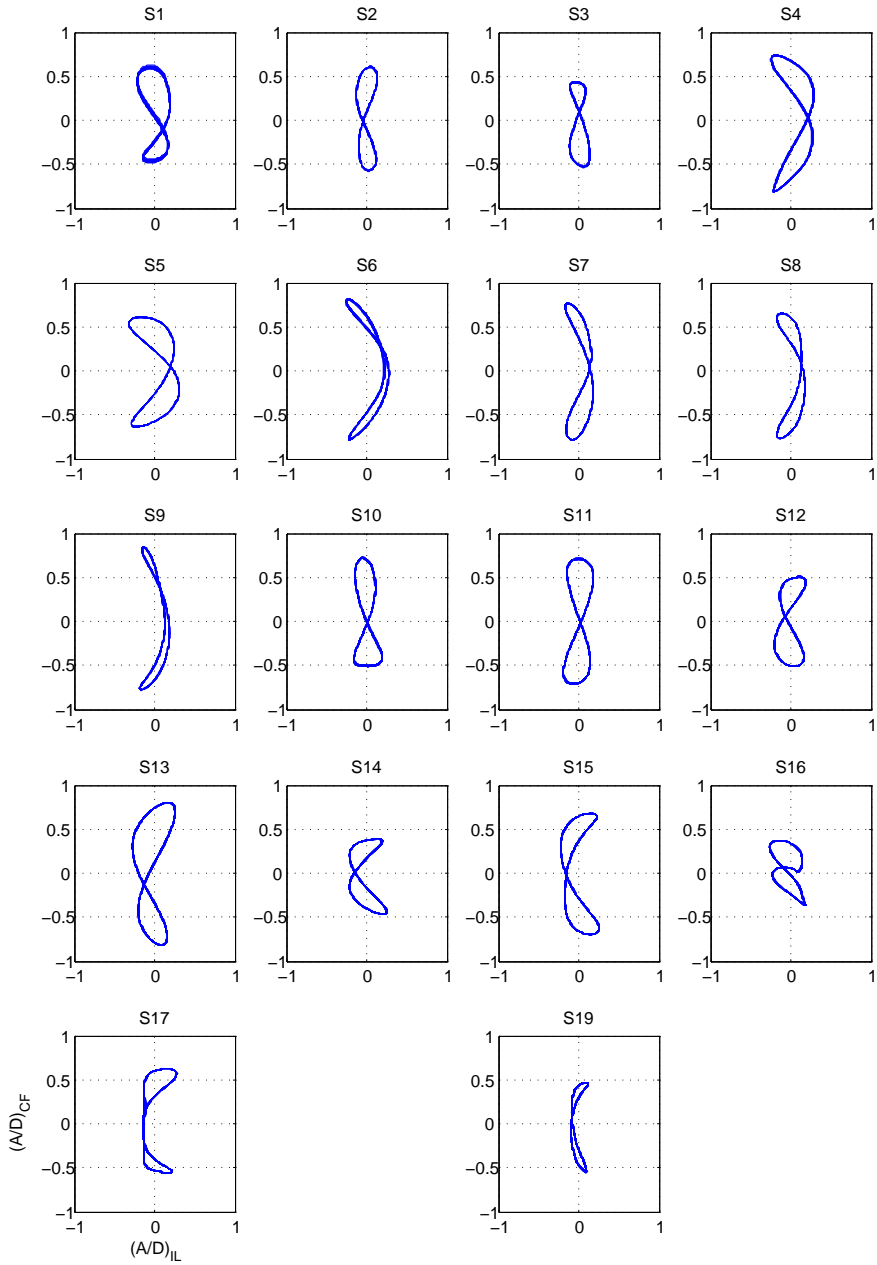


Figure B.8: Periodic orbits of 19 cross sections for NDP case 2430.

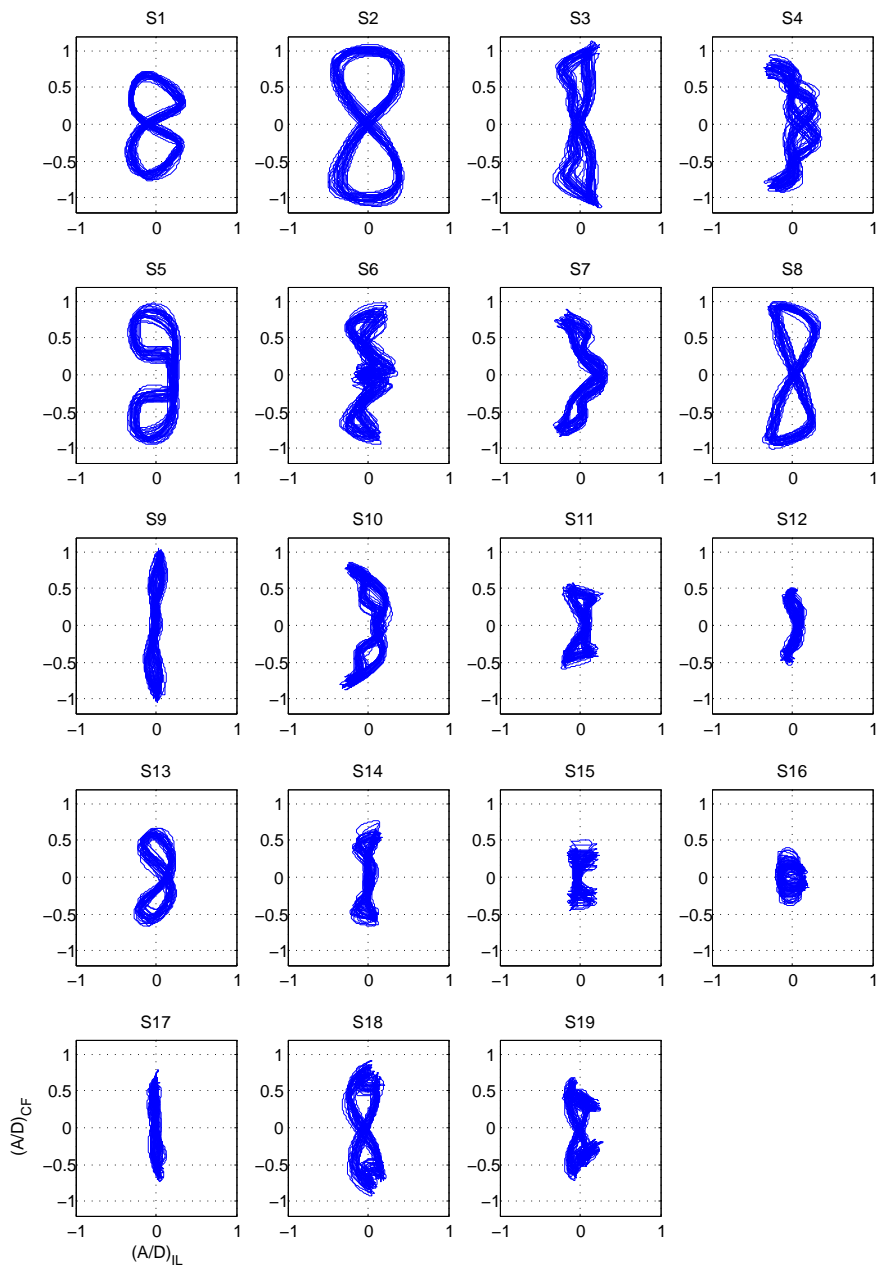


Figure B.9: Observed orbits of 19 cross sections for NDP case 2030.

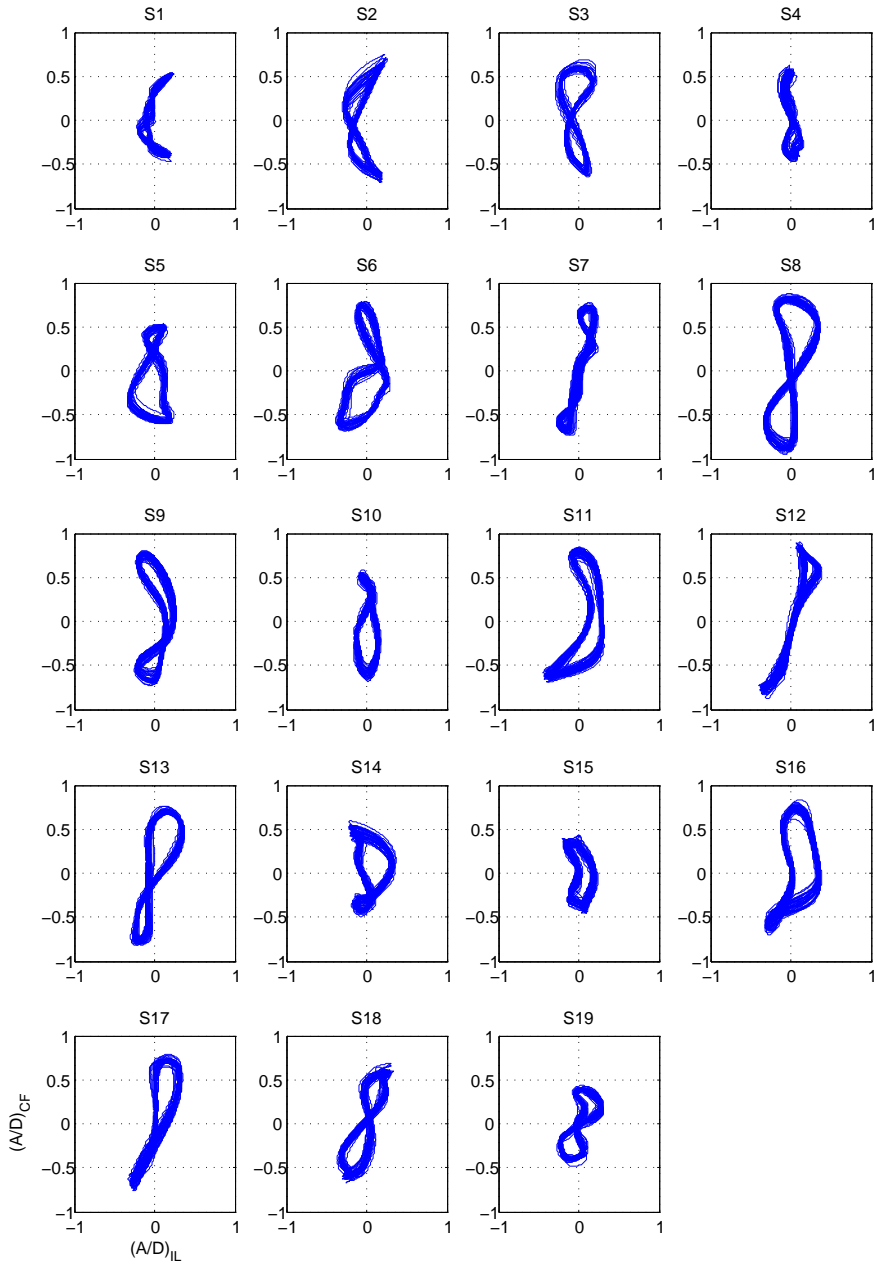


Figure B.10: Observed orbits of 19 cross sections for NDP case 2340.

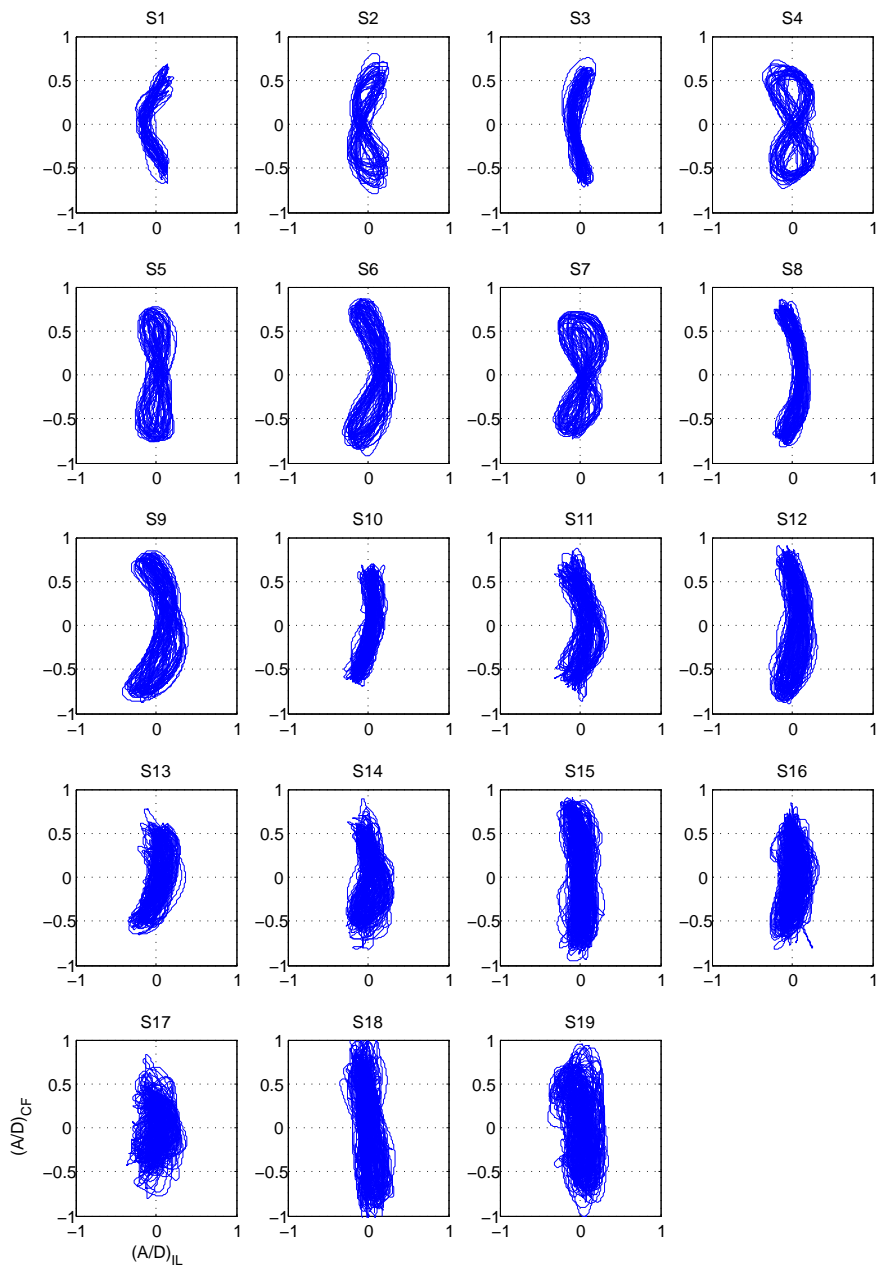


Figure B.11: Observed orbits of 19 cross sections for NDP case 2370.

Appendix C

Equations used in uncertainty analysis

It is normal to assume that if a measurement is repeated infinitely many times the measured values will follow a Gaussian distribution around a mean. And the Gaussian distribution is called the parent distribution.

$$f(X) = \frac{1}{\sigma\sqrt{2\pi}} e^{-\frac{(x-\mu)^2}{2\sigma^2}} \quad (\text{C.1})$$

Infinite number of samples

Mean: μ

Standard deviation: σ

Confidence interval of a sample: $Prob(X_j - t\sigma \leq \mu \leq X_j + t\sigma) = \gamma$,

$\gamma = 0.95$, $t \approx 1.96$

N samples

Mean: $\bar{X} = \frac{1}{N} \sum_{j=1}^N X_j$

Standard deviation (of the N samples) is: $S_x = \sqrt{\frac{1}{N-1} \sum_{j=1}^N (X_j - \bar{X})^2}$

Confidence interval: $Prob(t \leq \frac{X_j - \mu}{S_x} \leq t) = \gamma$

$\frac{X_j - \mu}{S_x}$ is random and follows a Student's t distribution with N-1 degrees of freedom. $t = F^{-1}(\frac{1}{2}(1 + \gamma))$.

The precision limit for a sample: $P_x = tS_x$

the mean value of N samples \bar{X}

It is normally distributed with μ .

Mean: μ

Standard deviation: $S_{\bar{X}} = \frac{S_x}{\sqrt{N}}$

Precision limit (N repetitions): $P_{\bar{X}} = t \frac{S_{\bar{X}}}{\sqrt{N}} = z_{\alpha/2} \frac{S_{\bar{X}}}{\sqrt{N}}$

100(1 - α)% confidence interval: $(\bar{X} - z_{\alpha/2} \frac{S_x}{\sqrt{N}}, \bar{X} + z_{\alpha/2} \frac{S_x}{\sqrt{N}})$

As we consider 95% confidence interval, $\alpha = 0.05$, $z_{\alpha/2} = 2.021$.

Appendix D

2^{nd} order replication level cases

Table D.1: PIV runs with relative error less than 0.1.

32	CF		IL	
0.1	NO.	%	NO.	%
C_e A side	22	68.75	23	71.88
C_e B side	22	68.75	21	65.63
C_a A side	23	71.88	24	75.00
C_a B side	23	71.88	24	75.00

Table D.2: Phase angle between displacement and force at first 4 frequency components of signals at B side for case 21002.

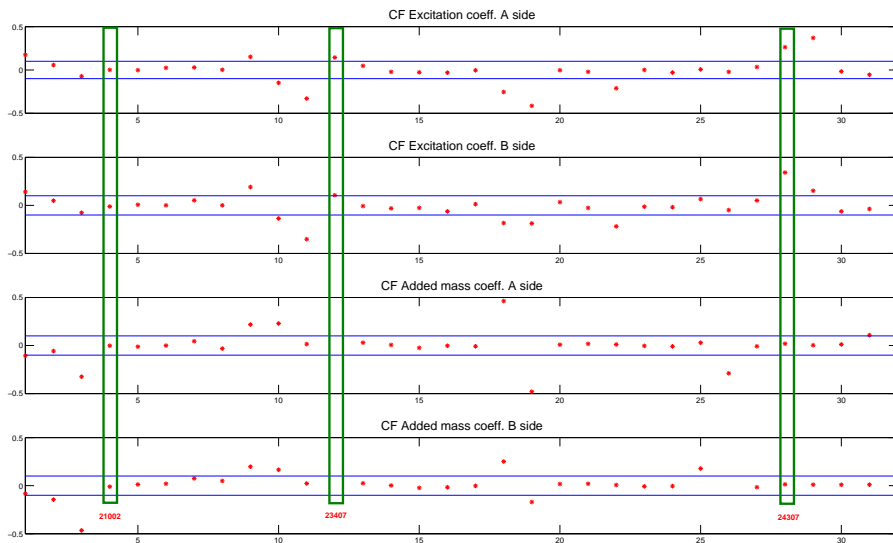
Force	Bside CF 21002				Bside IL 21002			
	Phase A		Phase B		Phase A		Phase B	
	Mean	Std.	Mean	Std.	Mean	Std.	Mean	Std.
1ω	16.80	1.10	17.16	0.95	3.92	0.58	3.75	0.29
2ω	2.90	0.42	2.76	0.49	5.61	0.19	5.67	0.24
3ω	10.78	0.39	10.71	0.38	1.70	0.23	1.64	0.22
4ω	2.81	0.26	2.74	0.36	3.26	0.13	3.30	0.15

Table D.3: Phase angle between displacement and force at first 4 frequency components of signals at B side for case 24307.

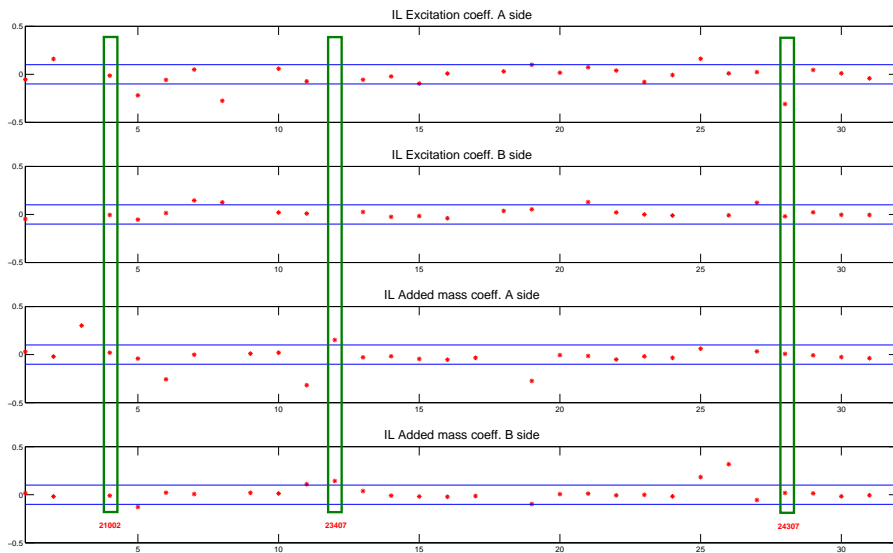
Force	Bside CF 24307				Bside IL 24307			
	Phase A		Phase B		Phase A		Phase B	
	Mean	Std.	Mean	Std.	Mean	Std.	Mean	Std.
1ω	12.71	0.28	12.35	0.19	0.30	0.12	0.29	0.10
2ω	1.35	0.12	1.29	0.13	7.06	0.19	6.80	0.15
3ω	2.56	0.13	2.55	0.11	0.68	0.13	0.60	0.15
4ω	0.34	0.10	0.43	0.09	1.56	0.11	1.52	0.12

Table D.4: Phase angle between displacement and force at first 4 frequency components of signals at B side for case 23407.

Force	Bside CF 23407				Bside IL 23407			
	Phase A		Phase B		Phase A		Phase B	
	Mean	Std.	Mean	Std.	Mean	Std.	Mean	Std.
1ω	0.77	0.29	0.48	0.17	0.26	0.05	0.29	0.03
2ω	0.33	0.06	0.42	0.12	0.42	0.03	0.41	0.05
3ω	0.33	0.07	0.24	0.05	0.32	0.05	0.28	0.04
4ω	0.19	0.03	0.23	0.02	0.79	0.03	0.77	0.03

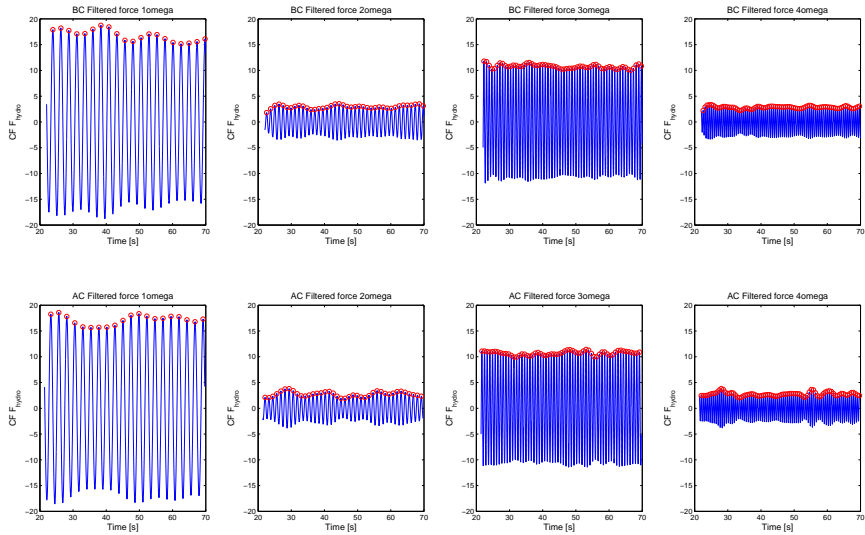


(a) CF direction.

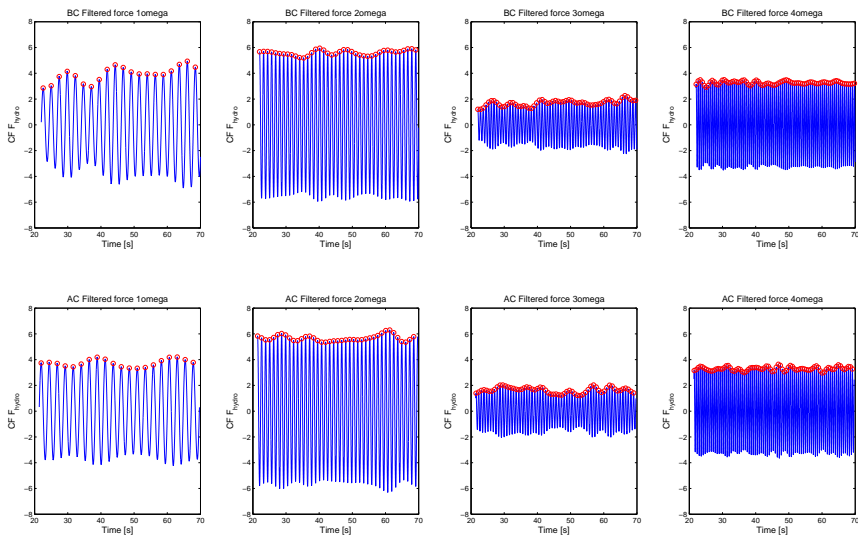


(b) IL direction.

Figure D.1: Relative error of hydrodynamic coefficients of 32 PIV cases.

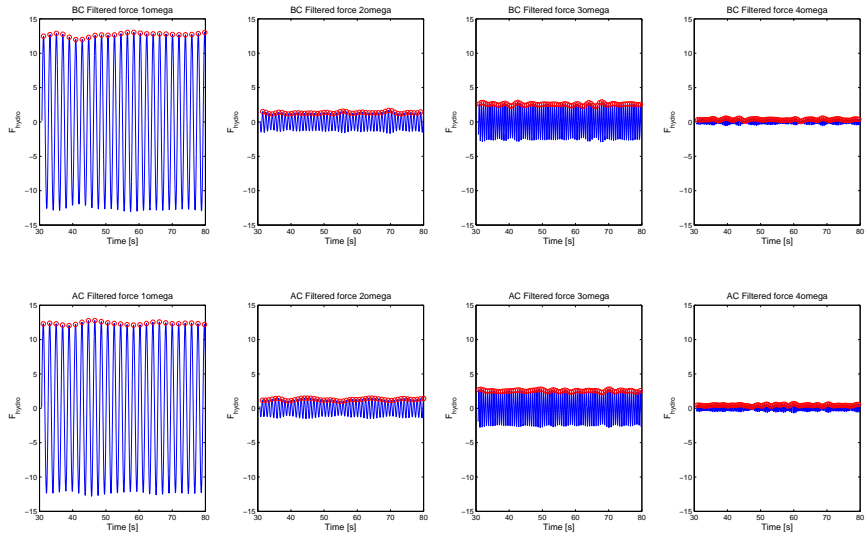


(a) CF force comparison of 21002.

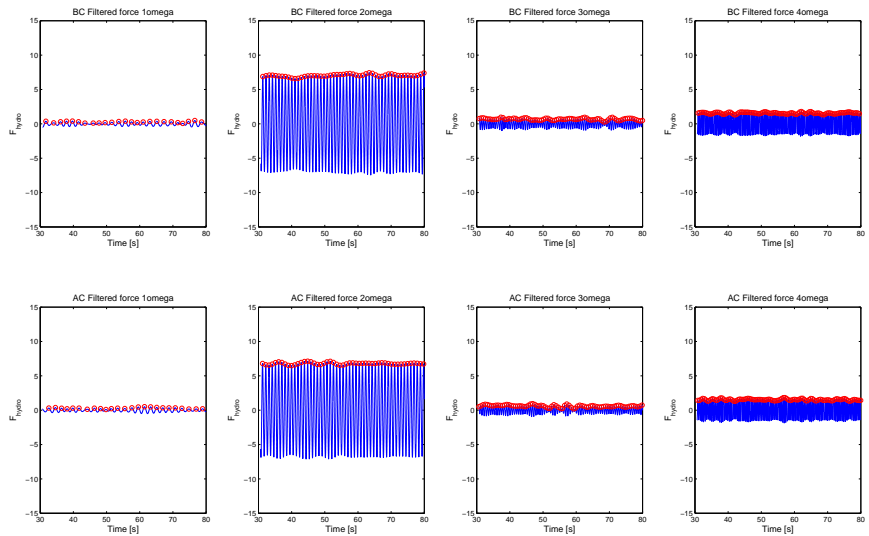


(b) IL force comparison of 21002.

Figure D.2: CF and IL hydrodynamic forces at first four harmonics of case 21002.

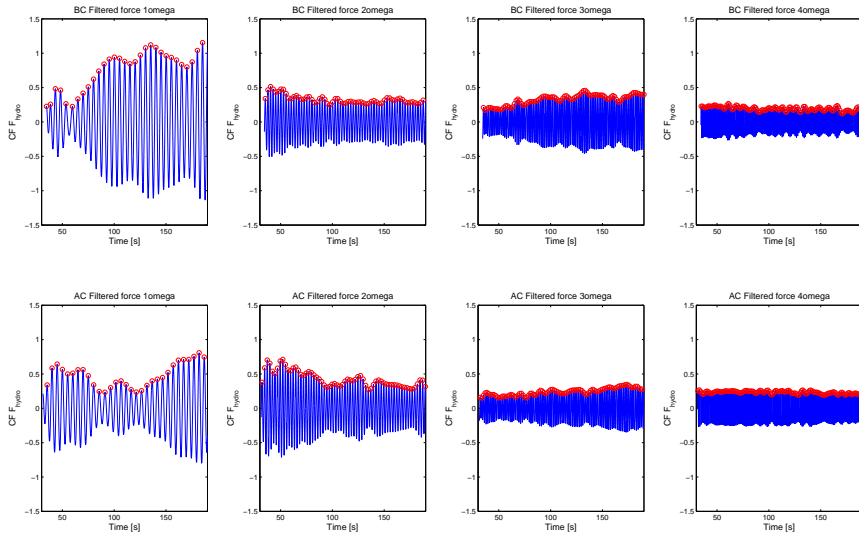


(a) CF force comparison of 24307.

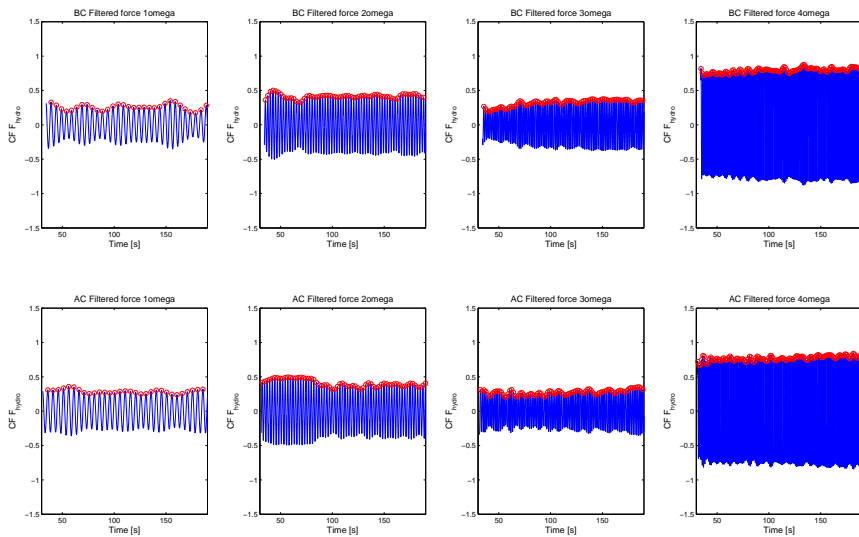


(b) IL force comparison of 24307.

Figure D.3: CF and IL hydrodynamic forces at first four harmonics of case 24307.



(a) CF force comparison of 23407.



(b) IL force comparison of 23407.

Figure D.4: CF and IL hydrodynamic forces at first four harmonics of case 23407.

Appendix E

Displacements in time-space of NDP cases

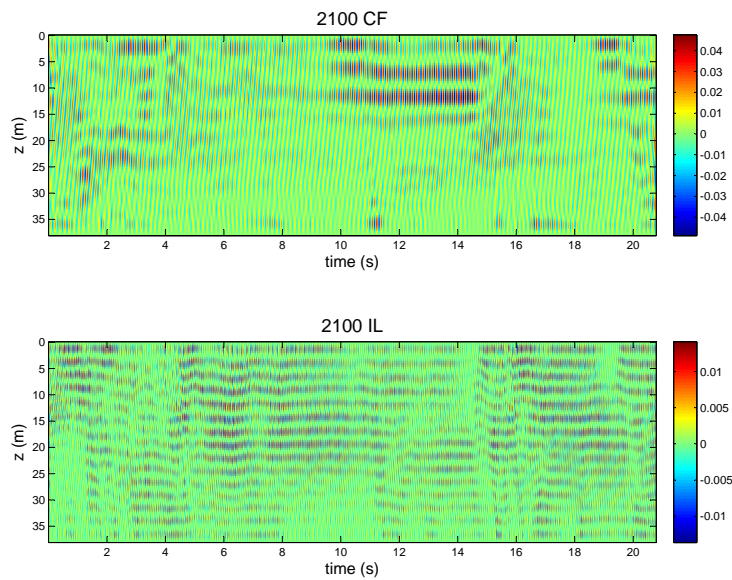


Figure E.1: CF & IL displacement in time and space for NDP uniform flow case 2100, $U = 1.2$ m/s.

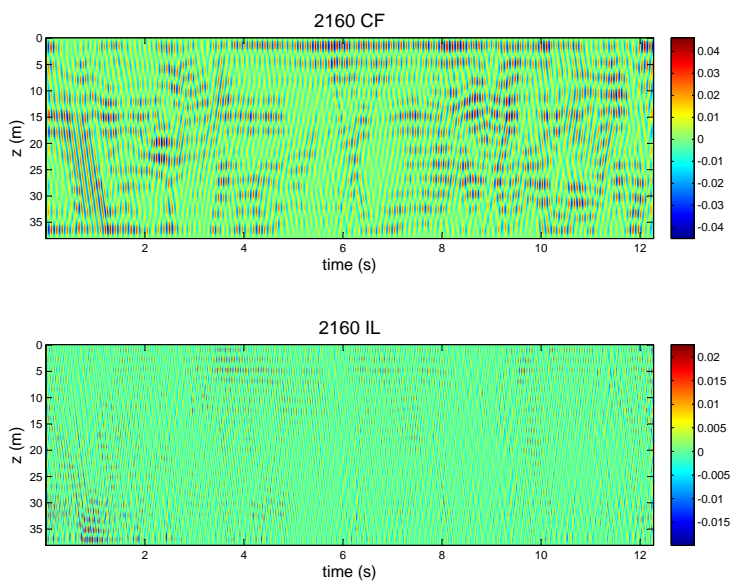


Figure E.2: CF & IL displacement in time and space for NDP uniform flow case 2160, $U = 1.8 \text{ m/s}$.

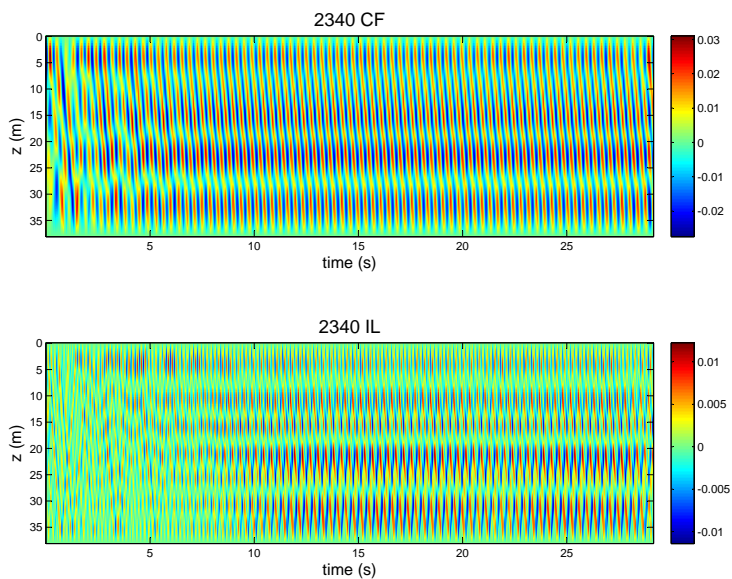


Figure E.3: CF & IL displacement in time and space for NDP shear flow case 2340, $U_{max} = 0.6 \text{ m/s}$.

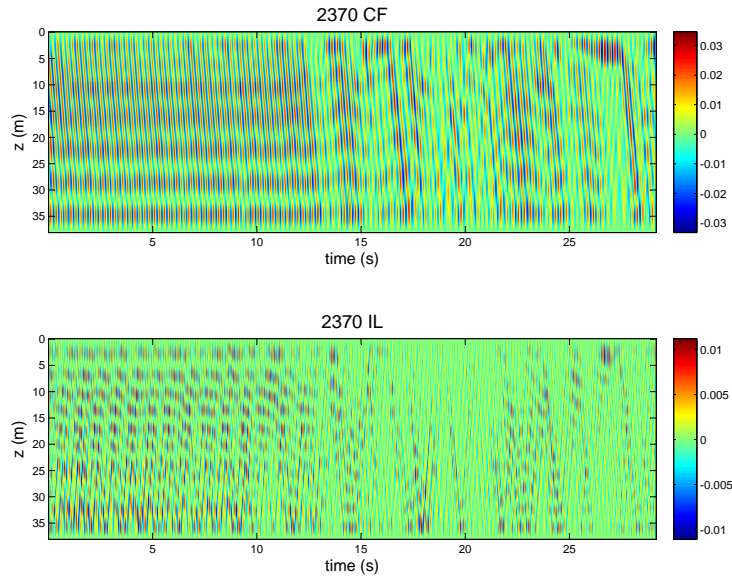


Figure E.4: CF & IL displacement in time and space for NDP shear flow case 2370, $U_{max} = 0.9$ m/s.

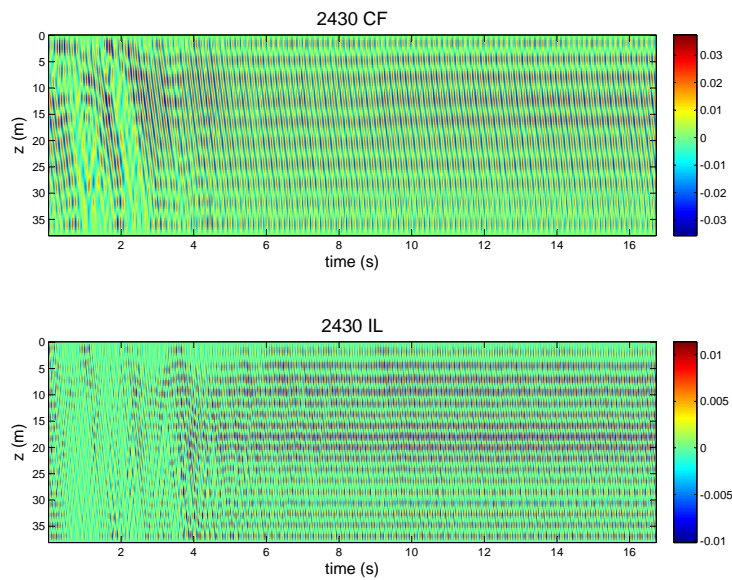
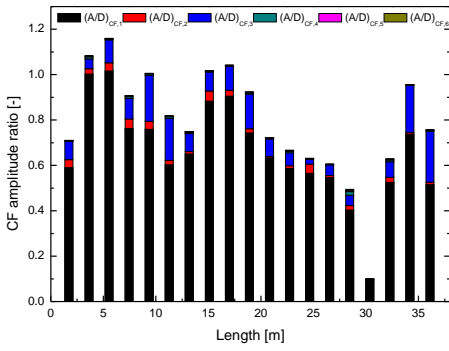


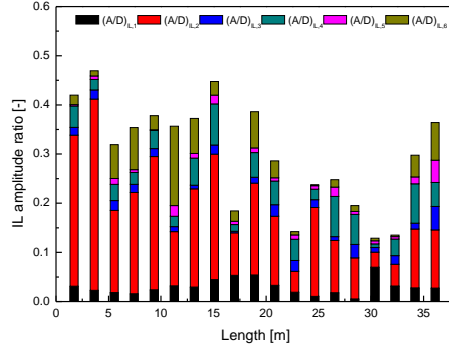
Figure E.5: CF & IL displacement in time and space for NDP shear flow case 2430, $U_{max} = 1.5$ m/s.

Appendix F

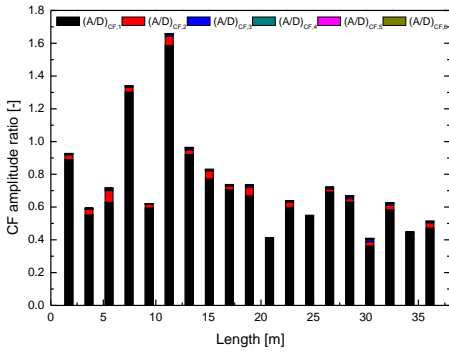
Higher order harmonic displacements and forces



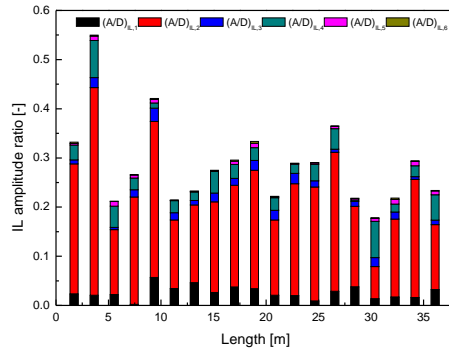
(a) NDP2030 CF



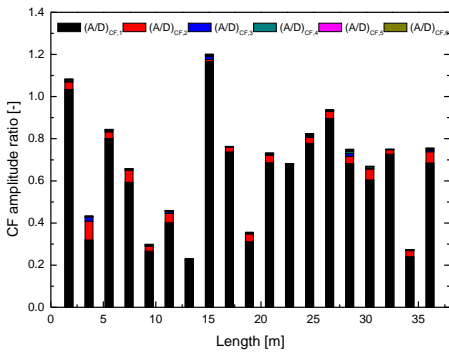
(b) NDP2030 IL



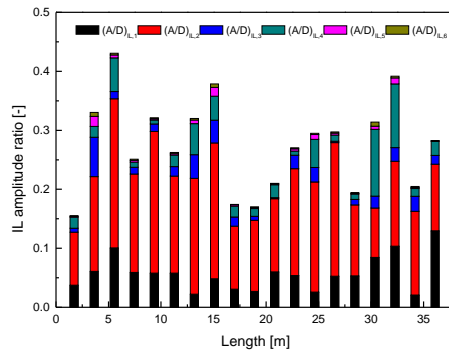
(c) NDP2100 CF



(d) NDP2100 IL

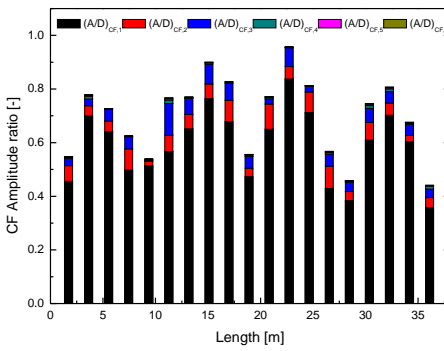


(e) NDP2160 CF

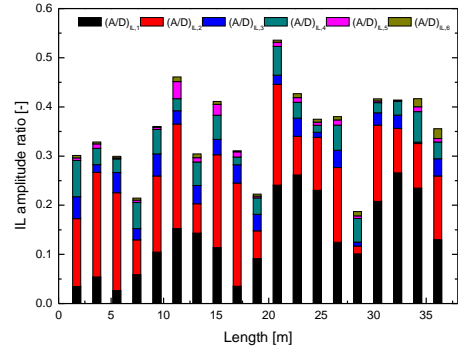


(f) NDP2160 IL

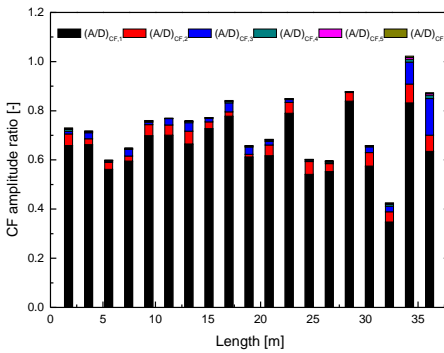
Figure F.1: Amplitude components of three NDP uniform flow cases.



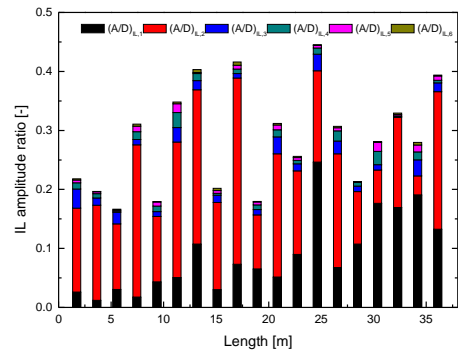
(a) NDP2340 CF



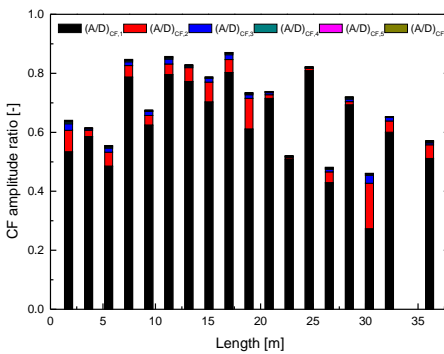
(b) NDP2340 IL



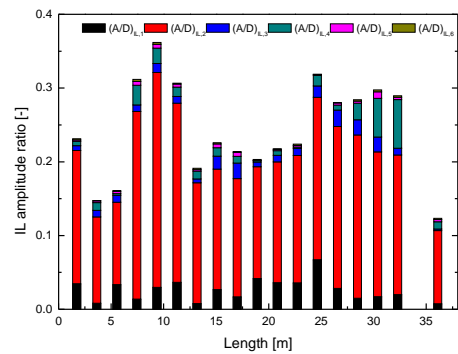
(c) NDP2370 CF



(d) NDP2370 IL



(e) NDP2430 CF



(f) NDP2430 IL

Figure F.2: Amplitude components of three NDP shear flow cases.

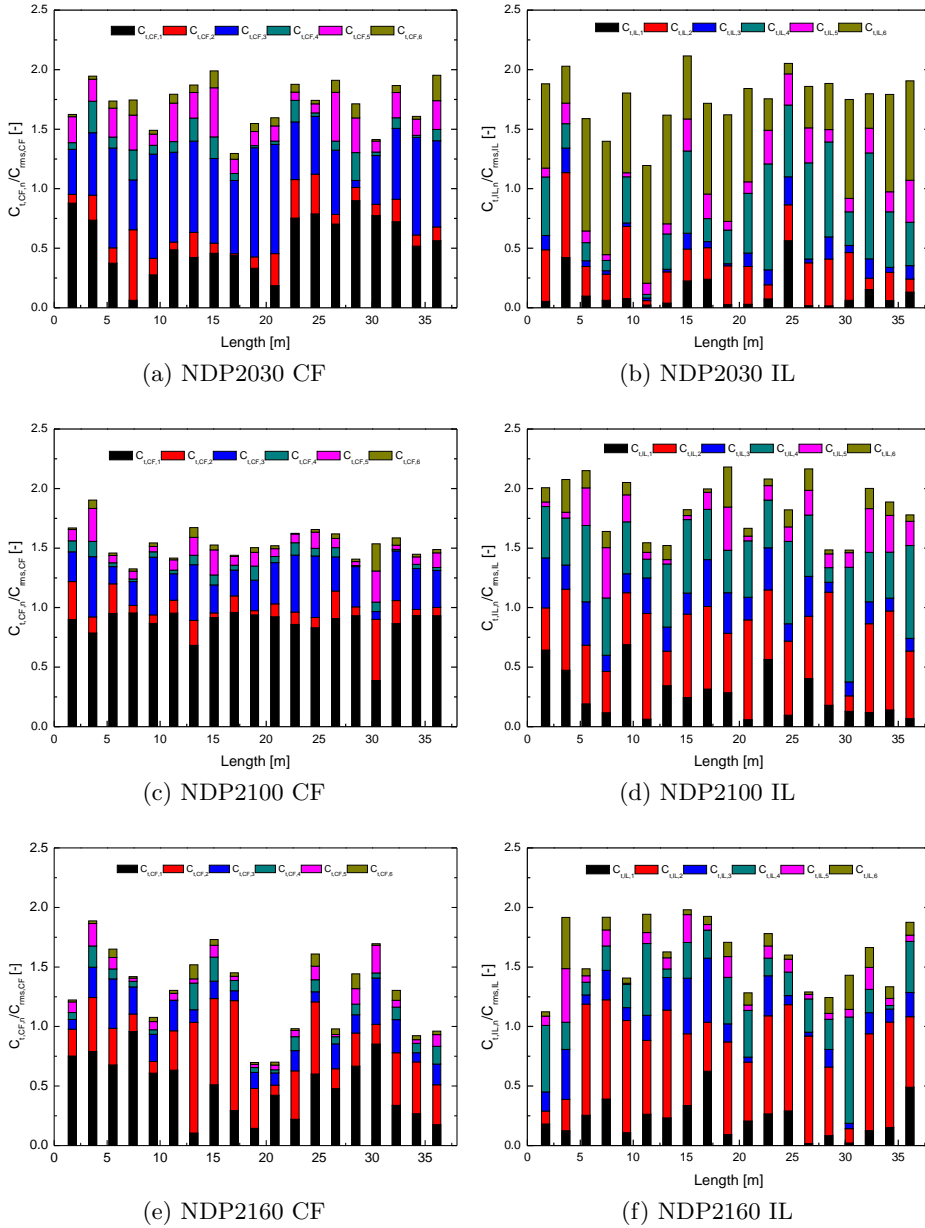


Figure F.3: Force components of three NDP uniform flow cases.

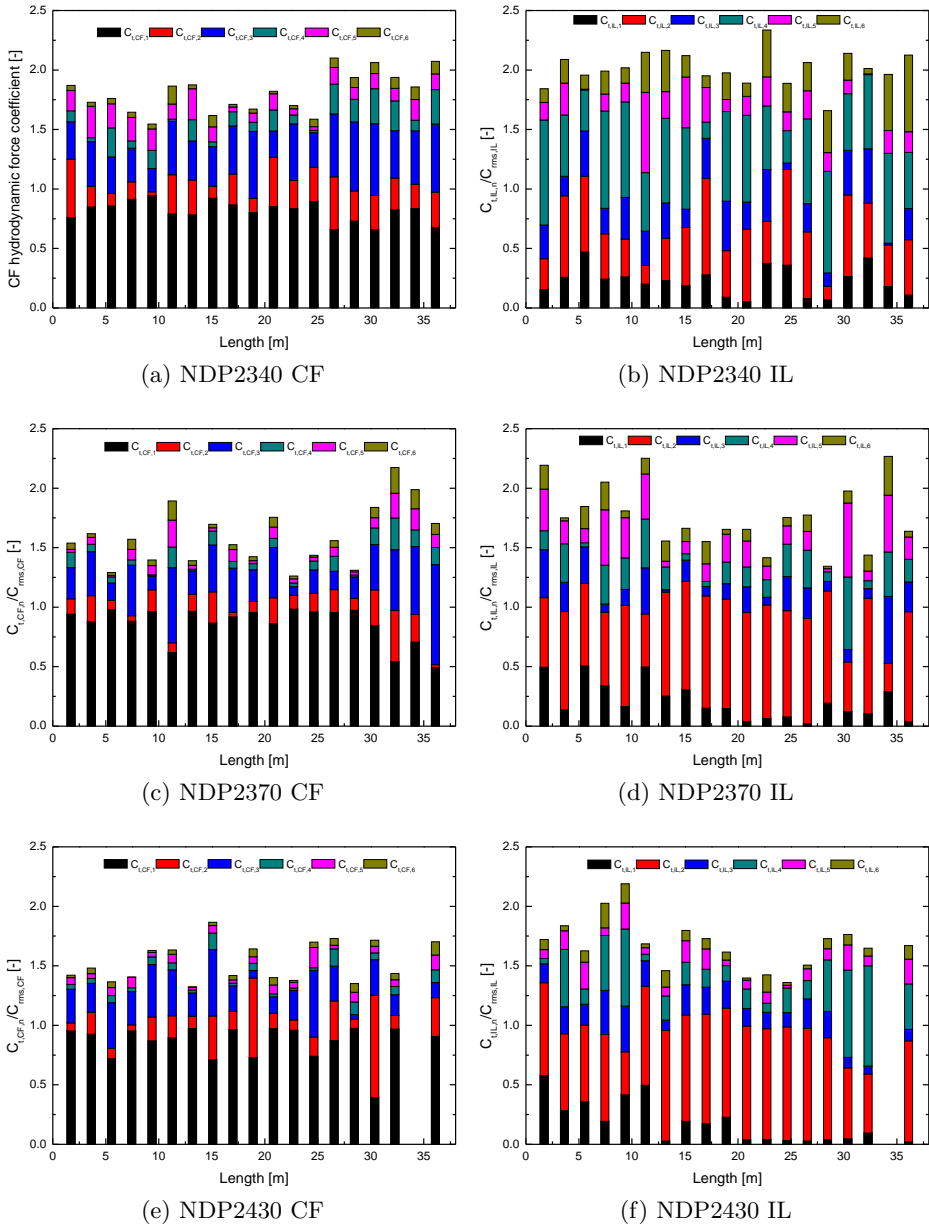


Figure F.4: Force components of three NDP shear flow cases.

Appendix G

Additional 3D simulation results of Case N2340

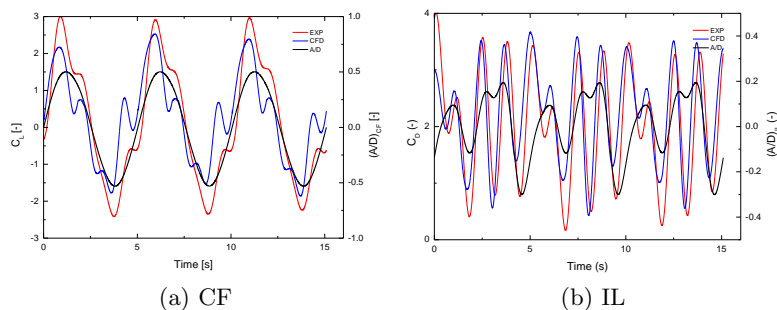


Figure G.1: Hydrodynamic force comparison, Case N23405.

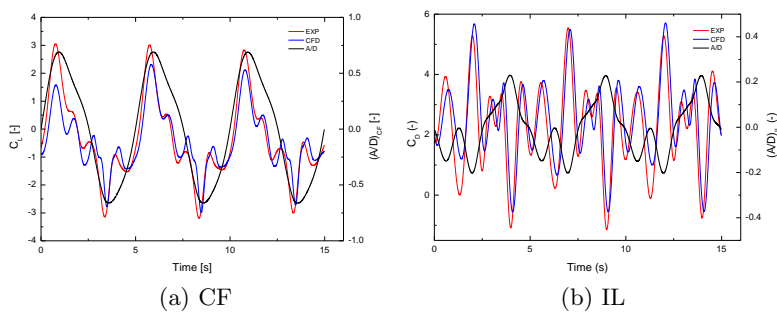


Figure G.2: Hydrodynamic force comparison, Case N23407.

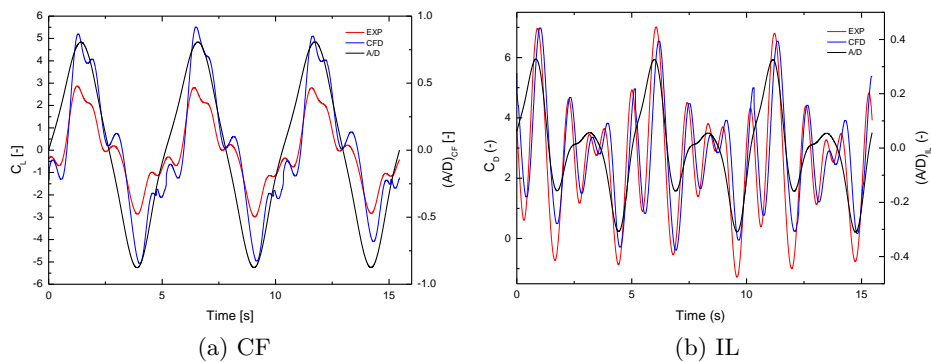


Figure G.3: Hydrodynamic force comparison, Case N23408.

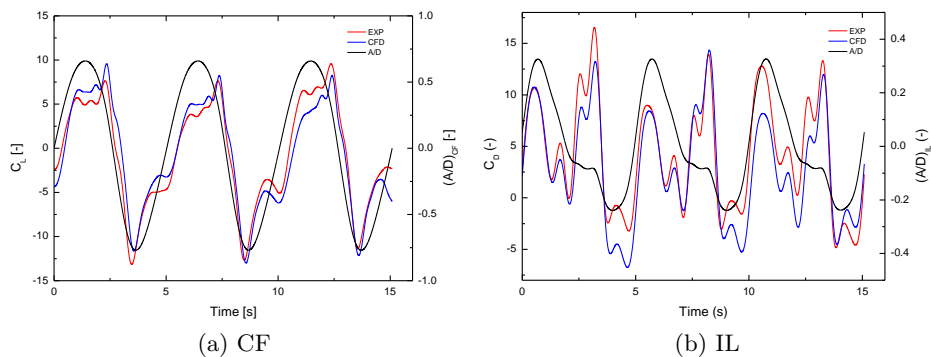


Figure G.4: Hydrodynamic force comparison, Case N234013.

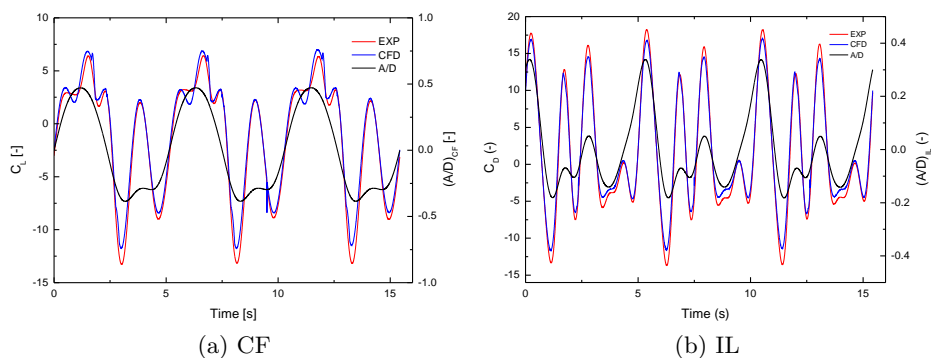


Figure G.5: Hydrodynamic force comparison, Case N234014.

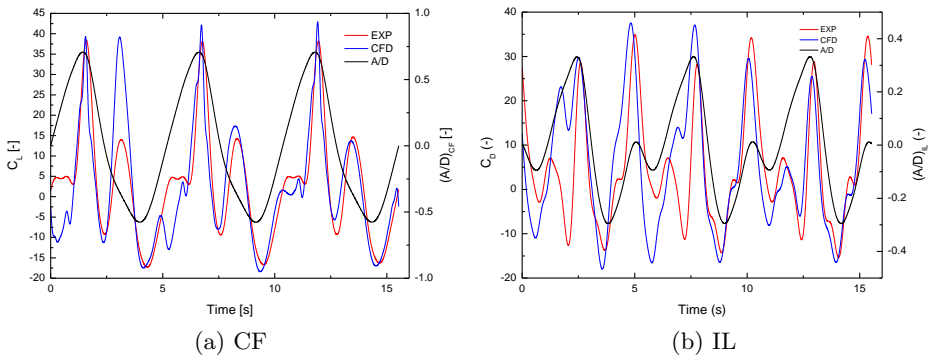


Figure G.6: Hydrodynamic force comparison, Case N234016.

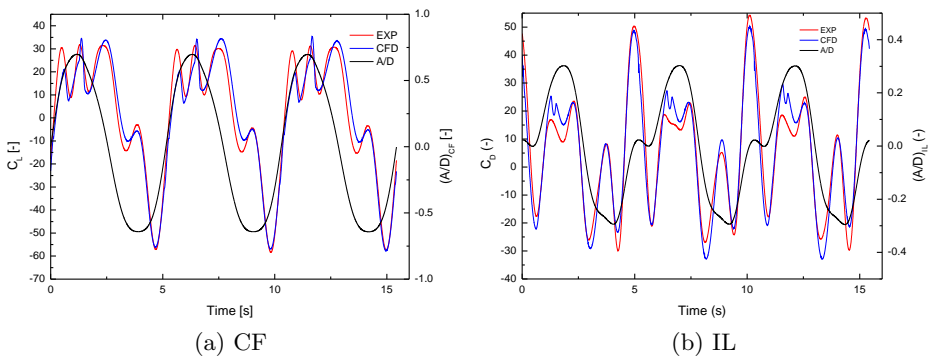


Figure G.7: Hydrodynamic force comparison, Case N234017.

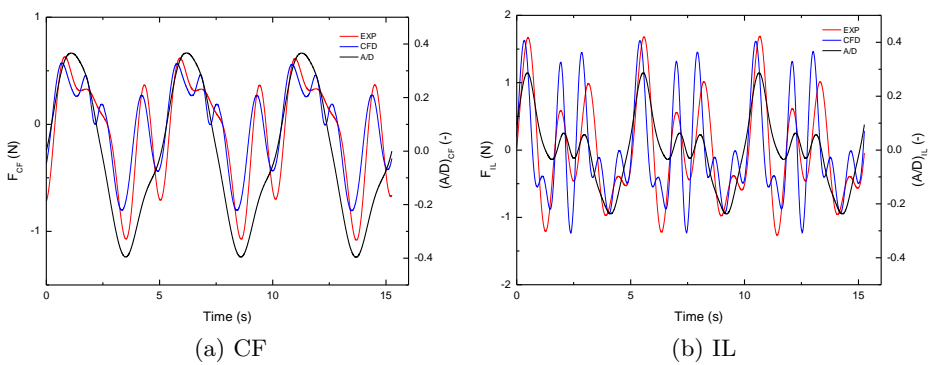


Figure G.8: Hydrodynamic force comparison, Case N234019.

**Previous PhD theses published at the Departement of Marine Technology
(earlier: Faculty of Marine Technology)
NORWEGIAN UNIVERSITY OF SCIENCE AND TECHNOLOGY**

Report No.	Author	Title
	Kavlie, Dag	Optimization of Plane Elastic Grillages, 1967
	Hansen, Hans R.	Man-Machine Communication and Data-Storage Methods in Ship Structural Design, 1971
	Gisvold, Kaare M.	A Method for non-linear mixed -integer programming and its Application to Design Problems, 1971
	Lund, Sverre	Tanker Frame Optimization by means of SUMT-Transformation and Behaviour Models, 1971
	Vinje, Tor	On Vibration of Spherical Shells Interacting with Fluid, 1972
	Lorentz, Jan D.	Tank Arrangement for Crude Oil Carriers in Accordance with the new Anti-Pollution Regulations, 1975
	Carlsen, Carl A.	Computer-Aided Design of Tanker Structures, 1975
	Larsen, Carl M.	Static and Dynamic Analysis of Offshore Pipelines during Installation, 1976
UR-79-01	Bright Hatlestad, MK	The finite element method used in a fatigue evaluation of fixed offshore platforms. (Dr.Ing. Thesis)
UR-79-02	Erik Pettersen, MK	Analysis and design of cellular structures. (Dr.Ing. Thesis)
UR-79-03	Sverre Valsgård, MK	Finite difference and finite element methods applied to nonlinear analysis of plated structures. (Dr.Ing. Thesis)
UR-79-04	Nils T. Nordsve, MK	Finite element collapse analysis of structural members considering imperfections and stresses due to fabrication. (Dr.Ing. Thesis)
UR-79-05	Ivar J. Fylling, MK	Analysis of towline forces in ocean towing systems. (Dr.Ing. Thesis)
UR-80-06	Nils Sandsmark, MM	Analysis of Stationary and Transient Heat Conduction by the Use of the Finite Element Method. (Dr.Ing. Thesis)
UR-80-09	Sverre Haver, MK	Analysis of uncertainties related to the stochastic modeling of ocean waves. (Dr.Ing. Thesis)
UR-81-15	Odland, Jonas	On the Strength of welded Ring stiffened cylindrical Shells primarily subjected to axial Compression
UR-82-17	Engesvik, Knut	Analysis of Uncertainties in the fatigue Capacity of

Welded Joints

UR-82-18	Rye, Henrik	Ocean wave groups
UR-83-30	Eide, Oddvar Inge	On Cumulative Fatigue Damage in Steel Welded Joints
UR-83-33	Mo, Olav	Stochastic Time Domain Analysis of Slender Offshore Structures
UR-83-34	Amdahl, Jørgen	Energy absorption in Ship-platform impacts
UR-84-37	Mørch, Morten	Motions and mooring forces of semi submersibles as determined by full-scale measurements and theoretical analysis
UR-84-38	Soares, C. Guedes	Probabilistic models for load effects in ship structures
UR-84-39	Aarsnes, Jan V.	Current forces on ships
UR-84-40	Czujko, Jerzy	Collapse Analysis of Plates subjected to Biaxial Compression and Lateral Load
UR-85-46	Alf G. Engseth, MK	Finite element collapse analysis of tubular steel offshore structures. (Dr.Ing. Thesis)
UR-86-47	Dengody Sheshappa, MP	A Computer Design Model for Optimizing Fishing Vessel Designs Based on Techno-Economic Analysis. (Dr.Ing. Thesis)
UR-86-48	Vidar Aanesland, MH	A Theoretical and Numerical Study of Ship Wave Resistance. (Dr.Ing. Thesis)
UR-86-49	Heinz-Joachim Wessel, MK	Fracture Mechanics Analysis of Crack Growth in Plate Girders. (Dr.Ing. Thesis)
UR-86-50	Jon Taby, MK	Ultimate and Post-ultimate Strength of Dented Tubular Members. (Dr.Ing. Thesis)
UR-86-51	Walter Lian, MH	A Numerical Study of Two-Dimensional Separated Flow Past Bluff Bodies at Moderate KC-Numbers. (Dr.Ing. Thesis)
UR-86-52	Bjørn Sortland, MH	Force Measurements in Oscillating Flow on Ship Sections and Circular Cylinders in a U-Tube Water Tank. (Dr.Ing. Thesis)
UR-86-53	Kurt Strand, MM	A System Dynamic Approach to One-dimensional Fluid Flow. (Dr.Ing. Thesis)
UR-86-54	Arne Edvin Løken, MH	Three Dimensional Second Order Hydrodynamic Effects on Ocean Structures in Waves. (Dr.Ing. Thesis)
UR-86-55	Sigurd Falch, MH	A Numerical Study of Slamming of Two-Dimensional Bodies. (Dr.Ing. Thesis)
UR-87-56	Arne Braathen, MH	Application of a Vortex Tracking Method to the Prediction of Roll Damping of a Two-Dimension Floating Body. (Dr.Ing. Thesis)

UR-87-57	Bernt Leira, MK	Gaussian Vector Processes for Reliability Analysis involving Wave-Induced Load Effects. (Dr.Ing. Thesis)
UR-87-58	Magnus Småvik, MM	Thermal Load and Process Characteristics in a Two-Stroke Diesel Engine with Thermal Barriers (in Norwegian). (Dr.Ing. Thesis)
MTA-88-59	Bernt Arild Bremdal, MP	An Investigation of Marine Installation Processes – A Knowledge - Based Planning Approach. (Dr.Ing. Thesis)
MTA-88-60	Xu Jun, MK	Non-linear Dynamic Analysis of Space-framed Offshore Structures. (Dr.Ing. Thesis)
MTA-89-61	Gang Miao, MH	Hydrodynamic Forces and Dynamic Responses of Circular Cylinders in Wave Zones. (Dr.Ing. Thesis)
MTA-89-62	Martin Greenhow, MH	Linear and Non-Linear Studies of Waves and Floating Bodies. Part I and Part II. (Dr.Tech. Thesis)
MTA-89-63	Chang Li, MH	Force Coefficients of Spheres and Cubes in Oscillatory Flow with and without Current. (Dr.Ing. Thesis)
MTA-89-64	Hu Ying, MP	A Study of Marketing and Design in Development of Marine Transport Systems. (Dr.Ing. Thesis)
MTA-89-65	Arild Jæger, MH	Seakeeping, Dynamic Stability and Performance of a Wedge Shaped Planing Hull. (Dr.Ing. Thesis)
MTA-89-66	Chan Siu Hung, MM	The dynamic characteristics of tilting-pad bearings
MTA-89-67	Kim Wikstrøm, MP	Analysis av projekteringen for ett offshore projekt. (Licenciat-avhandling)
MTA-89-68	Jiao Guoyang, MK	Reliability Analysis of Crack Growth under Random Loading, considering Model Updating. (Dr.Ing. Thesis)
MTA-89-69	Arnt Olufsen, MK	Uncertainty and Reliability Analysis of Fixed Offshore Structures. (Dr.Ing. Thesis)
MTA-89-70	Wu Yu-Lin, MR	System Reliability Analyses of Offshore Structures using improved Truss and Beam Models. (Dr.Ing. Thesis)
MTA-90-71	Jan Roger Hoff, MH	Three-dimensional Green function of a vessel with forward speed in waves. (Dr.Ing. Thesis)
MTA-90-72	Rong Zhao, MH	Slow-Drift Motions of a Moored Two-Dimensional Body in Irregular Waves. (Dr.Ing. Thesis)
MTA-90-73	Atle Minsaas, MP	Economical Risk Analysis. (Dr.Ing. Thesis)
MTA-90-74	Knut-Aril Farnes, MK	Long-term Statistics of Response in Non-linear Marine Structures. (Dr.Ing. Thesis)
MTA-90-75	Torbjørn Sotberg, MK	Application of Reliability Methods for Safety Assessment of Submarine Pipelines. (Dr.Ing. Thesis)

		Thesis)
MTA-90-76	Zeuthen, Steffen, MP	SEAMAID. A computational model of the design process in a constraint-based logic programming environment. An example from the offshore domain. (Dr.Ing. Thesis)
MTA-91-77	Haagensen, Sven, MM	Fuel Dependant Cyclic Variability in a Spark Ignition Engine - An Optical Approach. (Dr.Ing. Thesis)
MTA-91-78	Løland, Geir, MH	Current forces on and flow through fish farms. (Dr.Ing. Thesis)
MTA-91-79	Hoen, Christopher, MK	System Identification of Structures Excited by Stochastic Load Processes. (Dr.Ing. Thesis)
MTA-91-80	Haugen, Stein, MK	Probabilistic Evaluation of Frequency of Collision between Ships and Offshore Platforms. (Dr.Ing. Thesis)
MTA-91-81	Sødahl, Nils, MK	Methods for Design and Analysis of Flexible Risers. (Dr.Ing. Thesis)
MTA-91-82	Ormberg, Harald, MK	Non-linear Response Analysis of Floating Fish Farm Systems. (Dr.Ing. Thesis)
MTA-91-83	Marley, Mark J., MK	Time Variant Reliability under Fatigue Degradation. (Dr.Ing. Thesis)
MTA-91-84	Krokstad, Jørgen R., MH	Second-order Loads in Multidirectional Seas. (Dr.Ing. Thesis)
MTA-91-85	Molteberg, Gunnar A., MM	The Application of System Identification Techniques to Performance Monitoring of Four Stroke Turbocharged Diesel Engines. (Dr.Ing. Thesis)
MTA-92-86	Mørch, Hans Jørgen Bjelke, MH	Aspects of Hydrofoil Design: with Emphasis on Hydrofoil Interaction in Calm Water. (Dr.Ing. Thesis)
MTA-92-87	Chan Siu Hung, MM	Nonlinear Analysis of Rotordynamic Instabilities in Highspeed Turbomachinery. (Dr.Ing. Thesis)
MTA-92-88	Bessason, Bjarni, MK	Assessment of Earthquake Loading and Response of Seismically Isolated Bridges. (Dr.Ing. Thesis)
MTA-92-89	Langli, Geir, MP	Improving Operational Safety through exploitation of Design Knowledge - an investigation of offshore platform safety. (Dr.Ing. Thesis)
MTA-92-90	Sævik, Svein, MK	On Stresses and Fatigue in Flexible Pipes. (Dr.Ing. Thesis)
MTA-92-91	Ask, Tor Ø., MM	Ignition and Flame Growth in Lean Gas-Air Mixtures. An Experimental Study with a Schlieren System. (Dr.Ing. Thesis)
MTA-86-92	Hessen, Gunnar, MK	Fracture Mechanics Analysis of Stiffened Tubular Members. (Dr.Ing. Thesis)

MTA-93-93	Steinebach, Christian, MM	Knowledge Based Systems for Diagnosis of Rotating Machinery. (Dr.Ing. Thesis)
MTA-93-94	Dalane, Jan Inge, MK	System Reliability in Design and Maintenance of Fixed Offshore Structures. (Dr.Ing. Thesis)
MTA-93-95	Steen, Sverre, MH	Cobblestone Effect on SES. (Dr.Ing. Thesis)
MTA-93-96	Karunakaran, Daniel, MK	Nonlinear Dynamic Response and Reliability Analysis of Drag-dominated Offshore Platforms. (Dr.Ing. Thesis)
MTA-93-97	Hagen, Arnulf, MP	The Framework of a Design Process Language. (Dr.Ing. Thesis)
MTA-93-98	Nordrik, Rune, MM	Investigation of Spark Ignition and Autoignition in Methane and Air Using Computational Fluid Dynamics and Chemical Reaction Kinetics. A Numerical Study of Ignition Processes in Internal Combustion Engines. (Dr.Ing. Thesis)
MTA-94-99	Passano, Elizabeth, MK	Efficient Analysis of Nonlinear Slender Marine Structures. (Dr.Ing. Thesis)
MTA-94-100	Kvålsvold, Jan, MH	Hydroelastic Modelling of Wetdeck Slamming on Multihull Vessels. (Dr.Ing. Thesis)
MTA-94-102	Bech, Sidsel M., MK	Experimental and Numerical Determination of Stiffness and Strength of GRP/PVC Sandwich Structures. (Dr.Ing. Thesis)
MTA-95-103	Paulsen, Hallvard, MM	A Study of Transient Jet and Spray using a Schlieren Method and Digital Image Processing. (Dr.Ing. Thesis)
MTA-95-104	Hovde, Geir Olav, MK	Fatigue and Overload Reliability of Offshore Structural Systems, Considering the Effect of Inspection and Repair. (Dr.Ing. Thesis)
MTA-95-105	Wang, Xiaozhi, MK	Reliability Analysis of Production Ships with Emphasis on Load Combination and Ultimate Strength. (Dr.Ing. Thesis)
MTA-95-106	Ulstein, Tore, MH	Nonlinear Effects of a Flexible Stern Seal Bag on Cobblestone Oscillations of an SES. (Dr.Ing. Thesis)
MTA-95-107	Solaas, Frøydis, MH	Analytical and Numerical Studies of Sloshing in Tanks. (Dr.Ing. Thesis)
MTA-95-108	Hellan, Øyvind, MK	Nonlinear Pushover and Cyclic Analyses in Ultimate Limit State Design and Reassessment of Tubular Steel Offshore Structures. (Dr.Ing. Thesis)
MTA-95-109	Hermundstad, Ole A., MK	Theoretical and Experimental Hydroelastic Analysis of High Speed Vessels. (Dr.Ing. Thesis)
MTA-96-110	Bratland, Anne K., MH	Wave-Current Interaction Effects on Large-Volume Bodies in Water of Finite Depth. (Dr.Ing. Thesis)
MTA-96-111	Herfjord, Kjell, MH	A Study of Two-dimensional Separated Flow by a Combination of the Finite Element Method and

		Navier-Stokes Equations. (Dr.Ing. Thesis)
MTA-96-112	Æsøy, Vilmar, MM	Hot Surface Assisted Compression Ignition in a Direct Injection Natural Gas Engine. (Dr.Ing. Thesis)
MTA-96-113	Eknes, Monika L., MK	Escalation Scenarios Initiated by Gas Explosions on Offshore Installations. (Dr.Ing. Thesis)
MTA-96-114	Erikstad, Stein O., MP	A Decision Support Model for Preliminary Ship Design. (Dr.Ing. Thesis)
MTA-96-115	Pedersen, Egil, MH	A Nautical Study of Towed Marine Seismic Streamer Cable Configurations. (Dr.Ing. Thesis)
MTA-97-116	Moksnes, Paul O., MM	Modelling Two-Phase Thermo-Fluid Systems Using Bond Graphs. (Dr.Ing. Thesis)
MTA-97-117	Halse, Karl H., MK	On Vortex Shedding and Prediction of Vortex-Induced Vibrations of Circular Cylinders. (Dr.Ing. Thesis)
MTA-97-118	Igländ, Ragnar T., MK	Reliability Analysis of Pipelines during Laying, considering Ultimate Strength under Combined Loads. (Dr.Ing. Thesis)
MTA-97-119	Pedersen, Hans-P., MP	Levendefiskteknologi for fiskefartøy. (Dr.Ing. Thesis)
MTA-98-120	Vikestad, Kyrre, MK	Multi-Frequency Response of a Cylinder Subjected to Vortex Shedding and Support Motions. (Dr.Ing. Thesis)
MTA-98-121	Azadi, Mohammad R. E., MK	Analysis of Static and Dynamic Pile-Soil-Jacket Behaviour. (Dr.Ing. Thesis)
MTA-98-122	Ulltang, Terje, MP	A Communication Model for Product Information. (Dr.Ing. Thesis)
MTA-98-123	Torbergsen, Erik, MM	Impeller/Diffuser Interaction Forces in Centrifugal Pumps. (Dr.Ing. Thesis)
MTA-98-124	Hansen, Edmond, MH	A Discrete Element Model to Study Marginal Ice Zone Dynamics and the Behaviour of Vessels Moored in Broken Ice. (Dr.Ing. Thesis)
MTA-98-125	Videiro, Paulo M., MK	Reliability Based Design of Marine Structures. (Dr.Ing. Thesis)
MTA-99-126	Mainçon, Philippe, MK	Fatigue Reliability of Long Welds Application to Titanium Risers. (Dr.Ing. Thesis)
MTA-99-127	Haugen, Elin M., MH	Hydroelastic Analysis of Slamming on Stiffened Plates with Application to Catamaran Wetdecks. (Dr.Ing. Thesis)
MTA-99-128	Langhelle, Nina K., MK	Experimental Validation and Calibration of Nonlinear Finite Element Models for Use in Design of Aluminium Structures Exposed to Fire. (Dr.Ing. Thesis)
MTA-99-	Berstad, Are J., MK	Calculation of Fatigue Damage in Ship Structures.

129		(Dr.Ing. Thesis)
MTA-99-130	Andersen, Trond M., MM	Short Term Maintenance Planning. (Dr.Ing. Thesis)
MTA-99-131	Tveiten, Bård Wathne, MK	Fatigue Assessment of Welded Aluminium Ship Details. (Dr.Ing. Thesis)
MTA-99-132	Søreide, Fredrik, MP	Applications of underwater technology in deep water archaeology. Principles and practice. (Dr.Ing. Thesis)
MTA-99-133	Tønnessen, Rune, MH	A Finite Element Method Applied to Unsteady Viscous Flow Around 2D Blunt Bodies With Sharp Corners. (Dr.Ing. Thesis)
MTA-99-134	Elvekrok, Dag R., MP	Engineering Integration in Field Development Projects in the Norwegian Oil and Gas Industry. The Supplier Management of Norge. (Dr.Ing. Thesis)
MTA-99-135	Fagerholt, Kjetil, MP	Optimeringsbaserte Metoder for Ruteplanlegging innen skipsfart. (Dr.Ing. Thesis)
MTA-99-136	Bysveen, Marie, MM	Visualization in Two Directions on a Dynamic Combustion Rig for Studies of Fuel Quality. (Dr.Ing. Thesis)
MTA-2000-137	Storteig, Eskild, MM	Dynamic characteristics and leakage performance of liquid annular seals in centrifugal pumps. (Dr.Ing. Thesis)
MTA-2000-138	Sagli, Gro, MK	Model uncertainty and simplified estimates of long term extremes of hull girder loads in ships. (Dr.Ing. Thesis)
MTA-2000-139	Tronstad, Harald, MK	Nonlinear analysis and design of cable net structures like fishing gear based on the finite element method. (Dr.Ing. Thesis)
MTA-2000-140	Kroneberg, André, MP	Innovation in shipping by using scenarios. (Dr.Ing. Thesis)
MTA-2000-141	Haslum, Herbjørn Alf, MH	Simplified methods applied to nonlinear motion of spar platforms. (Dr.Ing. Thesis)
MTA-2001-142	Samdal, Ole Johan, MM	Modelling of Degradation Mechanisms and Stressor Interaction on Static Mechanical Equipment Residual Lifetime. (Dr.Ing. Thesis)
MTA-2001-143	Baarholm, Rolf Jarle, MH	Theoretical and experimental studies of wave impact underneath decks of offshore platforms. (Dr.Ing. Thesis)
MTA-2001-144	Wang, Lihua, MK	Probabilistic Analysis of Nonlinear Wave-induced Loads on Ships. (Dr.Ing. Thesis)
MTA-2001-145	Kristensen, Odd H. Holt, MK	Ultimate Capacity of Aluminium Plates under Multiple Loads, Considering HAZ Properties. (Dr.Ing. Thesis)
MTA-2001-146	Greco, Marilena, MH	A Two-Dimensional Study of Green-Water Loading. (Dr.Ing. Thesis)

MTA-2001-147	Heggelund, Svein E., MK	Calculation of Global Design Loads and Load Effects in Large High Speed Catamarans. (Dr.Ing. Thesis)
MTA-2001-148	Babalola, Olusegun T., MK	Fatigue Strength of Titanium Risers – Defect Sensitivity. (Dr.Ing. Thesis)
MTA-2001-149	Mohammed, Abuu K., MK	Nonlinear Shell Finite Elements for Ultimate Strength and Collapse Analysis of Ship Structures. (Dr.Ing. Thesis)
MTA-2002-150	Holmedal, Lars E., MH	Wave-current interactions in the vicinity of the sea bed. (Dr.Ing. Thesis)
MTA-2002-151	Rognebakke, Olav F., MH	Sloshing in rectangular tanks and interaction with ship motions. (Dr.Ing. Thesis)
MTA-2002-152	Lader, Pål Furset, MH	Geometry and Kinematics of Breaking Waves. (Dr.Ing. Thesis)
MTA-2002-153	Yang, Qinzhen, MH	Wash and wave resistance of ships in finite water depth. (Dr.Ing. Thesis)
MTA-2002-154	Melhus, Øyvinn, MM	Utilization of VOC in Diesel Engines. Ignition and combustion of VOC released by crude oil tankers. (Dr.Ing. Thesis)
MTA-2002-155	Ronæss, Marit, MH	Wave Induced Motions of Two Ships Advancing on Parallel Course. (Dr.Ing. Thesis)
MTA-2002-156	Økland, Ole D., MK	Numerical and experimental investigation of whipping in twin hull vessels exposed to severe wet deck slamming. (Dr.Ing. Thesis)
MTA-2002-157	Ge, Chunhua, MK	Global Hydroelastic Response of Catamarans due to Wet Deck Slamming. (Dr.Ing. Thesis)
MTA-2002-158	Byklum, Eirik, MK	Nonlinear Shell Finite Elements for Ultimate Strength and Collapse Analysis of Ship Structures. (Dr.Ing. Thesis)
IMT-2003-1	Chen, Haibo, MK	Probabilistic Evaluation of FPSO-Tanker Collision in Tandem Offloading Operation. (Dr.Ing. Thesis)
IMT-2003-2	Skaugset, Kjetil Bjørn, MK	On the Suppression of Vortex Induced Vibrations of Circular Cylinders by Radial Water Jets. (Dr.Ing. Thesis)
IMT-2003-3	Chezhan, Muthu	Three-Dimensional Analysis of Slamming. (Dr.Ing. Thesis)
IMT-2003-4	Buhaug, Øyvind	Deposit Formation on Cylinder Liner Surfaces in Medium Speed Engines. (Dr.Ing. Thesis)
IMT-2003-5	Tregde, Vidar	Aspects of Ship Design: Optimization of Aft Hull with Inverse Geometry Design. (Dr.Ing. Thesis)

IMT-2003-6	Wist, Hanne Therese	Statistical Properties of Successive Ocean Wave Parameters. (Dr.Ing. Thesis)
IMT-2004-7	Ransau, Samuel	Numerical Methods for Flows with Evolving Interfaces. (Dr.Ing. Thesis)
IMT-2004-8	Soma, Torkel	Blue-Chip or Sub-Standard. A data interrogation approach of identity safety characteristics of shipping organization. (Dr.Ing. Thesis)
IMT-2004-9	Ersdal, Svein	An experimental study of hydrodynamic forces on cylinders and cables in near axial flow. (Dr.Ing. Thesis)
IMT-2005-10	Brodtkorb, Per Andreas	The Probability of Occurrence of Dangerous Wave Situations at Sea. (Dr.Ing. Thesis)
IMT-2005-11	Yttervik, Rune	Ocean current variability in relation to offshore engineering. (Dr.Ing. Thesis)
IMT-2005-12	Fredheim, Arne	Current Forces on Net-Structures. (Dr.Ing. Thesis)
IMT-2005-13	Heggernes, Kjetil	Flow around marine structures. (Dr.Ing. Thesis)
IMT-2005-14	Fouques, Sebastien	Lagrangian Modelling of Ocean Surface Waves and Synthetic Aperture Radar Wave Measurements. (Dr.Ing. Thesis)
IMT-2006-15	Holm, Håvard	Numerical calculation of viscous free surface flow around marine structures. (Dr.Ing. Thesis)
IMT-2006-16	Bjørheim, Lars G.	Failure Assessment of Long Through Thickness Fatigue Cracks in Ship Hulls. (Dr.Ing. Thesis)
IMT-2006-17	Hansson, Lisbeth	Safety Management for Prevention of Occupational Accidents. (Dr.Ing. Thesis)
IMT-2006-18	Zhu, Xinying	Application of the CIP Method to Strongly Nonlinear Wave-Body Interaction Problems. (Dr.Ing. Thesis)
IMT-2006-19	Reite, Karl Johan	Modelling and Control of Trawl Systems. (Dr.Ing. Thesis)
IMT-2006-20	Smogeli, Øyvind Notland	Control of Marine Propellers. From Normal to Extreme Conditions. (Dr.Ing. Thesis)
IMT-2007-21	Storhaug, Gaute	Experimental Investigation of Wave Induced Vibrations and Their Effect on the Fatigue Loading of Ships. (Dr.Ing. Thesis)
IMT-2007-22	Sun, Hui	A Boundary Element Method Applied to Strongly Nonlinear Wave-Body Interaction Problems. (PhD Thesis, CeSOS)
IMT-2007-23	Rustad, Anne Marthine	Modelling and Control of Top Tensioned Risers. (PhD Thesis, CeSOS)
IMT-2007-24	Johansen, Vegar	Modelling flexible slender system for real-time simulations and control applications

IMT-2007-25	Wroldsen, Anders Sunde	Modelling and control of tensegrity structures. (PhD Thesis, CeSOS)
IMT-2007-26	Aronsen, Kristoffer Høye	An experimental investigation of in-line and combined inline and cross flow vortex induced vibrations. (Dr. avhandling, IMT)
IMT-2007-27	Gao, Zhen	Stochastic Response Analysis of Mooring Systems with Emphasis on Frequency-domain Analysis of Fatigue due to Wide-band Response Processes (PhD Thesis, CeSOS)
IMT-2007-28	Thorstensen, Tom Anders	Lifetime Profit Modelling of Ageing Systems Utilizing Information about Technical Condition. (Dr.ing. thesis, IMT)
IMT-2008-29	Berntsen, Per Ivar B.	Structural Reliability Based Position Mooring. (PhD-Thesis, IMT)
IMT-2008-30	Ye, Naiquan	Fatigue Assessment of Aluminium Welded Box-stiffener Joints in Ships (Dr.ing. thesis, IMT)
IMT-2008-31	Radan, Damir	Integrated Control of Marine Electrical Power Systems. (PhD-Thesis, IMT)
IMT-2008-32	Thomassen, Paul	Methods for Dynamic Response Analysis and Fatigue Life Estimation of Floating Fish Cages. (Dr.ing. thesis, IMT)
IMT-2008-33	Pákozdi, Csaba	A Smoothed Particle Hydrodynamics Study of Two-dimensional Nonlinear Sloshing in Rectangular Tanks. (Dr.ing.thesis, IMT/ CeSOS)
IMT-2007-34	Grytøyr, Guttorm	A Higher-Order Boundary Element Method and Applications to Marine Hydrodynamics. (Dr.ing.thesis, IMT)
IMT-2008-35	Drummen, Ingo	Experimental and Numerical Investigation of Nonlinear Wave-Induced Load Effects in Containerships considering Hydroelasticity. (PhD thesis, CeSOS)
IMT-2008-36	Skejic, Renato	Maneuvering and Seakeeping of a Singel Ship and of Two Ships in Interaction. (PhD-Thesis, CeSOS)
IMT-2008-37	Harlem, Alf	An Age-Based Replacement Model for Repairable Systems with Attention to High-Speed Marine Diesel Engines. (PhD-Thesis, IMT)
IMT-2008-38	Alsos, Hagbart S.	Ship Grounding. Analysis of Ductile Fracture, Bottom Damage and Hull Girder Response. (PhD-thesis, IMT)
IMT-2008-39	Graczyk, Mateusz	Experimental Investigation of Sloshing Loading and Load Effects in Membrane LNG Tanks Subjected to Random Excitation. (PhD-thesis, CeSOS)
IMT-2008-40	Taghipour, Reza	Efficient Prediction of Dynamic Response for Flexible amd Multi-body Marine Structures. (PhD-thesis, CeSOS)
IMT-2008-41	Ruth, Eivind	Propulsion control and thrust allocation on marine

		vessels. (PhD thesis, CeSOS)
IMT-2008-42	Nystad, Bent Helge	Technical Condition Indexes and Remaining Useful Life of Aggregated Systems. PhD thesis, IMT
IMT-2008-43	Soni, Prashant Kumar	Hydrodynamic Coefficients for Vortex Induced Vibrations of Flexible Beams, PhD thesis, CeSOS
IMT-2009-43	Amlashi, Hadi K.K.	Ultimate Strength and Reliability-based Design of Ship Hulls with Emphasis on Combined Global and Local Loads. PhD Thesis, IMT
IMT-2009-44	Pedersen, Tom Arne	Bond Graph Modelling of Marine Power Systems. PhD Thesis, IMT
IMT-2009-45	Kristiansen, Trygve	Two-Dimensional Numerical and Experimental Studies of Piston-Mode Resonance. PhD-Thesis, CeSOS
IMT-2009-46	Ong, Muk Chen	Applications of a Standard High Reynolds Number Model and a Stochastic Scour Prediction Model for Marine Structures. PhD-thesis, IMT
IMT-2009-47	Hong, Lin	Simplified Analysis and Design of Ships subjected to Collision and Grounding. PhD-thesis, IMT
IMT-2009-48	Koushan, Kamran	Vortex Induced Vibrations of Free Span Pipelines, PhD thesis, IMT
IMT-2009-49	Korsvik, Jarl Eirik	Heuristic Methods for Ship Routing and Scheduling. PhD-thesis, IMT
IMT-2009-50	Lee, Jihoon	Experimental Investigation and Numerical in Analyzing the Ocean Current Displacement of Longlines. Ph.d.-Thesis, IMT.
IMT-2009-51	Vestbøstad, Tone Gran	A Numerical Study of Wave-in-Deck Impact using a Two-Dimensional Constrained Interpolation Profile Method, Ph.d.thesis, CeSOS.
IMT-2009-52	Bruun, Kristine	Bond Graph Modelling of Fuel Cells for Marine Power Plants. Ph.d.-thesis, IMT
IMT 2009-53	Holstad, Anders	Numerical Investigation of Turbulence in a Skewed Three-Dimensional Channel Flow, Ph.d.-thesis, IMT.
IMT 2009-54	Ayala-Uraga, Efrén	Reliability-Based Assessment of Deteriorating Ship-shaped Offshore Structures, Ph.d.-thesis, IMT
IMT 2009-55	Kong, Xiangjun	A Numerical Study of a Damaged Ship in Beam Sea Waves. Ph.d.-thesis, IMT/CeSOS.
IMT 2010-56	Kristiansen, David	Wave Induced Effects on Floaters of Aquaculture Plants, Ph.d.-thesis, IMT/CeSOS.
IMT 2010-57	Ludvigsen, Martin	An ROV-Toolbox for Optical and Acoustic Scientific Seabed Investigation. Ph.d.-thesis IMT.
IMT 2010-58	Hals, Jørgen	Modelling and Phase Control of Wave-Energy Converters. Ph.d.thesis, CeSOS.

IMT 2010- 59	Shu, Zhi	Uncertainty Assessment of Wave Loads and Ultimate Strength of Tankers and Bulk Carriers in a Reliability Framework. Ph.d. Thesis, IMT/ CeSOS
IMT 2010-60	Shao, Yanlin	Numerical Potential-Flow Studies on Weakly-Nonlinear Wave-Body Interactions with/without Small Forward Speed, Ph.d.thesis,CeSOS.
IMT 2010-61	Califano, Andrea	Dynamic Loads on Marine Propellers due to Intermittent Ventilation. Ph.d.thesis, IMT.
IMT 2010-62	El Khoury, George	Numerical Simulations of Massively Separated Turbulent Flows, Ph.d.-thesis, IMT
IMT 2010-63	Seim, Knut Sponheim	Mixing Process in Dense Overflows with Emphasis on the Faroe Bank Channel Overflow. Ph.d.thesis, IMT
IMT 2010-64	Jia, Huirong	Structural Analysis of Intact and Damaged Ships in a Collision Risk Analysis Perspective. Ph.d.thesis CeSoS.
IMT 2010-65	Jiao, Linlin	Wave-Induced Effects on a Pontoon-type Very Large Floating Structures (VLFS). Ph.D.-thesis, CeSOS.
IMT 2010-66	Abrahamsen, Bjørn Christian	Sloshing Induced Tank Roof with Entrapped Air Pocket. Ph.d.thesis, CeSOS.
IMT 2011-67	Karimirad, Madjid	Stochastic Dynamic Response Analysis of Spar-Type Wind Turbines with Catenary or Taut Mooring Systems. Ph.d.-thesis, CeSOS.
IMT - 2011-68	Erlend Meland	Condition Monitoring of Safety Critical Valves. Ph.d.-thesis, IMT.
IMT – 2011-69	Yang, Limin	Stochastic Dynamic System Analysis of Wave Energy Converter with Hydraulic Power Take-Off, with Particular Reference to Wear Damage Analysis, Ph.d. Thesis, CeSOS.
IMT – 2011-70	Visscher, Jan	Application of Particle Image Velocimetry on Turbulent Marine Flows, Ph.d.Thesis, IMT.
IMT – 2011-71	Su, Biao	Numerical Predictions of Global and Local Ice Loads on Ships. Ph.d.Thesis, CeSOS.
IMT – 2011-72	Liu, Zhenhui	Analytical and Numerical Analysis of Iceberg Collision with Ship Structures. Ph.d. Thesis, IMT.
IMT – 2011-73	Aarsæther, Karl Gunnar	Modeling and Analysis of Ship Traffic by Observation and Numerical Simulation. Ph.d.Thesis, IMT.
IMT – 2011-74	Wu, Jie	Hydrodynamic Force Identification from Stochastic Vortex Induced Vibration Experiments with Slender Beams. Ph.d.Thesis, IMT.
IMT – 2011-75	Amini, Hamid	Azimuth Propulsors in Off-design Conditions. Ph.d.Thesis, IMT.

IMT – 2011-76	Nguyen, Tan-Hoi	Toward a System of Real-Time Prediction and Monitoring of Bottom Damage Conditions During Ship Grounding. Ph.d.thesis, IMT.
IMT- 2011-77	Tavakoli, Mohammad T.	Assessment of Oil Spill in Ship Collision and Grounding, Ph.d.thesis, IMT.
IMT- 2011-78	Guo, Bingjie	Numerical and Experimental Investigation of Added Resistance in Waves. Ph.d.Thesis, IMT.
IMT- 2011-79	Chen, Qiaofeng	Ultimate Strength of Aluminium Panels, considering HAZ Effects, IMT
IMT- 2012-80	Kota, Ravikiran S.	Wave Loads on Decks of Offshore Structures in Random Seas. Ph.d.thesis, CeSOS.
IMT- 2012-81	Sten, Ronny	Dynamic Simulation of Deep Water Drilling Risers with Heave Compensating Sysetm, IMT.
IMT- 2012-82	Berle, Øyvind	Risk and resilience in global maritime supply chains, IMT.
IMT- 2012-83	Fang, Shaoji	Fault Tolerant Position Mooring Control Based on Structural Reliability, CeSOS.
IMT- 2012-84	You, Jikun	Numerical studies on wave forces and moored ship motions in intermediate and shallow water, CeSOS.
IMT- 2012-85	Xiang ,Xu	Maneuvering of two interacting ships in waves, CeSOS
IMT- 2012-86	Dong, Wenbin	Time-domain fatigue response and reliability analysis of offshore wind turbines with emphasis on welded tubular joints and gear components, CeSOS
IMT- 2012-87	Al Ryati, Nabil	Technical Condition Indexes for Auxiliary Marine Diesel Engines, IMT
IMT- 2012-88	Zhu, Suji	Investigation of Wave-Induced Nonlinear Load Effects in Open Ships considering Hull Girder Vibrations in Bending and Torsion, CeSOS
IMT- 2012-89	Ushakov, Sergey	Particulate matter emission characteristics from diesel enignes operating on conventional and alternative marine fuels, IMT
IMT- 2012-90	Zhou, Li	Numerical and Experimental Investigation of Station-keeping in Level Ice, CeSOS
IMT- 2013-1	Yin, Decao	Experimental and Numerical Analysis of Combined In-line and Cross-flow Vortex Induced Vibrations, CeSOS